COHERENT MANIPULATION OF SINGLE ATOM QUBITS USING RYDBERG STATES

by

Erich Urban

A dissertation submitted in partial fulfillment of
the requirements for the degree of

Doctor of Philosophy

(Physics)

at the

UNIVERSITY OF WISCONSIN–MADISON

2009

To Amanda and my Parents

ACKNOWLEDGMENTS

When I entered graduate school, the quantum computing laboratory in the basement of Sterling Hall consisted of a single optical table that looked more like an air hockey table than a functioning quantum computer. Without a doubt, developing a project of this magnitude required a lot of help and support to culminate in the experiments that I present in this thesis. I am truly thankful for all of the people that have helped me along the way.

First and foremost I would like to thank my Ph.D. advisor Thad Walker and my co-advisor Mark Saffman for inviting me into that rather empty laboratory many years ago. They have provided me with the opportunities and support necessary to succeed. In particular I would like to thank Thad for sharing his vast knowledge and unique perspective of atomic physics with me. His feedback and encouragement has been invaluable.

I have also been fortunate to receive the guidance from several truly great postdocs: Marie Delany, Charles Sukenik, Pasad Kulatunga and Deniz Yavuz. In particular I would like to thank Pasad for imparting some of his practical experimental wisdom upon me and Deniz for *always* answering my questions in a way that I could understand and often providing me a completely new way of understanding physics.

I have also benefited from having worked along side a phenomenal group of graduate students. In particular I was truly fortunate to have been given the opportunity to work with Todd Johnson. Our research styles complemented each other very well [Johnson, 2008]. I would like to thank him for teaching me the joys of making order of magnitude estimates as we took our weekly lunch trips to get burritos. I am relieved to know that this experiment is being passed along to some very talented graduate students: Larry Isenhower, Thomas Henage, and Alex Gill. I wish them continued success and hope they derive the same joy

from the experiment that I have found. I would like to thank Will Williams, the members of 'Thadlab′, the members of the Yavuz lab, and all of the other physics graduates and undergraduates that I have meet along the way.

I am deeply grateful for my family and the support that they have given me. My parents and sister always have words of encouragement and have been there to listen to all of my ideas. They have truly given me a wonderful life.

I owe a great deal to my wife, Amanda. Meeting her was easily the most important part of my graduate career. She has been infinitely patient and supportive of my late nights in lab and is always there to make me smile. Thank you for sharing your life with me and repeatedly reminding me that there is more to life than physics.

ABSTRACT

This thesis presents experimental observations of the coherent manipulations of Rubidium-87 atoms via two photon excitations. Atoms are cooled using a magneto-optical trap (MOT) into two far off resonance traps (FORT) that are separated by 10 micrometers. State sensitive single atom detection is performed by gathering the fluorescence signal of two atoms trapped in the FORT potentials with an electron-multiplying CCD camera. A custom built multiplexing optical system is used to individually address the FORT potentials. A microwave modulated 780nm laser is used to coherently Rabi flop atoms between the F=1 and F=2 hyperfine ground states via two photon excitations. Cavity stabilized lasers at 780nm and 480nm are used to conduct two photon excitations of F=2 hyperfine ground state atoms to Rydberg states with principal quantum numbers ranging from n=43 to n=97.

This experiment is the first to observe coherent Rabi oscillations at megahertz rates between ground and Rydberg levels. These coherent Rydberg Rabi oscillations are used to demonstrate Rydberg blockade at a single atom level for the first time. The Rydberg Rabi oscillations of a target atom are observed to be 75% blockaded by the presence of a Rydberg atom more than 10 micrometers away. This paper reports on the preliminary work towards the first neutral atom controlled-NOT (CNOT) gate, and on preliminary experiments working towards deterministic loading of single atoms in a FORT potential.

DISCARD THIS PAGE

TABLE OF CONTENTS

Page

Appendix

Page

DISCARD THIS PAGE

LIST OF FIGURES

Appendix
Figure Page

Appendix
Figure Page

Appendix
Figure Page

Appendix
Figure Page

Appendix
Figure Page

Appendix
Figure Page

Appendix
Figure Page

Appendix
Figure Page

Appendix
Figure Page

Appendix
Figure Page

Appendix
Figure Page

Figure Page

Appendix
Figure

Figure Page

Figure Page

COHERENT MANIPULATION OF SINGLE ATOM QUBITS USING RYDBERG STATES

Erich Urban

Under the supervision of Professor Thad Walker

At the University of Wisconsin-Madison

This thesis presents experimental observations of the coherent manipulations of Rubidium-87 atoms via two photon excitations. Atoms are cooled using a magneto-optical trap (MOT) into two far off resonance traps (FORT) that are separated by 10 micrometers. State sensitive single atom detection is performed by gathering the fluorescence signal of two atoms trapped in the FORT potentials with an electron-multiplying CCD camera. A custom built multiplexing optical system is used to individually address the FORT potentials. A microwave modulated 780nm laser is used to coherently Rabi flop atoms between the F=1 and F=2 hyperfine ground states via two photon excitations. Cavity stabilized lasers at 780nm and 480nm are used to conduct two photon excitations of F=2 hyperfine ground state atoms to Rydberg states with principal quantum numbers ranging from n=43 to n=97.

This experiment is the first to observe coherent Rabi oscillations at megahertz rates between ground and Rydberg levels. These coherent Rydberg Rabi oscillations are used to demonstrate Rydberg blockade at a single atom level for the first time. The Rydberg Rabi oscillations of a target atom are observed to be 75% blockaded by the presence of a Rydberg atom more than 10 micrometers away. This paper reports on the preliminary work towards the first neutral atom controlled-NOT (CNOT) gate, and on preliminary experiments working towards deterministic loading of single atoms in a FORT potential.

Thad Walker

Chapter 1

Defining a Neutral Atom Qubit

1.1 Introduction to the DiVincenzo Criteria

Moores law describes the long-term trend in the history of classical computing hardware where the number of transistors that can be cost effectively placed on a computer chip has doubled nearly every two years. It is anticipated that at some point this trend will reach a point of diminishing returns and a better means of information processing will need to be developed. Furthermore, one of the most recognized proponents of quantum computing, Richard Feynman, observed that it appears impossible to efficiently simulate the evolution of a quantum mechanical system on a classical computer. This desire to fabricate smaller and more efficient systems capable of using entanglement and the superposition of states as a means of processing information is a significant driving force in neutral atom quantum computing.

David DiVincenzo is credited with formalizing the requirements of actualizing a realistic quantum computer [DiVincenzo, 2000]. He outlines five criteria that must be met in order to actualize the benefits of a quantum computing architecture. The DiVincenzo criteria help distinguish quantum computers from devices that perform calculations classically and systems that are simply quantum mechanical in nature. A quantum computer must possess well defined scalable quantum bits that can be initialized to arbitrary values and allow for reliable readout of each quantum bit, or qubit. Furthermore, the quantum computer requires a universal set of entangling gates, whose rates exceed the decoherence of these quantum bits.

At its most fundamental level, this experiment investigates coherent manipulations of neutral Rubidium-87 atoms confined in optical dipole traps. However, this research is motivated by the desire to utilize coherent state manipulation to implement a neutral atom quantum computer. These cornerstones of quantum computing motivate many of the important design choices made in how we cool and confine our atom samples, the coherent processes we use to drive the atomic wave functions, and which atomic states we choose to drive the ^{87}Rb atoms between. This chapter begins by outlining the fundamental requirements of quantum computing and how they have influenced our experimental set-up. This chapter concludes with a summary of the experiments performed to help lay the foundation for a neutral atom quantum computer.

1.2 A Well Defined Qubit

As stated earlier, a quantum computer must be a physically scalable device with well defined qubits. A qubit is an abstract entity similar to a classical bit of information. Unlike a classical bit that can be represented as a 0 or 1, qubits are quantum mechanical in nature and can be represented by a superposition of logic states 0 or 1. Using Dirac notation the state of a qubit can be represented by a wavefunction.

$$|\psi\rangle = \alpha|0\rangle + \beta|1\rangle$$

where

$$|\alpha|^2 + |\beta|^2 = 1$$

The abstract quantum state of a qubit can also be represented pictorially, as in Figure 1.1. Here the vector $|\psi\rangle$ represents the qubit state on the Bloch sphere. Since $|\alpha|^2 + |\beta|^2 = 1$, the vector $|\psi\rangle$ always lies on the two dimensional surface of the Bloch sphere which contains all possible qubit states. The qubit states $|0\rangle$ and $|1\rangle$ lie at opposite poles of the Bloch sphere, while the equatorial positions of the Bloch sphere are equally weighted superpositions of $|0\rangle$ and $|1\rangle$ with varying degrees of relative phase. The amplitudes α and β can be negative and

imaginary thus expressing the relative phase as well as the amplitudes of the superposition states $|0\rangle$ and $|1\rangle$.

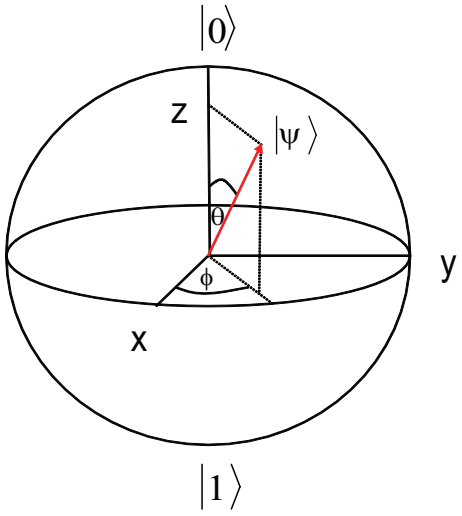

Figure 1.1 The Bloch sphere representation of a single qubit state $|\psi\rangle$. The angle θ expresses the relative amplitudes of the $|0\rangle$ and $|1\rangle$ superposition of states. The relative phase information of the qubit is contained within the variable ϕ. Any point on the Bloch sphere is given by: $|\psi\rangle = \cos(\frac{\theta}{2})|0\rangle + e^{i\phi}\sin(\frac{\theta}{2})|1\rangle$.

The states $|0\rangle$ and $|1\rangle$ can be represented directly by atomic wavefunctions or through linear combinations of atomic wavefunctions thus creating decoherence free sub-spaces [Lidar et al., 1998]. The physical manifestations of our qubits utilize single neutral Rubidium-87 atoms cooled and confined within optical dipole traps. Using neutral atoms and confining them in an optical well helps mitigate the interaction of the environment with our qubits. Likewise, this prevents the neutral atoms from perturbing each other, thus eliminating any undesirable ground state atom-atom interactions. We choose to define particular magnetic sublevels of the ground state hyperfine energy levels of the atoms as our logical $|0\rangle$ and $|1\rangle$ states. A variety of energy levels have been identified as possible candidates for qubit basis states [Yavuz et al., 2006], [Urban et al., 2009]. Our work focuses on using the following

pairs of Rubidium-87 magnetic hyperfine levels as basis states.

$$|0\rangle \longrightarrow |5s_{1/2}, F = 1, m_F = 0\rangle$$

$$|1\rangle \longrightarrow |5s_{1/2}, F = 2, m_F = 0\rangle$$

and

$$|0\rangle \longrightarrow |5s_{1/2}, F = 1, m_F = 1\rangle$$

$$|1\rangle \longrightarrow |5s_{1/2}, F = 2, m_F = 2\rangle$$

In accordance with the DiVincenzo criteria we use well characterized quantum systems to represent our qubits. The hyperfine structure and Zeeman splittings of Rubidium-87 have been thoroughly studied for laser cooled ^{87}Rb frequency standards [Bize et al., 1999], [Steck]. The internal Hamiltonian of the qubits is well understood, and through using laser cooling and trapping techniques the ground state atom-atom interactions between two qubits are negligible.

The coherent manipulation of these qubit states requires laser beams to drive the atoms from one atomic state to another. We implement optical systems capable of addressing single qubit sites for the purpose of coupling of external optical fields to an individual qubit. These optical fields are used to conduct two photon excitations of our neutral atoms. One set of laser fields is used to coherently drive the atom between the $|0\rangle$ and $|1\rangle$ logic states. A second set of laser fields are used to coherently drive atoms in the $|1\rangle$ logic state into a highly excited energy level. Atomic states with large principal quantum numbers ($n > 20$) are referred to as Rydberg states.

1.3 Constructing a Universal Set of Gates

In classical computing all logic operations can be decomposed into a compilation of NAND gates. Consequently, the NAND gate is considered a universal gate for classical computing. Similarly quantum computing complex logic gates can be decomposed into a compilation of simpler operations. There exists a universal set of gates, from which any

other operation can be derived. The universal set of gates can be thought of in terms of single qubit operations and qubit entangling operations. In general terms a single qubit operation is a unitary operation that transforms the quantum logic state of a single qubit. During a unitary operation, the qubit state $|\psi\rangle$ rotates about a vector $\hat{n}$ on the Bloch sphere (Figure 1.2). In regards to single qubit operations a universal set of gates allows us to

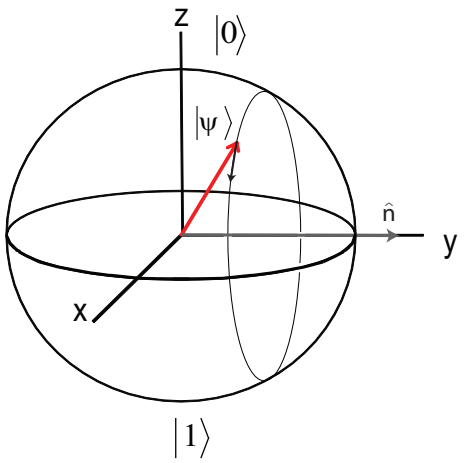

Figure 1.2 Bloch sphere illustrating a qubit rotation about vector $\hat{n}$.

reach any point on the surface of the Bloch sphere to some arbitrary level of accuracy. As previously mentioned we use two photon excitations to drive our atomic qubit states between the logic states $|0\rangle$ and $|1\rangle$. We demonstrate through two-photon Rabi flopping and Ramsey experiments our ability to perform single qubit logic operations (see Chapter 8).

Two qubit, or conditional operations, alter the state of a target qubit based on the logic state of a control qubit. Coupled with the appropriate single qubit operations the controlled-NOT operation (CNOT) can be used to create all other multiqubit operations [Nielsen and Chuang, 2000]. The CNOT operation flips the input state of a target qubit, $|0\rangle \leftrightarrow |1\rangle$, if and only if the control qubit is in the $|1\rangle$ logic state. Several methods of generating a two qubit CNOT gate via Rydberg-Rydberg interactions have been proposed [Jaksch et al., 2000], [Lukin et al., 2001].

As previously mentioned we have developed a laser system capable of optically addressing and promoting individual qubits into Rydberg states via two photon excitations. Our ability to generate Rydberg atoms has provided us with a means of generating an entangling gate. The van der Waals interaction between Rydberg-Rydberg atoms is utilized to entangle the states of two neighboring atoms. This entanglement is developed into two qubit gate.

1.4 Initialization

Qubit initialization requires that at the start of every calculation our qubits must be prepared into a desired state. Placing a random value into a computer′s register without knowledge of what the input state was would be pointless. Much like a classically computed algorithm, quantum information processing performed on randomly assigned qubit states would be meaningless. For this reason DiVincenzo points out the computing requirement that quantum registers should be initialized to a known value before the start of a computation [DiVincenzo, 2000]. Furthermore, quantum error correction requires a continuous, fresh supply of qubits in low-entropy states. Without quantum error correction to compensate for imperfect logic gates and qubit decoherence quantum calculations would become prohibitively difficult [Nielsen and Chuang, 2000]. For these reasons we must require the ability to initialize the atoms into a particular state at the beginning of every calculation. In our experiments this is accomplished through laser cooling techniques which optically pump atoms into particular atomic states. It is feasible to optically pump the atoms with high efficiencies to the $|F = 2, m_F = 2\rangle$ [Johnson et al., 2008], [Urban et al., 2009] and the $|F = 2, m_F = 0\rangle$ states. Our definition of the qubit logic states show that this procedure is equivalent to initializing the qubits to the logical $|1\rangle$ state.

1.5 Decoherence Versus Gate Time

The coupling between a quantum system and its environment inevitably lead the quantum system to evolve in an irreversible manner. The dynamics of the quantum system become non-unitary and information from the local quantum system appears to be lost. For

this reason, decoherence is seen as a serious problem for quantum information processing. Fault tolerant quantum computation algorithms have been proposed to deal with these issues. However, the majority of these fault tolerant schemes still require the time scale of qubit decoherence to be on the order of 10^4 to 10^5 longer than the time required to conduct an individual gate [DiVincenzo, 2000]. Work performed by [Rakreungdet et al., 2008] demonstrates a fidelity of 0.99 for single qubit rotations. We have demonstrated single qubit clock rates on the order of 1 MHz and have seen decoherence times on the order of 1 ms. Our current work on Rydberg blockade mechanisms required about 5μs to entangle adjacent atoms. With additional laser power and enhancements to our atomic cooling and trapping techniques it is imaginable that one can achieve faster gate times and decoherence rates capable of sustaining meaningful quantum computations.

1.6 Readout

The ability to measure the states of specific qubits within our system is another fundamental requirement of quantum computing. Ultimately we must possess the ability to see the result of our calculation. Detecting a single atom and determining its state with high fidelity is a nontrivial matter. Spatial resolution of each qubit is achieved via fluorescence imaging of the atoms trapped in the optical potentials. The spatial distribution of the fluorescence image is magnified and projected onto a CCD camera such that each site is resolvable. In determining the state of the qubit we perform a destructive measurement. Atoms in the $|1\rangle$ state are ejected from the qubit register with an on resonant laser beam. Any atoms remaining in the register must be in the $|0\rangle$ state. Ejecting atoms of particular states and scattering light off the remaining atoms is clearly a destructive measurement. Upon making the measurement, the quantum register will need to be reloaded and reinitialized. Despite the fact that this measurement technique is destructive, it still provides us with a means of determining the states of each quantum bit individually.

In the future, it may be beneficial to attain the ability to perform nondemolition measurements. As described by [DiVincenzo, 2000], nondemolition measurements have the advantage that performing a measurement can simultaneously readout the atoms and initialize the qubits. While not a requirement of quantum computing, nondemolition measurements would prove beneficial to the experiment.

1.7 Scalability

The viability of the quantum computer also depends upon the system′s scalability. A scalable quantum computer remains suitably efficient and practical when applied to large situations. For instance, a quantum computer implemented to factor a number is scalable if the system remains efficient and practical as the size of the number we require factored increases. Scalability is thus dependent upon the efficiency of our quantum algorithm as well as the practicalities of implementing the algorithm. A variety of efficient quantum algorithms are known to exist [Nielsen and Chuang, 2000], [Shor, 1996]. Therefore, we must create a system in which the number of physical resources and time required to implement an algorithm scales polynominally with the size of the computation.

Our experiment demonstrates a linear scaling for the number of resources required to generate the atom trapping sites of the quantum register. Specifically, the amount of laser power required to generate additional optical traps to hold more qubits has a polynomial scaling. However, we are still limited by stochastic methods of loading atoms into the quantum register. Therefore, the number of required qubits places an exponentially increasing demand on the time required to properly initialize the system. Deterministic loading protocols utilizing dipole-dipole Rydberg atom interactions have been proposed to solve this problem. It is conceivable to use dipole blockade as a method of preparing a single atom in each optical well [Saffman and Walker, 2002]. Recent experiments have demonstrated that sub-Poissonian loading of our optical potentials is possible utilizing van der Waals interactions. With more optimal Rydberg pulse sequences a more deterministic loading protocol

is foreseeable. Attaining scalability will demonstrate that all five DiVincenzo criteria are attainable within the architecture of this quantum computing scheme.

1.8 Summary of Thesis

This thesis begins (Chapters 2, 3, 4, 5, 6) by providing descriptions of the experimental apparatus used to study the coherent manipulation of Rubidium-87 atoms. Chapter 2 provides a very broad overview of the primary components and experimental protocols used throughout this thesis. This overview illustrates the function of these optical assemblies and how they are combined to work as a single experimental apparatus. The experimental protocol section outlined at the end of Chapter 2 provides descriptions of the various laser pulse sequences implemented to characterize experimental parameters and measure the interaction of our optical driving fields with the trapped atoms.

Chapter 3 provides a detailed description of the Magneto Optical Trapping (MOT) laser system, optics, and magnetic fields used to cool atoms from a background atomic vapor. The atom density of the MOT cloud is of order 10^9 atoms per cm^3. The flexibility of the MOT laser system also enables fluorescence imaging of the Rubidium atoms, optical pumping, and a state selective means of ejecting atoms from our atomic lattices. This chapter also explains the MOT experimental timing protocols used to execute these tasks.

Chapter 4 provides background information on the optical dipole traps used to confine our atoms. This chapter goes on to discuss the optical array used to simultaneously focus two 1064nm laser beams to $1/e^2$ Gaussian beam waists of $\sim 3.0\mu$m. These foci are separated by 10.2μm. The resulting far off resonance traps (FORTs) have trap depths of approximately 5.0mK in temperature units. This chapter also introduces an optical array used to simultaneously generate 6 FORTs illustrating the scalability of the optical potentials.

Chapter 5 introduces the camera system used to image atoms confined within the FORT potentials. The system has a total optical efficiency of approximately 8% and an effective pixel size of $2.15\mu\text{m} \times 2.15\mu$m. The spatial resolution and high signal to noise ratio of the camera enable the detection of single atoms trapped within the optical potentials. This

chapter outlines how the camera is calibrated to identify single atom signals. Using these single atom signal calibrations the FORT lifetime is measured to be 3.7 seconds. The imaging system also provides a means of characterizing average atom distributions and temperatures within the FORT potentials. In the 5.0mK FORT the atoms are typically $\sim$200μK and occupy a Gaussian distributions of 5.6μm along the trapping laser axis and 0.45μm in the transverse direction.

Chapter 6 describes the optical systems used to individually address the FORT potentials. A microwave modulated $\sim$780nm laser diode is used to simultaneously generate two laser frequencies capable of driving an atom between the $|5s_{1/2}, F = 1, m_F = 0\rangle \leftrightarrow |5s_{1/2}, F = 2, m_F = 0\rangle$ ground state energy levels via two photon Raman transitions. A second two photon Raman laser system ($\lambda_1\sim$480nm and $\lambda_2\sim$780nm) is used to drive atoms between $|5s_{1/2}, F = 2\rangle \leftrightarrow |nd_{5/2}\langle$, where n $>$ 40. This chapter also describes the acousto-optic modulator (AOM) based system used to focus the laser beams to $\sim$10μm beam waists and rapidly scan the laser beams between the two FORT potentials.

Chapter 7 provides theoretical background on the two photon Raman transitions used in this experiment. This discussion reviews how a three level ladder type atomic structure can be simplified using the adiabatic elimination of the intermediate state. Through eliminating the intermediate state the two photon Raman transition can be modeled by an apparent two level system. A similar analysis is applied for a three level Λ system. The ladder and Λ type atomic structures are respectively used to represent the two photon transitions between the $|5s_{1/2}, F = 2\rangle \leftrightarrow |nd_{5/2}\rangle$ states and the $|5s_{1/2}, F = 1, m_F = 0\rangle \leftrightarrow |5s_{1/2}, F = 2, m_F = 0\rangle$ states. These simplifications enable us to develop evolution matrices describing the effective Rabi flopping observed for these transitions.

Chapter 8 summarizes the methods and results obtained from performing two photon Raman transitions between the $|5s_{1/2}, F = 1, m_F = 0\rangle \leftrightarrow |5s_{1/2}, F = 2, m_F = 0\rangle$ states. This chapter begins with an explanation of how state dependent atom readout is performed. State dependent atom readout enables us to perform single atom two photon Raman spectroscopy between the two m_F=0 ground states of the atom. The atom is found to be resonant with the

driving field when the driving laser fields have a difference frequency equal to 6834.48MHz. Two photon Raman spectroscopy also provides a means of measuring the magnetic bias field used to Zeeman split the magnetic sublevels of the F=1 and F=2 hyperfine ground states. The field used in these experiments is observed to be 3.6 gauss. This chapter also presents single atom Rabi flopping between the $|5s_{1/2}, F = 1, m_F = 0\rangle \leftrightarrow |5s_{1/2}, F = 2, m_F = 0\rangle$ states. The effective two photon Rabi flopping rate is observed to be $2\pi\times$0.910MHz. The level of crosstalk observed from this particular experiment is approximately 0.275. Data is also presented showing that crosstalk between neighboring FORT potentials can be mitigated through the use of smaller addressing laser beams and a smaller intermediate laser detuning. The level of crosstalk under these conditions is suppressed to 1.44×10^{-3}.

The application of the two photon excitation lasers cause a differential AC Stark shift of the ground state energy levels. By applying two excitation pulses to an atom separated by a delay time, it is possible to observe a phase precession of the unperturbed atomic energy levels relative to the driving fields. For our particular experimental conditions this phase precession is observed to be $2\pi\times$188kHz. The application of two excitation pulses are also used to observe Ramsey fringes. Plotting the contrast of the Ramsey fringes as a function of time provide us with an estimate of our qubit decoherence rate. The T_2 time is observed to be approximately 870μs.

Chapter 9 documents two photon excitations between ground and Rydberg states. This chapter begins with a discussion of how Rydberg atoms are detected through photoionization. This method of detection is determined to be approximately 90% efficient for n$\sim$97. Two photon Raman spectroscopy measurements of the $|5s_{1/2}, F = 2, m_F = 2\rangle \leftrightarrow |79d_{5/2}, m_J = +1/2\rangle$ and $|5s_{1/2}, F = 2, m_F = 0\rangle \leftrightarrow |97d_{5/2}, m_J = +5/2\rangle$ transitions are performed. The laser powers and polarizations used in each of these experiments are outlined in this chapter as well. The FWHM of these transitions are 0.700MHz and 1.26MHz respectively. Two photon spectroscopy is used to measure the magnetic bias field applied while exciting atoms to n=97. We also perform Rabi flopping experiments between ground and Rydberg states. The effective Rabi flopping rate observed for the $|5s_{1/2}, F = 2, m_F = 2\rangle \leftrightarrow |79d_{5/2}, m_J =$

$+1/2\rangle$ transition is approximately $2\pi\times0.51$MHz. Crosstalk between adjacent FORT sites is observed to be negligible for Rydberg excitations.

In Chapter 10 we examine Rydberg-Rydberg van der Waals interactions. This chapter reports on the observed dephasing of an atomic ensemble confined in a single FORT potential being driven to a Rydberg state. This chapter also reports on the observation of Rydberg blockade between two single atoms confined in separate FORT potentials. The probability of exciting a target atom into a Rydberg state can be drastically reduced by the presence of an adjacent Rydberg atom. The effective Rabi flopping amplitude of the $|5s_{1/2}, F = 2, m_F = 2\rangle \leftrightarrow |79d_{5/2}, m_J = +1/2\rangle$ transition is observed to be reduced from $\sim$0.4 to $\sim$0.2. This observation agrees well with an average effective blockade shift of $\sim$1.1MHz. A stronger blockade effect is observed by implementing excitations to a higher principal quantum number (n=90).

Chapter 11 concentrates on the implementation of a CNOT gate. This chapter reviews several proposed methods of how this entangling operation can be implemented. The experimental protocol used to generate an entangling gate is also outlined in this chapter. To evaluate the entangling operation we measure the probabilities of obtaining each possible output state from each of the four possible input states. This preliminary attempt at generating a CNOT gate has a fidelity of 54%. The entangling operation is also performed upon superposition input states. The observed output states are consistent with those of entangled states.

Chapter 12 focuses on the possibility of using a blockade mechanism to achieve deterministic single atom loading within an optical potential. This provides a description of the Rydberg and ground state excitation pulse scheme used to try and attain sub-Poissonian atom loading in an FORT potential. Approximately 33% of the trails result in a single atom being loaded into the FORT.

Chapter 2

Experimental Overview

The primary focus of this experiment is directed towards the development of a quantum computer using neutral atoms as qubits. Like a classical computer, this system requires memory, a means of manipulating the logic states held in the memory, and a means of reading out the logic states after performing a calculation. The quantum register stores information in neutral atom qubits. This register is generated by laser cooling and trapping atoms into optical potentials. Atomic state manipulations, carried out by optical excitations, are used to control the logic states of the qubits. These laser driven excitations are used to perform both single qubit operations, and entangling quantum logic gates. By detecting the fluorescence of the neutral atoms we can readout the qubit logic states. This chapter briefly outlines the optical systems used in atom trapping, optical excitations, and atom detection. The later half of this chapter illustrates the modular nature of the experiment protocols used to characterize our qubits and carry out qubit operations.

2.1 Overview of Experimental Apparatus

The optical systems outlined in Figure 2.1 displays the physical layout of the modular laser and optics assemblies used by this experiment. The custom frequency narrowed lasers were all linked via optical fibers to the various optical systems before being transmitted to the experiment′s vacuum chamber. The primary laser systems used to trap the atoms are the magneto optical trap (MOT) lasers, discussed in Section 3.2, and the far off resonant trap (FORT) laser, discussed in Section 4.2. There are two main laser systems used to

drive the atoms between specific atomic states. State manipulation between the ground and various Rydberg states use a cavity stabilized 780nm and a second harmonic generation (SHG) 480nm laser. The SHG laser uses a 960nm laser that is locked to the same reference cavity as the 780nm laser. These systems are discussed further in Section 6.3. In order to perform stimulated Raman transitions between two hyperfine ground states we use a cavity filtered microwave modulated 780nm laser (see Section 6.2).

The laser systems are complemented by precision optics for the purpose of stably aligning the various laser beams to the vacuum chamber. These optical assemblies surround a Kimball Physics 4.8″ dia spherical cube vacuum chamber. The optical fields of the MOT are created by three sets of nearly orthogonal beams. Water cooled solenoids are used to generate the MOT′s requisite magnetic field gradients. An optical assembly, oriented above the vacuum chamber, enables us to optically pump the atom samples. These optical systems are discussed further in Section 3.3. An optical train is used to create the FORT potentials capable of isolating single atoms. This assembly is discussed further in Section 4.3. A high numerical aperture camera is used for fluorescence imaging of the trapped atoms (see Section 5.1). The manipulation of the neutral atom qubits is performed via two optical assemblies located on opposite sides of the vacuum chamber. The design of these optical arrays is discussed further in chapter 6.

2.2 Experimental Protocols

These components briefly outlined in Section 2.1 are used together to trap single atoms, perform single qubit rotations, and investigate two qubit entangling operations. Like the physical hardware used to study these phenomena, the experimental protocols implemented are also designed to be modular in nature. A National Instruments VXI-1501 controller is used to control the sequence of laser pulses within an experiment cycle. A typical experiment cycle consists of three segments: atom loading, camera readout and atom manipulation. The exact parameters of each segment are varied depending upon the requirements of each experiment. A typical experiment cycle begins by loading atoms into a MOT and then transferring

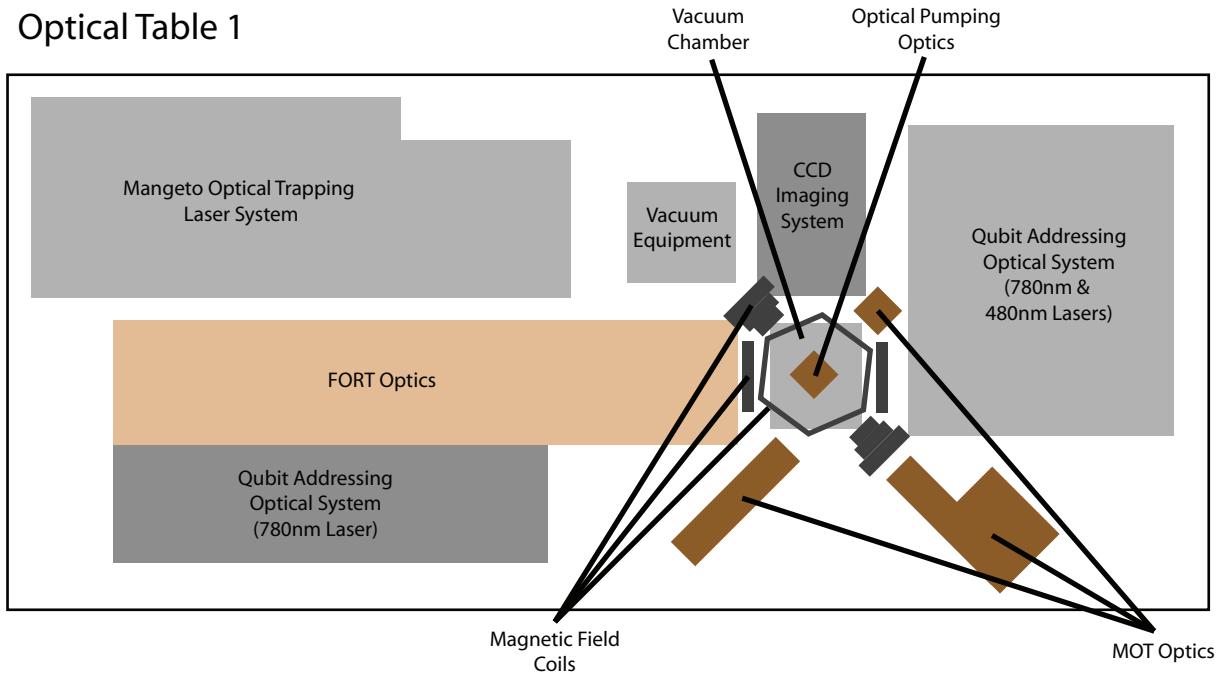

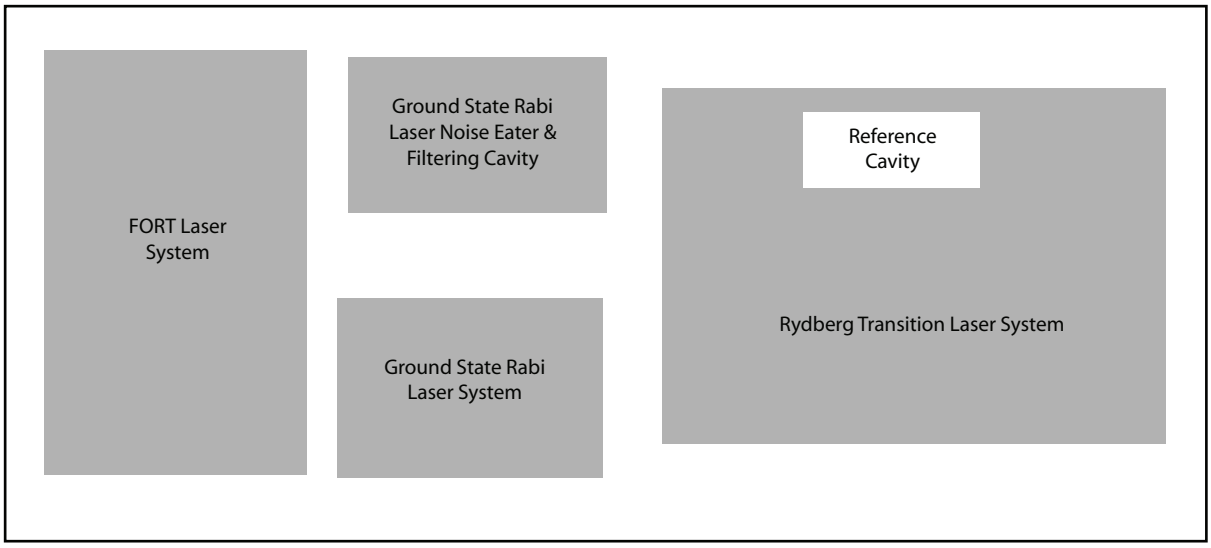

Figure 2.1 Overview of optical systems used by the Quantum Computing Experiment. The laser systems and optics used to deliver the lasers to the vacuum camber can be thought of as modular structures. These units are connected by optical fibers to assist in system alignment and laser beam characterizations. Optical fibers omitted for clarity.

these atoms into a FORT potential. Camera readouts are implemented to measure the number of atoms present in the FORT potential. These readouts are often performed both before and after performing an atom manipulation. Atomic state manipulations include performing optical pumping of an atomic sample, single qubit rotations, and two qubit operations. Performing atomic state manipulations enable us to initialize an atom into a desired atomic state, perform spectroscopic measurements of excitation transitions, prepare qubits for state sensitive camera readouts, and enable the entanglement of two distant atoms. Statistics of a particular phenomena are acquired by repeating the full experiment cycle many times.

A typical experiment cycle begins with a MOT loading period of 500 ms. During this period the MOT laser beam detuning and intensities are set to cool ensembles of the rubidium-87 isotopes from a background vapor. During this period the FORT laser is superimposed on top of the gathering atomic ensemble. Sufficiently cold atoms collect in the optical potential generated by the tightly focused FORT. The MOT lasers are turned off at the end of the loading phase to allow atoms not collected by the FORT to disperse. By changing the duration of this loading phase we can control the average number of atoms that are typically transferred into the FORT.

During a camera readout phase the MOT lasers and CCD camera are used to image the atoms via fluorescence imaging. The fluorescence signal is generated by scattering the MOT lasers off the atoms trapped in the FORT potentials. The FORT and MOT lasers are modulated out of phase with each other. The MOT laser intensity and frequency parameters are configured to optimize the fluorescence signal during this period. The readout phases are typically used just after a loading phase and after the atom state manipulation phase. Performing two camera measurements during a trial in this manner provides information about how many atoms are present before and after addressing the trapped atoms with various laser pulses. The protocols used for atom loading and readout measurements are discussed further in Section 3.5.

The atom state manipulation phase provides us with a versatile means of characterizing intrinsic properties of the atoms as well as the ability to prepare and readout particular

atomic states. During this portion of an experiment a wide variety of operations can take place. As will be illustrated in later chapters this time can be used to optically pump atoms (chapter 3), conduct optical trap diagnostics (Sections 5.3 and 5.4), excite two-photon Rabi transitions (chapters 8 and 9), and selectively remove atoms residing in particular hyperfine energy levels from the FORT (Section 3.3). Our ability to treat the experiment cycle in this modular fashion relies heavily upon the fact that all of the optical assemblies and lasers are integrated into a single controller. This controller allows us the flexibility to rapidly change an experiment cycle to measure a wide variety of qubit parameters.

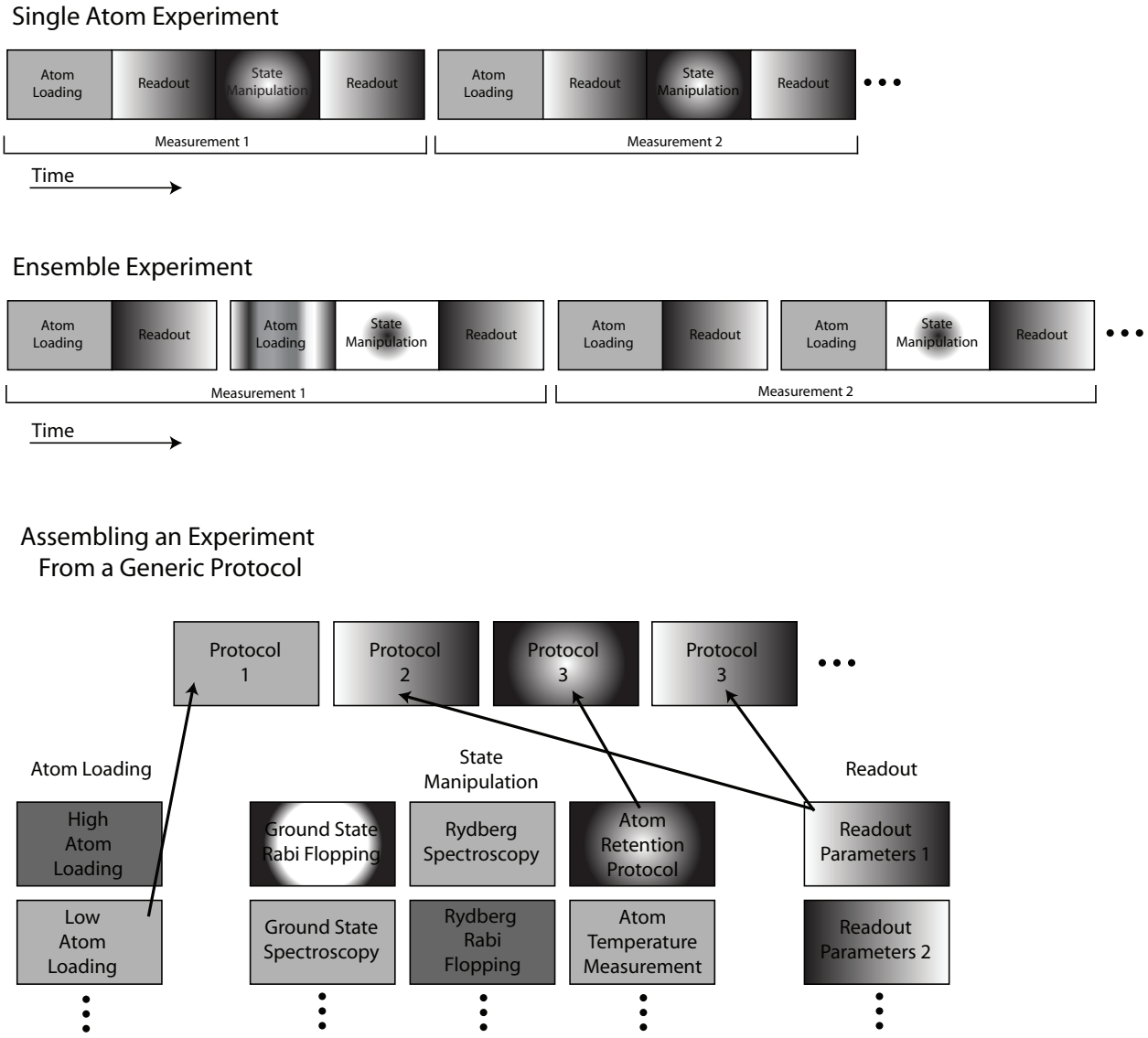

Figure 2.2 Experiment protocols are designed to be modular in nature. Through linking the experiment's hardware to a single computer controller we possess the ability to rapidly modify experiments and measure a wide variety of parameters. Typically, the atom loading and camera readout protocols are identical from one experiment to the next. The state manipulation protocols are merely substituted. Note that the experiment cycle is typically set to repeat to accumulate statistics for a particular set of parameters. Experiments can be designed to measure the response of atomic ensembles as well as single atoms.

Chapter 3

Magneto Optical Trap

3.1 Introduction to Magneto Optical Traps

The versatility and robust characteristics of the magneto optical trap (MOT) make this method of cooling and trapping atoms applicable to a wide variety of experiments in atomic physics. Consequently, MOT dynamics is a thoroughly studied and documented phenomenon [Raab et al., 1987], [Wieman et al., 1995], and [Frese et al., 2000]. While quite interesting in and of itself, the MOT is merely used as a tool in these experiments. The focus of this chapter is to point out several unique features on how we implement our MOT setup. The MOT lasers assist in cooling and trapping atoms, initializing the atomic qubit states, and reading out the particular logic states of the atoms through fluorescence imaging. The optical fields of the MOT are established by two custom built laser systems (see Section 3.2). These lasers use a series of acousto-optic modulators (AOMs) to control the laser′s detuning from particular atomic transitions during various phases of the experiment. The modulation frequencies are controlled via voltage controlled oscillators (VCO) while laser intensities are controlled with voltage controlled attenuators (VCA). Both the VCO and VCA are interfaced to a computer controller through a digital to analog converter (DAC). This computer control enables us to rapidly change the MOT laser parameters during various stages of an experiment cycle. This is important due to the fact that the MOT lasers assist in qubit initialization and state readout of the individual qubits and need different detunings and intensities to perform these tasks. Our MOT is capable of producing atom clouds with atom densities of order $10^9/cm^3$ [Yavuz et al., 2006].

3.2 Trapping Lasers

The optical fields of the MOT are established by two custom built laser systems. A schematic of the laser systems and their accompanying AOMs are shown below in Figure 3.1. A master-slave diode laser system is used to drive the $|5s_{\frac{1}{2}}, F = 2\rangle \leftrightarrow |5p_{\frac{3}{2}}, F' = 3\rangle$ cycling transition of Rubidium-87. The master laser diode is a 70mW CiruLaser diode from Blue Sky Research. The laser is frequency stabilized with a Littman-Metcalf external feedback cavity configuration [Littman and Metcalf, 1978], [Preston, 1996]. The output power of the cavity feedback system is typically 18mW. About 6mW is used to injection lock a 120mW Sharp laser diode. About 5mW of the master laser power is used to stabilize the laser to a rubidium reference cell via frequency modulation (FM) spectroscopy [Bjorklund, 1980] and [Hall et al., 1981]. FM sidebands of 10.11MHz on the laser beam are generated with an electro-optic modulator (EOM). The F=2$\leftrightarrow$F$'$=1-3 cross-over is used as the laser's spectroscopic reference. It should be noted that a double passed AOM, operating at 200MHz, is used to shift the master laser frequency a total of -400MHz prior to passing through the saturated absorption cell. This preemptive frequency shift ensures that the master laser is locking to a frequency blue detuned from the MOT$'$s cycling transition (see Figure 3.3). This ensures that any light inadvertently leaking through the AOM to the experiment will not be near any Rb-87 resonance frequency.

The majority of the master laser power is used to seed a Sharp 120mW diode laser. The 56 mW output from this slave laser is sent on to a double passed AOM. The -1st order of the AOM is used to shift the frequency of the laser red of the cycling transition (see Figure 3.3). In addition to controlling the detuning of the MOT laser beams this AOM is also used to attenuate the beam intensities. Any AOM light leakage will therefore be far blue detuned from any transitions. This prevents atoms from accidentally being driven through extraneous transitions. The master laser frequency and accompanying AOM shifts are displayed along side a Rb-87 energy levels diagram in Figure 3.3.

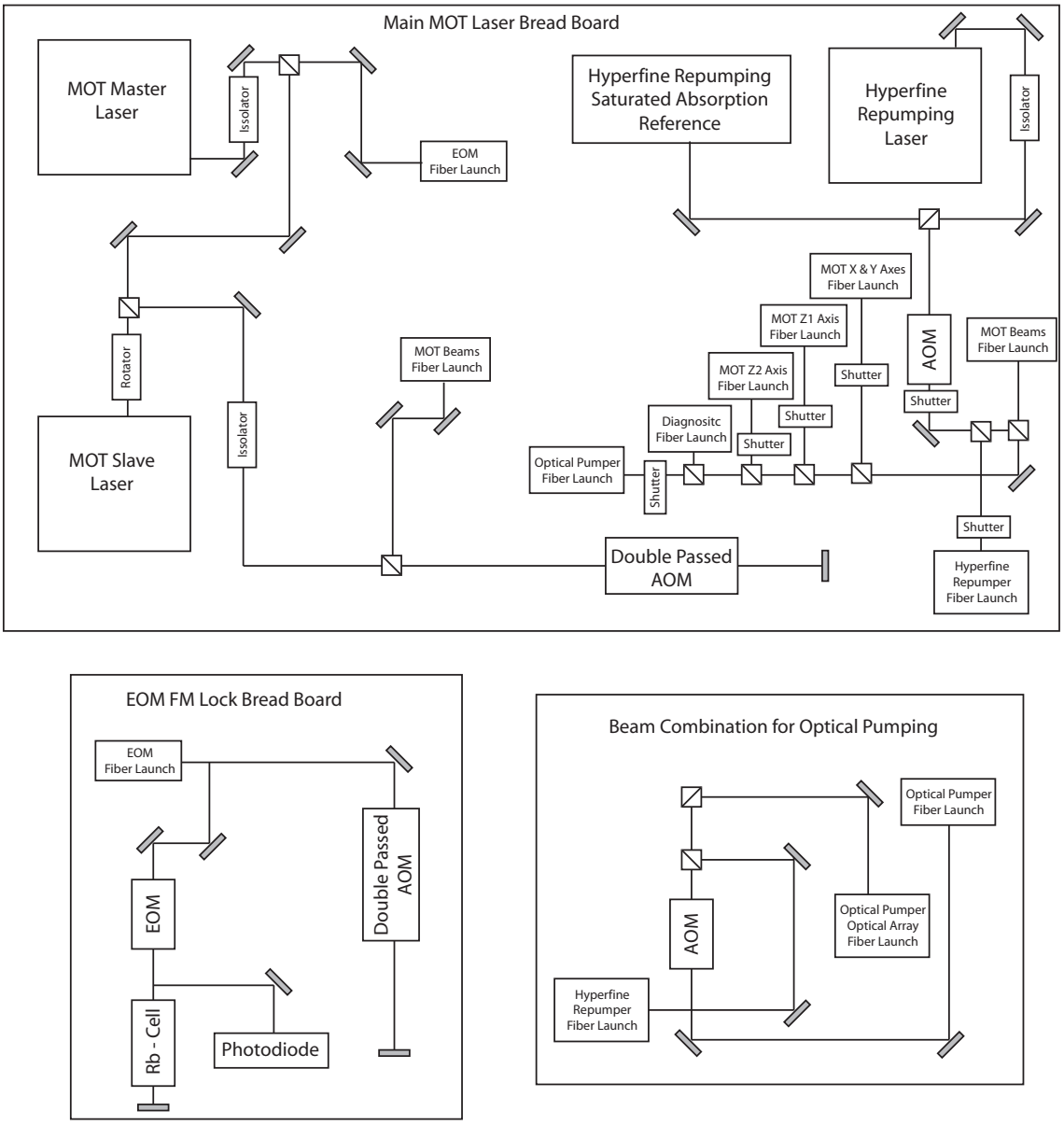

Figure 3.1 This diagram outlines how the master, slave, and hyperfine MOT lasers are locked and combined before being sent onto the vacuum chamber. Lenses and waveplates have been omitted for clarity. The side assembly used to produce the optical pumping laser beam is used when optically pumping to the $|5s_{1/2}, F = 2, m_F = 0\rangle$ state. When optically pumping to the $|5s_{1/2}, F = 2, m_F = +2\rangle$ state the output of the 'Optical Pumper Fiber Launch' is sent directly to the optical pumping optics. The beam paths and layout of the AOMs and EOM help illustrate how the laser beam frequencies are being adjusted. Details on which AOM beam orders are utilized can be found in the text.

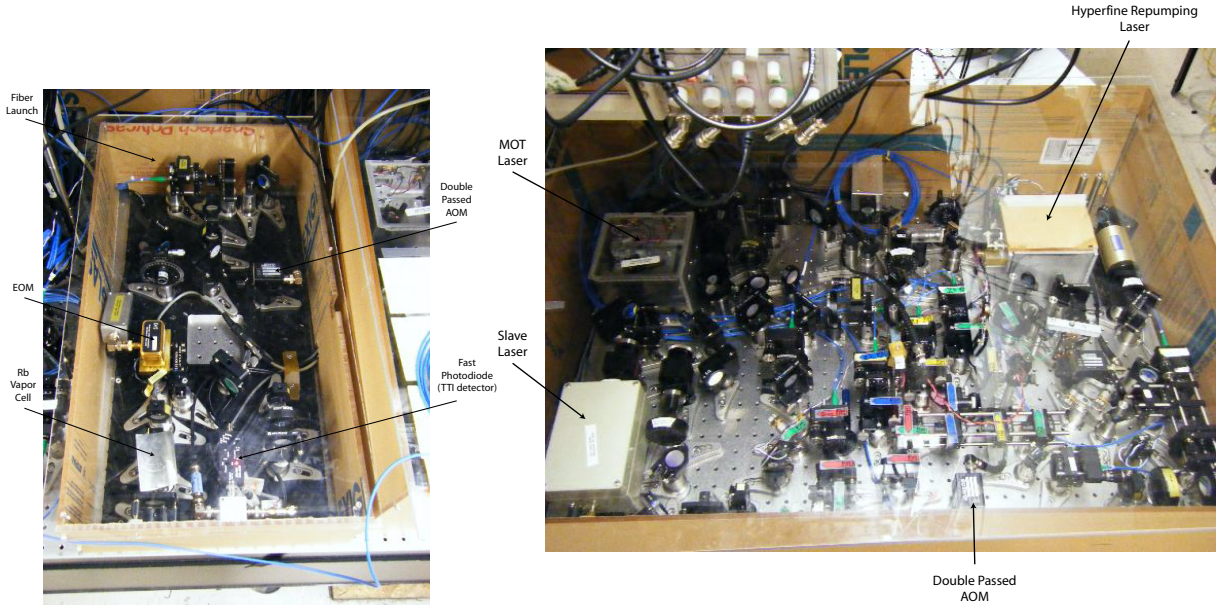

Figure 3.2 Pictures of the MOT laser optics.

A separate hyperfine repumping laser is necessary to prevent atoms from becoming lost to the F=1 ground state. Atoms lost from the cycling transition via spontaneous decay and Raman transitions will decay into the F=1 hyperfine structure. Atoms in these dark-states must be driven, or repumped, via another laser frequency to reenter the cycling transition. A saturated absorption lock is used to hold this laser′s frequency to the F=1↔F′=1-2 cross-over peak [Preston, 1996]. This laser has an optical power output of about 20 mW. Like the master-slave laser system, the intensity and detuning of the light is controlled with an AOM via the DAC computer controller. The pertinent atomic transition used to lock this laser are also shown in Figure 3.3.

3.3 Vacuum Chamber and Optical Beam Paths

As shown in Figure 3.1, both the light from the master-slave laser (10mW) and the hyperfine laser (100uW) are combined on a polarizing beam splitter. Using a combination of waveplates and polarizing beam splitters, this light is divided and coupled into five optical fibers for delivery to the vacuum chamber. This light is used to create a MOT in a customized

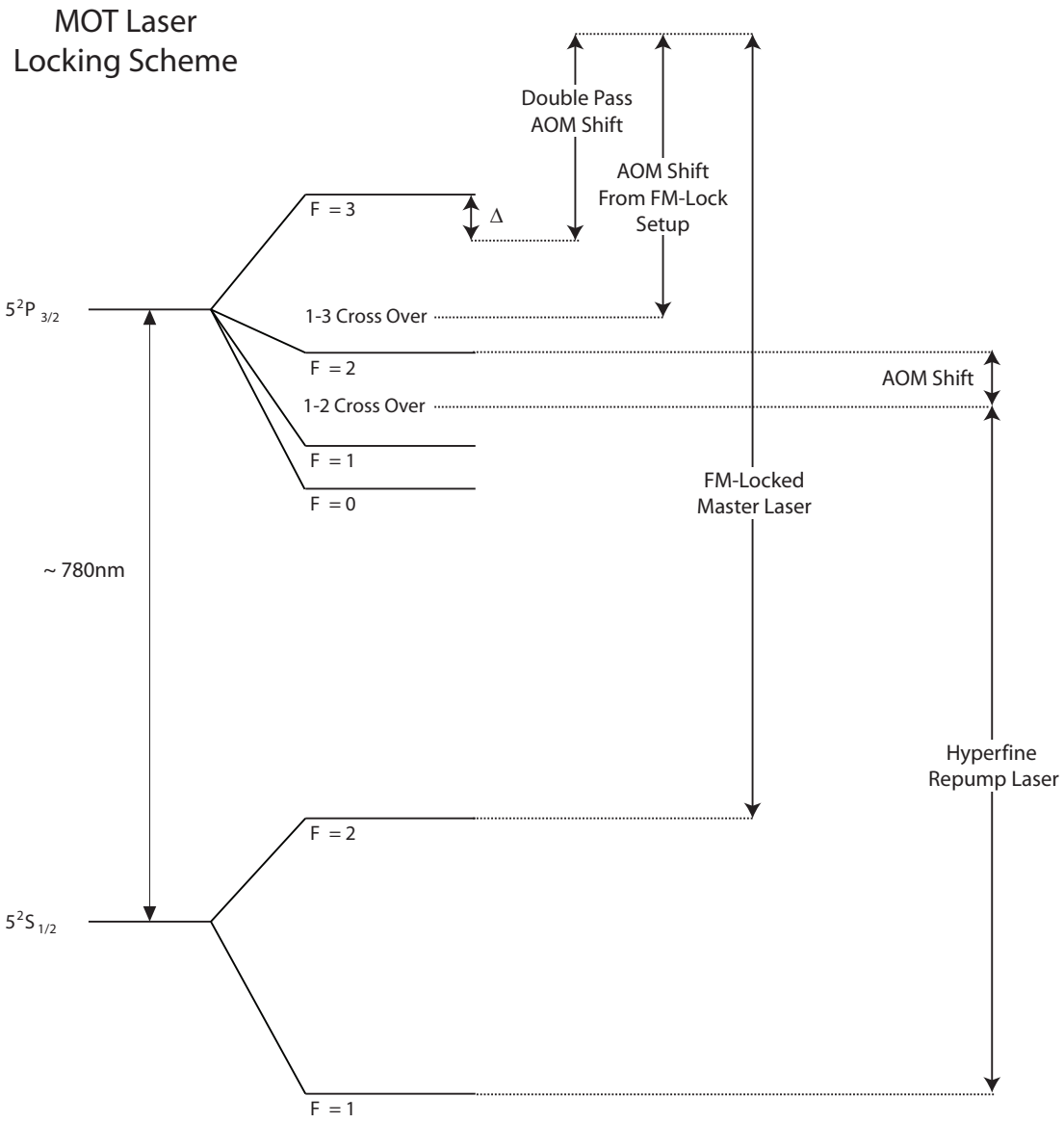

Figure 3.3 Laser locking scheme used in frequency stabilizing the MOT lasers. Both the MOT and Hyperfine repumping laser are included in the illustration. Note that the double passed AOM used in establishing the master laser lock forces the master laser to be blue detuned of the desired cycling transition. A second double passed AOM is used to shift the laser red detuned of the cycling transition. The second double passed AOM is used to control the MOT lasers detuning throughout the experiment. Both the master and hyperfine repumping lasers are referenced to cross-over transitions indicated in the diagram. The AOMs referenced in this illustration are indicated in Figure 3.1.

Kimball Physics spherical cube vacuum chamber. The chamber is roughly 4.8″ in diameter, and possesses six $4\frac{1}{2}''$ ConFlat (CF) port windows. These large aperture ports are reserved for vacuum lines, generating an optical dipole trap, atom imaging, and state manipulation of the atoms. The geometry of our MOT is constrained by the limited remaining optical access to the center of the vacuum chamber. Nominally a MOT is generated by three orthogonal sets of counter-propagating laser beams. Two sets of Gaussian laser beams are aligned through the chamber using four of the $1\frac{1}{3}''$ CF ports located at opposite corners of the vacuum chamber, see Figure 3.4. The Gaussian beams have $1/e^2$-beam waists of ∼6.1mm and meet in the center of the chamber at an obtuse angle of approximately 109.5 degrees. To intersect the plane defined by these four laser beams we must use port windows attached to the chamber by narrow extension tubes (40mm x 2mm) to establish the last set of counter propagating optical fields. The $1/e^2$ Gaussian beam waists entering the chamber through these narrow tubes are about 0.9mm.

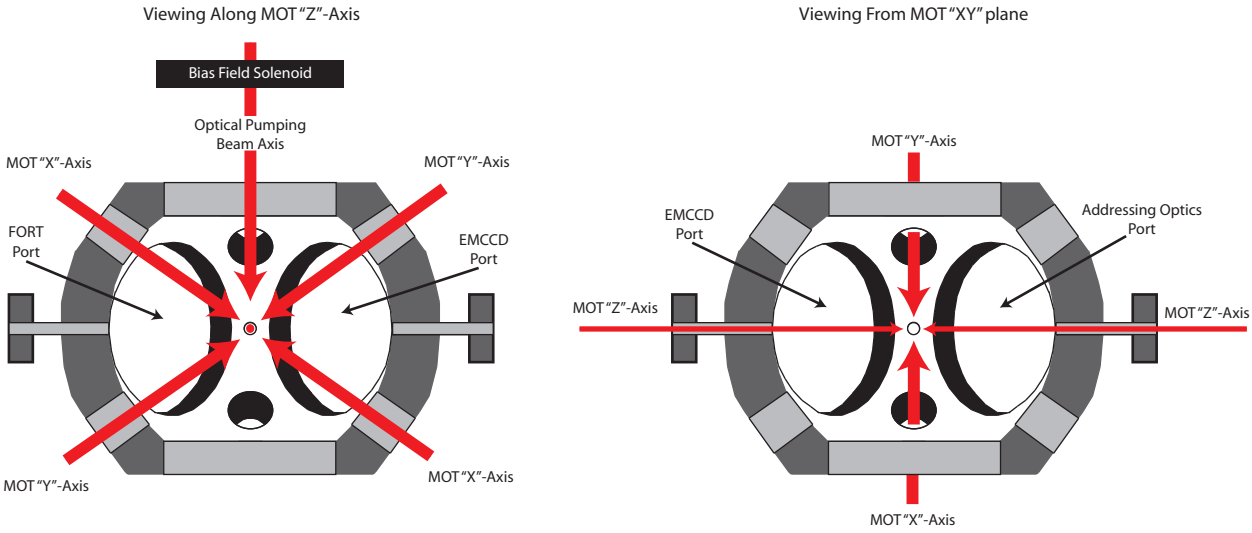

Figure 3.4 Exploded view of the vacuum chamber. The vacuum port windows and the horizontally oriented solenoids have all been removed for clarity. The large MOT gradient solenoids lie along the MOT Z-axis. The second set of magnetic bias field coils are axially aligned to the FORT-Addressing Optics axis. Details on beam waist are included in the text.

The tightly focused MOT ‘‘Z′′-axis lasers and nonorthogonal sets of beams give rise to a very small trapping volume. The confining forces of a MOT are based on the rate at which photons are being scattered off the atom. An atom moving through the magnetic gradient field of the MOT will experience a force differential due to Doppler and Zeeman shifts. Consequently a red detuned laser will exhibit a scattering force proportional to the atom′s velocity and position. These forces only provide an effective trap in regions where all three pairs of counter propagating lasers overlap. The scattering forces from the nonorthogonal laser beams produce unequal damping and restoring forces in the vertical and horizontal directions, as viewed from the MOT ‘‘Z′′-axis (Figure 3.4, left). The horizontal forces should be approximately 30% larger than the vertically oriented damping and restoring forces. The intersection of the narrow laser beams limits the available trapping volume. The trapping region is limited to a sphere of roughly $\frac{3}{4}\text{mm}^3$.

In addition to the six MOT beams, a separate optical pumping laser is directed into the vacuum chamber through the top port window. This laser is fiber coupled and then free launched through a Glan-Taylor polarizing beam splitter before being magnified to a beam waist of 5mm. The polarization of this beam is set to be σ^+ with a $\lambda/4$ wave plate when optical pumping to the $|F = 2, m_F = 2\rangle$ is required. The laser beam is aligned axially with respect to a magnetic field coil used to Zeeman split the ground state energy levels. The same laser beam is also used to achieve optical pumping to the $|F = 2,\, m_F = 0\rangle$ state. The magnetic field and beam polarization, however, must be reoriented to enable this optical pumping scheme. This magnetic field is generated by a set of solenoids aligned axially with the large vacuum ports used for the FORT and the addressing optics. The optical pumping beam polarization is set to be π polarized relative to this field with the use of a $\lambda/2$ wave plate instead of a $\lambda/4$ wave plate. The optical pumping transitions are quickly outlined in Figure 3.5, and implementation of optical pumping is discussed further in Section 3.5.

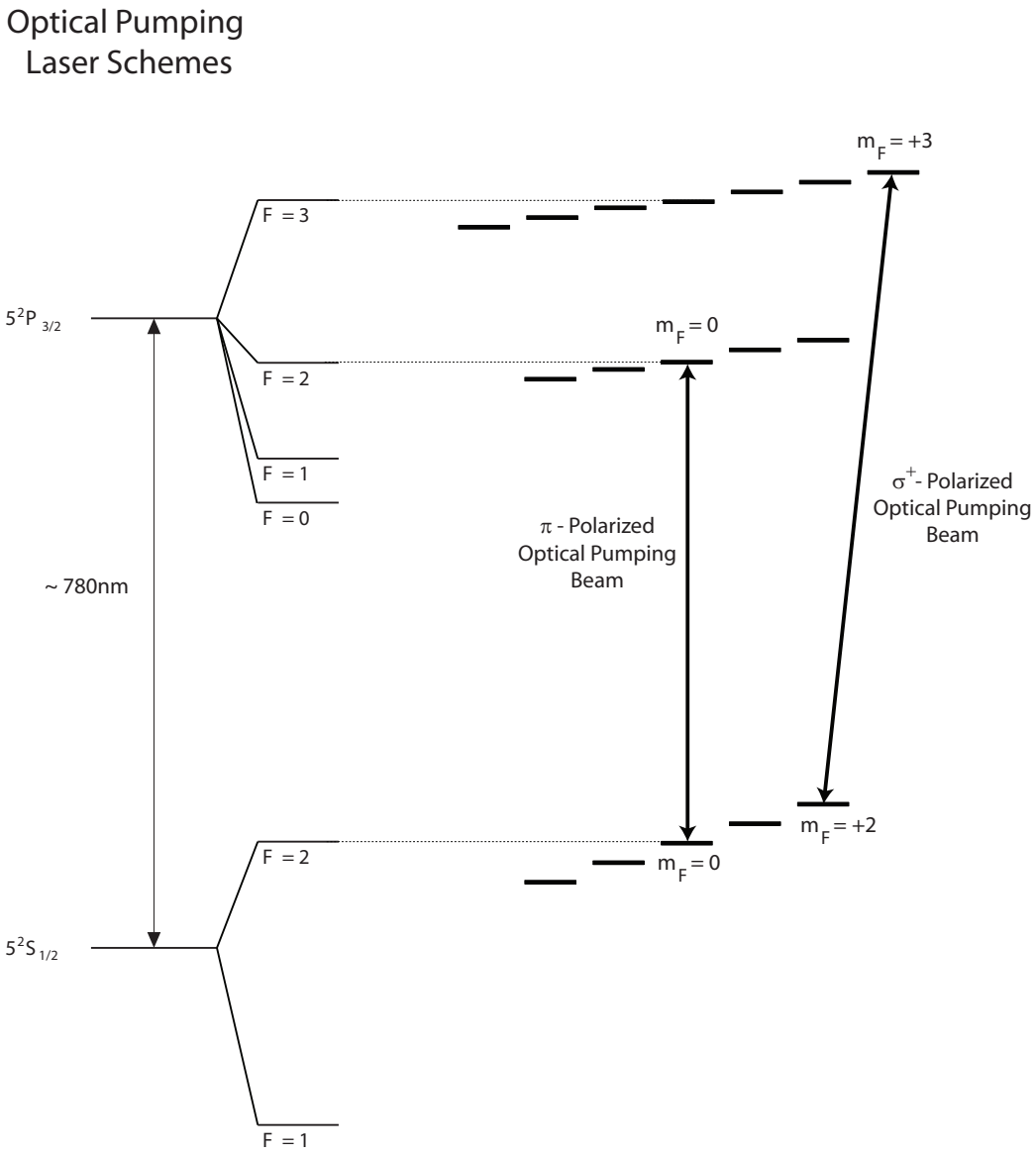

Figure 3.5 Energy level diagram illustrating the transitions used to achieve optical pumping to the F=2, m_F=0 or the F=2, m_F=+2 levels. The energy level splittings are not drawn to scale. The hyperfine repumping laser is not shown. Both schemes rely upon the hyperfine repumping laser which drives atoms from F=1 to F′=2. This laser returns atoms lost from the F=2 to F′=2 cycling transition through spontaneous decay to the F=1 state. The optical pumping laser frequency (F=2 ↔ F′=2) is set using AOMs.

3.4 Magnetic Fields

The trapping capacity and temperature of atoms within a MOT depend greatly upon the gradient field used to confine the atoms. The gradient field induces a spatially varying

Zeeman shift upon the atoms. Combined with the appropriate laser fields the Zeeman shifts help to establish the spatial dependent force of a MOT. This magnetic field gradient is generated with a set of custom built water cooled solenoids. The solenoids can not be positioned in an ideal anti-Helmholtz configuration due to the constraints imposed by the vacuum chamber geometry. It is necessary to separate the coils further and give them a conical shape, thus restricting their solid angle access to the vacuum chamber. A cross-section of a magnetic field coil is shown in (Figure 3.6).

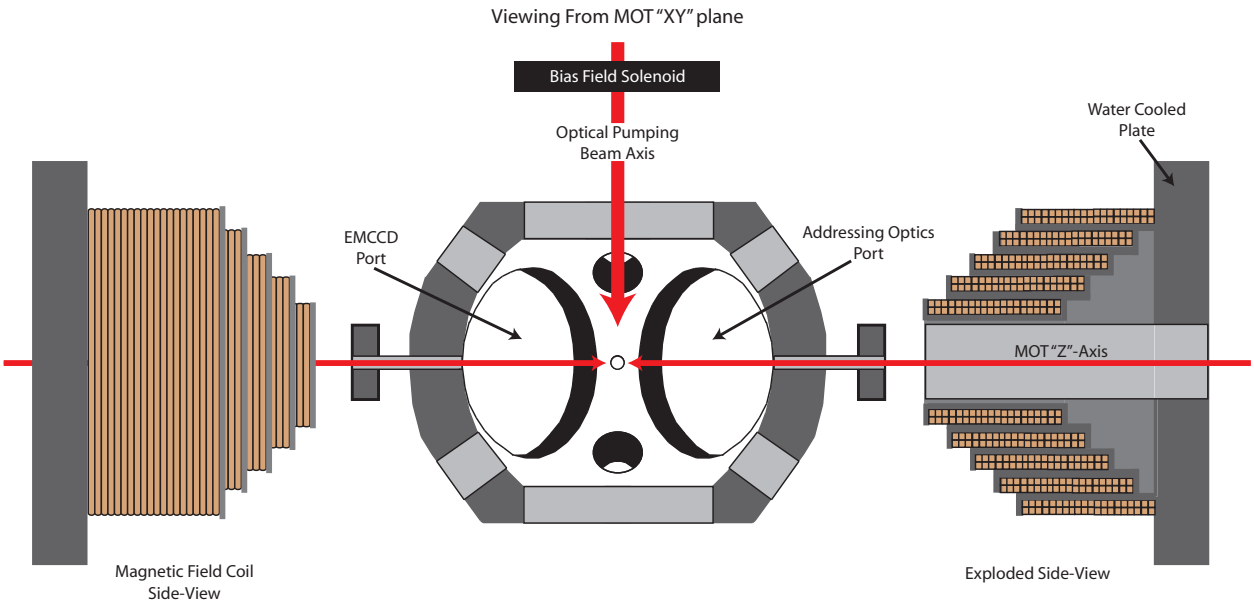

Figure 3.6 Water cooled MOT magnetic field coils (not to scale). The water cooling lines are not included for clarity. The cross-section of the field coils illustrates how the magnetic field coil is constructed from five smaller solenoids. The vertically mounted bias magnetic field coils are shown in this figure as well. The shim coils used to null background fields at the center of the chamber are wrapped around the large vacuum port windows.

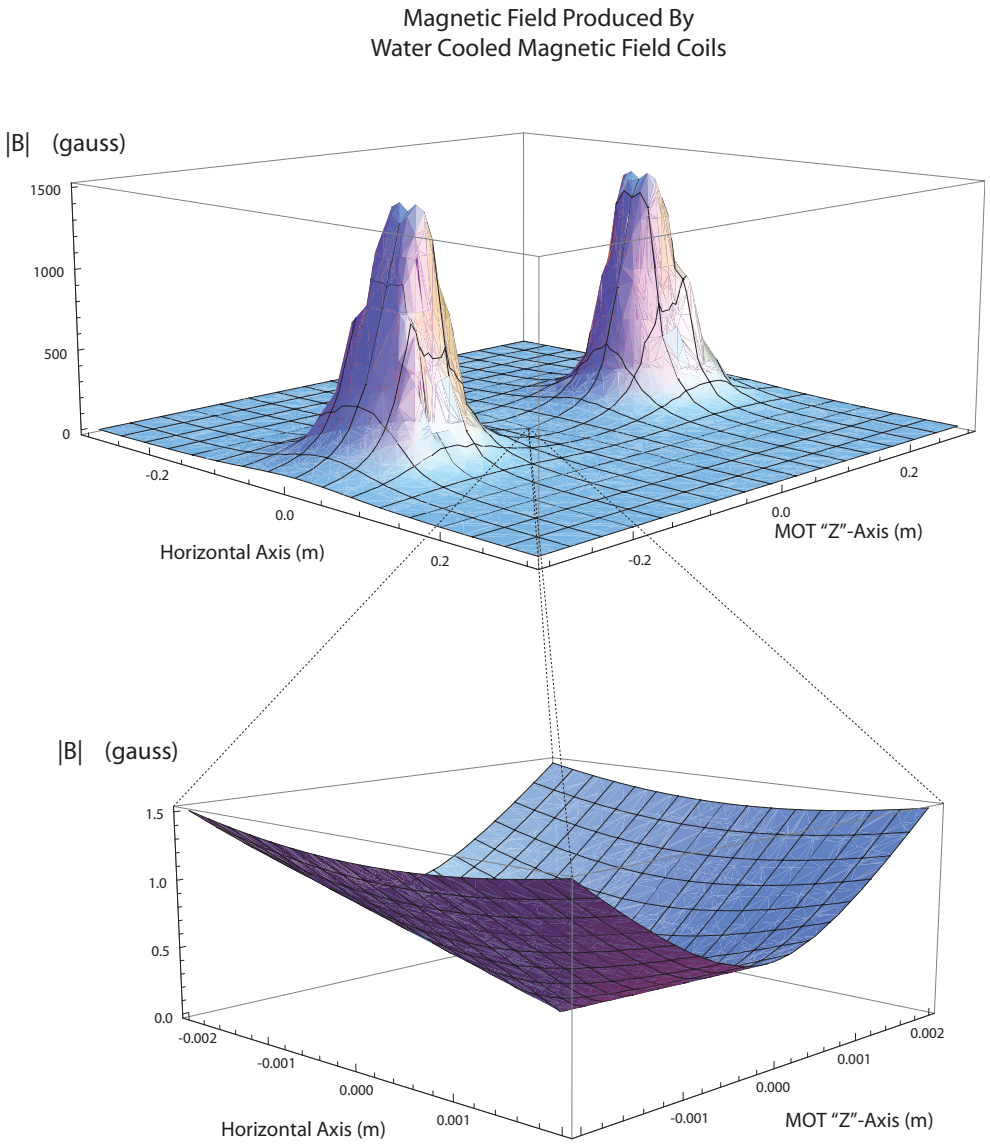

Figure 3.7 Plot showing calculated magnitudes of the magnetic field generated by the water cooled solenoids. The field's magnitude in gauss is calculated assuming the current is set to 56.35 Amps. The field coils are broken into 5 separate solenoids, each with two layers and 19 turns. The plot axes are in meters and lie along the MOT Z-axis and the orthogonal axis running parallel with the optical table's surface. The magnitude of the field inside the coils needs to be very large in order to attain a reasonable gradient field near the center of the vacuum chamber. The smaller plot focuses on the field near the center of the chamber.

The coils are a segmented design and contain 190 turns of 11 AWG square wire. The coils were typically run at 56.35A in order to generate a steady state field gradient of 6.7 Gauss/cm at the center of the chamber. Water cooled chilling plates are used to dissipate about 1.25 kWatts of power from the coils. The null of this field is maneuvered in the chamber using three sets of orthogonal magnetic field shim coils. The shim coils are wrapped around the large vacuum chamber port windows.

A set of magnetic field coils are used to apply bias magnetic fields to our trapped atoms. These coils are used during optical pumping and various spectroscopy experiments. The vertically aligned coil, shown in Figure 3.6, is used while optically pumping to the $|F = 2, m_F = 2\rangle$ ground state. Operating at a current of 26A this coil produces a bias field strength of 11.5 gauss. When optically pumping our atoms into the $|F = 2, m_F = 0\rangle$ states it is necessary to use a different magnetic field orientation. A pair of coils are wrapped around opposing vacuum chamber port windows to generate a 3.5 gauss field while operating at 1.58 amps, and $\sim$3.9 volts. This field is oriented along the axis of the optical dipole trap laser. Both sets of field coils have a 10%-90% rise time of about $\sim$25ms. The fields reach a stable field strength of after $\sim$100ms.

3.5 MOT Laser Timing Protocols

The detuning and intensities of the MOT laser beams vary throughout all of the experiment cycles. By allowing the laser parameters to change it is possible to optimize and use the MOT laser beams for a variety of purposes throughout the experiment. Specifically, the MOT laser beams are implemented in cooling and trapping atoms into a MOT, fluorescence imaging of atoms trapped in an optical dipole potential, optical pumping the atoms, and in the removal of F=2 atoms from our optical dipole trap. As mentioned briefly, the MOT laser′s frequency is controlled using a double passed AOM, and the laser intensity is controlled by adjusting the AOM′s diffraction efficiency. The MOT beams can be individually sent into the vacuum chamber through the use of mechanical shutters. In this section we focus on the MOT laser timing protocols used to implement particular functions of our experiment. As

explained in Section 2.2, these MOT laser protocols can be linked in succession to generate the experimental conditions to perform spectroscopic experiments, and qubit operations.

During the MOT loading phase, the double passed AOM used to control the intensity and frequency of the slave laser is nominally engaged for 500ms. During this time the optical shutters controlling the hyperfine repumping laser and the MOT XY, Z1 and Z2 beam paths are opened thereby establishing our 6 beam MOT. The MOT typically operates at a detuning of roughly -14MHz. During this time atoms are typically being transferred to an optical potential (see Chapter 4). The MOT loading phase is concluded by using the double passed AOM to extinguish the MOT laser beams. Residual MOT cloud atoms require less than 50ms to dissipate from the center of the vacuum chamber after extinguishing the laser beams.

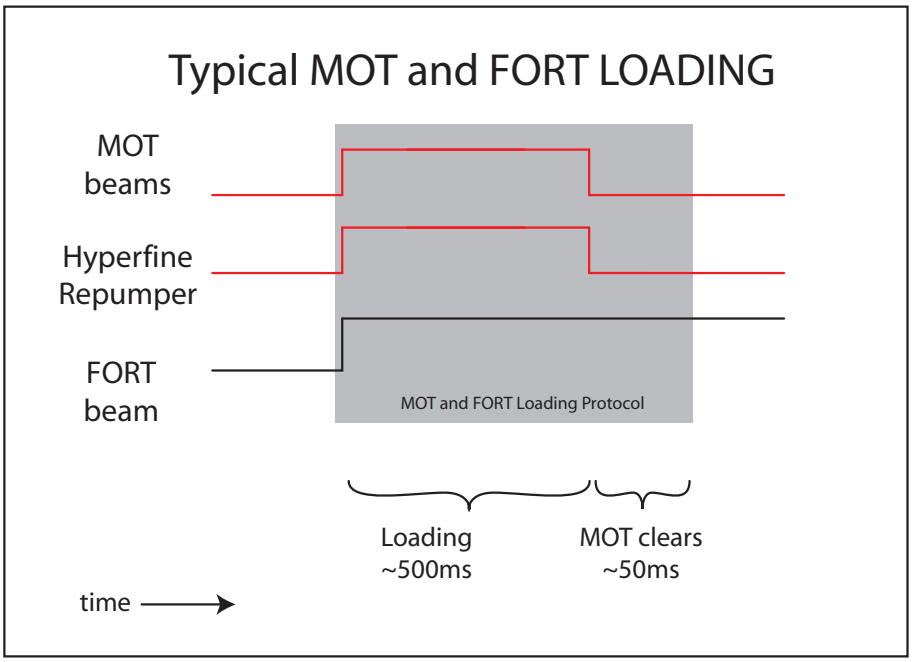

Figure 3.8 Timing of laser beams used to load atoms into the MOT and the FORT (see Section 4). The Hyperfine repumping laser must be used to prevent atoms from escaping from the $|5s_{1/2}, F = 2\rangle \leftrightarrow 5p_{3/2}, F' = 3$ cycling transition.

The MOT lasers are also used to enable fluorescence imaging of atoms trapped within the FORT potentials (see Chapter 5). Like the MOT loading protocol, the single atom detection

protocol requires the use of all six MOT trapping lasers. The detuning of the laser beams however are now set to be about -8.5MHz detuned from the cycling transition. This light is scattered off atoms being held in an optical dipole trap. To circumvent the light shifts induced by the FORT, it is necessary to modulate the MOT and FORT lasers out of phase with each other. The MOT beams are typically modulated at 1.67MHz for 30-50ms with a duty cycle of 30%, while the optical trapping laser, discussed in Chapter 4, is modulated at the same rate, but using a 50% duty cycle. This modulation is illustrated in Figure 3.9.

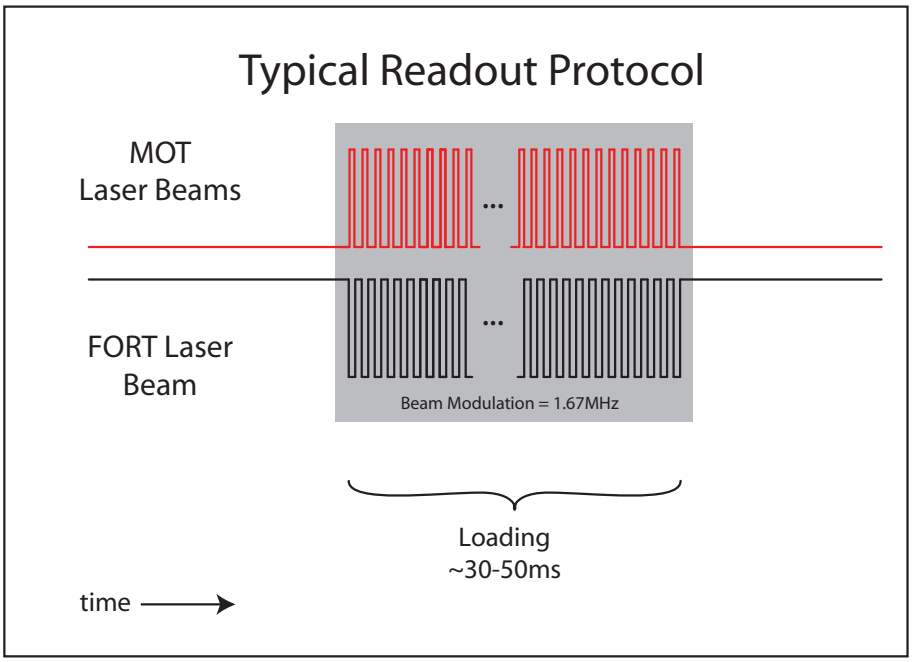

Figure 3.9 Timing diagram illustrating how the laser beams from the MOT and FORT (Chapter 4) are modulated out of phase with each other. The required modulation period used in an experiment is typically 30 or 50ms. When implementing multiple readout protocols in a single cycle, the modulation duration is set to be the same for each readout. The laser beams are modulated at 1.67MHz. To ensure the two trapping laser beams are never on at the same time the MOT laser beams are modulated with a 30% on duty cycle, while the FORT is modulated with a 50% duty cycle.

During an experimental cycle it is typically necessary to optically pump an atom sample into a particular magnetic hyperfine sublevel. Optical pumping is nominally used to prepare an atom sample into the $|5s_{1/2}, F = 2, m_F = +2\rangle$ or the $|5s_{1/2}, F = 2, m_F = 0\rangle$ state.

The optical pumping protocol requires a magnetic bias field to be activated to Zeeman shift atomic energy levels. The orientation of the bias field used while optically pumping depends upon which state we are trying to initialize the atoms. The optical field used to optically pump the atoms is obtained from the MOT laser system. The required laser frequency is dependent upon which optical pumping scheme is being used (see Figure 3.10 and 3.12). The MOT laser frequency is easily shifted to the appropriate detuning using the AOMs outlined in Section 3.2. The orientation and polarizations used in optical pumping are discussed further in Section 3.3.

The structure of the optical pumping timing protocol is independent of which optical pumping scheme is used. The protocol begins by allotting ∼150ms for a bias field to ramp up to its full strength. During this period, mechanical shutters are engaged to block the MOT′s X, Y, and Z optical beam paths. The shutter nominally engaged to block the optical pumping beam is now disengaged. In this configuration the Hyperfine repumper and MOT laser will enter the vacuum chamber through the optical pumping beam path. All other beam paths are isolated from the vacuum chamber. Like the readout protocol, the optical pumping laser is modulated at 1.67 MHz via the double passed AOM.

While initializing to the $|F = 2, m_F = 2\rangle$ state the optical power of the beam is set to $\sim 41\mu$W with a detuning of -2.7MHz from the $|F = 2, m_F = +2\rangle \leftrightarrow |F' = 3, m_F = +3\rangle$ transition. The magnetic field strength was approximately 11.5 gauss. This pumping process is driven with $\sigma+$ light for 5ms yielding an optical pumping efficiency around 95%.

When pumping atoms into the $|F = 2, m_F = 0\rangle$ state with π-polarized light the laser frequency is adjusted to approximate the energy splitting of the $|F = 2, m_F = 0\rangle \leftrightarrow |F' = 2, m_F = 0\rangle$ dipole forbidden transition. Shifting the laser frequency this far requires the use of an additional AOM and a separate pickoff from the hyperfine laser (see Figure 3.2). The laser beams for this optical pumping scheme are engaged for 1.4ms. The optical pumping efficiency achieved for this particular scheme is typically between 90% and 95%. The optical pumping efficiency is determined by observing the maximum attainable population transfer via two photon ground state Rabi flopping, which is disscussed further in Section 8.3.

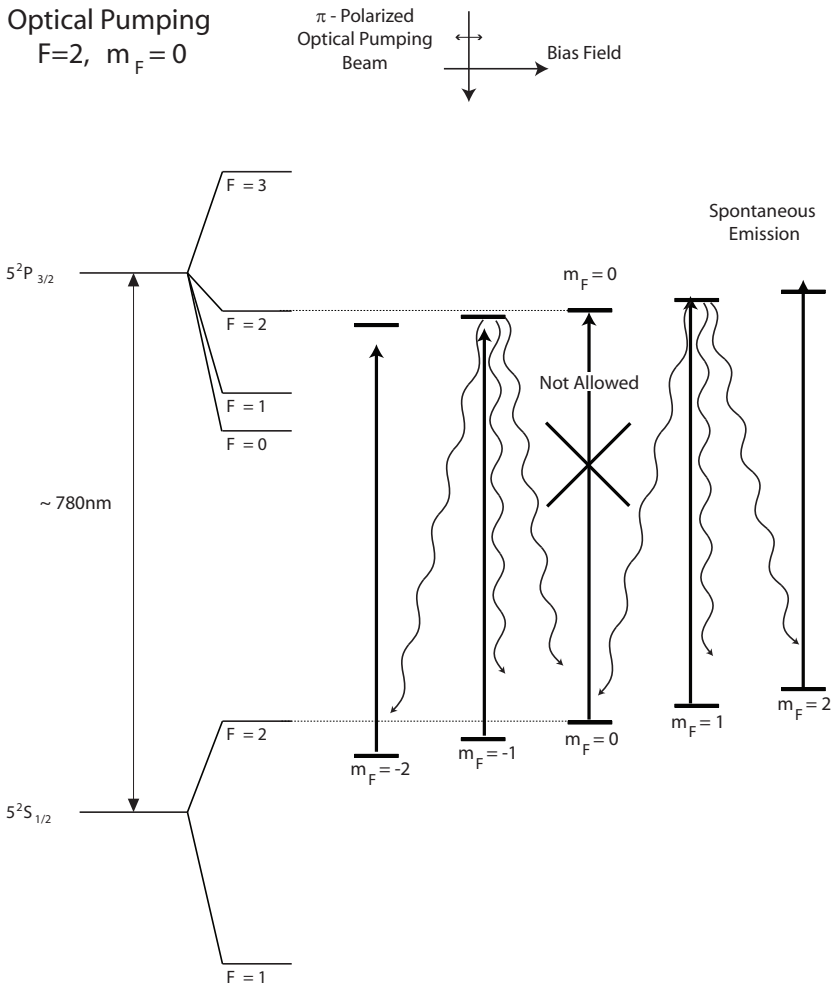

Figure 3.10 Energy level diagram illustrating how optical pumping is used to initialize atoms to the $|F = 2, m_F = 0\rangle$ state. Energy level splittings are not drawn to scale. The hyperfine repumping laser is not shown. Atoms are driven on the F=2 $\rightarrow$ F'=2 transition with π polarized light. Because the $|F = 2, m_F = 0\rangle \rightarrow |F' = 2, m_F = 0\rangle$ is a dipole forbidden transition, $|F = 2, m_F = 0\rangle$ is a dark state. Atoms will accumulate in the m_F=0 state because there in no mechanism to remove them. Excitations to the other F'=2 states can spontaneously decay into this dark state. Atoms will collect and thus be initialized into the $|F' = 2, m_F = 0\rangle$ state. This optical pumping scheme requires the bias field to be aligned orthogonal to the optical pumping beam.

The readout protocol described earlier merely indicates whether or not an atom is present during the detection period. In order to transform this readout protocol into a state sensitive atom detection protocol, we selectively eject atoms from the optical dipole trap prior to

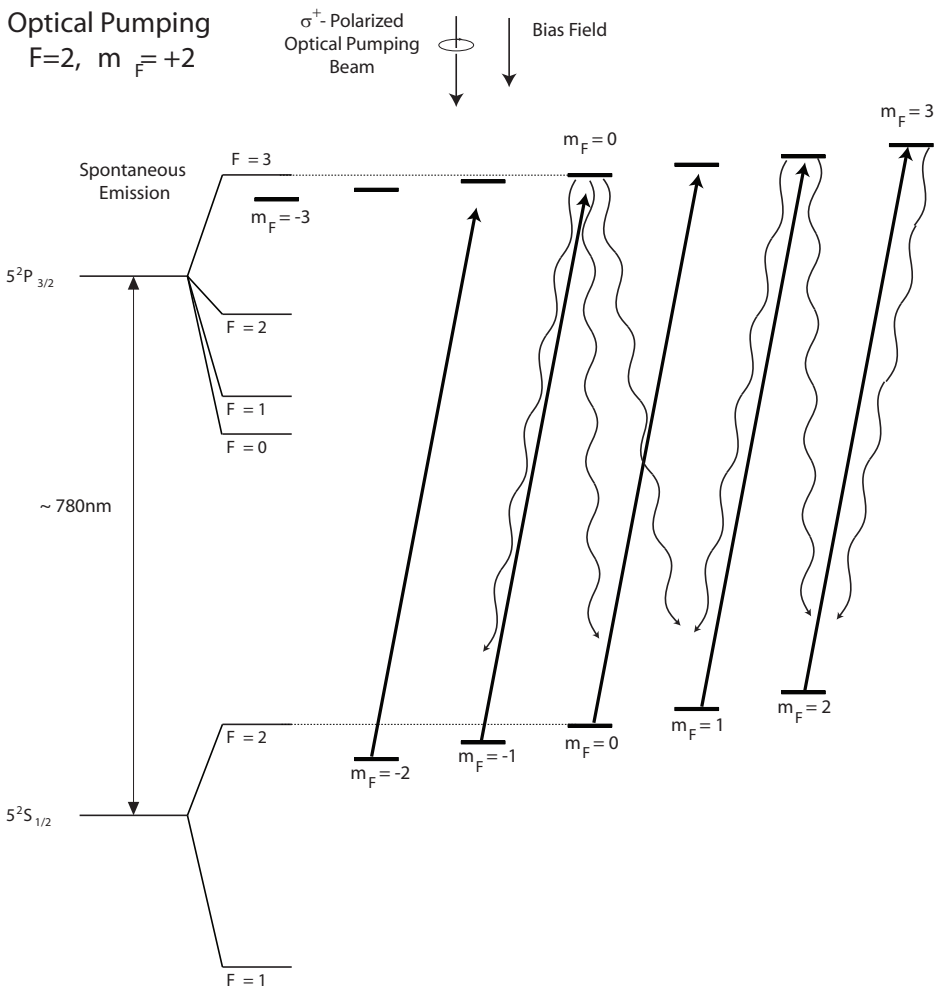

Figure 3.11 Energy level diagram illustrating how optical pumping is used to initialize atoms to the $|F = 2, m_F = +2\rangle$ state. Energy level splittings are not drawn to scale. The hyperfine repumping laser is not shown. Atoms are driven between the F=2 $\rightarrow$ F'=3 transition with σ^+ polarized light. Atoms are preferentially driven towards higher m_F values. Spontaneous emission from the $|F' = 3, m_F = +3\rangle$ only has one decay pathway back to the F=2 manifold. This ultimately results in the atoms collecting in the $|F = 2, m_F = +2\rangle$ state. This optical pumping scheme requires the bias field to be oriented vertically with respect to the optical table.

engaging the readout. Specifically, we eject atoms residing in the F=2 ground state from the trap. Therefore, any atoms observed during the subsequent readout protocol were occupying the F=1 ground state. This state selective atom ejection, or blow-away protocol, once again

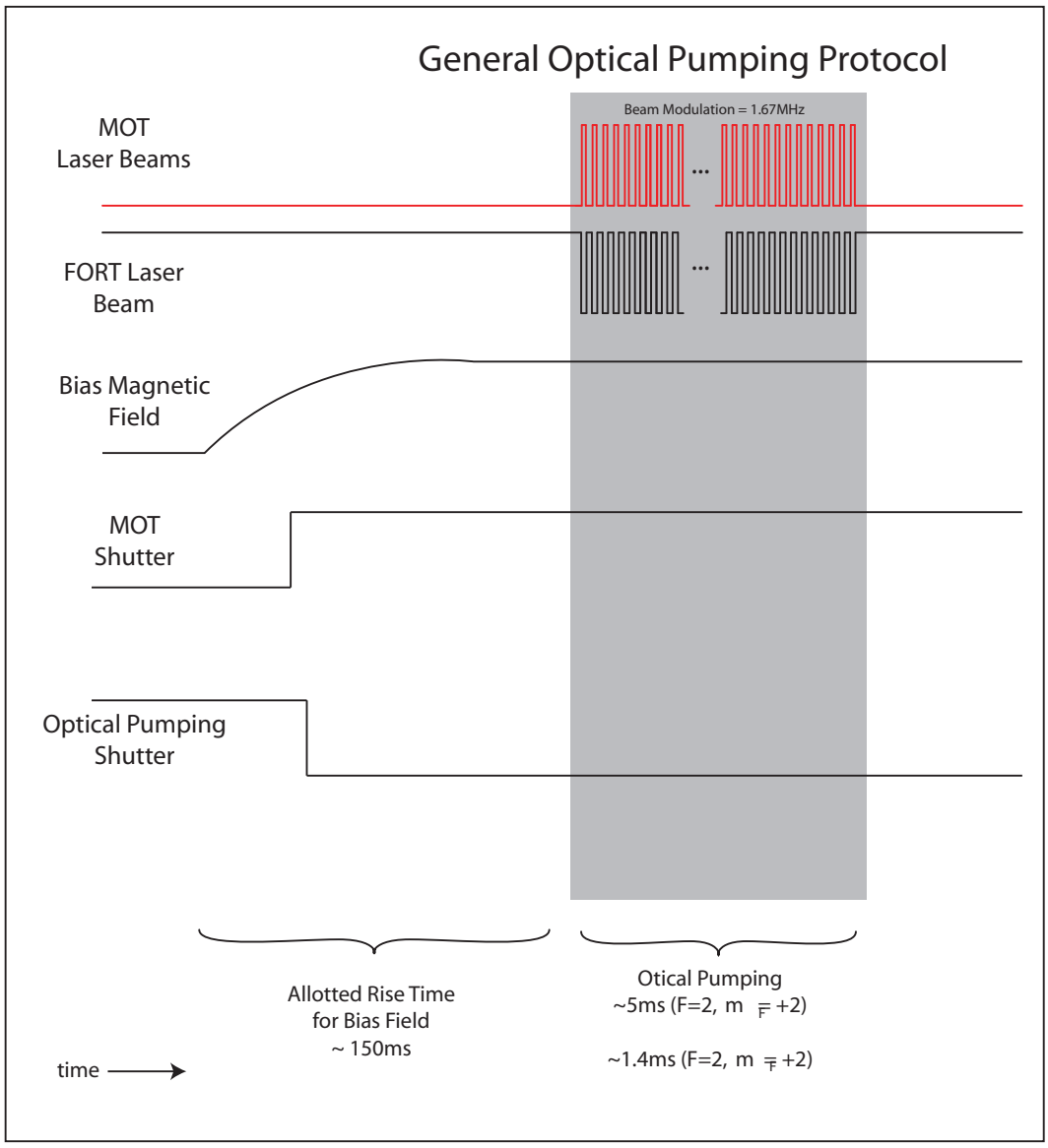

Figure 3.12 Optical pumping timing scheme. Note that mechanical shutters are used to allow light from the MOT lasers to enter the vacuum chamber through the optical pumping beam path. The MOT laser beam paths are prevented from reaching the atoms during this period. The bias magnetic field is given ample time to reach a steady state value before the optical pumping laser beam is engaged.

relies upon the MOT laser system. During blow-away, the atom sample is unidirectionally illuminated with one of the MOT Z axis lasers that is blue detuned from the $|F = 2, m_F = 0\rangle \leftrightarrow |F = 3, m_F = 0\rangle$ transition by approximately +2.25MHz. While driving this excitation

shutters are used to disable the hyperfine repumper, the optical pumping beam, and the other MOT laser beam paths. By exciting the atoms unidirectionally with a blue detuned laser we selectively eject atoms in the F=2 ground state from our atom sample. During the blow-away protocol the unbalanced laser beam is modulated at 0.5MHz with a 40% on time duty cycle. This process is typically 99% effective at removing all F=2 atoms, while leaving the F=1 atoms virtually undisturbed. The timing of the laser beams is shown in Figure 3.13.

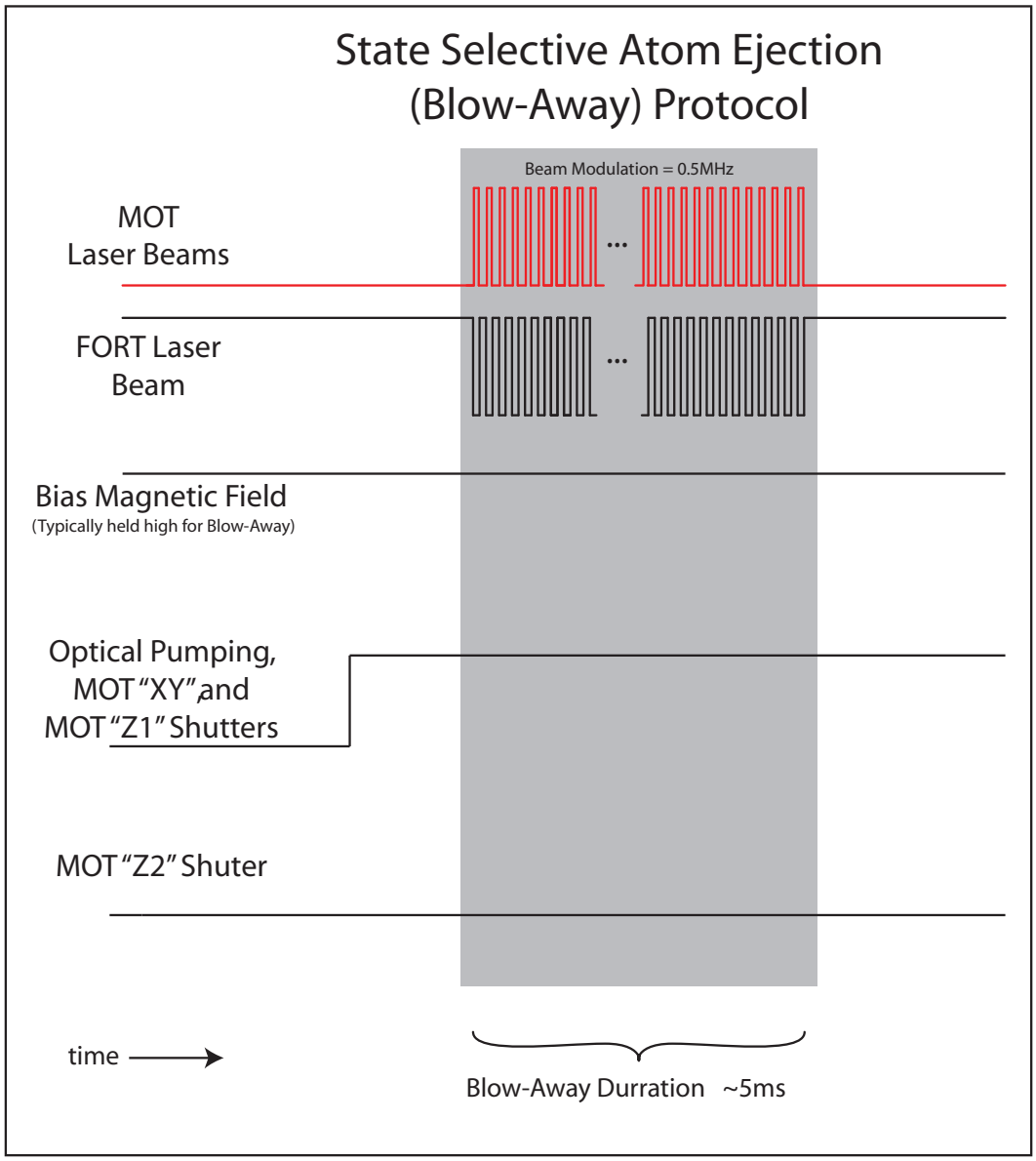

Figure 3.13 State selective atom ejection timing scheme (blow-away protocol). The mechanical shutters are used to prevent all, but one of the MOT laser beam paths from reaching the atom sample. The bias magnetic field is nominally high during the blow-away protocols. Once again, the MOT laser light must be modulated out of phase with the optical dipole trapping laser.

Chapter 4

Optical Dipole Traps

4.1 Overview of Optical Dipole Traps

The atom samples that we study are localized to small volumes of space with the use of optical dipole traps. The trapping potential is generated by a tightly focused laser beam that is far detuned from the D1 and D2 ground state transitions of rubidium-87. This far off resonance trap, or FORT, relies upon the dipole induced within an atom while in the presence of a large electric field. This interaction between the induced dipole and the perturbing electric field is known as the light shift or AC Stark effect. The spatial dependence of the dipole potential generated by a linearly polarized laser beam propagating along the z-axis is described by:

$$U(r,z) = -\frac{\alpha_0 |E_0|^2}{4} e^{-2r^2/w^2(z)} \quad \left(\frac{w_0}{w(z)}\right)^2 \tag{4.1}$$

Where r^2=x^2+y^2, and E_0 is the maximum electric field amplitude at the focus of the laser. The scalar polarizability, α_0, of the ground state is $114A^3$ at 1064nm [Kadar-Kallen et al, 1992]. The laser beam is defined to have a $1/e^2$-waist, w_0, at its focus. Due to divergence the beam waist of a collimated laser beam will expand. The Gaussian beam waist observed some distance, z, from the collimated beam waist is characterized by:

$$w(z) = w_0 \sqrt{1 + \left(\frac{z\lambda}{\pi w_0}\right)^2} \tag{4.2}$$

From these equations we can conclude that the dipole force on each atom is proportional to the intensity of the laser beam ($I = \epsilon_0 c |E_0|^2/2$) and that the conservative trapping potential has an ellipsoidal spatial dependence.

Unlike the MOT, the FORT potential is not dependent upon momentum kicks due to photons scattering off the atom. The optical potential is linearly dependent upon the scalar polarizability of the atom, and the intensity of the laser beam. At a large detuning from an atomic transition the probability of an atom absorbing a photon is inversely proportional to the square of the laser detuning. The scalar polarizability is approximately proportional to the inverse of the laser detuning. The scattering rate of the potential will decline faster than the trapping potential′s depth as the detuning is increased. Through controlling the FORT laser′s detuning and intensity one can attain a modest trapping potential with very small scattering rates. Through experimental demonstrations FORT traps have been proven to be a robust means of confining atoms for several seconds at a time [Chu et al., 1986], [Miller et al., 2002], and [Kuppens et al., 2000].

The spatial confinement of these traps is anisotropic due to the diffractive nature of the Gaussian beam. Atom confinement along the beam′s propagation direction is much looser than confinement along the transverse directions. Since atoms are cooled into the traps and primarily reside at the bottom of the potentials we use a parabolic expansion of the FORT potential to model the effective spring constants of the trap [Saffman and Walker, 2005].

$$k_r = \frac{|\alpha_0||E_0|^2}{w_0^2} = 4\frac{|U_m|}{w_0^2} \tag{4.3}$$

$$k_r = \frac{|\alpha_0|\lambda^2|E_0|^2}{2\pi^2 w_0^2} = 2\frac{|U_m|\lambda^2}{\pi^2 w_0^2} \tag{4.4}$$

We use $|U_m|$ to define the maximum depth of the potential at the center of the FORT well in temperature units. The corresponding harmonic oscillation frequencies are:

$$\omega_r = \frac{2}{w_0}\sqrt{\frac{|U_m|}{m}} \tag{4.5}$$

$$\omega_z = \frac{\lambda}{w_0^2\pi^2}\sqrt{\frac{2|U_m|}{m}} \tag{4.6}$$

These asymmetric spring constants give rise to a anisotropic atom distribution. For a given temperature, T_a, Boltzman factors can be used to estimate the time averaged variances of

the atom positions as, [Saffman and Walker, 2005]:

$$\langle r_d \rangle = \frac{w_0^2 T_a}{4|U_m|} \langle z_d \rangle = \frac{\pi^2 w_0^2 T_a}{2\lambda^2 |U_m|} \tag{4.7}$$

Being a conservative potential, the FORT merely provides spatial confinement for atoms, and lacks the ability to cool an atom sample. Loading atoms into the FORT, therefore, requires us to superimpose the MOT (Chapter 3) over the FORT laser beams. By temporally and spatially overlapping these trapping mechanisms, atoms cooled by the MOT are stochastically transferred into the FORT. The fiber coupled lasers and large numerical aperture optics used to generate the FORT are discussed in Sections 4.2 and 4.3. The typical trapping conditions implemented in the experiments are explained in 4.4. A six site ‘‘proof of principle″ variation of our typical FORT is explained in Section 4.5.

4.2 Trapping Lasers

A high power laser system fiber coupled to an optical array is used to generate the optical dipole traps. In the course of these experiments a variety of different laser sources were used. Early experiments utilized a 6W ELS Versadisk laser which operated at $\lambda \approx 1030$nm. This laser system was later replaced by a NuFERN $\sim$10W fiber amplifier system seeded by a NP-Photonics Scorpio fiber laser operating at $\lambda \approx 1064$nm. The Scorpio seed laser is capable of generating 80mW at a wavelength of 1064nm. These lasers were both passed through an AOM before being fiber coupled to the FORT optics and vacuum chamber. The AOM is used to control the FORT laser intensities throughout the experiment. As explained in Section 3.5, the FORT intensity is modulated during particular experimental protocols to momentarily eliminate the AC Stark shifts imposed upon the atoms. The first order diffraction efficiency of the AOM is typically higher than 60%. The 10-90% rise time of the laser beam modulation is less than 40ns. The first order laser beam is coupled into a polarization maintaining optical fiber (Oz Optics PMJ-3a3a-980-4/125-3-5-1) with 75% coupling efficiency. The fiber output is adjoined to an optical array used to generate the FORT potentials.

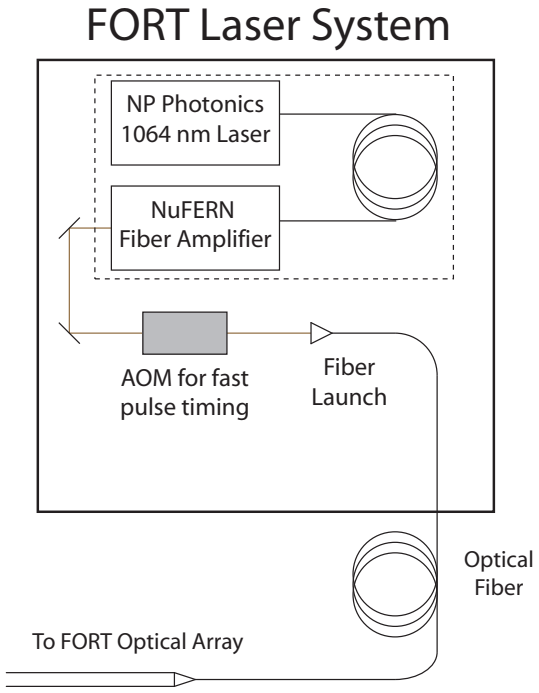

Figure 4.1 Overview of the FORT laser system. NuFERN laser amplifier is mounted to a water cooled plate. The 1030nm ELS laser, described in text, was previously used in place of the 1064nm laser system (outlined in figure).

4.3 Dipole Trap Optics

The optics used to shape and transmit the FORT potentials to the center of the vacuum chamber are mounted to a custom built optical breadboard and cage system. This rigid construction allows us to characterize the FORT assembly prior to aligning the entire optical breadboard to the vacuum chamber. A detailed discussion on how the laser beams are characterized and aligned through the optical array can be found in Appendices B and E.

The optical fiber output is collimated with a Thorlabs, C110TM-B f≈6.24mm aspherical lens to a $1/e^2$ beam waist of approximately 700μm. The collimated laser beam traverses a $\lambda/2$ wave plate. The half wave plate is used to adjust the laser beam′s linear polarization axis before it passes through the calcite beam displacer. The calcite crystal is cleaved such that vertical and horizontal polarizations are split into two separate but parallel beams.

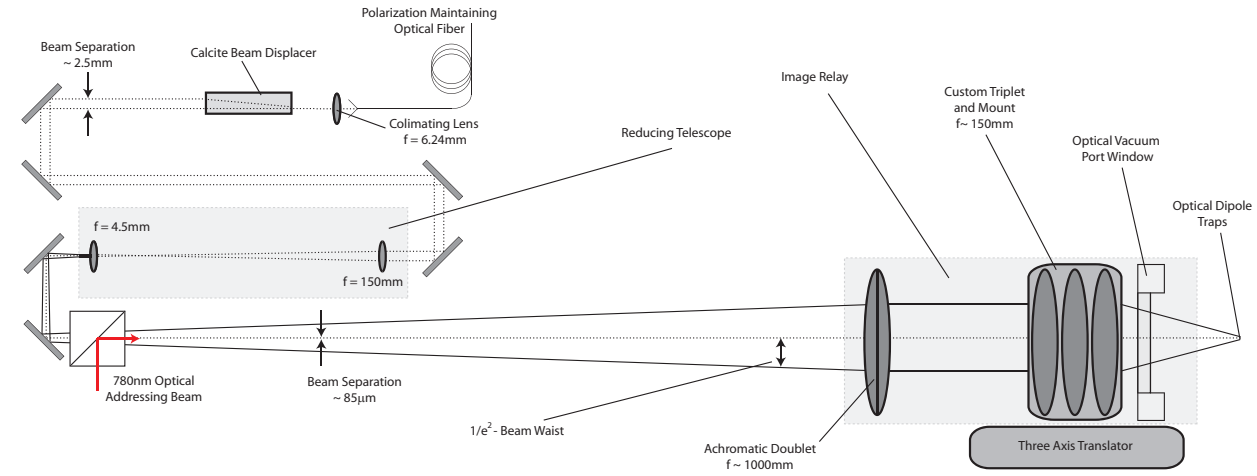

Figure 4.2 Side view diagram of the FORT optical array (not to scale). An optical fiber is used to couple light into the system. Dashed ray trances are used to represent axes of the laser beam propagation. Solid rays illustrate diverging beam waists. The collimated output is split into two parallel laser beams by a calcite beam displacer. This technique, of projecting two laser beams through the optical train, enables us to generate multiple FORT sites simultaneously. The dashed lines represent the two separate laser beams. The solid rays in the optical beam path represent the $1/e^2$ Gaussian beam waist. Together the optical elements image the output facet of the calcite crystal into the center of the vacuum chamber. A dichroic beam splitter is used to integrate an optical addressing laser beam into the FORT assembly (see Chapter 6).

At the crystal′s exit facet these beams are separated by ∼2.5mm. By adjusting the beam polarization we have control over the relative output beam intensities of the calcite crystal. The parallel laser beams are passed through a telescope constructed from a Thorlabs LA1433-B, f=150mm planoconvex lens and a C230TM-B, f=4.5mm asphere. The telescope output is passed through an image relay which is used to reduce the beam′s waists and beam separation by a factor of approximately 6.8. The large beam divergence, found after the first telescope, forces us to construct the image relay from 100mm diameter lenses. The first relay lens is a Linos Photonics Inc. custom antireflection coated f≈1007mm achromatic doublet (PN 322313525). A large diameter high numerical aperture custom designed f≈148mm triplet is used to refocus the light through the 6.5mm thick vacuum port windows. The optical

parameters of the vacuum window are integrated into the design of the custom triplet. This custom designed air-spaced triplet is mounted in a five axis translation stage, to control its position, pitch, and yaw relative to the FORT beam propagation. The relative spacing between two of the triplet elements are optimized with a set of high pitch actuators. Further details on the lens and actuator design are contained in Appendix B. Since the FORT laser beams are collimated between the optical elements of the image transport, the final focus can be repositioned in the vacuum chamber by simply translating the final triplet. Alignment techniques and consequences of misalignments are discussed further in Appendix B.

4.4 Nominal Operating Condition

As previously discussed, the trap depth scales inversely with the laser detuning but linearly with respect to the laser′s intensity. The photon scattering rate of the atoms in the potential is inversely proportional to the square of the detuning. The photon scattering rates encountered will limit our ability to retain an atom in a dipole trap, and qubit coherence times. The scaling of the scattering rate makes operating in a far detuned regime with high laser intensities appealing. We nominally operate in a regime where the trapping wavelength, λ, is $\approx$1064nm. This wavelength is far detuned from the ^{87}Rb D1 and D2 transitions ($\sim$795nm and $\sim$780nm).

Using the ELS 1035nm laser source, the beam waists generating the optical potentials are measured to be approximately 2.9μm with a separation of 10.2μm. The wavelength of the FORT laser nominally operates at 1064nm. The FORT laser beams are typically established using about 450mW of power in each beam, thus delivering a peak intensity of about 3.3MW/cm^2. Using equation 4.1, the peak trap depth used to retain the atoms is approximately 5.0mK in temperature units. Drifts in the polarization output of the optical fiber cause the balance of power between the two FORT sites to vary by about $\pm$30mW. The characteristic axial and transverse oscillation frequencies of a typical FORT are 6kHz and 75kHz, respectively.

4.5 Variant of Optical Dipole Trap

As briefly discussed in Section 1.7, a quantum computer must be scalable. Scalability of our quantum register requires us to develop the ability to generate additional lattice potentials and initialize single atoms into these potentials. Neither of these processes can be allowed to place exponential demands upon the system′s resources; such as: time required to load all lattice sites, energy requirements to create additional dipole traps, and number of physical components required to generate more lattice sites. The issue of deterministic loading is discussed further in Chapter 12. This section presents an elegant and scalable solution for the generation of additional optical potentials. We demonstrated that our FORT sites can be modified to generate six optical potentials by merely adding two additional lenses and a diffractive element to the FORT optical train. This change is illustrated in Figure 4.3.

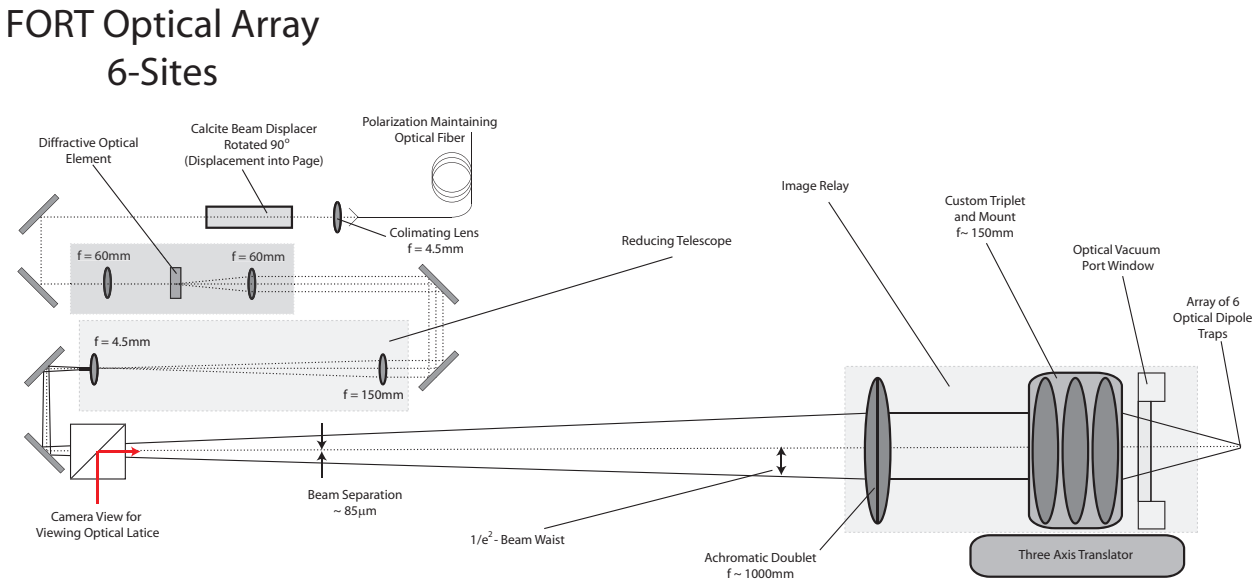

Figure 4.3 FORT optics array used to generate a 2×3 lattice potential. Note the addition of the 1:1 telescope and diffractive optical element. The calcite crystal has been rotated 90^o so that the beam displacement is now into the page. The dichroic beam splitter is being used to view the lattice potentials from end on.

The two original FORT beams are rotated 90^o and focused with a 60mm achromatic doublet onto a Stocker Yale multiple dot pattern diffractive optical element. The grating

pattern has a period, d, of 25μm and is designed to diffract a collimated laser beam into five additional beams ($\pm$2, $\pm$1, 0 orders). The diffraction angle between the 0^{th} and m^{th} order beams is given by $\theta = \sin^{-1}(m\lambda/d)$. The diffraction angle of adjacent orders is 2.37^o when using a λ=1035nm laser. A second 60mm achromatic doublet is used to collimate and set all of the beam paths parallel with one another. The final beam waists are $\sim$2.9μm, and the lattice spacings are of order $\sim$10μm. Direct observation of the optical lattice pattern on a CCD camera revealed that the highest order diffracted beams are significantly weaker in intensity. Upon further investigation this loss in beam power is primarily due to the outermost laser beams clipping on the edges of the mirrors.

The ELS laser is used to generate the optical potentials in this experiment. Approximately 2.5W of power are used to generate the 10 laser beams. While using the ELS laser 660mW are typically required for two FORT potentials. Due to the low FORT beam power it is necessary to load the MOT and FORT for several seconds to successfully trap atoms in the lattice potentials. Figure 4.4 is a compilation of 340 camera images of the FORT potentials. Atom detection methods will be discussed further in Chapter 5. These images clearly indicate that we possess the ability to generate and load multiple optical potentials.

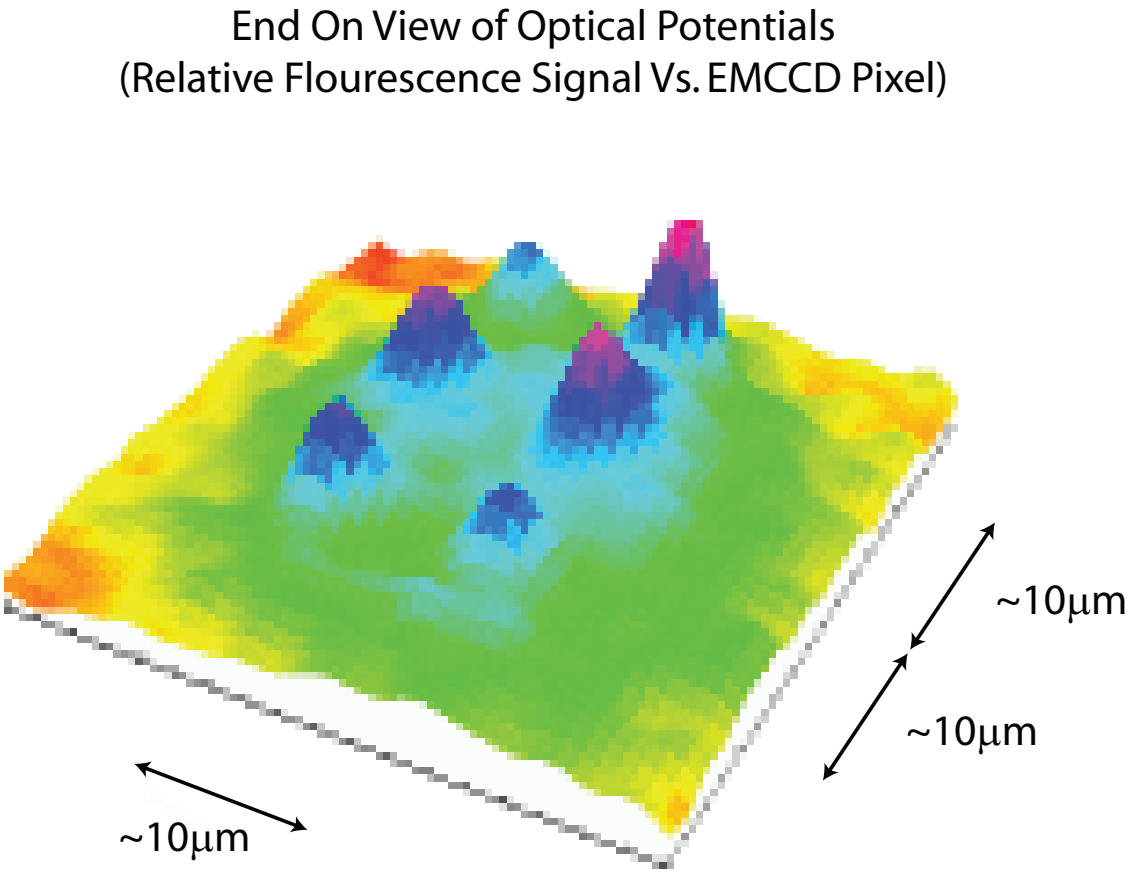

Figure 4.4 Viewing atoms loaded into 6 optical dipole potentials. Lattice spacing is of order $\sim 10\mu$m. The electron multiplying CCD (EMCCD) camera image is obtained by viewing the atoms through the last two elements of the FORT optics (see figure 4.3). The plot shows the average relative fluorescence signal obtained per pixel. 340 camera images are compiled to create the image above. Each camera shot uses a 7 second experiment cycle.

Chapter 5

Single Atom Imaging

This chapter discusses the specially fabricated system used to detect the atoms confined within the various FORT potentials (Chapter 4). Section 5.1 discusses the performance of the camera and optical array used to perform single atom imaging. Section 5.2 illustrates how the fluorescence images gathered by the camera are processed to identify single atom signals. This atom detection provides us with a means of characterizing the lifetime of the FORT trapping potential, and the atom distribution within the FORT as illustrated in Sections 5.3, and 5.4.

5.1 Atom Imaging Hardware

The readout of individual qubit states is performed with an optical array coupled to a digital camera. An Andor Ixon DU-860 electron multiplying charge coupled device (EMCCD) camera is used to collect the photons scattered off atoms confined by a FORT. The CCD pixels are 24μm x 24μm and are laid out in a 128 x 128 pixel array. This camera differs from a typical CCD array in the fact that the CCD chip is cooled to -70^o Celsius, and uses a gain register to amplify the photoelectron signals transferred from each individual pixel. This greatly improves the signal to noise ratio at low light levels thus enabling single photon and single atom detection. The camera internally converts the amplified signal into counts [Johnson, 2008]. The overall camera gain is calibrated to generate approximately 7.5 $\pm$ 0.8 counts per photoelectron [Johnson, 2008].

Figure 5.1 illustrates the large numerical aperture lenses and optical filters used to reimage the fluorescence signal onto the EMCCD. The photon collection efficiency is limited by the aperture of the vacuum port window. The port window is approximately 70mm in diameter located roughly 79.5mm from the center of the chamber. Therefore, the solid angle of this aperture, $\Omega_{s.a.}$, is approximately 0.53 steradians.

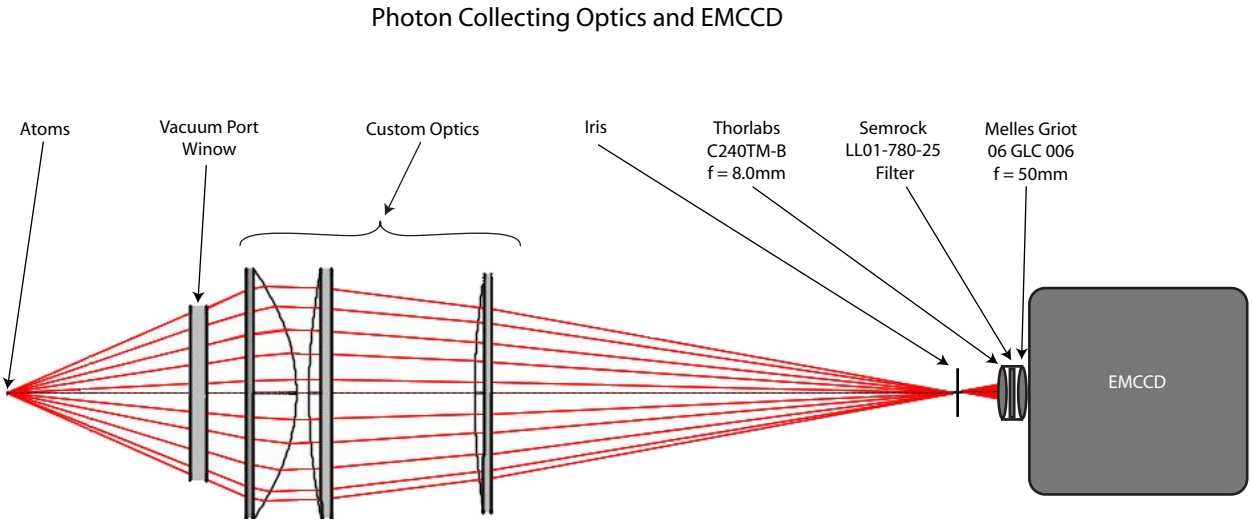

Figure 5.1 Optics used to image atoms confined within the FORT potentials. The atoms sit at the object plane of a set of high numerical aperture custom designed optics. The image plane is set to coincide with a spatial filter (iris). The fluorescence signal passes through an image relay to the EMCCD. A narrow bandpass filter is placed between the image relay′s optical elements to filter out FORT light scattering off the vacuum chamber′s interior surfaces.

In order to collect all of the light from this solid angle it is necessary to use a set of 100mm diameter lenses to generate an intermediate image of the trapped atoms. An adjustable iris is used at the image plane to help restrict stray background light from reaching the EMCCD. The intermediate image is transferred through an image relay to acquire additional spatial magnification. The lenses used in the relay are a Thorlabs f=8mm C230TM-B asphere and a Melles Griot f=50mm triplet (06 GLC 006). A Semrock LL01-780-25 filter is placed near the Fourier plane of this image relay. Filtering the light is crucial in removing scattered light from the FORT laser system. The transmission efficiency of this filter at 780nm is ≈98%.

The transmission efficiency through the large aperture lenses and a mock port window is approximately 88%. This transmission measurement is determined by aligning the tip of an optical fiber (NA≈0.21) to the object plane of the imaging system. The transmitted power is measured at the intermediate focal plane. The total optical transmission efficiency is ≈86%. The factory specified quantum efficiency of the camera was 74% [Andor, 2004]. The total optical efficiency, η, of the system was approximately:

$$\eta \;=\; \frac{\Omega_{s.a.}}{4\pi}\eta_{optics}\eta_{qe} \;=\; \frac{1.56}{4\pi}(0.86)(0.74) \;\approx\; 8\% \tag{5.1}$$

The spatial magnification of the imaging system is characterized using a standard 1951 USAF resolution chart. Using this calibration technique the magnification of the optical system is found to be approximately 11.16, thus making the effective pixel size approximately 2.15μm (see Appendix A.1). The depth of focus of the optical system is fixed by the numerical aperture of the system. The numerical aperture is given by nsin(θ_w), where n is the index of refraction and θ_w is the half-angle of the maximum cone of light that can enter the optical system. As previously noted, this angle is constrained by the port window of the vacuum chamber. For this system n=1, NA=0.4, and the wavelength of light being imaged, λ, is ∼780nm. The depth of focus of a magnifying system can be approximated using Equation 5.2, [Young et al., 1993].

$$\Delta z = \frac{\lambda}{4n\left(1-\sqrt{1-(\frac{NA}{n})^2}\right)} \tag{5.2}$$

Therefore, the depth of focus is ∼2.3μm for our optical system. The precision with which the camera can be positioned relative to the FORT is on the same order of magnitude as the depth of focus (see Appendix A.2). Fortunately, the spatial distributions of the atoms in the FORT′s transverse dimension are of the same order of magnitude as the depth of focus of our optical system. Therefore, the vast majority of light projected by an atom will originate from a region within the camera′s depth of focus.

5.2 Single Atom Signals

The optical system is nominally aligned orthogonally to the FORT′s propagation axis providing us with a clear side-view of both FORT trapping sites. As explained in the Section 3.5, a typical image is collected by modulating our FORT and MOT laser beams out of phase while recording the resulting atom fluorescence signal. A typical 50ms camera exposure is shown in Figure 5.2. Averaging collections of these images helps establish a region of interest (ROI) over which the fluorescence signal is most typically observed (see Figure 5.2).

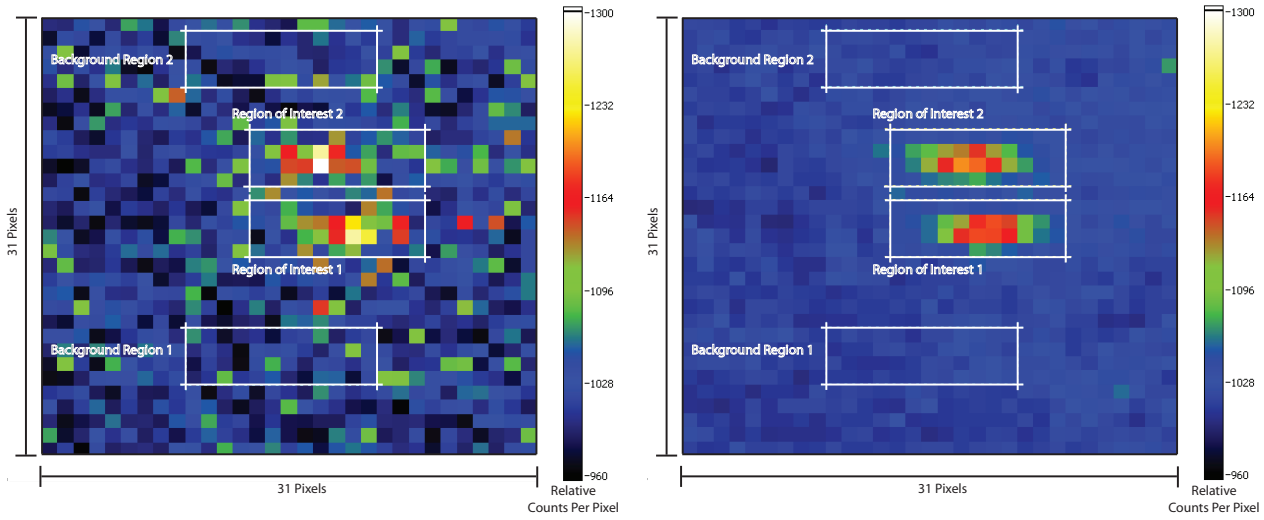

Figure 5.2 On the left is an EMCCD image of single atoms trapped in two FORT potentials. To the right is a composite image generated by averaging 57 single atom events. The signal is reported in relative counts. Both images identify the regions of interest (ROI) and the regions used for background signal subtraction. Each pixel is roughly $\sim 2.15\mu$m$\times\sim 2.15\mu$m.

Individual camera images are processed by removing an averaged background signal from each pixel of the EMCCD array and then integrating the relative signal strength over a particular ROI. The number of camera counts registered in the ROI is then converted to photoelectrons as discussed by [Johnson, 2008]. The integrated background subtracted ROI

signal in a sequence of atom images is plotted below in Figure 5.3. An ROI signal sequence can be used to generate a histogram as shown in Figure 5.4.

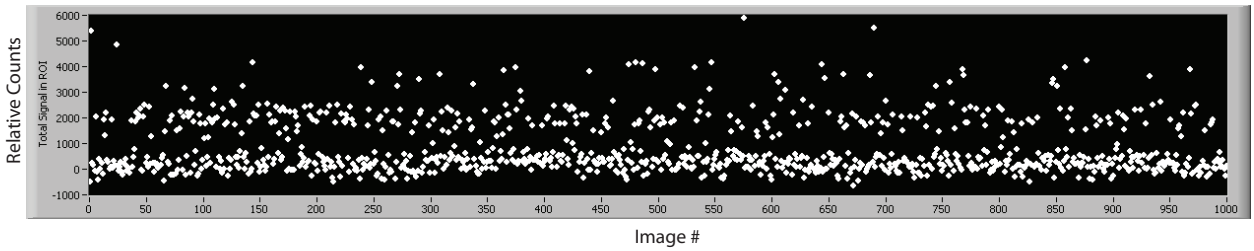

Figure 5.3 Plot of relative signal observed in ROI-2 for a series of 1000 experiment cycles. Note the discrete nature of where the ROI signal falls.

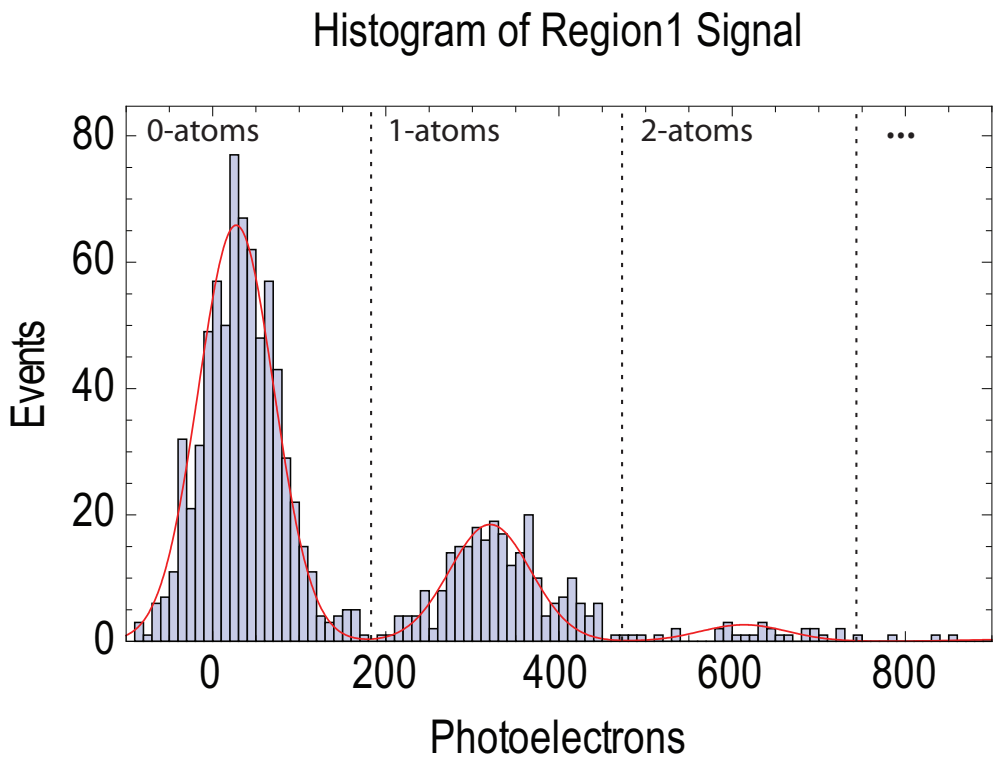

Figure 5.4 Histogram of the signals observed in Figure 5.3. The raw CCD camera signal was converted into photoelectrons before being binned into one of the 100 bins implemented. The red curve is a fit function describing a Poissonian atom loading. The fit function and parameters are described in the text.

The quantized nature of the histogram is used to calibrate the camera for single atom fluorescence signals. The first peak of the histogram in Figure 5.4, located at approximately 0-photoelectrons, is generated by dark counts and stray light reaching the detector. The negative photoelectron signals in Figure 5.4 are the result of background subtraction. The histogram′s second peak, located at ∼293 photoelectrons, corresponds to the signal produced by single atoms. A subsequent peak appears at roughly twice the single atom photoelectron signal. This peak in the histogram represents fluorescence signals generated by two trapped atoms. By properly controlling the MOT and FORT loading conditions, the average number of atoms trapped in the FORT for a series of pictures can easily be maintained to be less than five atoms. A Poissonian distribution is thus used to describe the stochastic atom loading process. The average number of atoms loaded in the FORT will be defined as N. The probability of observing k discrete atoms within the FORT during a particular camera exposure is given by Equation 5.3 [Johnson, 2008].

$$f_{atom}(k) = \frac{N^k e^{-N}}{k!} \tag{5.3}$$

The creation of photoelectrons is statistical in nature as well. The number of photoelectrons generated by an ROI is dependent upon the number of atoms trapped, the fluorescence scattering rate of each atom, and the camera exposure time. The fluorescence rate and exposure times are constant for each camera image. Background signals also contributed to the number of photoelectrons observed in each shot. The background photoelectron signal is $n_{be}= \sim 1900$ for the histogram in Figure 5.4. The total number of photoelectrons observed in each readout is much larger than 50. It is, therefore, valid to model the distribution for each histogram peak with a Gaussian distribution [Johnson, 2008]. If an atom typically generates a signal of σ, then the probability of observing n_{pe} photoelectrons from k atoms would be given by:

$$g(n_{pe}) = \frac{e^{-(n_{pe}-(n_{bg}+k\sigma))^2/(2(n_{bg}+k\sigma))}}{\sqrt{2\pi(n_{bg}+k\sigma)}} \tag{5.4}$$

The histogram relies upon convolving the Poissonian atom distribution with the Gaussian photoelectron distribution to appropriately fit the data. The final fit function is arrived at

by limiting the fit function to a five atom signal, applying a multiplicative scaling constant, and inserting an offset to the mean value of the Gaussian photoelectron signal [Johnson, 2008]. This results in Equation 5.5 shown below.

$$f(n_{pe}) = A\sum_{k=0}^{5}\frac{\mathrm{N}^k e^{-\mathrm{N}}}{k!}\frac{e^{-(npe-n_{off}-k\sigma)^2/(2(n_{bg}+k\sigma))}}{\sqrt{2\pi(n_{bg}+k\sigma)}} \tag{5.5}$$

In Figure 5.4, the average number of atoms loaded into the FORT after performing 1000 loading cycles is approximately 0.30. The particular MOT conditions used during the readout protocol generate ~ 293 photoelectrons per atom, while the background signal produces a signal equivalent to roughly ~ 6.5 atoms. This analysis provides a metric for digitizing the fluorescence signals. A camera image with an ROI signal between 180 and 465 photoelectrons is likely to contain a single atom. This knowledge provides us with a means of filtering our ROI signals for discrete atom signals. This technique is used in later experiments to digitize our atom signals, and remove 0-atom signals from our experiments.

5.3 FORT Retention

Binning the fluorescence signals allows us to clearly observe quantized signals. This observation is important in developing experimental protocols capable of determining the number of atoms present during a particular experimental trial. Experimental protocols typically contain two camera readout phases: one at the beginning and a second at the end of each experiment cycle. This provides us with a measurement of the number of atoms in an optical trap at the beginning and end of each experimental cycle. In Figure 5.5 the fluorescence signal of the second camera readout is plotted as a function of the signal recorded during the first camera readout.

Once again, the fluorescence signals within Figure 5.5 cluster indicating that the ROI data is quantized for both camera exposures. The mean number of photoelectrons observed for a single atom signal is approximately equal for both the first and second camera exposures. This feature allows us to determine how often an atom observed in the first camera image is also observed in the subsequent camera exposure. Signals indicating the presence of a

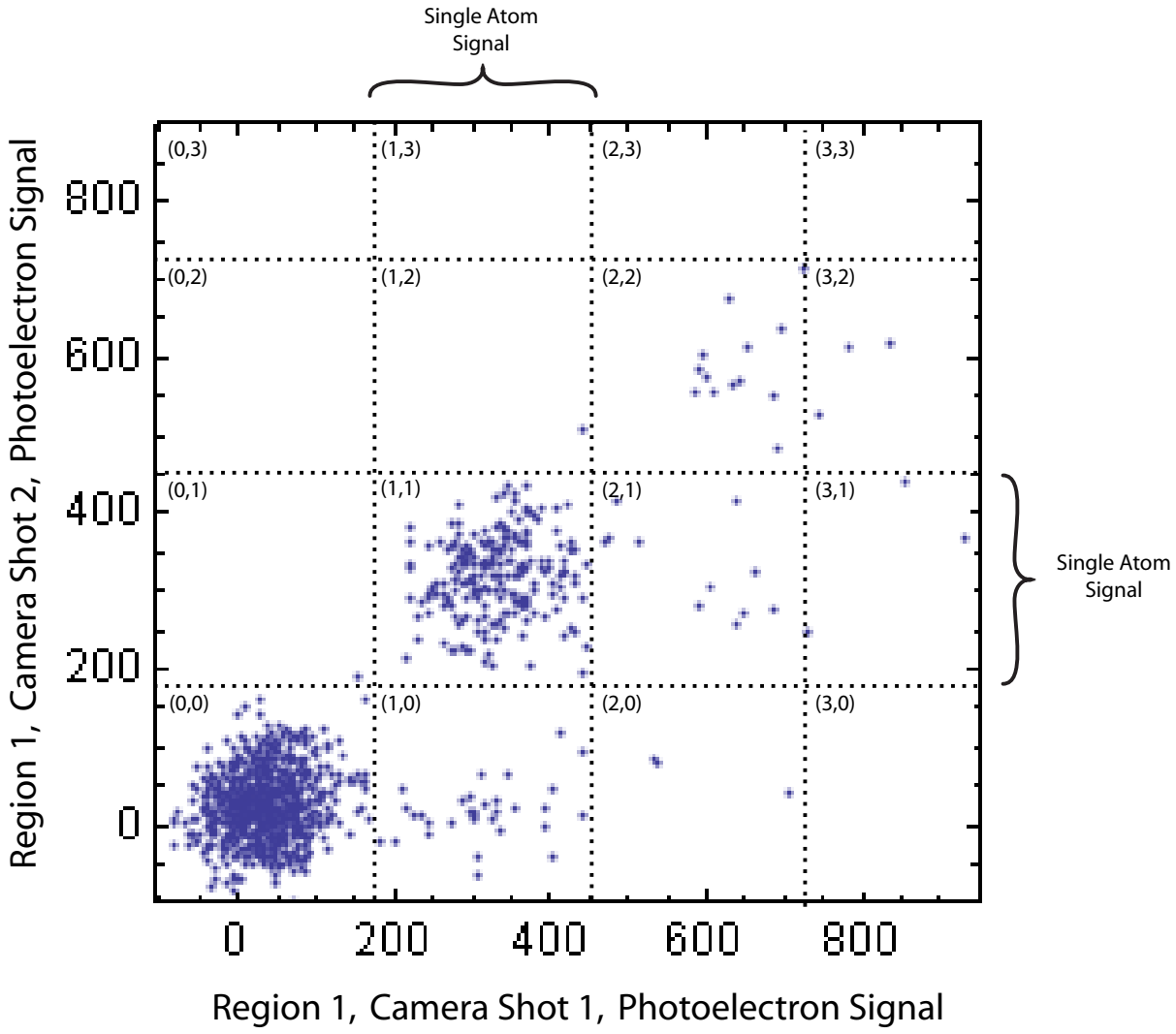

Figure 5.5 Plot of observed fluorescence signal from an experiment cycle implementing two readout protocols. The fluorescence signal from ROI-1 during the second camera exposure is plotted as a function of the signal detected in ROI-1 during the first camera exposure. In both the first and second camera exposures the fluorescence signals are clearly discrete.

single atom signal in both camera images are outlined in region (1,1) in Figure 5.5. In this particular plot the percentage of atoms retained between the first and second image is approximately 87%. In Figure 5.5 the region marked (1,0) indicates trials where an atom is observed in the first shot, but lost before or during the second camera exposure. It should

be noted that the number of atoms observed in the second shot never exceeds the number of atoms observed in the first camera exposure. This indicates that the MOT light used during the readout protocols is not loading additional atoms into the FORT.

Performing two camera readouts in sequence can be used to measure the lifetime of a single atom in the FORT. Atoms cannot remain trapped in the FORT indefinitely due to FORT photon scattering and background gas collisions [Saffman and Walker, 2005]. In order to measure the lifetimes of single trapped atoms we acquire statistics on the number of atoms retained by the FORT as a function of time between two successive camera measurements. A typical data set demonstrating this measurement is shown in Figure 5.6.

The protocol used to generate a typical lifetime measurement is initiated with a MOT and FORT loading protocol (see Section 3.5). Two camera readout protocols are then used to observe how many atoms are trapped after each loading protocol, and how many atoms are still present in the trap 400ms later. After recording several hundred sets of camera images the time delay between the successive camera exposures are increased by 200ms. This entire process is iterated 21 times. The data is post processed by retaining only the sets of camera images where a single atom signal is identified in the first camera exposure. These filtered ROI signals are then digitized to reflect the number of atoms recorded during each readout protocol. The average number of retained atoms is plotted as a function of time between camera shots. Each data point in Figure 5.6 reflects the average of approximately $\sim$40 sets of camera exposures. The error bars reflect the standard error of the averaged digitized signals. This plot is curve fit with an exponential decay, thereby allowing us to characterize the trap retention as a function of time.

$$R(t) = e^{-t/\tau_{FORT}}$$

The FORT lifetime is observed to have a time constant of approximately 3.7sec. This lifetime is dominated by background gas collisions. The measurement of the FORT lifetime is an important consideration due to the fact that all experiments performed on single atom samples require two time delayed camera exposures. The majority of the experimental protocols require a minimum of 400 ms between camera exposures. This time requirement places

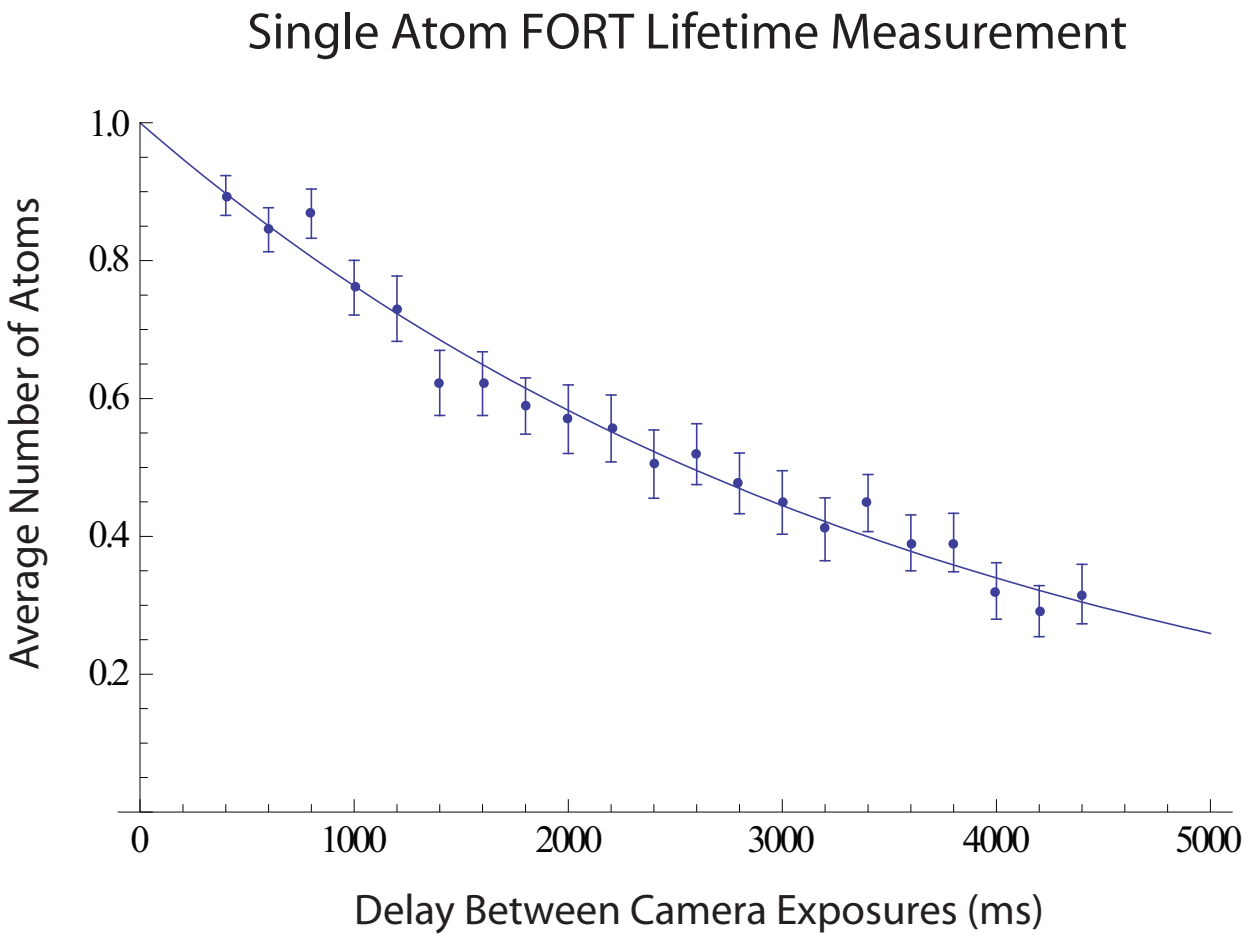

Figure 5.6 Measurement of the lifetime of a single atom in the FORT. The average number of atoms retained in the FORT during the second readout protocol plotted as a function of the time between camera exposures. The error bars represent the standard error of the digitized mean atom number. The data is fit with an exponential decay, $R(t) = e^{-t/\tau_{FORT}}$. The lifetime τ_{FORT} is approximately 3.7 seconds.

an upper bound of ∼90% on the atom retention between imaging phases. In experiment protocols that rely upon the presence of a single atom, it will be necessary to renormalize our data to account for these nominal atom losses. By taking 1000 camera shots and analyzing the retention for a particular time delay, the atom retention can be determined to within ±5%. These control experiments are performed daily to determine the appropriate renormalization factors to use when processing data.

5.4 FORT Temperature Measurements

Due to the optical system′s small depth of focus and the very small fluorescence signal generated by a single atom it is not possible to use standard free-fall time-of-flight measurement techniques to determine the temperature of atoms held in the FORT. Single atom detection typically requires signal integration from 30ms to 50ms. While it is possible to identify a single localized atom, it is not feasible to distinguish a single slowly dispersing atom from the fluorescence of background gas atoms. A more appropriate method of ascertaining the atom′s temperature is necessary. Measurements of the spatial distribution of trapped atoms are used in conjunction with a drop and recapture technique to determine the atom temperatures [Reymond et al., 2003], [Johnson, 2008], [Urban et al., 2009].

Figure 5.7 illustrates the atom distribution within the optical potential. The image is generated by averaging 146 camera exposures. Line profiles extracted from the image are used to determine the separation of the FORT potentials as well as back out an approximate point spread function of the imaging optics and a Gaussian distribution of the trapped atoms. As demonstrated in Equation 4.7, the transverse and axial spatial distributions are related to the temperature of the atoms. The data in Figure 5.7 suggest that the optical potentials are 3.0μm, and that the temperature of the atoms are approximately $\sim 200\mu$K [Johnson, 2008], [Urban et al., 2009].

This analysis is corroborated by a drop and recapture measurement of the FORT atoms. The experimental protocol used to perform drop and recapture measurements is illustrated in Figure 5.8. The experimental cycle begins by loading atoms into the FORT, and performing a camera readout protocol. In the middle of the experiment cycle the FORT laser is turned off, thus dropping any trapped atoms. The FORT laser is reestablished after a predetermined delay in an attempt to recapture the atom. The probability of recapturing an atom is dependent upon the atom′s temperature. The data presented in Figure 5.9 is generated by gathering statistics on the probability of recapturing the atoms for a variety of different drop times. Data processing of the camera images, and signal renormalization to account for

nominal atom loss between camera shots is performed as described in Section 5.3. Comparing this plot with a numerical simulation of expected trap loss [Urban et al., 2009] indicates that the atom temperatures are expected to be between 150 and 300μK.

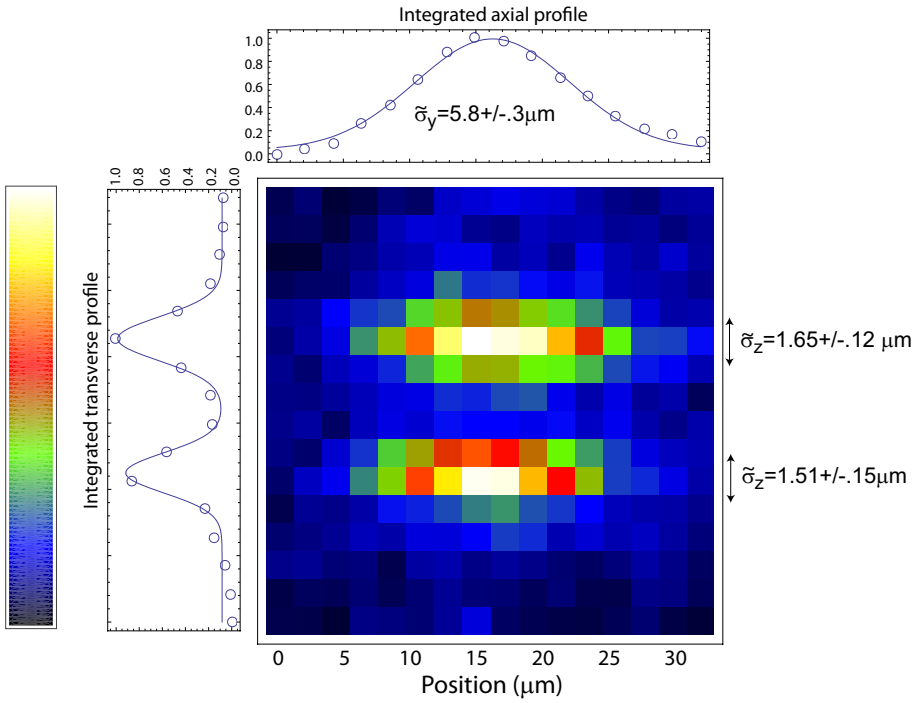

Figure 5.7 Spatial distribution of atoms trapped within the FORT potentials. The image is generated by averaging 146 readout protocols. The peaks are found to be separated by 10.2μm. After deconvolving spatial blurring from the optical system the Gaussian spatial distributions of the traps were inferred to possess standard deviations of 0.45μm and 5.6μm in the z and y axes.

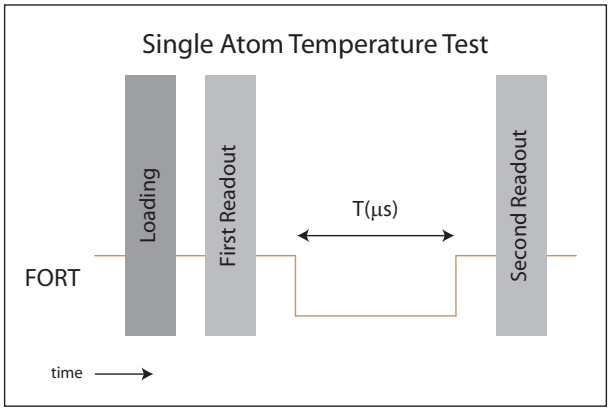

Figure 5.8 Timing protocol used to perform a drop and recapture experiment cycle.

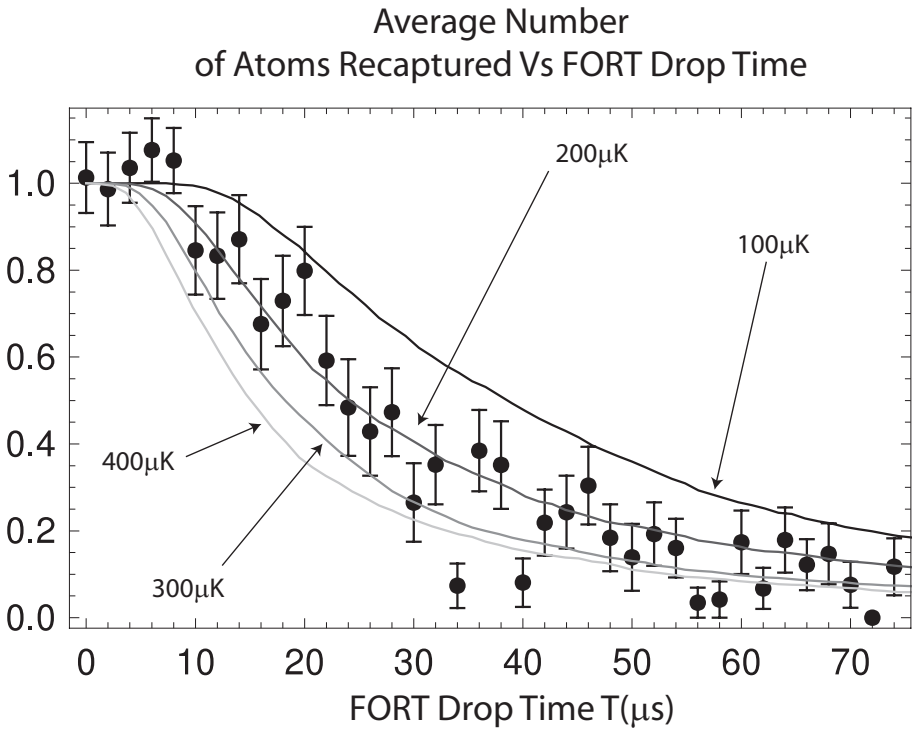

Figure 5.9 Data from a series of drop and recapture measurements. The number of retained atoms has been renormalized to account for nominal atom loss between readout protocols. Error bars represent the standard error of the averaged digitized atom signal. The lines plotted alongside the data represent the results from a numerical model. Visual comparison allow the temperature to be estimated between 150300μK.

Chapter 6

Qubit Addressing Lasers

6.1 Overview of Addressing Lasers

This quantum computing scheme relies upon two-photon transitions between hyperfine ground state levels to perform single qubit operations. Entangling operations are performed via two-photon transitions between the F=2 ground state and Rydberg levels. The laser beams used to address the single qubit sites must perform these excitations without perturbing the coherence of neighboring qubits. Three optical beam paths are utilized for the purpose of delivering these specifically timed laser pulses to the individual qubits. This chapter discusses the lasers used to drive these transitions, and the accompanying optics used to address individual FORT potentials.

6.2 Ground State Two Photon Raman Laser System

Single qubit operations are carried out via two photon transitions between specific magnetic sublevels of the F=1 and F=2 Rb-87 hyperfine sublevels. To avoid the effects of fluctuating Zeeman shifts the $|\mathrm{F}=1,m_F=0\rangle \leftrightarrow |\mathrm{F}=2,m_F=0\rangle$ transition is utilized. To first order, the energy levels of the m_F=0 magnetic sublevels are not susceptible to magnetic field perturbations, thereby making these states more robust for quantum computing. A schematic of the pertinent atomic energy levels and laser fields required to drive the two photon Raman process is shown in Figure 6.1.

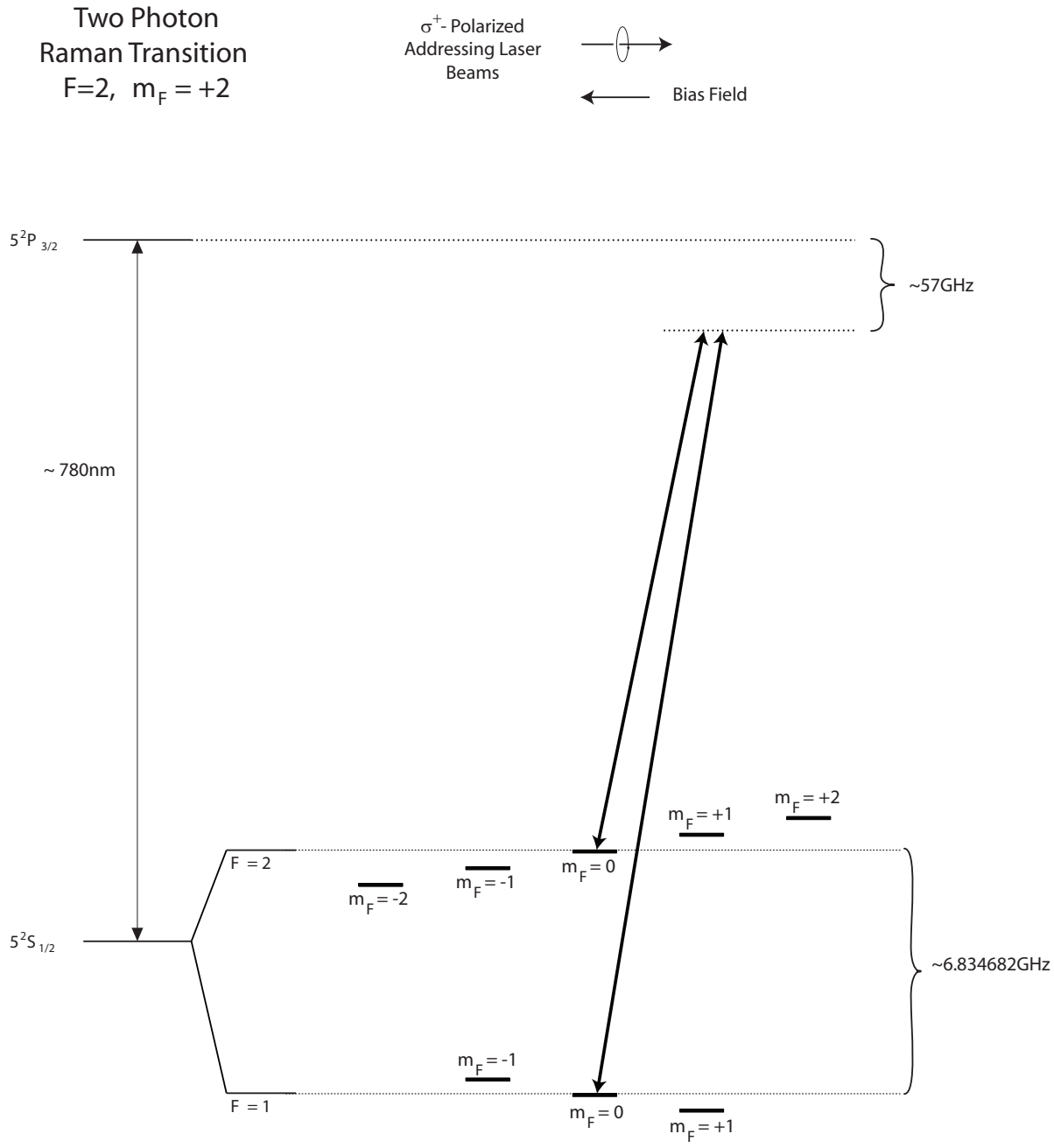

Figure 6.1 Energy level diagram illustrating the two photon transition between the $|\mathrm{F}{=}1, m_F{=}0\rangle \leftrightarrow |\mathrm{F}{=}2, m_F{=}0\rangle$ levels. The two photon transition is detuned from an intermediate state, $|5p_{3/2}\rangle$. The two driving lasers must have a frequency equivalent to the energy difference of the two $m_F{=}0$ ground state levels.

A microwave modulated laser system is used to drive the two photon transition. A 70mW VPSL0785-070X5A Circulaser diode from Blue Sky research is arranged in a Littrow configuration to produce a laser beam of 32mW at a frequency of ∼384175.5GHz. An Edmund Optics Holographic Grating (NT43-774) is used to establish feedback thus narrowing the laser linewidth to ≈1.5MHz. The laser diode and grating are separated by approximately 4.4cm to set the free spectral range (FSR) of the external feedback cavity to 3.4GHz. ($FSR = \frac{c}{2L} \approx 3.4GHz$) A picture of the laser cavity is shown in Figure 6.2. Establishing feedback in this manner ensures that the laser′s carrier frequency and the microwave modulation sidebands are simultaneously supported by the feedback cavity.

A Hewlett-Packard 8665B frequency generator and a set of Cougar (AC3579C) amplifiers are used to modulate the driving current of the laser diode. A steel washer is used to help impedance match the RF modulation to the diode laser. The washer suppresses the microwave modulation from transmitting back to the DC power supply. This in turn prevents the constant current DC power supply from stabilizing the RF modulation that we are trying to place on the diode laser. Modulating the laser injection current of a diode laser produces both AM and FM modulation of the optical field. However, the AM modulation is fairly small and can be neglected for the most part [Boyd et al., 1996]. For a sinusoidal modulation frequency of Ω the optical field can be modeled as

$$E(t) = E_0 e^{-i\omega_0 t - i\beta sin(\omega t)} \tag{6.1}$$

E_0 is the amplitude of the laser′s electric field, ω_0 is the laser carrier frequency, and β represents the amplitude of modulation being applied. This expression for the electric field can be expanded into a carrier wave and a series of sidebands [Boyd et al., 1996].

$$E(t) = E_0 J_0(\beta) e^{-i\omega_0 t} + E_0 \sum_{n=1}^{\infty} J_n(\beta)[e^{-i(\omega_0+n\omega)t} + (-1)^n e^{-i(\omega_0+n\omega)t}] \tag{6.2}$$

By applying a small frequency modulation, $\beta \ll 1$, we create two small sidebands around the laser′s carrier frequency. The relative intensities of the sidebands are approximately 10% of the carrier frequency. This light is fiber coupled to a single mode polarization maintaining fiber.

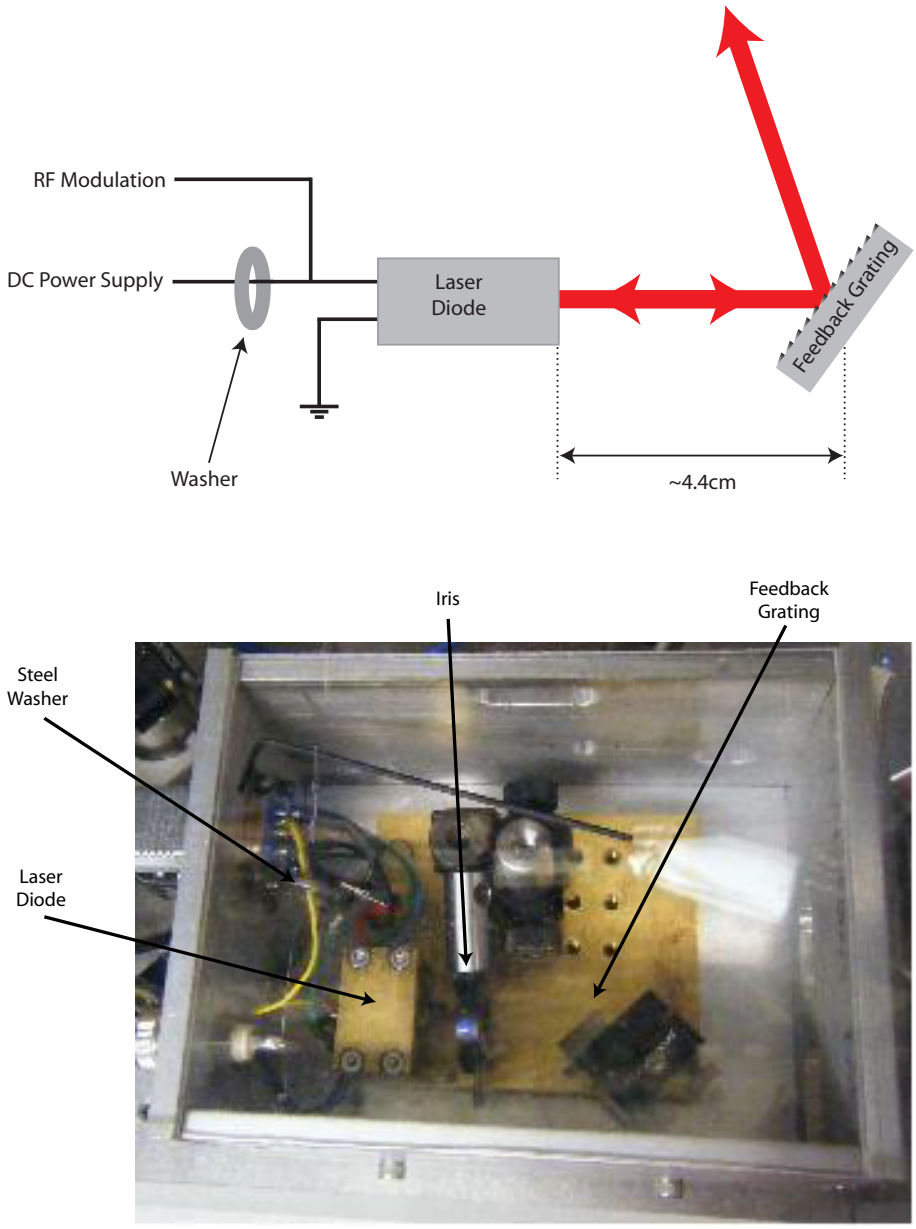

Figure 6.2 An illustration and a picture of the laser used to drive the ground state two photon transitions. The laser uses a Littrow cavity configuration. The feedback grating is separated from the diode by approximately 4.4cm. The washer is used to help couple the microwave modulation directly into the diode laser. The iris is used to facilitate the initial alignment of the laser's feedback cavity. The diode output is passed through an optical isolator and fiber coupled to a single mode polarization maintaining fiber.

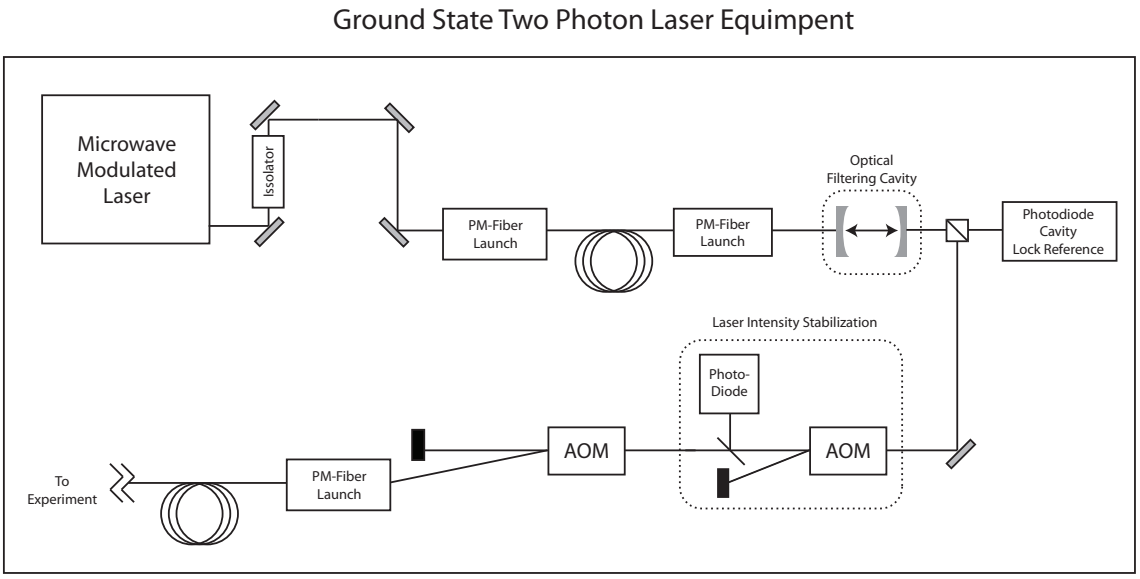

Figure 6.3 Optics to simultaneously establish a dichroic intensity stabilized laser beam. The separation of the non-confocal filtering cavity mirrors is approximately 2.2cm corresponding to a FSR of ≈6.8GHz. As the cavity length is scanned, via a ring piezo, the modulation sidebands simultaneously become resonant with the filtering cavity. The transmission signal of the sidebands provides a means of stabilizing the cavity length. The laser intensity is stabilized using an AOM based feedback loop.

The microwave modulated light is mode matched into a non-confocal optical filtering cavity. The Laseroptik cavity mirrors have radii of curvature of 500mm. One of the mirrors is mounted to a piezo electric element capable of scanning the cavity length. The FSR of this optical cavity is set to be twice the microwave modulation frequency, ≈6.8GHz. While scanning the length of the cavity the modulation sidebands are simultaneously resonant with the optical cavity. The cavity length is stabilized by referencing the optical transmission signal of the sidebands with a photodiode. A simple dither lock is used to dynamically stabilize the cavity′s length. The laser current is dithered at 42.2kHz to establish this lock. When the cavity length is stabilized to transmit the sideband frequencies, the carrier wave destructively interferes with itself, and is thus filtered from the laser beam. The finesse of the cavity is measured to be about 35. Under these conditions the output power of the laser beam is approximately 1.8mW.

The filtered laser beams are subsequently intensity stabilized using an AOM based feedback system. The +1st AOM beam order diverts a portion of the laser beam′s power into an optical beam dump (typically 10-20%). The 0th order laser beam passes through a pick-off, which is used to monitor the laser intensity. When the 0th order laser beam increases in intensity the feedback circuit will divert more power to the +1st order diffracted beam. The feedback system compensates for reductions in 0th order beam power by reducing the AOM′s diffraction efficiency. This diverts optical power from the beam dump back into the 0th order laser beam. The intensity noise is stabilized to less than 5% of the total optical power. The Raman laser traverses a second AOM before being fiber coupled to the atom addressing optics. This final AOM controls the timing and duration of the Raman laser pulses. The 10%-90% rise time of the final AOM is less than 40ns.

6.3 Rydberg State Two Photon Raman Laser System

This experiment utilizes two photon Raman transitions to drive atoms between the F= 2 hyperfine ground state and various Rydberg levels. Figure 6.4 outlines the atomic energy levels and the laser frequencies pertinent to these Rydberg transitions. The laser sources used to drive these transitions are frequency stabilized to a stable reference cavity. The 780nm source is directly locked to the cavity, while a 480nm laser beam is generated via second harmonic generation (SHG) of a stably locked 960nm diode. The pertinent details on establishing the laser locks can be found in [Johnson, 2008]. To establish resonance with the atoms the laser frequency of the 780nm laser diode is shifted by a double passed AOM. More thorough explanations on the laser frequency characterization and the hardware associated with controlling these lasers can be found in [Johnson, 2008]. The laser linewidths as deduced from Allan variance measurements are <500Hz, relative to a common reference cavity over timescales of 10μs [Urban et al., 2009]. These narrow frequency laser beams are fiber coupled to the atom addressing optics.

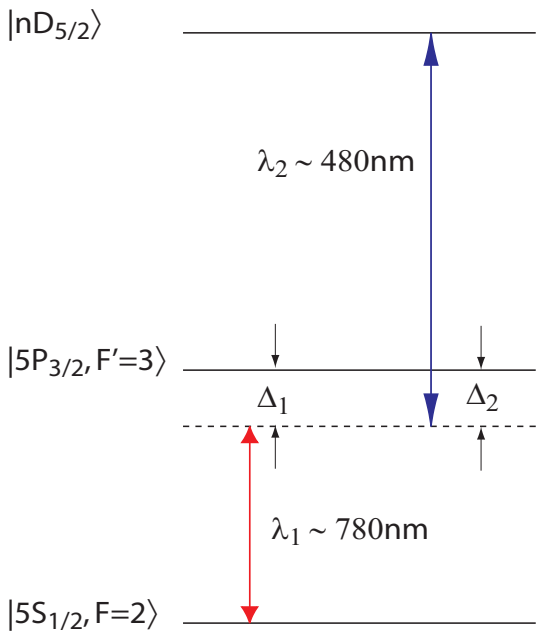

Figure 6.4 A general description of the two photon excitation of a ground state $|5s_{1/2}\rangle$ atom to a generic Rydberg level, $|n\ d_{5/2}\rangle$. The illustration demonstrates how independently, the excitation lasers are not resonant with an atomic transition. When both lasers are equally detuned from a common intermediate level and applied together, the laser fields drive the atom into a Rydberg state.

6.4 Addressing Single Qubits

The optical addressing systems are designed to generate tightly focused laser beams capable of manipulating the states of individual atoms. Individually addressing atoms separated by ∼10 microns is a particularly difficult task. In achieving this goal a variety of design constraints must be satisfied. The atoms must experience a uniform electric field for the duration of the excitation process to attain high fidelity state manipulations. Furthermore, the laser intensity delivered to an atom should be consistent for each excitation. Therefore, the laser beams must be larger than the atom distributions of the FORT potentials. However, the Gaussian beam waists used to excite the atoms cannot be too large; otherwise atoms adjacent to the targeted atom will undergo excitations as well. As previously discussed, atoms held within the FORT oscillate at the bottom of the optical trapping potential and

possess a spatial distribution modeled by Equations 4.7. As displayed in Figures 5.2 and 5.7, the atoms tend to be less confined in the axial dimension. Since the laser beams possess Gaussian spatial modes, it is necessary to address the atoms along the axial direction, thereby limiting the intensity variations observed by the atoms, as hown in Figure 6.5.

The laser beams used to implement the Rydberg transitions are given a counter propagating orientation in order to minimize Doppler broadening. To accommodate the beam orientations a dichroic beam splitter is used to combine the FORT and Rydberg 780nm laser beams. The polarization of the Rydberg 780nm laser beam and the ground state Raman laser beams often required different polarizations. The laser systems are given separate optical beam paths to allow for these different polarizations. This additional beam path for the ground state Raman laser is combined with the Rydberg 480nm laser beam. The Rydberg 780nm laser and the Raman laser beams are run through the same optical beam paths during experiments where they share the same polarizations. A simplified sketch of the optical layout is outlined in Figure 6.5.

6.4.1 Laser Beam Scanning

Generating stable laser beams with enough optical power to drive these optical transitions is a costly resource. To minimize these resources the laser beams are being multiplexed between the optical potentials. A variety of methods can be implemented to dynamically deflect the propagation of a laser beam. Several options include using optical elements mounted to piezoelectric translation stages, microelectromechanical systems (MEMS) [Knoernschild et al., 2008] and acousto-optic modulator (AOM) devices [Yavuz et al., 2006], [Kim et al., 2008].

While all of these systems possess the precision necessary to address single qubit sites, piezoelectric systems require millisecond or longer time scales to deflect a laser beam. While MEMS mirrors are capable of much faster switching speeds ($\sim 10\mu$s). Research is currently underway to develop and implement faster and more versatile MEMS devices into quantum

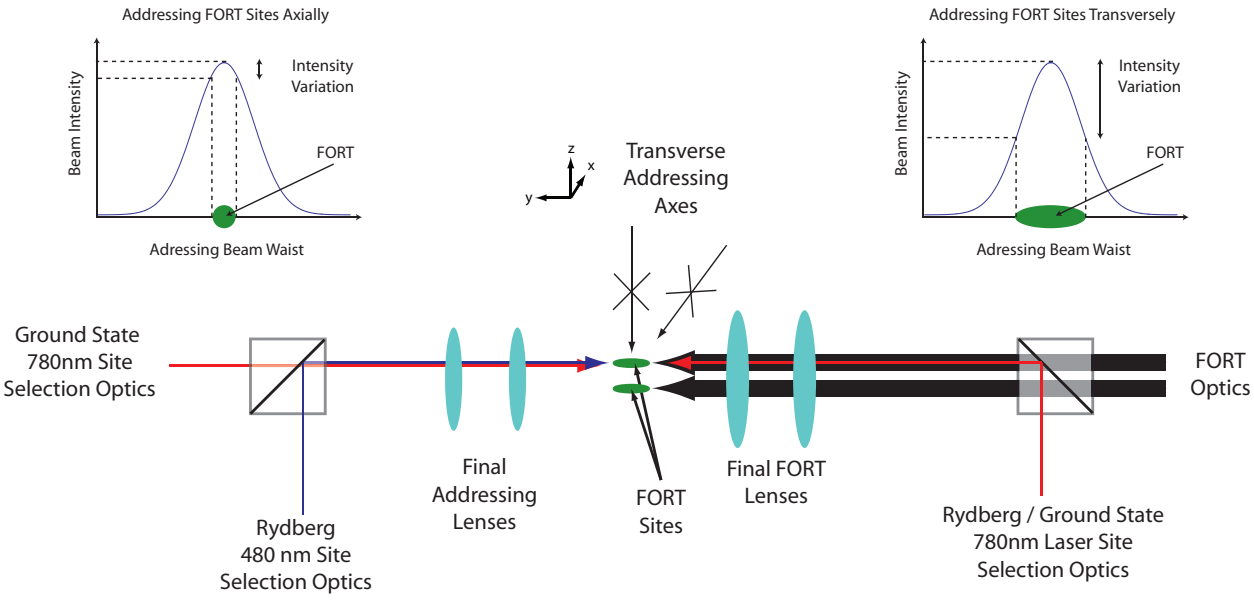

Figure 6.5 Illustration demonstrating the need to address the optical lattice sites axially with respect to the FORT laser beams. The inset plots illustrate the variation in laser beam intensity experienced by atoms restricted to a particular FORT spatial distribution. Addressing the FORT potential axially clearly incurs a smaller intensity distribution for a given beam size. The illustration also demonstrates how the various addressing beams are incorporated within the experiment.

computing systems [Knoernschild et al., 2008], [Kim et al., 2007]. Since the laser beams performing our qubit operations are being multiplexed, the gate time of our quantum computer is limited by the time required to switch the laser beam between sites. Additionally, this addressing scheme uses two very different wavelengths of light to perform logic operations. These design constraints can both be accommodated with the use of AOM devices.

AOM components operate over a wide variety of wavelengths and allow for fast electronic control of the intensity and position of laser beams. This is accomplished by launching an acoustic wave into an optical medium thus generating a refractive index wave that behaves like a sinusoidal grating. The grating will diffract the laser beam traversing the acoustic wave. The rapid rise time (T_{rise}) of an AOM is limited by the speed of the acoustic wave,

$V_{acoustic}$, propagating across the optical beam [Neo].

$$T_{rise} = \frac{2w_{(1/e)}}{1.5V_{acoustic}}$$

The rise time of an AOM device also depends upon the 1/e-waist, $w_{1/e}$, of the laser beam being diffracted. The acoustic velocity of TeO_2 is Va = 4.26x10^3 m/s. [Neo]. The 10%-90% switching times of the laser beams are outlined in Table 6.1.

Table 6.1 Site-site switching times of the AOM controlled optical addressing systems.

Laser Beam Path	Wavelength (nm)	Rise/Fall Time (ns)
Rydberg Blue Laser	∼480.5	150
Rydberg Red Laser	∼780.24	150
Raman Lasers	∼780.35	150

The Bragg diffraction angle of an AOM device is proportional to the wavelength of light and the acoustic frequency, while it is inversely proportional to the velocity of the sound waves [Yariv and Yeh, 1984].

$$\theta \propto \frac{\lambda \nu_{acoustic}}{V_{acoustic}}$$

In diffracting the laser beam the acoustic wave also imparts a frequency shift upon the light. This shift is equal to the diffraction order times the acoustic frequency being applied to the AOM device.

This dependence of the diffraction angle upon the wavelength of light has important consequences upon how the laser beams must be deflected. We require this system to be capable of deflecting all of the beams in unison and illuminating the targeted optical potentials with similarly sized Gaussian beams. Since the laser beams are being used to drive two photon transitions, careful consideration is required to ensure that the laser beam frequencies are still resonant with the atomic transition after being frequency shifted by the AOMs.

In order to maintain the two photon resonance condition for transitions to the Rydberg states, the 480nm and 780nm laser beam paths are designed to use opposite diffraction orders. The AOMs used for the laser beams are constructed to operate using the same modulation frequency. Using opposing diffraction beam orders ensures that as the lasers are spatially translated their net frequency shift is zero. This enables the two photon Rydberg transitions to remain resonant while spatially scanning. This design concept is illustrated in Figure 6.6.

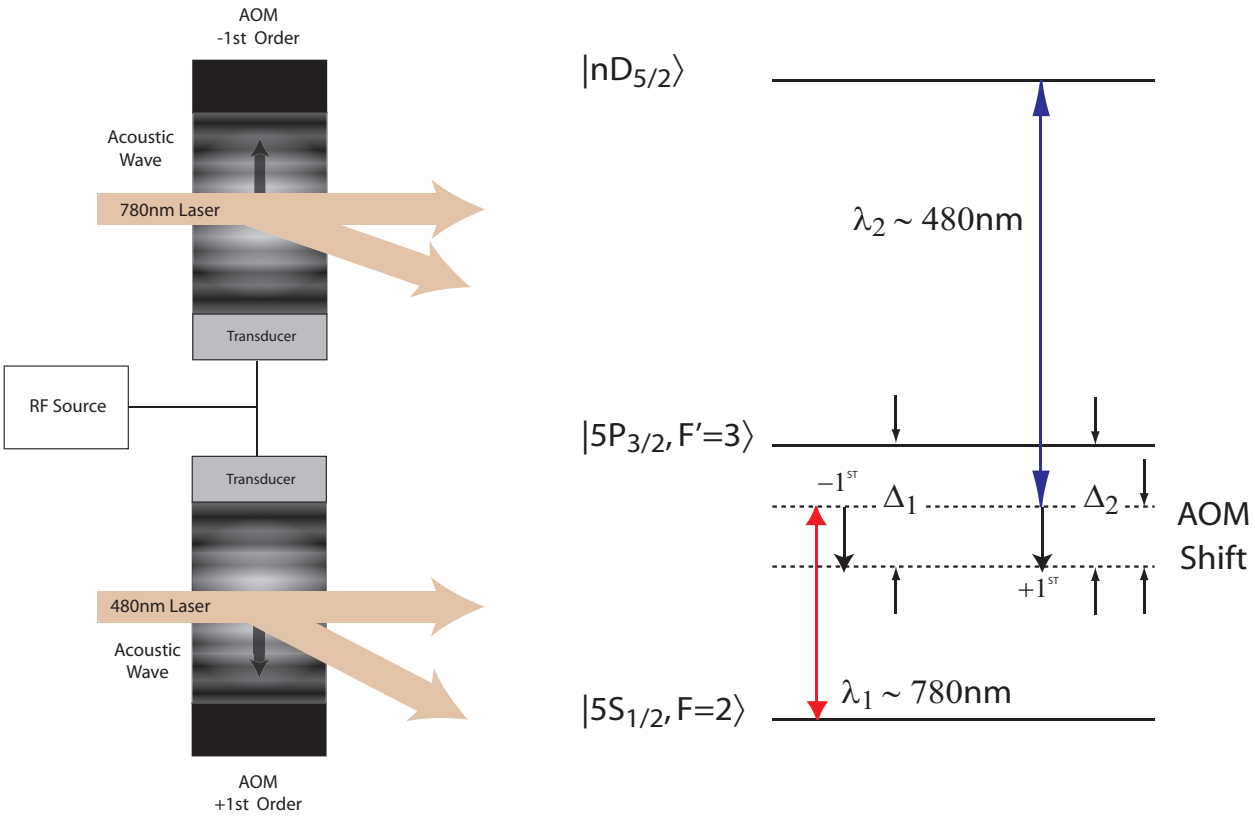

Figure 6.6 Figure illustrating how the AOM frequency shifts can be implemented such that the two photon transition remains resonant with the Rydberg transition. Transducers are shown referencing the same RF source. Note that the orientation of the transducers and TeO_2 crystals are inverted thus spatially shifting the beams in the same direction.

6.4.2 Optical Elements

Beam expanders and relay optics are used to simultaneously convert the angular beam deflections, generated by the AOMs, into linear translations. These optical elements are simultaneously used to resize all of the laser beams′ waists to be approximately 10um in size. These beam waists are found to be sufficiently small for individual qubit addressability, but still large enough to ensure that atoms localized to the spatial distribution of the trap will not experience drastically different laser beam intensities. Figure 6.7 illustrates a generic beam path, demonstrating how the optical assemblies are designed to simultaneously resize the lasers and convert the angular deflections of the AOMs into a linear translation at the trapping sites. Figures 6.8 and 6.10 give a more complete outline of the optics used in the beam addressing assemblies.

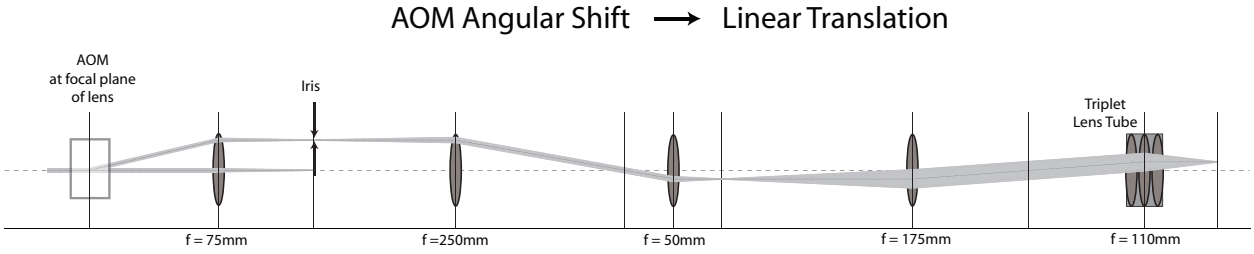

Figure 6.7 Illustration of how the angular deflection of the AOM is converted into a linear translation. The vertical lines indicate focal planes between the lenses (Figure not to scale). Increasing the angular deflection results in a larger linear translation at the final focal plane. The iris serves as a beam dump for the 0th order beam. Note that the final beam waist is being simultaneously demagnified. The focal lengths shown correspond to the 780nm laser beam path which is counter propagating to the FORT.

In both addressing systems the AOMs are placed at focal planes of the lenses, thus converting the angular beam deflections into linear translations. Table 6.4.2 provides a list of the most recent beam waist measurements and translational response to changes in the AOM RF frequency. These beam parameters are measured using a calibrated imaging system (see Appendix E). A description of how the system is aligned can be found in Appendix C.

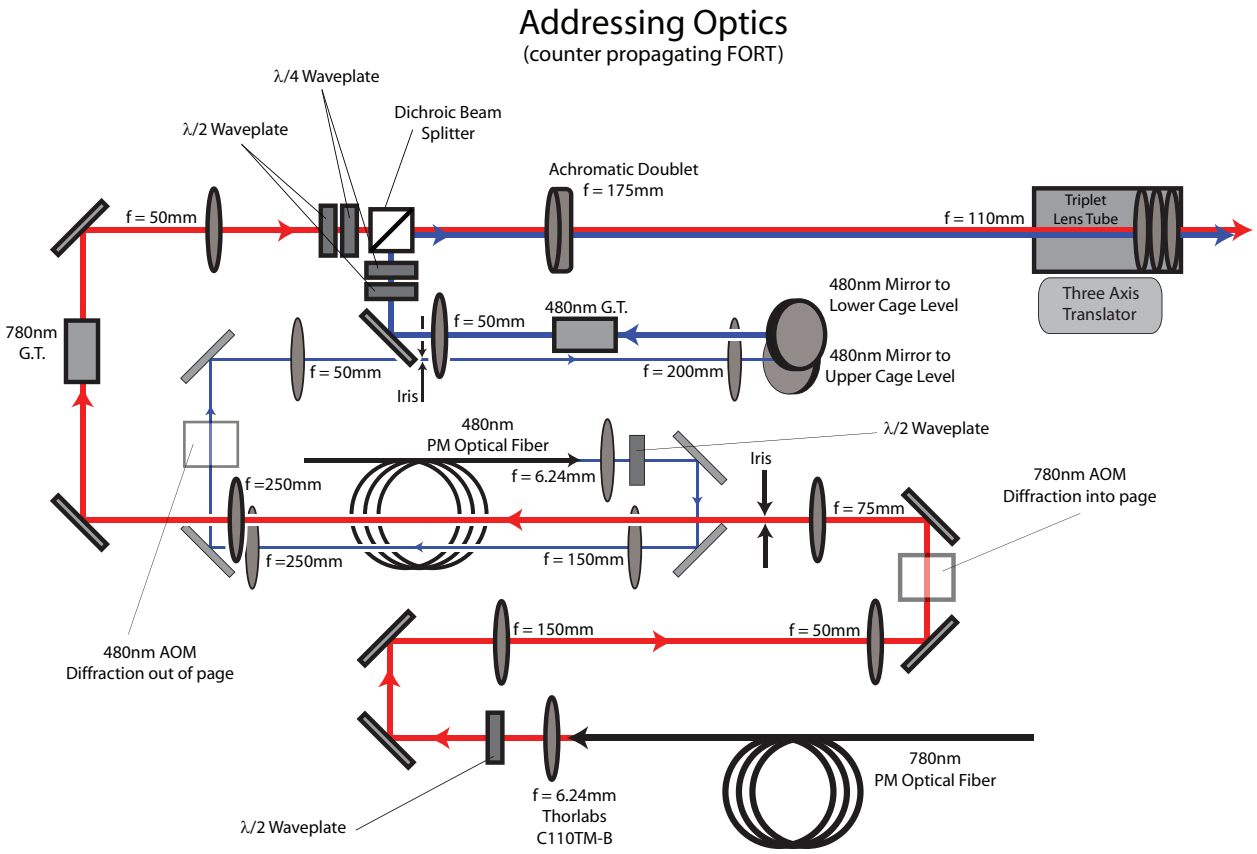

Figure 6.8 Addressing laser optics used to shape and combine the 480nm and 780nm lasers. The resulting beam path is counter propagating to the FORT laser. With exclusion of the final two lenses, the separation between lenses is approximately equal to the sum of the two adjacent focal lengths. The high speed photodiodes (TTI) and pick-offs used to monitor the laser beam timings are omitted for clarity. The system utilizes a Thorlabs cage system. To conserve space the beam paths are layered. The 175mm focal length lens is an achromatic doublet.

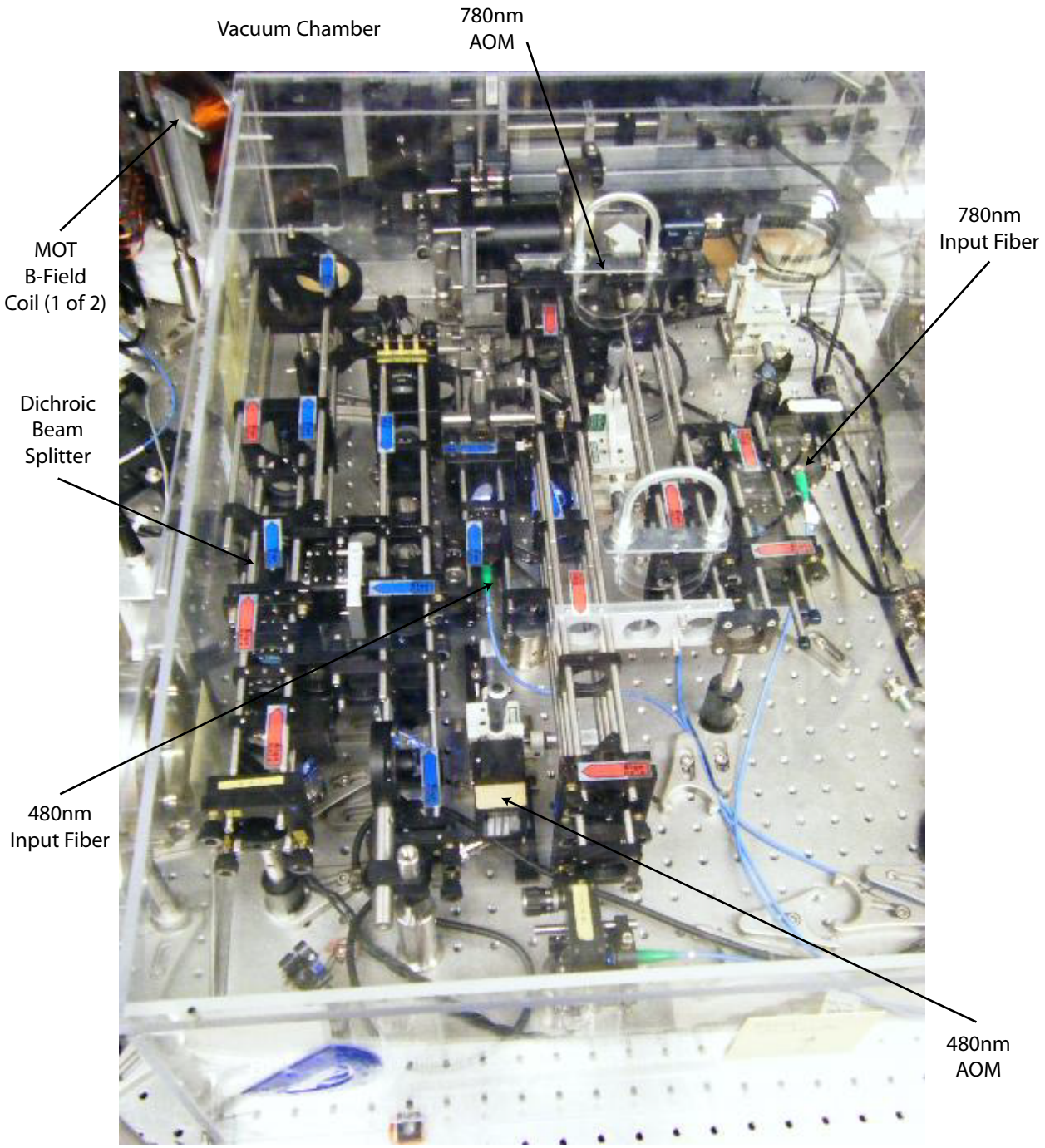

Figure 6.9 Picture of the addressing laser optics used to shape and combine the 480nm and 780nm lasers.

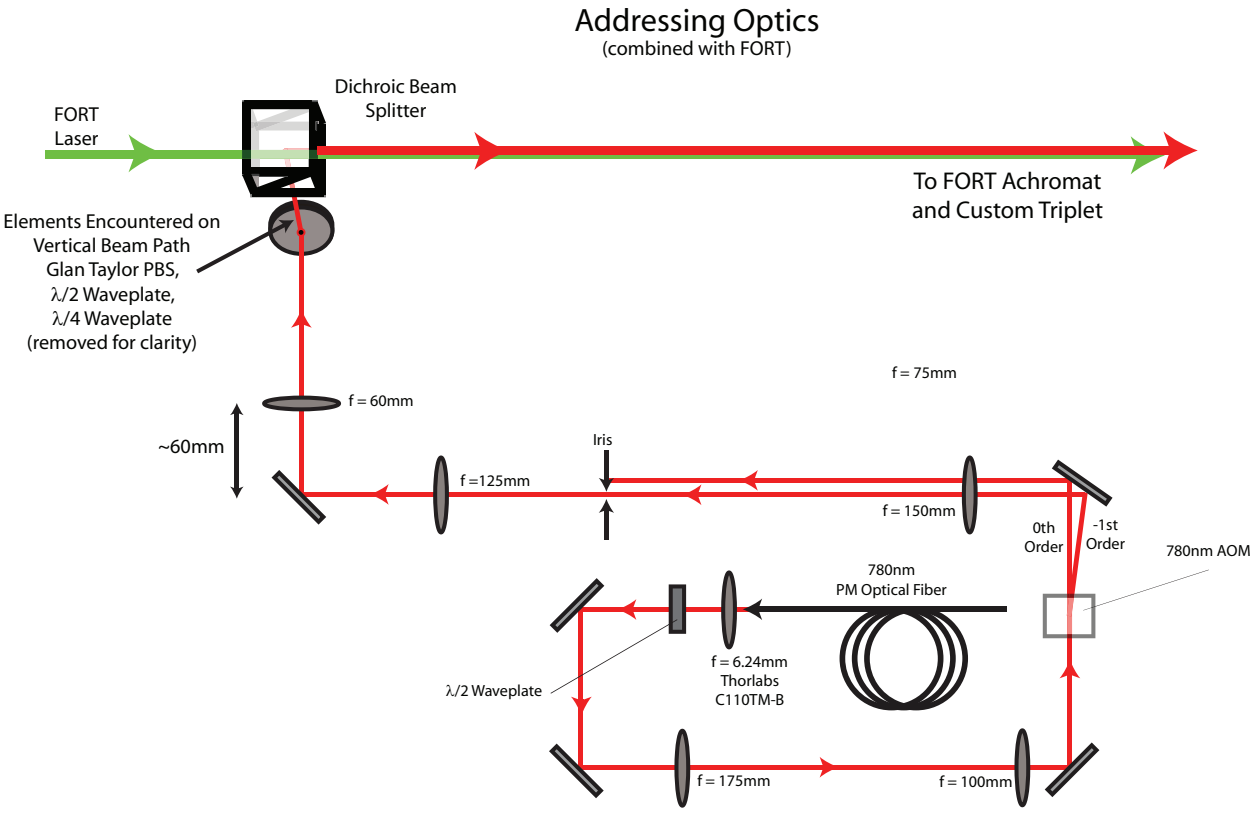

Figure 6.10 Optics used to shape and combine the 780nm laser with the FORT laser. The final FORT lenses have been omitted from the figure. Further details on the FORT optics can be found in Section 4.4. The separation between lenses is approximately equal to the sum of the two adjacent focal lengths. The high speed photodiodes (TTI) and pick-offs used to monitor the laser beam timings are omitted for clarity. To conserve space the beam paths are layered.

Table 6.2 Addressing Laser Beam Parameters

$1/e^2$ Laser Beam Waists	Horizontal w_x (μm)	Vertical w_y (μm)
480nm Laser Beam	9.1	10.5
780nm (FORT-side) Laser Beam	7.0	11.9
780nm (480nm-side) Laser Beam	6.8	12.9
AOM Translation	(μm/MHz)	
480nm Laser Beam	1.52	
780nm (FORT-side) Laser Beam	1.82	
780nm (480nm-side) Laser Beam	1.57	
Optical Transmission After Dichroic B.S. to Atoms	(%)	
480nm Laser Beam	87%	
780nm (FORT-side) Laser Beam	98%	
780nm (480nm-side) Laser Beam	97%	

Chapter 7

Interactions Between Atoms and Light

Two-photon transitions are utilized to perform both single-qubit as well as qubit entangling operations. Though more complicated than single photon interactions, utilization of these processes can give rise to a universal set of logic gates. The two-photon transitions used in these experiments rely upon a three level atomic structure in which the driving fields are detuned from an intermediate level. The subsequent sections of this chapter review models of how atoms can be driven between ground and Rydberg states, Section 7.1, and the mechanics behind atoms being driven between two ground states, Section 7.2. Several important consequences of utilizing three level systems are examined.

7.1 Two Photon Raman Transitions in a Three Level Ladder System

As mentioned in Section 6.3, our ground state atoms are excited into Rydberg states via two-photon excitations. The lasers used to drive these transitions are detuned from the intermediate $5P_{3/2}$ state. Understanding the dynamics of how atoms make these transitions is critical to the development of our quantum logic gates. The derivation presented here closely follows [Johnson, 2008].

This derivation of a three level atomic system being driven by two photon Raman transitions utilizes a semiclassical formalism. The effects of spontaneous emission are not included in this analysis. Though simple, this model is useful in explaining the coherent population transfer between atomic states, the consequences of laser detunings, and the origins of light

shifts within the system. This derivation assumes the ground state, $|g\rangle$, and excited state, $|r\rangle$, are respectively the lowest and highest energy levels of the system. The atomic energy levels are depicted in Figure 7.1.

This derivation presumes that the electric fields, E_1 and E_2, used to drive the transition are not resonant with the intermediate level $|p\rangle$. The monochromatic laser frequency ω_1 is detuned by Δ_1 from the $|g\rangle \rightarrow |p\rangle$ transition. Likewise, the driving field E_2 oscillates with a frequency of ω_2 and is detuned from the $|p\rangle \rightarrow |r\rangle$ transition by Δ_2. The driving fields and detunings are depicted in Figure 7.1. The single photon Rabi frequencies generated by the fields E_1 and E_2 are defined as Ω_1 and Ω_2.

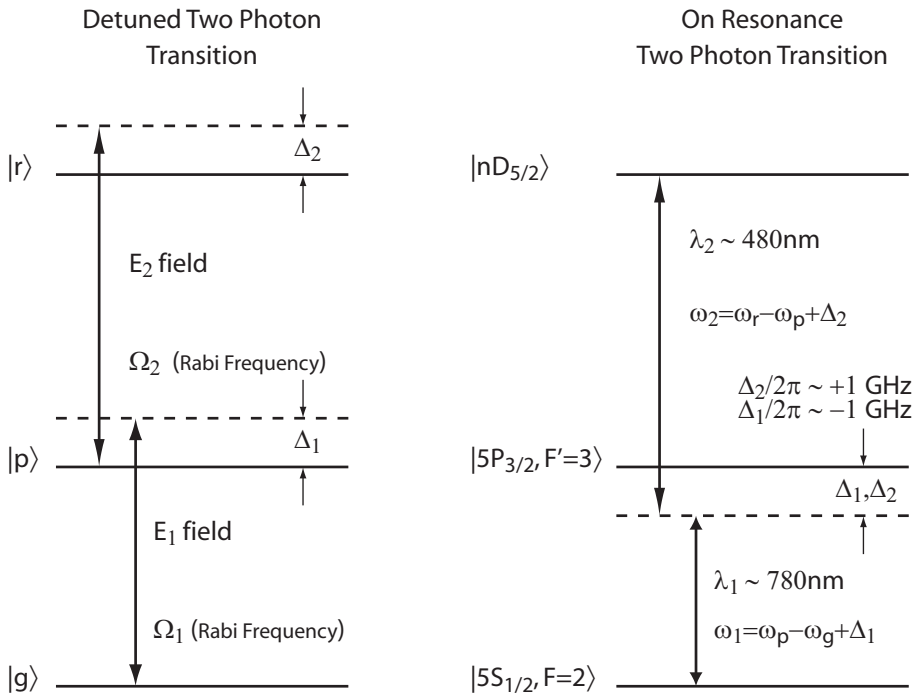

Figure 7.1 Diagram showing relevant energy levels for the three level Rydberg atom model. The two photon resonance condition requires that $\Delta = \Delta_1 + \Delta_2 = 0$.

This semiclassical model begins with the time dependent Schrödinger equation

$$i\hbar\frac{\partial}{\partial t}|\Psi(t)\rangle = \hat{H}(t)|\Psi(t)\rangle$$

The Hamiltonian $\hat{H}(t)$ can be written as the sum of an unperturbed Hamiltonian and an oscillating electric dipole perturbation. The unperturbed Hamiltonian is given by

$$\hat{H}_0 = \hbar\omega_g|g\rangle\langle g| + \hbar\omega_p|p\rangle\langle p| + \hbar\omega_r|r\rangle\langle r| \tag{7.1}$$

The perturbing electric field is merely the sum of the two driving laser fields. This field is given as

$$\vec{E}(t) = \vec{E}_1(t) + \vec{E}_2(t) = \frac{\vec{\mathcal{E}}_1}{2}e^{-i\omega_1 t} + \frac{\vec{\mathcal{E}}_1^*}{2}e^{i\omega_1 t} + \frac{\vec{\mathcal{E}}_2}{2}e^{-i\omega_2 t} + \frac{\vec{\mathcal{E}}_2^*}{2}e^{i\omega_2 t}$$

We assume that the $|g\rangle \leftrightarrow |p\rangle$ transition is primarily driven by the $\vec{E}_1(t)$ driving field. Field $\vec{E}_2(t)$ will have a large detuning from this transition and, therefore, will generate a negligible perturbation. The same logic is used to describe why the $|p\rangle \leftrightarrow |r\rangle$ transition is primarily driven by the $\vec{E}_2(t)$ field. Therefore, the perturbing dipole interaction $\hat{V}_d(t) = -\hat{d}\cdot\vec{E}(t)$ is given by

$$\hat{V}_d(t) = -E_1(t)d_{pg}|p\rangle\langle g| - E_1(t)d_{gp}|g\rangle\langle p| - E_2(t)d_{rp}|r\rangle\langle p| - E_2(t)d_{pr}|p\rangle\langle r| \tag{7.2}$$

The term d_{pg}, etc., indicates integration of the dipole operator $\hat{d}$ over the stationary wave-functions, $d_{pg} = \langle p|\hat{d}|g\rangle$, and depends upon the polarization of $\vec{E}(t)$ [Johnson, 2008]. The single atom wave function can be written as

$$|\Psi(t)\rangle = c_g(t)e^{-i\omega_g t}|g\rangle + c_p(t)e^{-i\omega_p t}|p\rangle + c_r(t)e^{-i\omega_r t}|r\rangle \tag{7.3}$$

By substituting Equations 7.3 and 7.2 into the Shrödinger equation one can arrive at a set of coupled differential equations. The rotating wave approximation is applied to simplify these equations. Furthermore, we also make use of the following substitutions for the laser detunings; $\Delta_1 = \omega_1 - (\omega_{pg})$, $\Delta_2 = \omega_2 - (\omega_{rp})$, $\omega_{pg} = \omega_p - \omega_g$, and $\omega_{pg} = \omega_p - \omega_g$. The Rabi frequencies Ω_1 and Ω_2 are given by: $\Omega_1 = \mathcal{E}_1 d_{gp}/\hbar$ and $\Omega_2 = \mathcal{E}_2 d_{pr}/\hbar$. These equations are written in matrix form below.

$$\begin{pmatrix} \dot{\tilde{c}}_g(t) \\ \dot{\tilde{c}}_p(t) \\ \dot{\tilde{c}}_r(t) \end{pmatrix} = \begin{pmatrix} 0 & i\frac{\Omega_1^*}{2}e^{i\Delta_1 t} & 0 \\ i\frac{\Omega_1}{2}e^{-i\Delta_1 t} & 0 & i\frac{\Omega_2^*}{2}e^{i\Delta_2 t} \\ 0 & i\frac{\Omega_2}{2}e^{-i\Delta_2 t} & 0 \end{pmatrix} \begin{pmatrix} \tilde{c}_g(t) \\ \tilde{c}_p(t) \\ \tilde{c}_r(t) \end{pmatrix} \tag{7.4}$$

At this point we will apply the adiabatic elimination of the intermediate state $|p\rangle$ [Brion et al., 2007], [Pedersen, 2006]. This approximation requires that the term $\widetilde{c_p}$ varies rapidly compared to the other coefficients. Specifically we require $|\Delta_1|$,$|\Delta_2| \gg |\Omega_1|$,$|\Omega_2|$. Further details on the substitutions utilized to make this transformation can be found in [Johnson, 2008]. The two photon Rabi frequency is defined as $\Omega_R = \Omega_1\Omega_2/\delta$, where $\delta = \Delta_1 - \Delta_2$. We also define $\Delta_1' = \Delta + |\Omega_1|^2/\delta$ and $\Delta_2' = \Delta - |\Omega_2|^2/\delta$, where $\Delta = \Delta_1 + \Delta_2$. Having eliminated the $\widetilde{c_p}$ terms, the resulting 2 x 2 matrix is

$$\begin{pmatrix} \dot{\widetilde{c}}_g(t) \\ \dot{\widetilde{c}}_r(t) \end{pmatrix} = \begin{pmatrix} -i\frac{\Delta_1'}{2} & -i\frac{\Omega_R^*}{2} \\ -i\frac{\Omega_R}{2} & i\frac{\Delta_2'}{2} \end{pmatrix} \begin{pmatrix} \widetilde{c}_g(t) \\ \widetilde{c}_r(t) \end{pmatrix} \tag{7.5}$$

The solution to this equation has a functional form of $\tilde{\mathbf{c}}(t) = \widetilde{\mathbf{U}}(t, t_0)\tilde{\mathbf{c}}(t_0)$, where the starting conditions of the system are defined by $\tilde{\mathbf{c}}(t_0)$. In arriving at this evolution matrix, $\widetilde{\mathbf{U}}(t, t_0)$, further substitutions are made. Specifically, $\Delta_\pm = (\Delta_1' \pm \Delta_2')/2$ and $\Omega' = \sqrt{|\Omega_R|^2 + \Delta_+^2}$. Ω' is the efective two photon Rabi frequency. A rotation matrix is applied to arrive at the final evolution matrix of the system. The 2x2 matrix $\mathbf{U}(t, t_0 = 0)$ describing the evolution of the vector $\mathbf{c}(t) = (c_g(t), c_r(t))^{\mathrm{T}}$ in time is now written as [Johnson, 2008]:

$$\mathbf{U}(t,0) = \begin{pmatrix} e^{i\frac{\Delta-\Delta_-}{2}t}\left(\cos\left(\frac{\Omega' t}{2}\right) - i\frac{\Delta_+}{\Omega'}\sin\left(\frac{\Omega' t}{2}\right)\right) & e^{i\frac{\Delta}{2}t}e^{-i\frac{\Delta_-}{2}t}\left(-i\frac{\Omega_R^*}{\Omega'}\sin\left(\frac{\Omega' t}{2}\right)\right) \\ e^{-i\frac{\Delta}{2}t}e^{-i\frac{\Delta_-}{2}t}\left(-i\frac{\Omega_R}{\Omega'}\sin\left(\frac{\Omega' t}{2}\right)\right) & e^{-i\frac{\Delta+\Delta_-}{2}t}\left(\cos\left(\frac{\Omega' t}{2}\right) + i\frac{\Delta_+}{\Omega'}\sin\left(\frac{\Omega' t}{2}\right)\right) \end{pmatrix} \tag{7.6}$$

As an initial consistency check we can examine the case where the magnitudes of the individual Rabi frequencies, $|\Omega_1|$ and $|\Omega_2|$, approach zero. In this regime $\Omega_R \to 0$, $\Omega' \to \Delta_+$, $\Delta_+ \to \Delta$, and $\Delta_- \to 0$. Therefore, removing the driving fields, or allowing the Rabi frequencies to go to zero, reduce the evolution matrix to the identity matrix regardless of how far the lasers are detuned from the atomic transitions. This mathematical interpretation agrees with what one would expect to see if the driving laser fields are extinguished.

7.2 Two Photon Raman Transitions in a Three Level Λ System

Since the hyperfine ground sates of the atoms are being designated as our logical qubit states $|0\rangle$ and $|1\rangle$ we require the ability to drive the atoms between these particular states.

While the simplicity, elegance, and reliability of merely using an on resonance microwave field to drive these transitions is alluring [Rakreungdet et al., 2008], this technique is impractical for our system′s architecture. Since the hyperfine energy levels are separated by roughly 6.8GHz, the transition would need to be driven by photons with wavelengths of approximately 4.4cm. The diffraction limited beam waists of the microwaves would prohibit qubits separated by $10\mu m$ from being individually addressed. In our quantum computing scheme it is necessary to utilize optical fields that can generate diffraction limited beam waists smaller than the inter-qubit separations.

Therefore, in order to access the qubits separately we utilize a two photon process to drive the atoms between hyperfine energy levels. The lasers used to drive these transitions will once again be detuned from an intermediate state. However, the energy level scheme considered is now a Λ-type system. The energy levels of interest are outlined in Figure 7.2. Understanding the dynamics of how atoms undergo these transitions is once again critical to the development of our quantum logic gates.

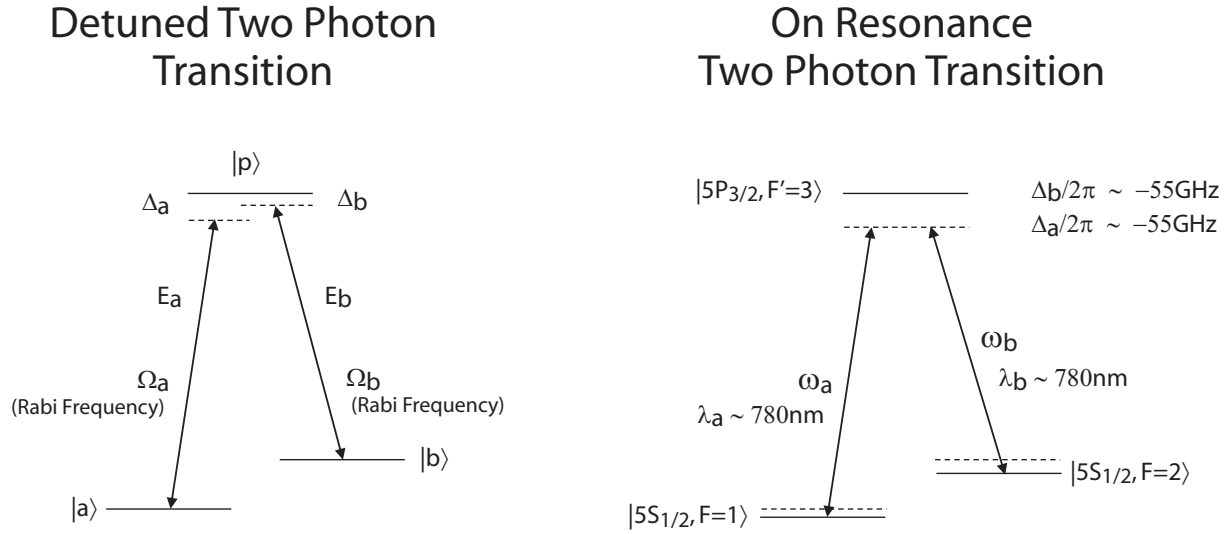

Figure 7.2 Atomic energy level diagram illustrating the three level Λ-system to be considered while driving the atom between ground state energy levels.

Reducing the three level Λ-system driven by a two photon process is very similar to the steps outlined in Section 7.1 and in [Johnson, 2008]. This reduction of a Λ-type system to an

equivalent two level atomic structure is demonstrated in [Brion et al., 2007] and [Pedersen, 2006]. This section merely outlines important conditions and substitutions utilized to arrive at a final evolution matrix that can be used to describe the excitation mechanism. A full description of the reduction can be found in [Brion et al., 2007] and [Pedersen, 2006], and closely mimic the steps outlined in Section 7.1.

The Lambda system is being driven by two laser fields, both of which are far detuned from the hyperfine to intermediate level transitions. The atomic energy levels are depicted in Figure 7.1. This derivation assumes the intermediate state, $|p\rangle$, is higher in energy than the two ground states which will be labeled $|a\rangle$ and $|b\rangle$. State $|a\rangle$ is lower in energy than state $|b\rangle$. The wave function of the system is given by:

$$|\Psi_\Lambda(t)\rangle = c_a(t)e^{-i\omega_a t}|a\rangle + c_p(t)e^{-i\omega_p t}|p\rangle + c_b(t)e^{-i\omega_b t}|b\rangle \tag{7.7}$$

The driving fields E_a and E_b oscillate at frequencies ω_a and ω_b, and are detuned from the intermediate transition by Δ_a and Δ_b. The single photon Rabi frequencies for the $|a\rangle \leftrightarrow |p\rangle$ and $|b\rangle \leftrightarrow |p\rangle$ transitions are Ω_a and Ω_b respectively. The two photon detuning of the Λ system is defined as Δ_{ab}. Unlike the ladder system the individual detunings of a Λ system cancel thus defining Δ_{ab} as $\Delta_{ab} = \Delta_a - \Delta_b$. The adiabatic elimination of the intermediate state is still performed in a rotating reference frame, and is permissible due to the fact that the intermediate state′s coefficient oscillates rapidly. This is true while $|\Delta_a + \Delta_b| \gg |\Omega_a|, |\Omega_b|, |\Delta_{ab}|$. For convenience multiple substitutions are made in the proof by [Pedersen, 2006]. Specifically, $\Delta' = \Delta_{ab} + \frac{|\Omega_a|^2 - |\Omega_b|^2}{2(\Delta_a+\Delta_b)}$, $\Omega_{ab} = \frac{\Omega_a \Omega_b^*}{\Delta_a+\Delta_b}$, $\Omega'_{ab} = \sqrt{|\Omega_{ab}|^2 + \Delta'^2}$. The resulting evolution matrix developed is:

$$\mathbf{U_r}(t) = e^{-i\frac{|\Omega_a|^2+|\Omega_b|^2}{4(\Delta_a+\Delta_b)}t} \times$$
$$\begin{pmatrix} e^{i\frac{\Delta_{ab}t}{2}}\left(\cos\left(\frac{|\Omega'_{ab}|t}{2}\right) - i\frac{\Delta'}{|\Omega'_{ab}|}\sin\left(\frac{|\Omega'_{ab}|t}{2}\right)\right) & -ie^{i\frac{\Delta_{ab}t}{2}}\frac{\Omega^*_{ab}}{|\Omega'_{ab}|}\sin\left(\frac{|\Omega'_{ab}|t}{2}\right) \\ -ie^{-i\frac{\Delta_{ab}t}{2}}\frac{\Omega_{ab}}{|\Omega'_{ab}|}\sin\left(\frac{|\Omega'_{ab}|t}{2}\right) & e^{-i\frac{\Delta_{ab}t}{2}}\left(\cos\left(\frac{|\Omega'_{ab}|t}{2}\right) + i\frac{\Delta'}{|\Omega'_{ab}|}\sin\left(\frac{|\Omega'_{ab}|t}{2}\right)\right) \end{pmatrix} \tag{7.8}$$

We can perform a consistency check again by allowing the individual Rabi frequencies, Ω_a and Ω_b, of the Λ system to approach zero. Consequently, $\Omega_{ab} \to 0$, $\Omega'_{ab} \to \Delta'$, and Δ'

$\rightarrow \Delta_{ab}$. By removing the driving fields, or allowing Ω_a, $\Omega_b \rightarrow 0$, the evolution matrix once again reduces to the identity matrix regardless of the individual lasers are detunings.

7.3 Important Features of Three Level Systems, Single Qubit Operations

The derived evolution matrices give insight into a variety of properties of the two photon transitions. The behavior of these two photon transitions mimics that of Rabi flopping driven by a single electric field. For either system, if we assume that an atom is initiated in the ground state then we can calculate the probability of finding the atom in the excited state after applying an excitation pulse. The probability is calculated as a function of the laser intensity, the two photon detuning, and the pulse duration. From the model of the ladder-type atomic structure we can expect the probability of finding an atom in the Rydberg level, P_{Ryd}(t), after a laser pulse of length t to be given by:

$$P_{Ryd}(t) = \frac{\Omega_R^2}{\Omega'^2}\ \sin^2\left(\frac{\Omega' t}{2}\right) \ = \ \frac{\Omega_R^2}{|\Omega_R|^2 + (\Delta_+)^2}\ \sin^2\left(\frac{t\sqrt{|\Omega_R|^2 + (\Delta_+)^2}}{2}\right)$$

From the Λ type model we see that the probability of observing an atom in the F=2 ground state after driving the system with an excitation pulse of length t is given by:

$$P_{(F=2)}(t) = \frac{\Omega_{ab}^2}{\Omega_{ab}'^2}\ \sin^2\left(\frac{\Omega'_{ab} t}{2}\right) \ = \ \frac{\Omega_{ab}^2}{|\Omega_{ab}|^2 + (\Delta')^2}\ \sin^2\left(\frac{t\sqrt{|\Omega_{ab}|^2 + (\Delta')^2}}{2}\right)$$

In both systems the maximum probability of finding the atom in the excited state is limited by the coefficient of a sinusoidally varying function. Making several substitutions we realize that these amplitudes are related to the two-photon detuning, Δ' and Δ_+, of the Λ-type and ladder-type systems. These detunings also dictate the rate at which the excited state probabilities oscillate. The greater the two-photon detuning the faster the system will oscillate. Figure 7.3 illustrates this point.

The two photon detuning depends upon the single photon Rabi rates being used to drive the Raman Rabi flopping. In the case of the ladder type system, this detuning, Δ_+, is given by $\Delta_+ = (\Delta_1' + \Delta_2')/2$, where $\Delta_1' = \Delta + |\Omega_1|^2/\delta$ and $\Delta_2' = \Delta - |\Omega_2|^2/\delta$. As the individual Rabi

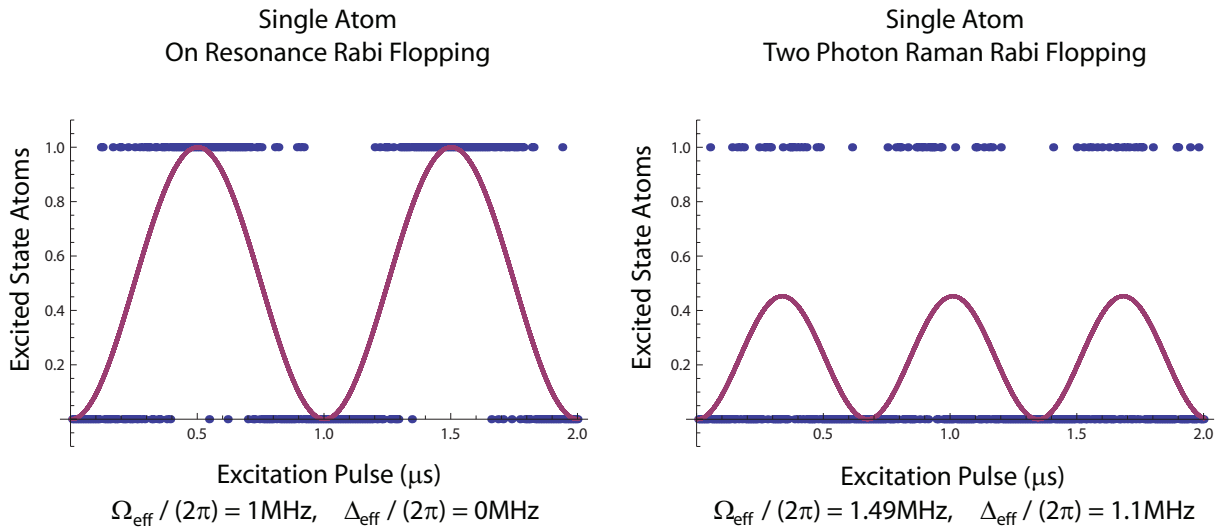

Figure 7.3 Hypothetical two photon Rabi flopping curves performed on single atom samples. Left plot depicts effect of an on resonance driving field. Right plot illustrates Raman, or detuned, Rabi flopping. Theoretical effective Rabi rates and detunings are reported below each graph. The solid lines indicate the excited state probability as a function of pulse duration for the given Rabi rates and detunings. The individual points represent what one would record if plotting multiple excited state measurements as a function of pulse duration. Individual measurements of atomic states are quantized as 0 or 1. The density of excited state observations is considerably smaller for the detuned Rabi flopping scenario.

rates of the system are increased, the overall two photon detuning will change. In order to drive the two photon transitions resonantly, Δ_+ must be equal to zero. A similar dependence exists for the Λ type atomic structure. The two-photon detuning, Δ', has a dependence upon the individual Rabi rates, Ω_a and Ω_b. These observations are useful in determining the necessary resonance conditions of each system. By performing two-photon spectroscopy experiments, Section 8.2, we observe maximum population transfers to the excited states when the conditions of the driving fields are set with the appropriate resonance conditions.

Since the Rydberg (ladder-type) transitions are being used to implement a quantum computer, we are primarily concerned with resonantly driven transitions. Though interesting, we do not require the ability to create superposition states of ground-Rydberg atoms. To

achieve unit probability of creating a Rydberg atom it is necessary to drive the two-photon Rydberg transition resonantly.

We also choose to operate resonantly while initiating single qubit operations via the Λ type transitions. Operating in an on-resonance regime provides us with the ability to create all possible superposition states of the atomic qubits. Driving this transition on resonance requires $\Delta' = 0$. By applying this condition to Equation 7.8 and removing a global phase factor the evolution operator of the Λ system becomes:

$$\mathbf{U_r}(t) = \begin{pmatrix} e^{i\frac{\Delta_{ab}t}{2}} \cos\left(\frac{|\Omega_{ab}|t}{2}\right) & -ie^{i\frac{\Delta_{ab}t}{2}} e^{-i\phi} \sin\left(\frac{|\Omega_{ab}|t}{2}\right) \\ -ie^{-i\frac{\Delta_{ab}t}{2}} e^{i\phi} \sin\left(\frac{|\Omega_{ab}|t}{2}\right) & e^{-i\frac{\Delta_{ab}t}{2}} \cos\left(\frac{|\Omega_{ab}|t}{2}\right) \end{pmatrix} \tag{7.9}$$

The phase factor, $e^{i\phi}$, is used to replace $\Omega_{ab}/|\Omega_{ab}|$. If we assume that the qubit states are initialized to a pure logic state prior to enacting this evolution matrix, this phase angle, ϕ, can arbitrarily be set equal to 0 without loss of generality.

In order to perform arbitrary single qubit manipulations we require the ability to perform another rotation, unique from $\mathbf{U_r}(t)$, upon the vector $c_a|a\rangle + c_b|b\rangle$. As pointed out earlier, the AC Stark shifts incurred from the single photon Rabi frequencies change the energy levels of the Λ type system. Upon removing the driving optical fields the energy levels will shift back to their original values. Therefore, the difference in photon energies necessary to drive a resonant two photon transition will not be equal to the difference in energy levels $|a\rangle$ and $|b\rangle$ of the unperturbed atom. The wavefunction provided in Equation 7.7 illustrates that the unperturbed state $|b\rangle$ accumulates a phase of $e^{-i(\omega_b - \omega_a)t}$ relative to state $|a\rangle$. While the driving fields are applied to the atom, the energy levels are Stark shifted giving rise to additional phase accumulation. This additional phase accumulation is $e^{-i(\frac{|\Omega_a|^2 - |\Omega_b|^2}{2(\Delta_a + \Delta_b)})t}$.

The driving field is prevented from interacting with the atom by deactivating an AOM as described in Section 6.2. Using an AOM in this manner allows us to extinguish the driving field without perturbing the phase relationship between the two laser beams used to drive the transition. Therefore, the phase angle ϕ, remains unaffected by shuttering the laser beams. Unlike the atomic energy levels, the relative phase accumulated between the two applied

laser fields will not change while the driving fields are prevented from interacting with the atomic states.

Naturally, the frequency of the laser field is set to oscillate resonantly with the atom, while the field is perturbing the atomic energy levels. If the driving field is momentarily prevented from interacting with the atom, the field and atom will no longer evolve at the same rate due to the AC Stark shifts. During this time the atom will accumulate a differential phase relative to the driving field. This phase angle is given by $(\frac{|\Omega_a|^2-|\Omega_b|^2}{2(\Delta_a+\Delta_b)})t_d$, where t_d is the time delay between pulses. This feature of our quantum computing system is used to accumulate the phase necessary to conduct controlled rotations. Neglecting global phase factors, this rotation is equivalent to:

$$\mathbf{U_z}(t) \;=\; \begin{pmatrix} 1 & 0 \\ 0 & e^{-i(\frac{|\Omega_a|^2-|\Omega_b|^2}{2(\Delta_a+\Delta_b)})t_d} \end{pmatrix} \;=\; \begin{pmatrix} 1 & 0 \\ 0 & e^{i\Delta_{ab}t_d} \end{pmatrix} \tag{7.10}$$

By merely turning our laser beams off for a predetermined length of time, we obtain an additional qubit operation. Upon accumulating the desired phase shift, the next qubit rotation can simply be applied by allowing the laser beams to interact with the atoms again. Through applying the proper laser pulse durations and allowing for appropriate delays between laser pulses these gates can be used to construct any other desired single qubit rotation.

Chapter 8

Single Atom Ground State Manipulations

In Section 7.3 we discussed a some what generic scenario where a Λ-type system is being driven by a two photon process between two nondegenerate ground states. In this chapter we explore in detail how these transitions are used to implement single qubit operations using a Rubidium-87 atom. The hyperfine ground state energy levels that we will concentrate on are the $|F = 1, m_F = 0\rangle$ and $|F = 2, m_F = 0\rangle$. The $|5P_{3/2}\rangle$ manifold is used as the intermediate level from which the driving fields are detuned.

The laser fields used to drive the transition are generated by the ground state two-photon Raman laser system (Section 6.2). The laser beams are navigated to the atoms through the optical addressing systems discussed in (Section 6.4). This chapter covers how state dependent atom detection is performed, how we determine the appropriate laser detuning to achieve two-photon resonance, the measurement of the Rabi flopping excitations, and finally how we observe phase accumulation by an atom placed in a superposition state in the absence of the driving fields.

8.1 State Dependent Detection

During the experimental protocols, a magnetic bias field is applied to the atoms, thus Zeeman splitting the magnetic sublevels of the F=1 and F=2 hyperfine states (see Section 3.4). Splitting the atomic structure in this manner allows us to perform optical pumping which is utilized for qubit initialization (see Sections 3.3, 3.4, and 3.5). Optical pumping into the $|F = 2, m_F = 0\rangle$ state is nominally $\sim 95\%$ efficient. The use of a magnetic field

quantization axis ensures that all of the ΔF=1, Δm_F=0 transitions are spectroscopically distinguishable, thereby allowing us to isolate and study two photon Rabi flopping between the $|F = 1, m_F = 0\rangle$ and $|F = 2, m_F = 0\rangle$ levels.

Transitions between the logic states are driven as described in Section 7.2. In characterizing the Rabi oscillations we require state dependent readout of our qubit states. The atom measurement protocols described in Sections 5.3 and 5.2 do not distinguish between atomic states. In order to identify the state of the atom we must perform a destructive measurement technique. After Rabi flopping we eject all atoms occupying the $|F = 2\rangle$ ground states from the FORT, using a unidirectional laser field generated by the MOT laser. This blow-away protocol is described at the end of Section 3.5. This state dependent removal of atoms ensures that only atoms in the $|F = 1\rangle$ states are detected. Figure 8.1 illustrates the efficiency of this process.

The optical pumping scheme, described in Section 3.5, is applied between two readout protocols to initialize the atoms into the $|F = 2, m_F = 0\rangle$ states. Figure 8.1(left) illustrates the nominal atom retention between camera shots. The application of blow-away pulses, Figure 8.1(right), demonstrates how F=2 atoms can be preferentially removed from the trap. Typically, less than 1% of the atoms in the F=2 state are retained after applying the blow-away protocol.

This technique of removing $|F = 2\rangle$ atoms from the FORT does not remove $|F = 1\rangle$ atoms. This is confirmed by optically pumping the atoms into the $|F = 1\rangle$ manifold with the isotropically polarized MOT optical fields for $\sim$10ms. The hyperfine repumping laser is removed during this period thus leading to atom shelving into the $|F = 1\rangle$ state. This optical pumping process requires the FORT and MOT laser beams to be modulated out of phase with each other, like the readout and optical pumping protocols. The blow away laser is applied to $|F = 1\rangle$ atoms for varying lengths of time. The blow-away protocol has virtually no effect upon the atoms as shown by Figure 8.2. This figure shows the normalized atom retention for varying durations of the blow-away protocol upon the F=1 atoms. The normalized atom retention accounts for the nominal atom loss observed between

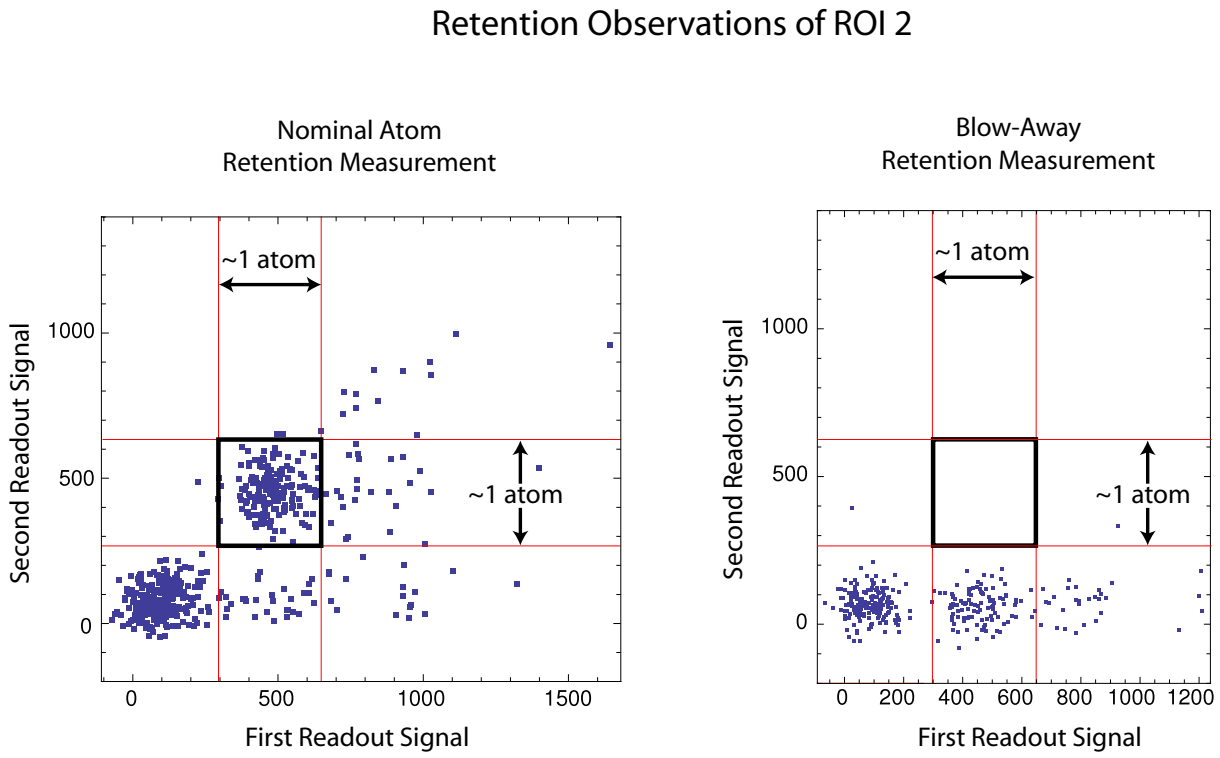

Figure 8.1 Atom retention measurements. These data sets utilize optical pumping to initialize the atoms into the F=2 state. Two readout protocols are performed per experiment cycle. The data to the right utilizes a blow-away protocol to eject F=2 atoms from the both FORT potentials. The data points displayed are the background subtracted photoelectron signals from the top FORT potential (ROI 2). ROI 1 data is omitted for clarity. The second readout signal is plotted as a function of the first readout signal. The plot to the left illustrates nominal atom retention ($\sim 85\%$). The plot to the right demonstrates nearly perfect removal of F=2 atoms from the trap. This illustrates our ability to design experiments capable of preferentially ejecting atoms from the F=2 state.

atom readout protocols. The process used to digitize and renormalize this data is discussed in Section 5. Each point represents the average of approximately 50 trials. The range of the error bars is equal to twice the standard error of the digitized mean. During nominal experiments the blow away pulses are typically applied for less than 5ms. Therefore, it is possible to perform a state sensitive measurement by applying a blow away sequence to the $|F = 2\rangle$ state before performing the atom measurement protocol. Utilization of the Zeeman splitting ensure that the only permissible transition exists between the $|F = 1, m_F = 0\rangle \leftrightarrow$

$|F = 2, m_F = 0\rangle$ states. Atoms remaining after the blow away pulse are from the $|F = 1\rangle$ state. This method of readout is utilized to measure the transfer of population between the logical qubits during various Rabi flopping experiments.

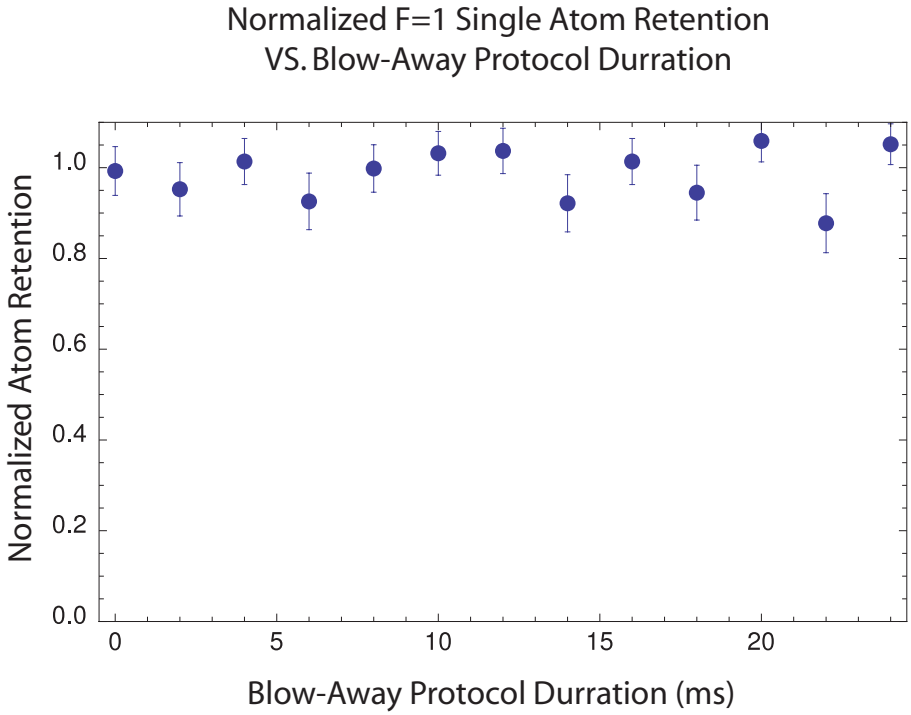

Figure 8.2 F=1 single-atom retention as a function of the blow-away pulsing duration for ROI 1. The normalized retention is virtually unaffected by the blow-away protocol. The nominal blow-away duration used to fully eject F=2 atoms is 5ms.

8.2 Ground State Two Photon Raman Spectroscopy

The implementation of our single qubit rotations requires us to resonantly drive atoms between the two hyperfine ground states. In Section 7.2 this resonance condition is shown to be dependent upon the intensity of the two driving lasers and their individual detunings from the $5P_{3/2}$ manifold. Nominally while performing ground state Rabi flopping the total laser beam power is regulated to be $\sim$100μW and is evenly divided between the two driving lasers. For the experiments presented in this section, the Rabi flopping laser beams are integrated

into the experiment through the 780nm beam line adjoining the FORT optical assembly (Section 6.4.2). This optical path generates Gaussian beam waists of $7.0 \times 11.9\mu m$, and gives the laser beams a σ^+-polarization. We experimentally determine what laser difference frequency is necessary to bring the driving fields on resonance with the two photon transition by performing two photon Raman spectroscopy between the $|F = 1, m_F = 0\rangle$ and $|F = 2, m_F = 0\rangle$ ground states. This experiment's timing protocol is shown in Figure 8.3.

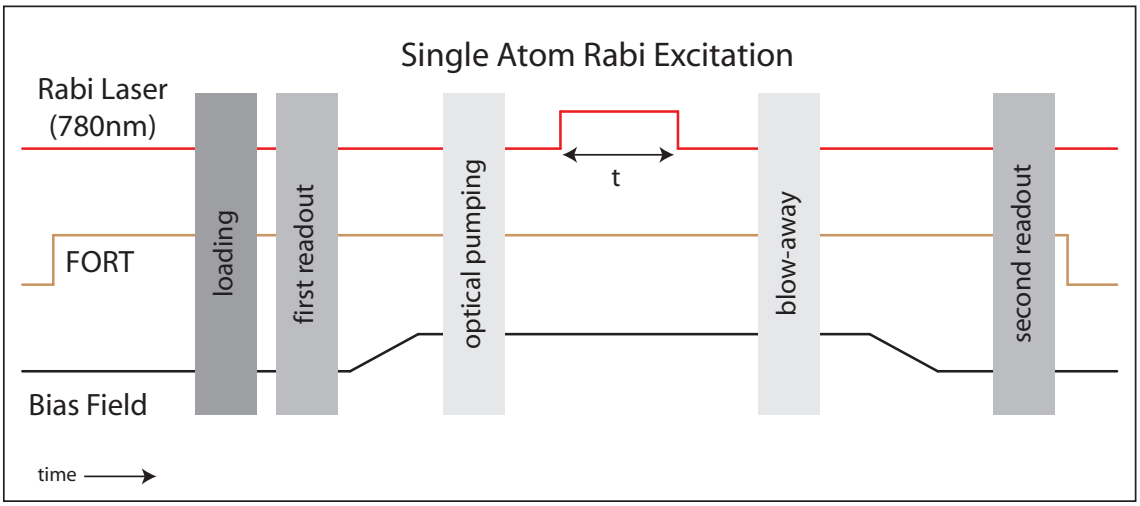

Figure 8.3 This figure illustrates the timing protocol used by most single atom two photon Rabi excitation experiments. A single atom is loaded and then observed in the FORT. The magnetic bias field is applied to the system, to allow optical pumping, Rabi flopping, and the blow-away protocol. The pulse duration, t, laser intensities and two photon detuning are all parameters that change according to the particular experiment we are performing. The bias field is turned off and the state of the atom is observed.

The probability of an atom initialized in the $|F = 2, m_F = 0\rangle$ state transferring into the $|F = 1, m_F = 0\rangle$ state after applying a Raman pulse of length t is given by:

$$P_{(F=1)} = \frac{\Omega_{ab}^2}{|\Omega_{ab}|^2 + (\Delta')^2} \sin^2\left(\frac{t\sqrt{|\Omega_{ab}|^2 + (\Delta')^2}}{2}\right) \tag{8.1}$$

This equation clearly exhibits the transition's dependence upon the two photon detuning, Δ'. By scanning the two-photon detuning and recording the probability of an atom undergoing a transition for a particular pulse length it is possible to observe this frequency dependence

as shown in Figure 8.4. The detuning in this plot is controlled by changing the microwave modulation frequency of the diode laser as described in Section 6.2.

The Rabi pulse length used in this experiment is 560ns long. This pulse length will result in a Bandwidth limited spectrum, with a FWHM of approximately $1/t_{pulse} \approx 1.8MHz$. It should be noted that Figure 8.4 plots the normalized atom signal as a function of the difference frequency between the two microwave modulated laser sidebands. To find the resonance frequency, this plot is fit using a function modeled after Equation 8.1. The free parameters will be t and f_{ab}, where $\Omega_{ab} = 2\pi \times f_{ab}$. The laser detuning f_Δ is the dependent variable and is realted to Δ' via $\Delta' = 2\pi \times f_\Delta$. A background offset, B_{offset}, and resonance frequency, f_0, are additional free parameters.

$$P_{(F=1)} = \frac{f_{ab}^2}{|f_{ab}|^2 + (f_\Delta - f_0)^2} \sin^2\left(\frac{2\pi t \sqrt{|f_{ab}|^2 + (f_\Delta - f_0)^2}}{2}\right) + B_{offset} \tag{8.2}$$

The Rabi flopping frequency, Ω_{ab}, is found to be $2\pi \times 1.07$MHz. Based on the optical power (102μW), the laser's carrier frequency (384173.5GHz), and the Gaussian laser beam waists ($w_x = 7.0\mu$m, $w_y = 11.9\mu$m) the expected resonant two photon Rabi frequency is $2\pi \times 1.12$MHz. The fit value of the pulse duration, t, is found to be 576ns which agrees well with the actual pulse length implemented in this experiment.

The peak microwave modulation frequency is found to be 6834.48 MHz. The unperturbed ground state energy levels are split by 6834.682610904MHz [Steck]. This frequency offset can be accounted for by the AC Stark shift acquired while driving the two photon transition. From Section 7.2 while driving the system resonantly $\Delta' \to 0$ leaving $\Delta_{ab} = -\frac{|\Omega_a|^2+|\Omega_b|^2}{2(\Delta_a+\Delta_b)}$. This means that the difference frequency of the laser fields must be detuned from the unperturbed energy level splitting.

In addition to determining the resonance condition for two photon Rabi flopping, two photon Raman spectroscopy is also used to calibrate the magnitude of the magnetic bias field applied to the atoms. This is accomplished by scanning the laser's modulation frequency in the same manner, however, in this experiment the atoms are not optically pumped into a particular m_F-hyperfine state. The atoms are allowed to randomly distribute themselves

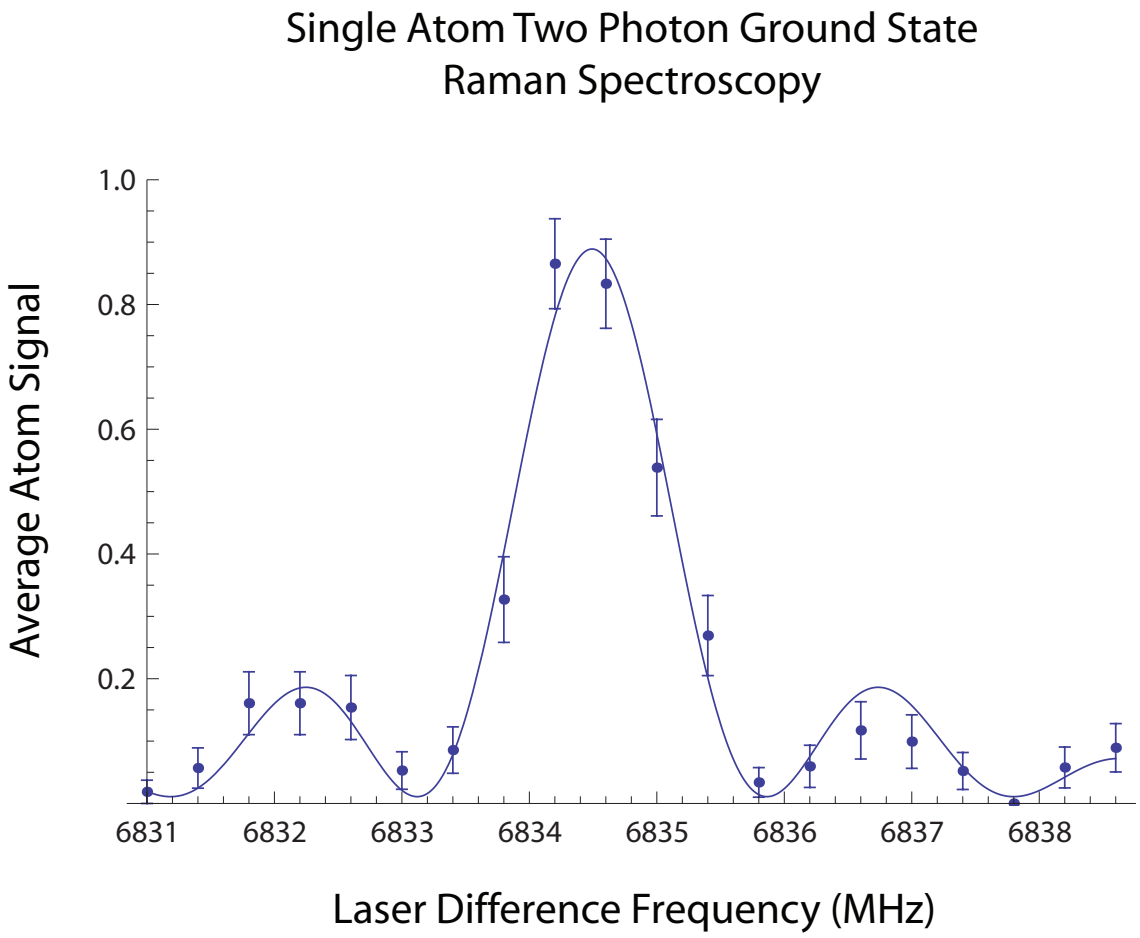

Figure 8.4 A two photon spectroscopy (TPS) scan demonstrating the system′s response to the two photon detuning. The $|F = 1, m_F = 0\rangle$ population is measured as a function of the difference frequency between the two microwave modulated laser sidebands (Section 6.2). The difference frequency of the two laser beams is equal to twice the modulation frequency. The data is fit using Equation 8.2. The full range of the error bars span twice the standard error of the mean of the digitized atom signal. Experimental parameters and fit values are explained in the main text.

throughout the magnetic sublevels of the F=2 hyperfine state. The laser modulation must also be allowed to scan a much greater range of frequencies. This enables us to observe transitions between the $|F = 1, m_F = -1\rangle \leftrightarrow |F = 2, m_F = -1\rangle$, and $|F = 1, m_F = 1\rangle \leftrightarrow |F = 2, m_F = 1\rangle$ states in addition to the $|F = 1, m_F = 0\rangle \leftrightarrow |F = 2, m_F = 0\rangle$ transition observed in 8.4. Figure 8.5 shows a spectrum in which the microwave modulation is scanned across

the $|F = 1, m_F = -1\rangle \leftrightarrow |F = 2, m_F = -1\rangle$ and the $|F = 1, m_F = 0\rangle \leftrightarrow |F = 2, m_F = 0\rangle$ transitions.

The peak populations transferred at the $\Delta m_F = 0$ resonance point is reduced by roughly a factor of five. Due to the reduced signal to noise of the spectrum, the peaks are fit using two Gaussian distributions. The spectroscopy peaks of Figure 8.5 are separated by 5.04MHz. The Zeeman shift is given as $\Delta E = g_F \mu_B m_F B$, where ΔE is the energy shift of a particular angular momentum projection, m_F, along a magnetic bias field strength B. The constant g_F is equal to -1/2 for F=1 states and +1/2 for the F=2 ground state energy levels. The gyromagnetic ratio $\mu_B/h \approx$ 1.4MHz/gauss. These relations allow us to determine that the magnetic bias field strength is approximately 3.6Gauss.

8.3 Rabi Flopping Between Atomic Ground States

With the ability to properly determine what laser frequency gives rise to on resonance two photon Raman transitions, it is possible to drive an atom between specific hyperfine magnetic sublevels with high fidelity. This gives rise to the qubit gate operations discussed in Section 7.3. In Figure 8.6 we perform a Rabi flopping experiment, where the difference in laser fields is held resonant between the two $m_F = 0$ ground state energy levels. The experiment timing protocol is shown in Figure 8.3. For this particular data set, the difference frequency of the driving fields is set to be 6834.50MHz. The duration of the atom-light interaction, t, is varied, thus revealing the time dependent transition probability. Each data point on Figure 8.6 is the average of > 50 digitized measurements. The error bars represent the standard error of the digitized mean.

The Rabi flopping curve is fit with the functional form, $P_{F=1}(t) = A - Ae^{-t/\tau_d}\cos(2\pi f'_{ab} t)$. The free parameters, A, τ_d, and f'_{ab} are used to generate a sinusoidally varying function that decoheres with a time constant of τ_d. The two photon Rabi frequency, Ω'_{ab} is equal to $2\pi \times f'_{ab}$, and is found to be equal to $2\pi \times$ 0.910MHz. The amplitude of the fit function, A, is 0.47, while τ_d is equal to $41.36\mu s$.

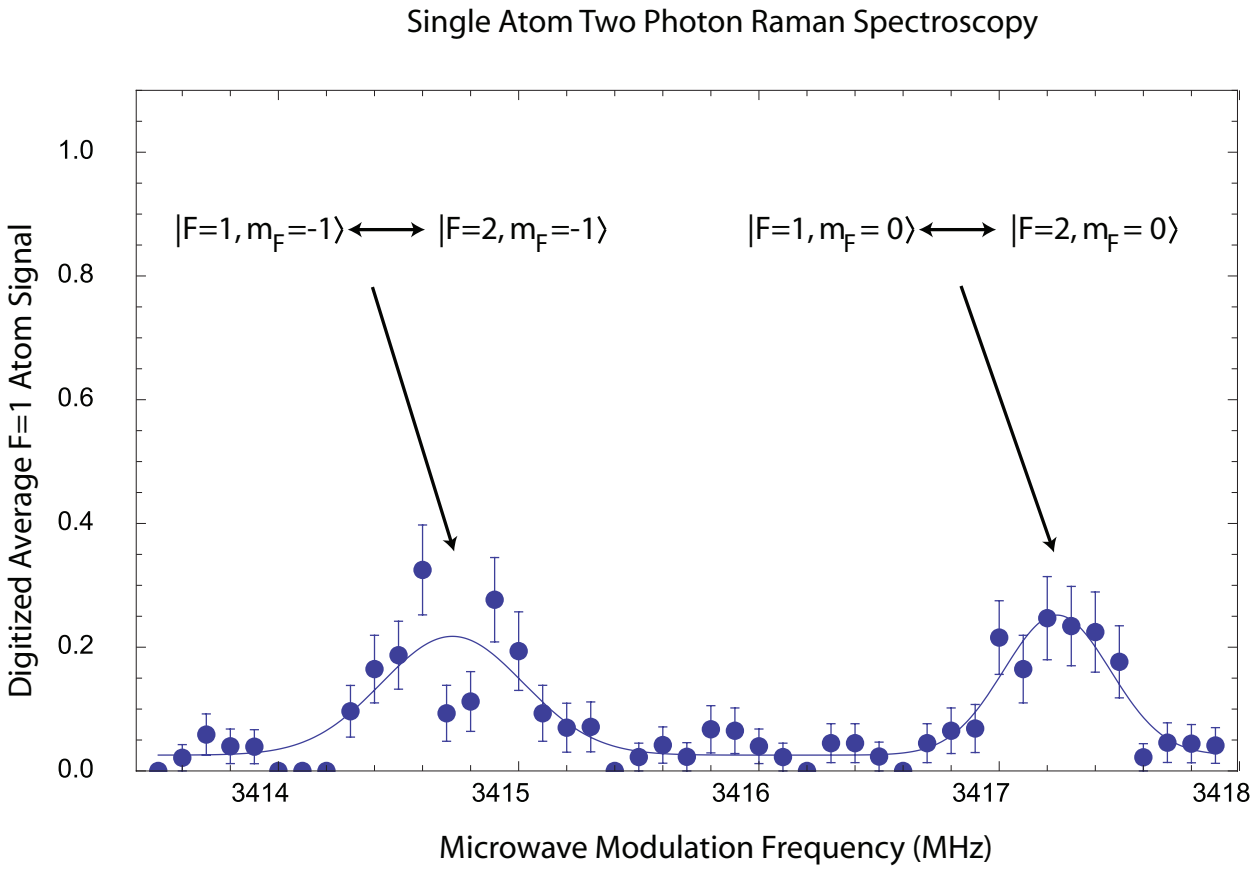

Figure 8.5 A two photon spectroscopy (TPS) scan measuring the Zeeman shift. The $|F = 1\rangle$ population is measured as a function of the two microwave modulation applied to the laser (Section 6.2). The difference frequency of the two laser beams is equal to twice the modulation frequency. The data is fit using the sum of two Gaussian distributions. The spectroscopy peaks are centered at 3414.72MHz and 3417.24MHz. The transitions therefore have an energy splitting corresponding to a frequency of 5.04MHz. This energy difference indicates that the magnetic bias field applied to the system is approximately 3.6gauss.

It is worth noting that the two photon spectroscopy scan, shown in Figure 8.4, predicts an effective Rabi oscillation frequency of $2\pi\times1.07$MHz. The Rabi flopping experiment in Figure 8.6 exhibits a frequency of $2\pi\times0.910$MHz. This difference can in part be explained by the finite atom temperatures and the Gaussian beam profile of the excitation lasers. It is foreseeable that from one experiment cycle to the next the laser intensities sampled by an atom will vary slightly, resulting in different Rabi flopping frequencies and AC Stark

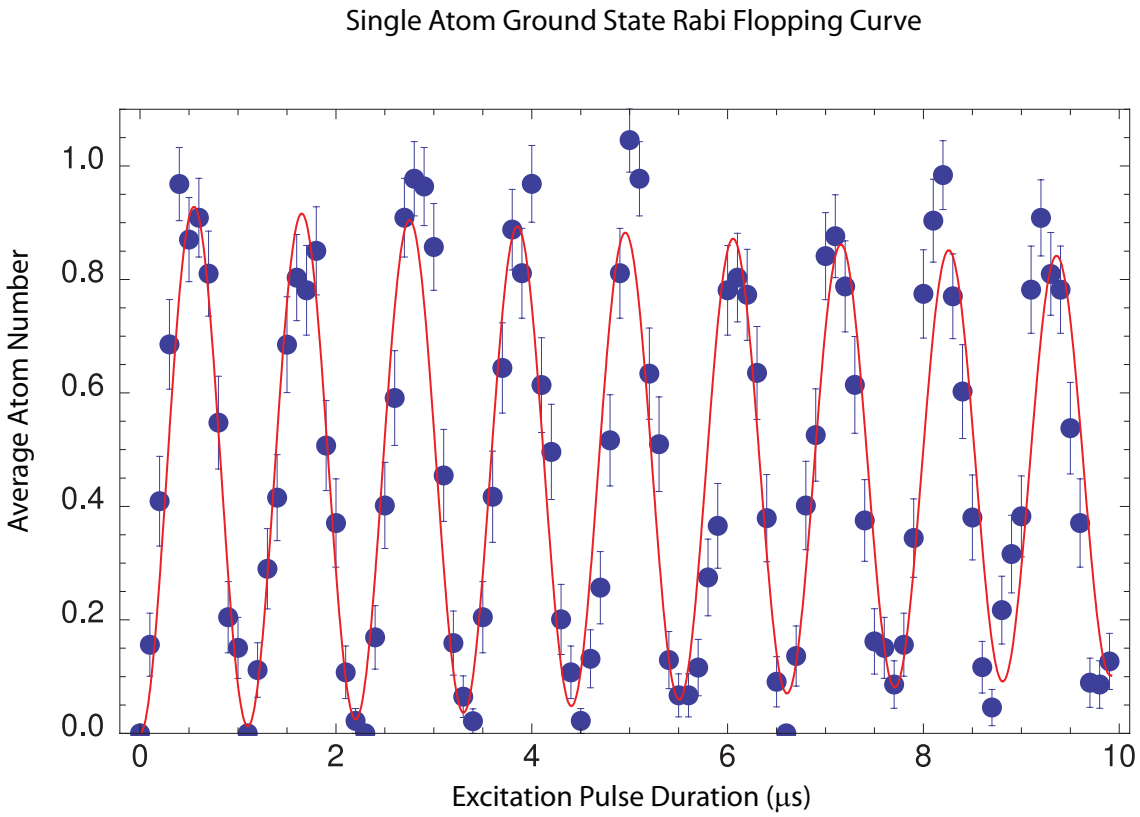

Figure 8.6 Resonant single atom two-photon Rabi flopping curve between the $|F = 2, m_F = 0\rangle \leftrightarrow |F = 1, m_F = 0\rangle$ states. The curve fit reveals that the effective two photon Rabi frequency, Ω'_{ab}, is $2\pi \times 910$kHz.

shifts for each trial. Likewise, Doppler broadening can contribute small shifts to the two photon transition detuning. These effects broaden the two photon spectroscopy curve (Figure 8.4). This broadening can help explain why the Rabi oscillation frequency fit to Figure 8.4 is slightly larger than the experimentally observed Rabi oscillation frequency observed in Figure 8.6. The problems associated with finite atom temperatures can in part explain the decoherence observed in the Rabi flopping experiments recorded in Figure 8.6. The decay constant, $41.3\mu s$, provides a lower bound of the qubit's T_2-time.

The amplitude fit to the sinusoidal data, A = 0.47, indicates that an atom only transfers into the $|F = 1, m_F = 0\rangle$ state about 94% of the time. Because the differential frequency of the lasers are set to drive the atoms resonantly, the amplitude of the observed oscillations

can be used to gauge the efficiency of the optical pumping used to initialize the qubits into the $|F = 2, m_F = 0\rangle$ state. Therefore, about 6% of the atoms are initialized to the wrong initial m_F level. Other optical pumping schemes can potentially give better initialization efficiencies.

From this Rabi flopping experiment we observe that the optical pulse duration necessary to perform $\pi/2$ and π pulses are respectively 275ns and 549ns long. These pulse durations indicate the interaction duration necessary to generate a superposition state or transfer the atom into the $|F = 1, m_F = 0\rangle$ state. These operations are crucial in performing single qubit state manipulations for later experiments.

In characterizing our ability to use Rabi flopping as a means of conducting single qubit operations, it is also necessary to quantify the crosstalk of the optical addressing system. This measurement is performed by addressing one qubit and measuring the Rabi flopping inadvertently sustained by an adjacent qubit. The amount of crosstalk observed should be related to the intensity of the addressing laser at the crosstalk qubit site (see Figure 8.7).

We quantify the crosstalk of the system as the ratio of the observed inadvertent Rabi frequency divided by the intentional on resonance Rabi frequency: $\Omega_{wrong-site}/\Omega_{target-site}$, [Yavuz et al., 2006]. The data collected from the previous Rabi flopping experiment, Figure 8.6, is reanalyzed to observe this crosstalk. The data points of Figure 8.6 represent the response of a single atom located in ROI 1. This data can be refiltered to observe the response of atoms located in ROI 2 while the addressing lasers remain targeted at ROI 1. The probability of exciting an atom located in ROI 2 is shown in Figure 8.8.

Despite the fact that the laser beam is not directly targeting the atom, the reduced intensity overlapping the atom still results in a population transfer that can still be modeled by Equation 8.1. The data is once again fit with the functional form, $P_{F=1}(t) = AAe^{-t/\tau_d}\cos(2\pi f'_{ab}t)$. When the lasers are addressing ROI 1, their difference frequency is set to be resonant for a particular laser intensity and AC Stark shift. Therefore,

$$\Delta' = 0 = \Delta_{ab} + \frac{|\Omega_a|^2 - |\Omega_b|^2}{2(\Delta_a + \Delta_b)}.$$

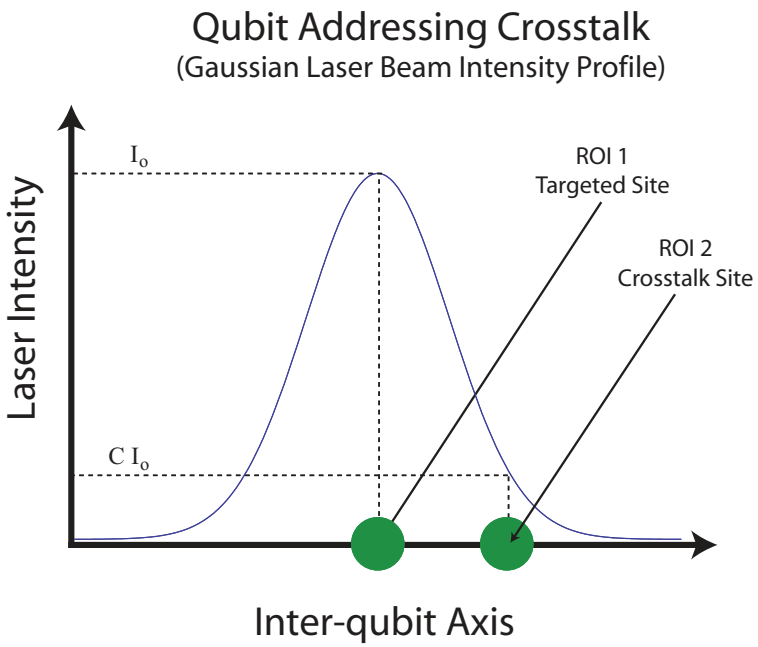

Figure 8.7 Illustration demonstrating the origin of crosstalk. The laser beams are targeting the qubit located within ROI 1 of the EMCCD camera. The qubit located in ROI 2 are inadvertently affected by the laser pulse used to manipulate the qubit in ROI 1.

Looking at the effect of the lasers upon ROI 2, we see that Δ_{ab} remains unchanged, but the laser intensities will dramatically decrease. The lower laser intensities reduce the terms $|\Omega_a|^2$ and $|\Omega_b|^2$. Therefore, $\Delta' \neq 0$ at ROI 2, and the atoms will be driven via a detuned two photon Raman process. The crosstalk observed is found to be $\approx$ 188kHz/910kHz $\approx$ 0.20.

Because Δ_{ab} is identical in both the crosstalk and Rabi flopping analysis we can relate the flopping rates and oscillatory amplitudes fit to these curves. The amplitude of the on resonance flopping curve, 8.6, is given by: $P_{(Max)} = \frac{|\Omega_{ab}|^2}{|\Omega_{ab}|^2+(\Delta')^2} \approx 1$, where $\Delta' = \Delta_{ab} + \frac{|\Omega_a|^2-|\Omega_b|^2}{2(\Delta_a+\Delta_b)} \approx 0$. While on resonance the AC Stark shift, and unperturbed two photon detuning, Δ_{ab}, are equal but opposite. At the cross talk site the intensity of the laser beams will be reduced thus resulting in a different two photon Rabi frequency, Ω_{ab}, and effective detuning, Δ'. The single photon Rabi frequencies, which are related to the effective detuning, will be reduced as well by this difference in intensity. The reduction in Rabi frequency is proportional to the laser beam's fractional intensity, which we will call C. We can write the

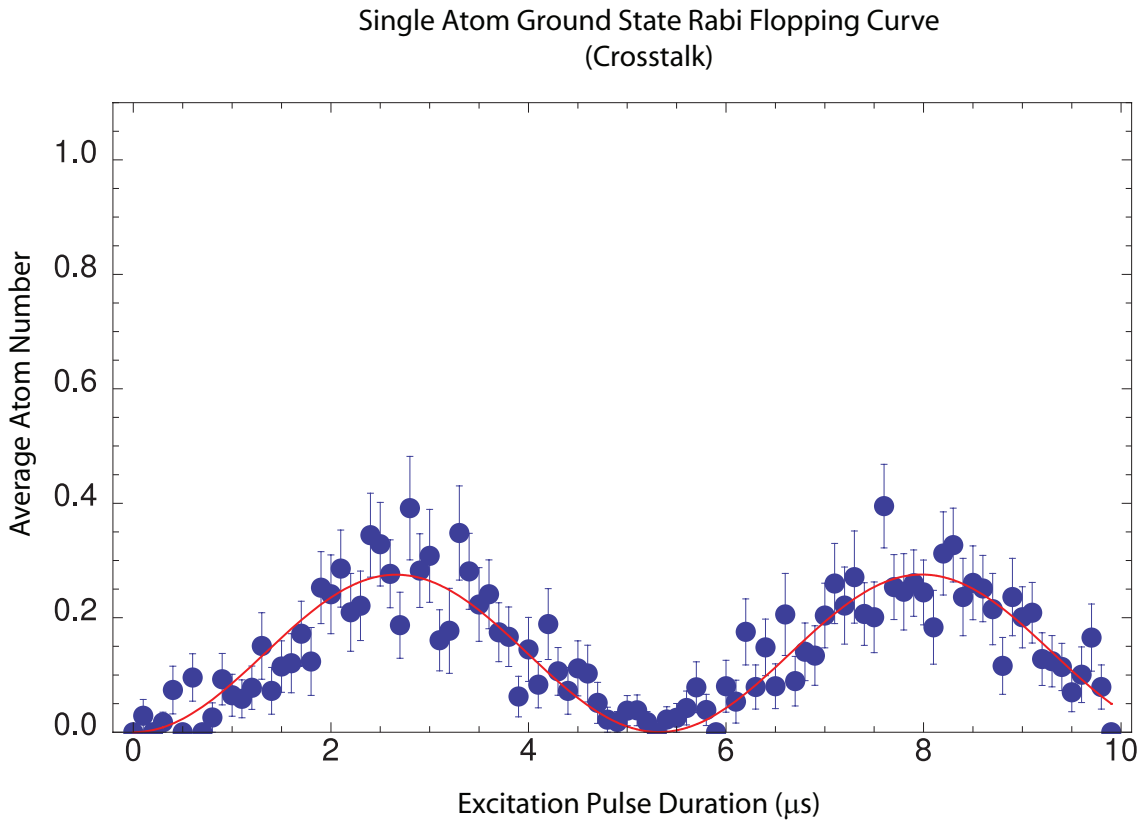

Figure 8.8 Rabi flopping crosstalk in ROI 2 resulting from addressing ROI 1. The Rabi flopping curve is fit with the functional form, $P_{F=1}(t) = AAe^{-t/\tau_d}\cos(2\pi f'_{ab}t)$. The observed effective two photon Raman Rabi flopping frequency $|\Omega_{ab}| \approx 2\pi \times 188$kHz. A maximum of about 27% of the population is observed to undergo the transition (A = 0.137).

maximum probability of transferring an atom in an adjacent site as:

$$P_{(Cross,Max)} = \frac{C|\Omega_{ab}|^2}{C|\Omega_{ab}|^2 + (\Delta_{ab} - C\Delta_{ab})^2} \approx 0.275 \tag{8.3}$$

The approximation in Equation 8.3 comes from the curve fit of Figure 8.8.

The intensity of a Gaussian laser beam has the functional form $I(r,z) = I_0\left(\frac{w_0}{w(z)}\right)^2 e^{(-2r^2/w^2(z))}$ where r and z characterize the transverse and axial displacement from the focus of the minimum beam waist w_0. From Equation 4.2, $w(z) = w_0\sqrt{1+\left(\frac{z\lambda}{\pi w_0}\right)^2}$. We will assume that the qubits and FORT sites are located in the same plane, thus setting $z \to 0$. Furthermore, we will allow r$\to$0 for the targeted qubit. The ratio, C, of the laser beam′s intensity at the crosstalk afflicted site relative to the intensity at the targeted qubit is given by: $C = e^{-2s^2/w^2}$

where s is the distance between qubits and w is the waist of the addressing beam along the inter-qubit axis.

Using the approximation, $P_{(Cross,Max)} \approx 0.275$, from Equation 8.3 and the experimentally determined parameters, $\Omega_{ab} = 2\pi 0.910$MHz, $\Delta_{ab} = 2\pi 0.1826$MHz, w=7.0$\mu m$ it is possible to determine the separation between the qubits, s, when observing this level of crosstalk. Using this technique the separation of the qubits is determined to be approximately 10.1μm which is in good agreement with the measurements provided in Chapter 5.

To demonstrate a blockade gate, this level of crosstalk is tolerable. In the future, conducting large series of quantum operations will require that the degree of crosstalk be carefully monitored and compensated, or drastically suppressed. The later solution is implemented through the use of smaller addressing beams and a smaller intermediate detuning (see Figure 8.9). Through the use of a 4.1μm addressing beam and a detuning of $2\pi \times$41GHz the cross

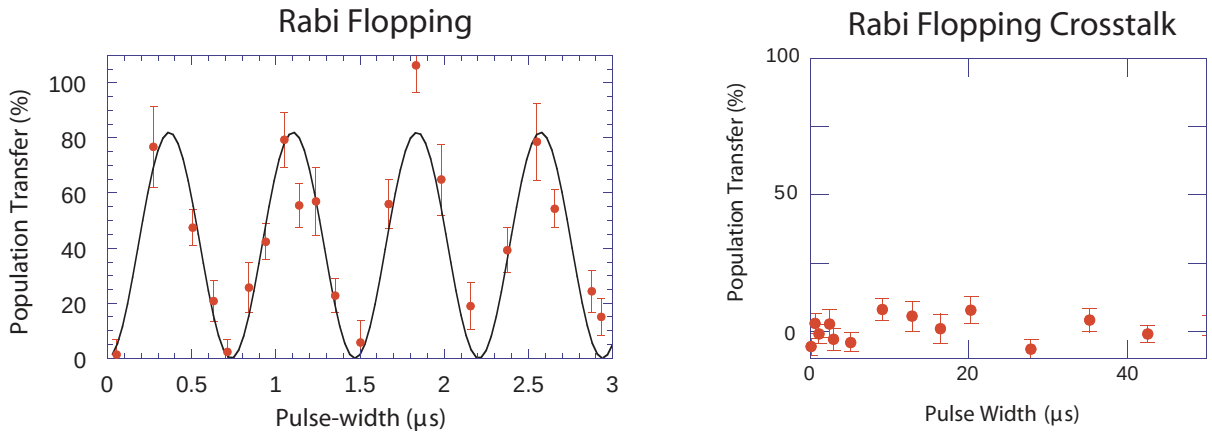

Figure 8.9 Rabi flopping ensemble of atoms trapped within 1mK FORT potential. Excitation beam waist is 4.1μm. Intermediate state detuning $\approx$ -2π $\times$ 41GHz. The observed two photon Rabi frequency is 2π $\times$ 1.36MHz.

talk between sites is reduced to less than 1.4×10^{-3} [Yavuz et al., 2006]. The smaller addressing beams are created by replacing the f=175mm achromatic doublet, Figure 6.8, with a f=400mm achromatic doublet. The Rabi flopping demonstrated in Figure 8.9 is performed on ensembles of atoms confined within a 1mK FORT potential [Yavuz et al., 2006]. Through

additional optimization of the addressing laser parameters it is believed that crosstalk can be further suppressed while simultaneously increasing the Rabi flopping rate of a single atom.

8.4 Ground State Phase Accumulation

As discussed in Section 7.3, the phase precession of an unperturbed atom can be utilized as a qubit operation. In order to implement specific qubit rotations and account for phase accumulation while the qubit is not being addressed, this phenomenon must be well characterized. This measurement is made with the timing protocol illustrated in Figure 8.10. The laser fields must be set to drive an atom resonantly. A single atom is initialized to the $|F = 2, m_F = 0\rangle$ state. The addressing beam is activated to apply a $\pi/2$-pulse,

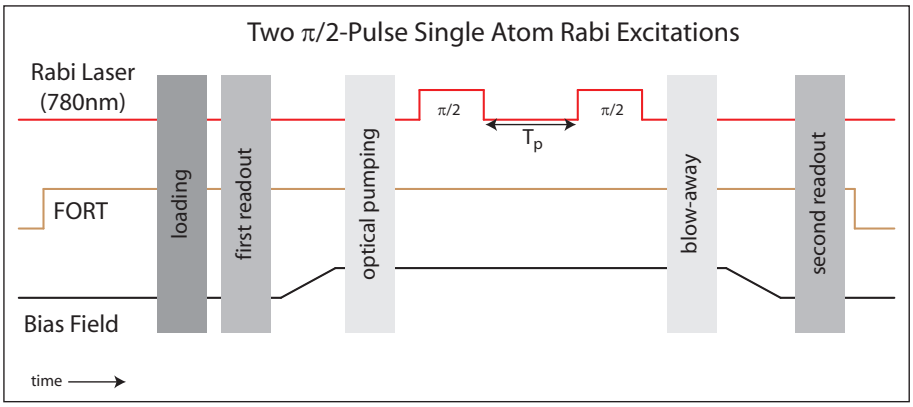

Figure 8.10 This figure illustrates the timing protocol used to study the phase accumulated between two Rabi excitation pulses. Two $\pi/2$-pulses are separated by a time delay, T_p, which is incrementally increased. The bias field is turned off and the state of the atom is observed.

$\mathbf{U_r}(t = \frac{\pi}{2|\Omega_{ab}|})$. This places the atom in a superposition state, $|0\rangle + e^{i\phi}|1\rangle$, where ϕ represents a relative phase angle. The atom is allowed to precess for time T_p before a second $\pi/2$ pulse is applied and the state of the atom is finally measured. The phase acquired by the atom during this free precession period, T_p, is equivalent to shifting the phase of the driving laser field (see Section 7.3). The final state of the atom is therefore dependent upon the amount of phase accumulated during T_p. If we record the final output state from this three step process,

as a function of T_p then we will observe a sinusoidally varying function. Such an experiment protocol is outlined in Figure 8.10. Figure 8.11 shows the data from this experiment.

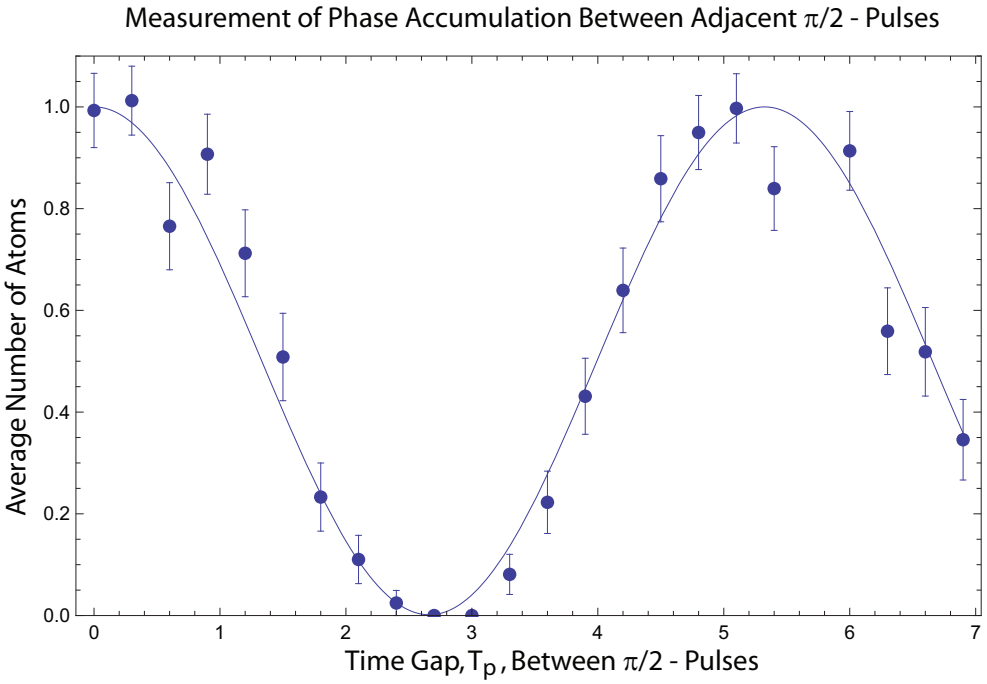

Figure 8.11 Measurement of phase accumulated while laser beams are not AC Stark shifting the F=1 and F=2 ground states. Atoms are prepared into the $|F = 2, m_F = 0\rangle$ ground state and are then addressed by a two photon Rabi $\pi/2$-pulse. A delay time T_p elapses prior to the application of a second $\pi/2$-pulse. The average number of atoms in the $|F = 1\rangle$ state are recorded as a function of T_p. The oscillatory frequency is found to be 188kHz.

Prior to performing this experiment the AC Stark shift is measured via two photon spectroscopy to be approximately 182kHz. The difference frequency of the two driving fields is therefore set to 6834.5MHz. The $\pi/2$-pulse duration was experimentally determined to be 300ns. The probability of transferring an atom into the $|F = 1, m_F = 0\rangle$ state is clearly a function of the delay time between laser pulses. The application of two $\pi/2$-pulses without a delay period, $T_p = 0$, results in nearly every trial transferring an atom into the $|F = 1, m_F = 0\rangle$ state. The data is therefore fit with the function $P_{F=1}(T_p) = A + Ae^{-T/\tau_d}\cos(2\pi f_{ac} T_p)$. The amplitude, A, of the sinusoidal function is found to be $\approx$0.5, indicating high fidelity

multiple pulse two photon Rabi flopping. The frequency of the oscillations, f_{ac}, are found to be 188kHz. This corresponds well with the requisite driving frequency. The compensated AC Stark shift corresponds to 182kHz. Due to very small decoherence observed within a 7μs delay time the decay constant fit to this scan provides an unreliable quantitative value. However, it is reasonable to assert that the decay constant is at least an order of magnitude larger than $7\mu s$.

8.5 Ramsey Spectroscopy

One method of measuring the decoherence time of our qubits is through Ramsey′s method of separated oscillatory fields. This method requires us to apply two $\pi/2$-pulses to our atoms as shown in Figure 8.10. However, unlike the ground state phase accumulation measurement performed in Section 8.4, a fixed time delay between laser pulses is used and the population transfered is measured as a function of the two photon detuning of the driving lasers. This population transfer once again exhibits an oscillatory pattern. Several plots of this behavior are shown in 8.12 for time delays, T_p, of 100μs, 300μs, 1ms, and 3ms. The data presented in Figure 8.12 is performed on an ensemble of atoms contained in a $\sim$1mK FORT. The Gaussian excitation beam used has a 4.1μm waist. Further experimental details are contained in [Yavuz et al., 2006]. It is possible to plot the contrast of these oscillatory curves as a function of the time delay set between excitation pulses. Figure 8.12 reveals an exponential decay in observed contrast as a function T_p. The best exponential fit to the data points yields a decay constant of $T_2 = 870\mu$s. The decay constant corresponds the rate of dephasing of the trapped atoms, and provide us with an order of magnitude estimate of a qubit decoherence rate.

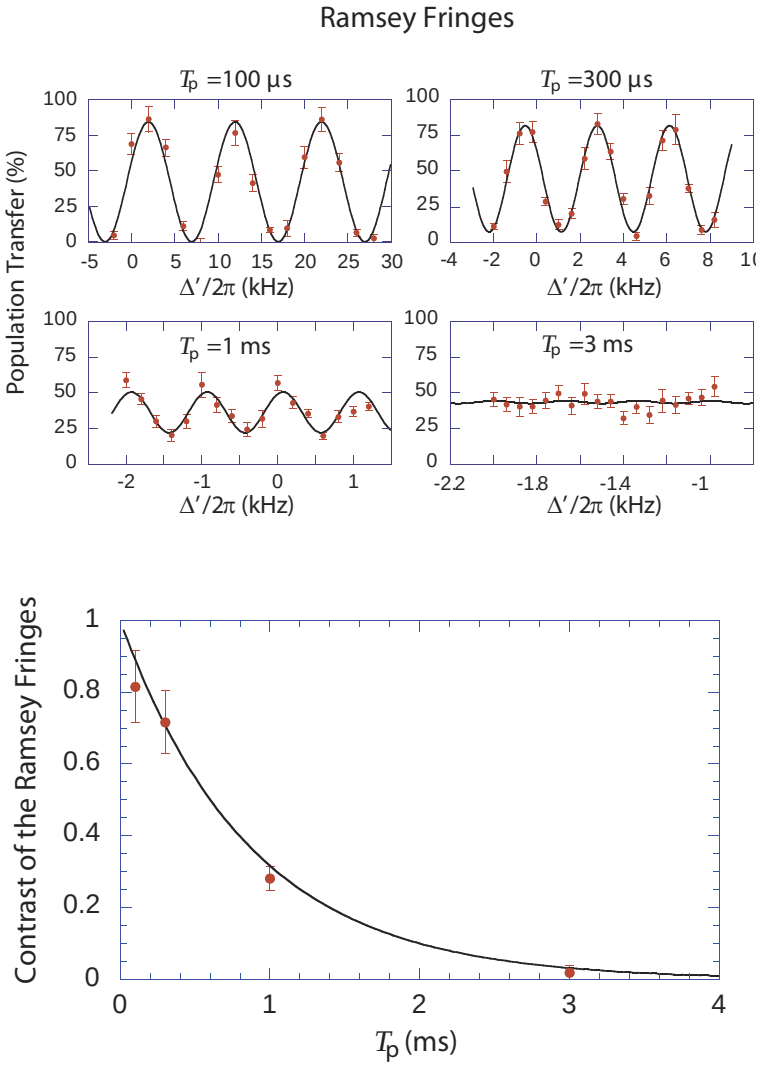

Figure 8.12 Decoherence time measurement. Ramsey spectroscopy experiments performed for different time delays, T_p. The detuning of the two photon excitation lasers is scanned across resonance. To the right we plot the fringe contrast as a function of T_p. The best exponential fit to the data points yield a dephasing time constant of $\sim 870 \mu$s.

Chapter 9

Rydberg Atom Excitations

As described in Sections 6.3 and 7.1 we excite atoms from the ground state hyperfine energy levels to high principal quantum numbers. The atomic radii of these highly excited atoms approximately follow a n^2 scaling when n$\gg$1. The outer electron′s wave packet of an n=100 Rydberg atom extends approximately 500nm away from the atom′s nucleus. The impressively large electron-nucleus separations of the Rydberg atoms make them hydrogenic in nature and give rise to a variety of interesting atomic properties. The large polarizabilities of Rydberg atoms making them highly sensitive to external electric fields, and enable Rydberg atoms to perturb one another. This chapter explains how we experimentally create and detect ^{87}Rb atoms.

9.1 Rydberg Atom Detection

Our apparatus is configured to detect Rydberg atoms though photoionization. In all Rydberg experimental protocols, the FORT laser beams must be extinguished momentarily while promoting an atom to a high principal quantum number. This is necessary to eliminate the induced AC Stark shifts of the FORT. If the FORT potential is removed for too long the atoms will not be recaptured when the optical potential is reestablished. This is demonstrated in Section 5.4, where the atom temperatures are measured by monitoring atom retention after removing and reestablishing the optical potential. Therefore, it is necessary to limit this FORT drop to approximately 7μs.

In the absence of the FORT the excitation lasers are engaged thus driving the two-photon Rydberg excitation. The particular pulse sequence utilized varies from experiment to experiment and will be discussed further in the forthcoming sections. Unlike the ground state atoms, Rydberg atoms become photoionized upon restoring the FORT, and are thus lost from the trap. By monitoring trap loss we can ascertain the probability of creating a particular Rydberg state for a given set of excitation parameters.

Decay mechanisms, from Rydberg states, influence our ability to detect the highly excited atoms with perfect efficiency. Specifically, if atoms naturally decay from the Rydberg level back to the ground state before the photoionizing FORT is reestablished, the detected signal level would not fully reflect the number of Rydberg atoms generated. Because Rydberg atoms are susceptible to the effects of small fields it is important to consider the effects of blackbody radiation upon the Rydberg lifetimes. At absolute zero the lifetime, τ_{nL}^0, of a Rydberg atom is dependent upon the effective principal quantum number and its orbital angular momentum. The effective principal quantum number n^* is defined as $n^* = n - \delta_{qd}$, where δ_{qd} is the empirically observed quantum defect for a particular angular momentum state, L. As discussed in [Saffman and Walker, 2005], an approximate expression for τ_{nL}^0 is given by:

$$\tau_{nL}^0 = \tau_L^0 (n^*)^{\alpha_L} \approx 2.09ns * (n^*)^{2.85} \tag{9.1}$$

At high temperatures and large n the blackbody rate can be related to the fine structure constant α through Equation 9.2.

$$\tau_{nL}^{bb} = \frac{3\hbar n^2}{4\alpha^3 k_B T} \tag{9.2}$$

Therefore, at finite temperatures an approximate characteristic Rydberg lifetime is given by, [Saffman and Walker, 2005]:

$$\frac{1}{\tau_{nL}} = \frac{1}{\tau_{nL}^0} + \frac{1}{\tau_{nL}^{bb}} \tag{9.3}$$

The experiments examined later in this chapter focus on the n = 43, 79, 90 and 97 $d_{5/2}$ levels. To achieve an order of magnitude estimation for the Rydberg decay lifetimes we approximate the parameters $\alpha_L \approx 2.85$, $\tau_L^0 \approx 2.09ns$, and $\delta_{qd} \approx 1.34$ [Gallagher, 1994], [Li

et al., 2003]. Therefore, at room temperature the expected radiative lifetimes are typically of order ∼45-310us for $43d_{5/2} < n < 97d_{5/2}$.

The photoionization rate of the FORT potential interacting with the Rydberg atoms will scale linearly with the FORT trap depth and inversely with n^3. In reference [Saffman and Walker, 2005] the photoionization rate of an n=50 Rydberg state was approximated to be $\gamma_{pi} \approx$31000/s for a 1mK FORT potential. As a rough approximation, we can scale this value to estimate the photoionization rates for other principal quantum numbers. The following equation is used in making these approximations:

$$\gamma_{pi} = \frac{U_m}{1mK}\left(\frac{n}{50}\right)^{-3}(31000)/s$$

In this equation U_m is the depth of the FORT in temperature units. Using this approximation, a 5mK FORT potential will have a photoionization rate of about 21000-243000/sec, depending on n.

The lifetime of the Rydberg atoms and the photoionization rate compete against each other, thus limiting the detection efficiency of Rydberg atoms. Atoms that decay back to a ground state cannot be distinguished from an atom that was never promoted to a Rydberg state. The detection efficiency will be compromised by the length of time that the atom must be held in the Rydberg level and the time necessary to photoionize the atoms. The amount of time the Rydberg atom must be maintained is dependent upon the type of experiment being performed. As we will see in Section 9.2, the FORT is typically engaged ∼100ns after the Rydberg atoms have been created. In more complicated pulse schemes used in Chapters 10, 11, and 12, the atoms are held in Rydberg states for several microseconds. The time from when the FORT laser is activated until the atom becomes photoionized can be approximated by $1/\gamma_{pi}$. At n=97 this characteristic time scale is of order $40\mu s$. For a given delay time, t_{delay}, between Rydberg atom creation and photoionization, the detection efficiency can be approximated by $E_{Ryd} \approx e^{(-t_{delay}/\tau^0_{nL})}$. When trying to measure the probability of Rydberg atom excitations the photoionizing FORT lasers are typically activated about 100ns after the production of a Rydberg atom. For n > 40 it is reasonable to approximate $t_{delay} \approx 1/\gamma_{pi}$.

Therefore, using a 5mK FORT trap, we can estimate that the detection efficiency of the $97d_{5/2}$ state is of order 88%.

9.2 Rydberg Two-Photon Raman Spectroscopy of Single Atoms

As discussed in Section 7.3, the two photon Rydberg Rabi transition must be driven resonantly to achieve a full population transfer. Like the Rabi flopping observed between two ground state energy levels, the resonance condition of the driving field must be experimentally determined. As explained in Section 6.3, the frequencies of the 780nm and 480nm driving fields are locked to a reference cavity. The longitudinal cavity modes used as references are selected such that the laser fields are nearly resonant with the two-photon transition. An AOM is used to fine tune the frequency of the 780nm laser. Unlike the ground state transitions, the lasers used to drive the Rydberg transition follow two separate counter propagating optical paths to the optical traps.

The experimental protocol used to determine these resonance conditions starts by loading atoms into the FORT followed by a camera exposure to determine how many atoms are trapped at the beginning of each trial. A magnetic bias field is applied to the atoms to allow for optical pumping. The orientation and magnitude of the magnetic bias field used depends upon which state the atoms are going to be optically pumped. A more detailed description of the magnetic field coils and the optical pumping protocols are outlined in Sections 3.4 and 3.5 respectively. The atoms are initialized into the $|F = 2, m_F = 2\rangle$ or $|F = 2, m_F = 0\rangle$ state depending upon what Rydberg level we wish to observe. After initializing the atoms, the FORT potential is removed to allow the addressing lasers to interact with the atom. The magnetic bias field coils are left on to Zeeman split the various magnetic sublevels of the Rydberg and ground state energy levels.

The optical addressing system, outlined in Section 6.4, is used to guide the 780nm and 480nm laser beams to a particular FORT site. The 480nm laser beam is turned off using the AOM within the addressing optics. This is accomplished by redirecting the laser beam to a beam dump within the optical train. As discussed in Section 6.4, the rise and fall time

of this AOM is of order 150μs. Therefore, the 480nm laser field is turned on (off) several milliseconds before (after) the FORT potential is removed (reestablished). The duration of time that the 780nm laser field is applied to the atoms is controlled by the double passed AOM which is also used to control two photon detuning of the Rydberg transition. Because the 480nm laser is always on, the double passed AOM ultimately controls the duration of the Rydberg Rabi flopping pulse.

As outlined in Section 9.1, the FORT potential is returned in order to photoionize the Rydberg atoms. A second camera exposure is taken to record the number of atoms observed after the experiment protocol. The atom signals of each trial are digitized and filtered as outlined in Section 5.2. After acquiring statistics on the number of atoms remaining after a particular Rydberg pulse sequence, we can determine what percentage of atoms are promoted into a Rydberg state.

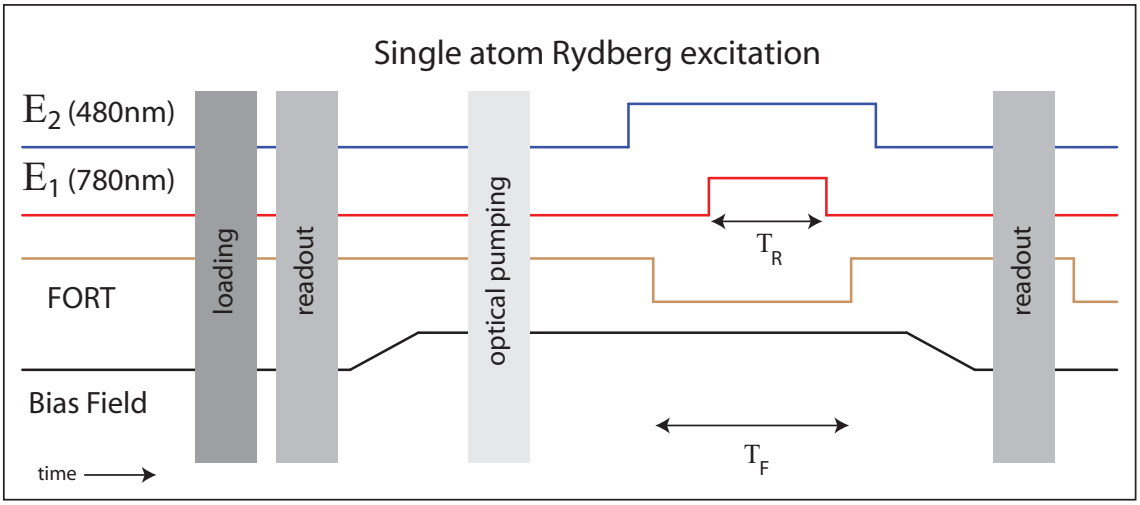

Figure 9.1 This generic timing chart illustrates a typical protocol used to conduct two photon spectroscopy of a Rydberg excitation. It should be noted that the bias magnetic field used for optical pumping is also engaged during the Rydberg Rabi flopping interaction time, T_R. The FORT laser is turned off for a time $T_F < \sim 8\mu$s.

As mentioned earlier, the atoms are optically pumped into one of two ground state magnetic sublevels, $|F = 2, m_F = 2\rangle$ or $|F = 2, m_F = 0\rangle$. A bias magnetic field is used to Zeeman shift the Rydberg and ground state energy levels during the course of the experiment.

The magnetic bias field is perpendicular to the propagation of the Rydberg excitation lasers while using π-polarized laser fields (see Section 3.4).

While driving the Rydberg transitions with π-polarized light there are 8 possible transitions between the $|5s_{1/2}, F = 2\rangle \leftrightarrow |nd_{5/2}\rangle$ states. These possible transitions are all shown in Figure 9.2. Each possible transition has a different Rydberg Rabi frequency. Therefore, if one were to try and observe Rabi flopping between the $|5s_{1/2}\rangle \leftrightarrow |nd_{5/2}\rangle$ without the presence of Zeeman splitting all possible transitions would be observed simultaneously. This would result in a very complicated oscillatory behavior which is not conducive to the controlled transfer of atoms to a Rydberg state. Through appropriately tuning the 780nm laser frequency and inducing a Zeeman splitting, it is possible to drive a transition to a specific Rydberg m_J level. Nominally, while operating with π-polarized laser fields we choose to excite $|F = 2, m_F = 2\rangle \leftrightarrow |n, d_{5/2}, m_J = +1/2\rangle$ transition.

The application of a magnetic bias field is also necessary when driving the atoms from the $|F = 2, m_F = 0\rangle$ initialized state. As described in Section 3.4, the orientation of the magnetic bias field is aligned in the propagation direction of the Rydberg excitation lasers when using this initialization state. While driving atoms from this ground state we use σ^+-σ^+ or σ^+-σ^- polarized laser fields. Once again, Zeeman shifting the atomic structure enables us to drive one particular transition at a time. The pertinent atomic energy level schemes are shown below in Figure 9.3. When driving the Rydberg transition with σ^+-σ^+ polarized light we drive the $|F = 2, m_F = 0\rangle \leftrightarrow |nd_{5/2}, m_J = 5/2\rangle$ transition. When using σ^+-σ^- fields and by scanning the frequency of the 780nm laser, we observe four different Rydberg transitions: $|F = 2, m_F = 0\rangle \leftrightarrow |nd_{5/2}, m_J = \pm 1/2\rangle$ and $|F = 2, m_F = 0\rangle \leftrightarrow |nd_{3/2}, m_J = \pm 1/2\rangle$.

To establish a resonance condition of a particular transition one must measure the probability of generating a Rydberg atom as a function of the combined laser frequencies. The transition line center is dependent upon the particular set of laser beam intensities used to drive the atom. By spectroscopically measuring the observed line center we automatically calibrate the laser frequency to compensate for AC Stark shifts generated by the lasers. The frequencies of the lasers will be locked to a reference cavity within $\pm$500MHz of the desired

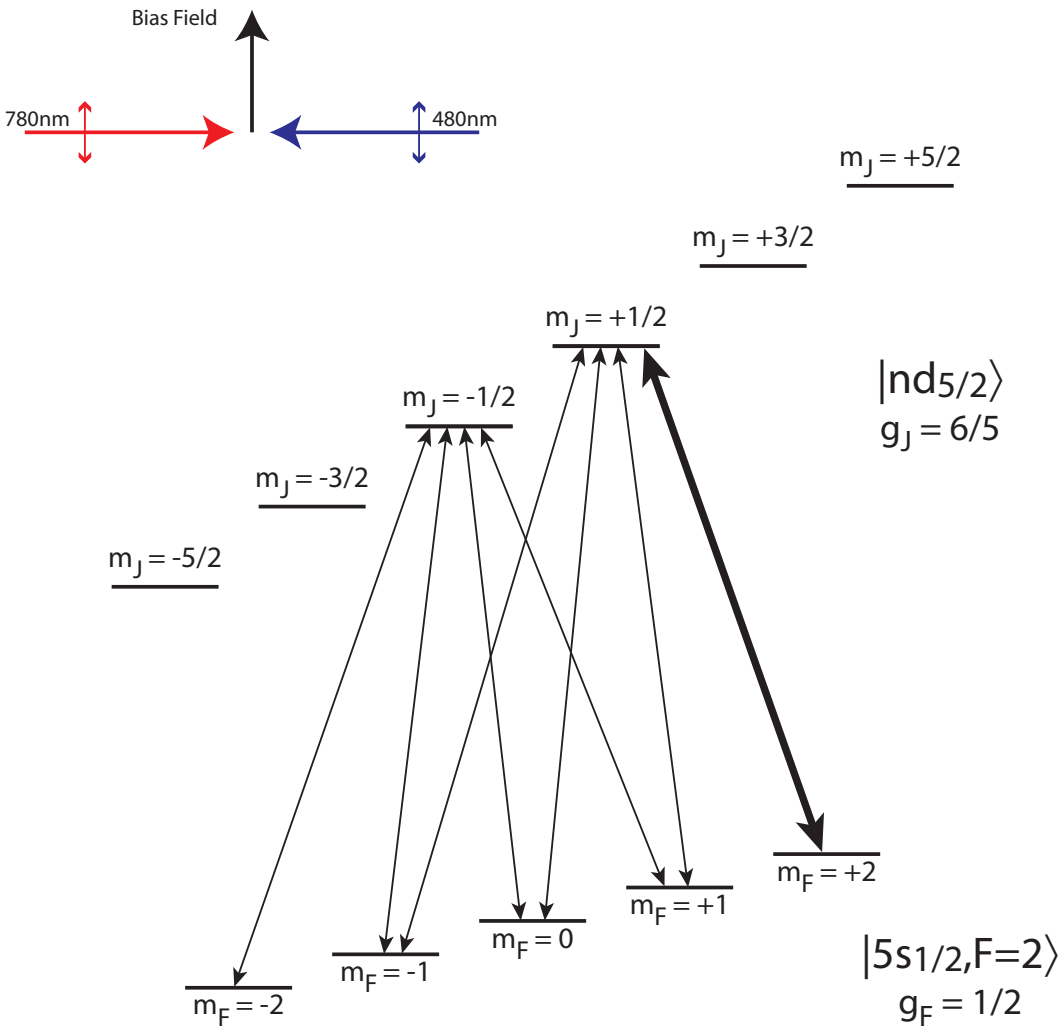

Figure 9.2 This figure illustrates the energy level splitting of the $|5s_{1/2}, F = 2\rangle$ and a generic Rydberg $|nd_{5/2}\rangle$ level. The arrows represent transitions made possible by driving the atoms with two π-polarized laser fields. The broad arrow between the $|5s_{1/2}, F = 2, m_F = 2\rangle$ and $|nd_{5/2}, m_J = +1/2\rangle$ states represents the transition most commonly utilized for single atom Rydberg spectroscopy, Rabi flopping, and blockade observations with π-polarized laser fields.

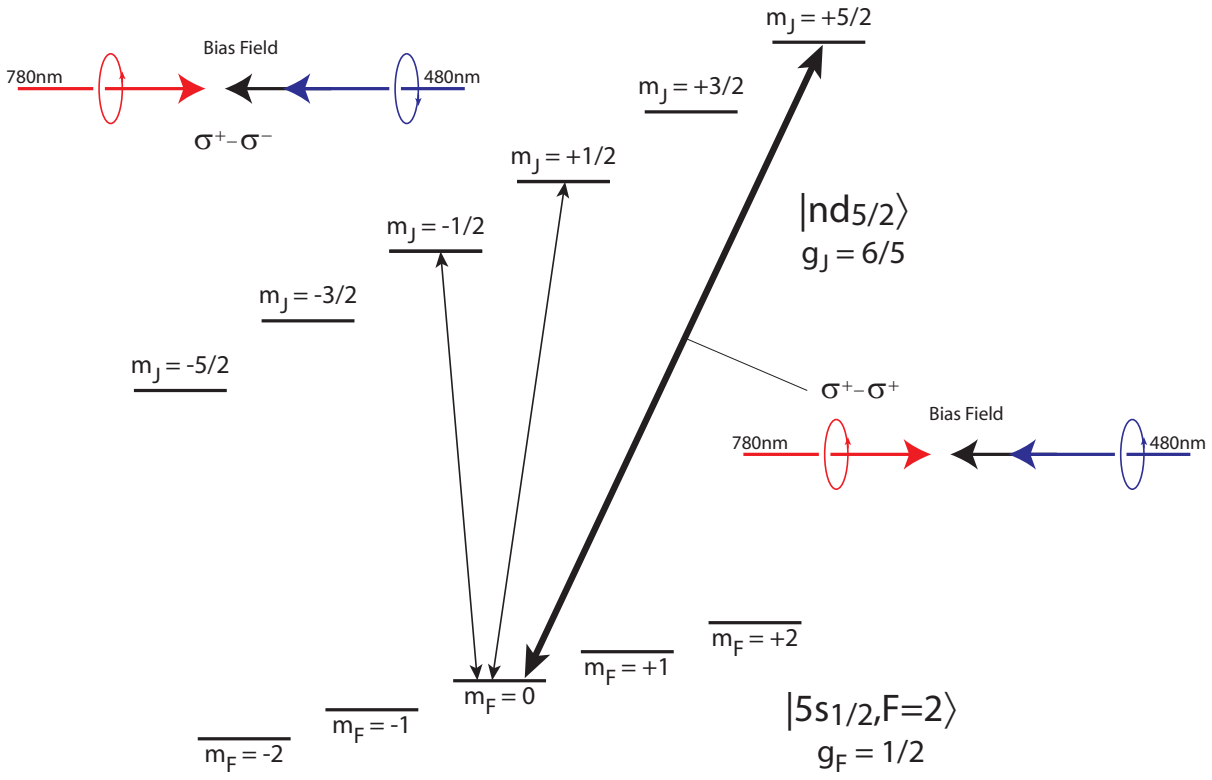

Figure 9.3 This figure illustrates the energy level splitting of the $|5s_{1/2}, F = 2\rangle$ and a generic Rydberg $|nd_{5/2}\rangle$ level. The bold arrow indicates the transition made when driving from the $|5s_{1/2}, F = 2, m_F = 0\rangle$ initialized state with σ^+-σ^+ fields. The narrow arrows represent two possible transitions made by driving the initialized state with a σ^+-σ^- pair of laser beams. The $|5s_{1/2}, F = 2, m_F = 2\rangle \leftrightarrow |97d_{5/2}, m_J = +5/2\rangle$ transition is used to generate a CNOT gate (Chapter 11) while σ^+-σ^- transitions are used to measure the bias field applied to the system (Figure 9.6).

transition (see Section 6.3). High resolution spectroscopy scans are achieved by first estimating the anticipated on resonance Rydberg Rabi frequency. This estimate is used to set the excitation pulse duration, T_R, used in the spectroscopy experiment (see timing Figure 9.1). Figure 9.4 illustrates how this technique is used to identify the resonance condition

for the $|5s_{1/2}, F = 2, m_F = +2\rangle \leftrightarrow |79d_{5/2}, m_J = +1/2\rangle$ transition. A FORT drop of $\sim 8\mu$s and a Rydberg excitation pulse length of $\sim 1\mu$s are used to study this transition. Table 9.2 outlines the beam parameters used to observe this spectrum. The observed resonance is fit with a Gaussian function of the form $B_{offset} - A * e^{-(f-f_0)^2/(2\sigma_f^2)}$, where B_{offset} is the spectrum background level, A is the peak amplitude, f is the modulation frequency applied to the double passed AOM, f_0 is the resonance frequency, and σ_f is the standard deviation in units of the AOM modulation frequency. Plotting the atom retention as a function of the AOM modulation frequency requires us to double the value of the standard deviation when extracting the FWHM of the transition. The FWHM of this transition was fit to be approximately 0.70MHz.

Table 9.1 Two photon rydberg transition parameters for the $|5s_{1/2}, F = 2, m_F = +2\rangle \leftrightarrow |79d_{5/2}, m_J = +1/2\rangle$ transition.

Parameter	Laser 1	Laser 2
λ (nm)	780.25	479.48
Polarization	π	π
Laser frequency: $\omega/2\pi$ (GHz)	384225.7	625250.5
Optical Power (mW)	0.002	26
Intermediate detuning: $\Delta/2\pi$ (GHz)	-2.4	2.4

To examine another transition the 480nm Rydberg laser is merely locked to a higher order longitudinal cavity mode. The resonance condition for the new transition is once again found by sweeping the 780nm Ryberg laser frequency through resonance. Figure 9.2 illustrates how the resonance point of the $|5s_{1/2}, F = 2, m_F = 0\rangle \leftrightarrow |97d_{5/2}, m_J = 5/2\rangle$ transition is calibrated. It should be noted that this transition also requires a different set of polarizations for the addressing laser beams ($\sigma^+ - \sigma^+$). Table 9.2 illustrates the laser detunings and optical powers used to generate this spectrum. The FWHM of the two photon

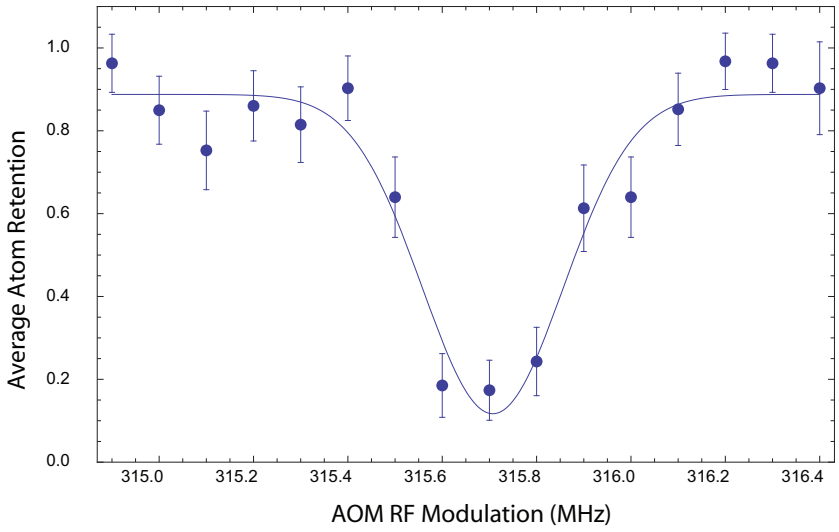

Figure 9.4 Two photon spectroscopy of the $|5s_{1/2}, F = 2, m_F = +2\rangle \leftrightarrow |79d_{5/2}, m_J = +1/2\rangle$ transition. A single excitation pulse of 1μs is used. Atom retention is plotted as a function of the Rydberg 780nm laser's double passed AOM modulation frequency. Data is fit with a functional form of $B_{offset} - A * e^{-(f-f_0)^2/(2{\sigma_f}^2)}$. The transition FWHM is ∼700kHz.

Rydberg transition is approximately 1.26MHz. The FORT is dropped for 7μs to allow for Rydberg excitations.

Two-photon spectroscopy is also used to measure the magnitude of the magnetic bias field applied to the atoms, as shown in Figure 9.6. This measurement is made by setting the polarizations of the driving fields to σ^+ (480nm laser) and σ^- (780nm laser) while driving atoms from the $|F = 2, m_F = 0\rangle$ state. In this particular spectrum the magnetic bias field is applied axially along the FORT laser's propagation direction.

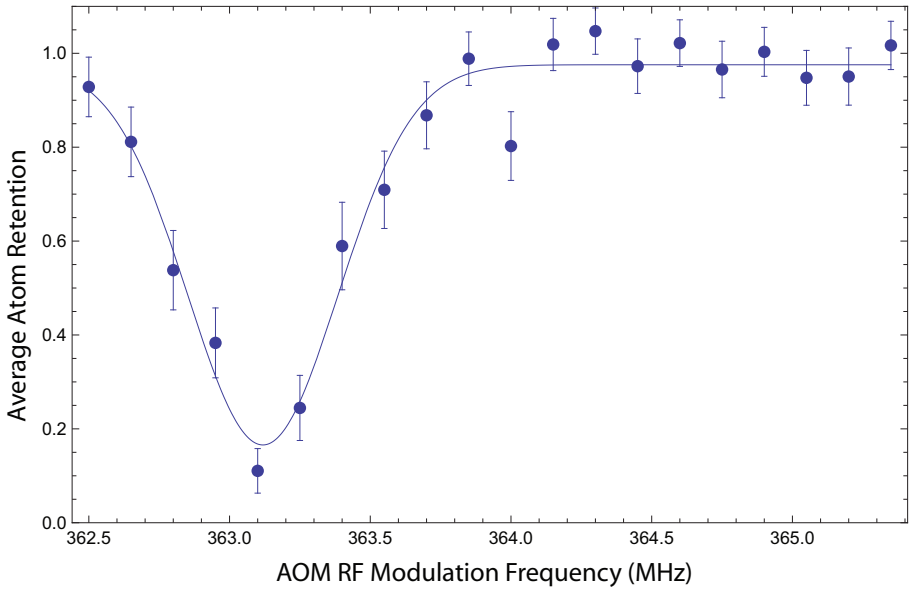

Figure 9.5 Two photon spectroscopy of the $|5s_{1/2}, F = 2, m_F = +2\rangle \leftrightarrow |97d_{5/2}, m_J = +5/2\rangle$ transition. A single excitation pulse of 600ns is used. Atom retention is plotted as a function of the Rydberg 780nm laser′s double passed AOM modulation frequency. Data is fit with a functional form of $B_{offset} - A * e^{-(f-f_0)^2/(2\sigma_f{}^2)}$. The transition FWHM is ∼1.26MHz.

Table 9.2 Two photon rydberg transition parameters for the $|5s_{1/2}, F = 2, m_F = 0\rangle \leftrightarrow |97d_{5/2}, m_J = +5/2\rangle$ transition.

Parameter	Laser 1	Laser 2
λ (nm)	780.25	479.33
Polarization	σ^+	σ^+
Laser frequency: $\omega/2\pi$ (GHz)	384226.2	625435.2
Optical Power (mW)	0.0023	12.2
Intermediate detuning: $\Delta/2\pi$ (GHz)	-1.1	1.1

There are four clearly distinguishable peaks in Figure 9.6 illustrating the dipole allowed Rydberg transitions. These peaks represent the $|F = 2, m_F = 0\rangle \leftrightarrow |97d_{5/2}, m_J = \pm 1/2\rangle$

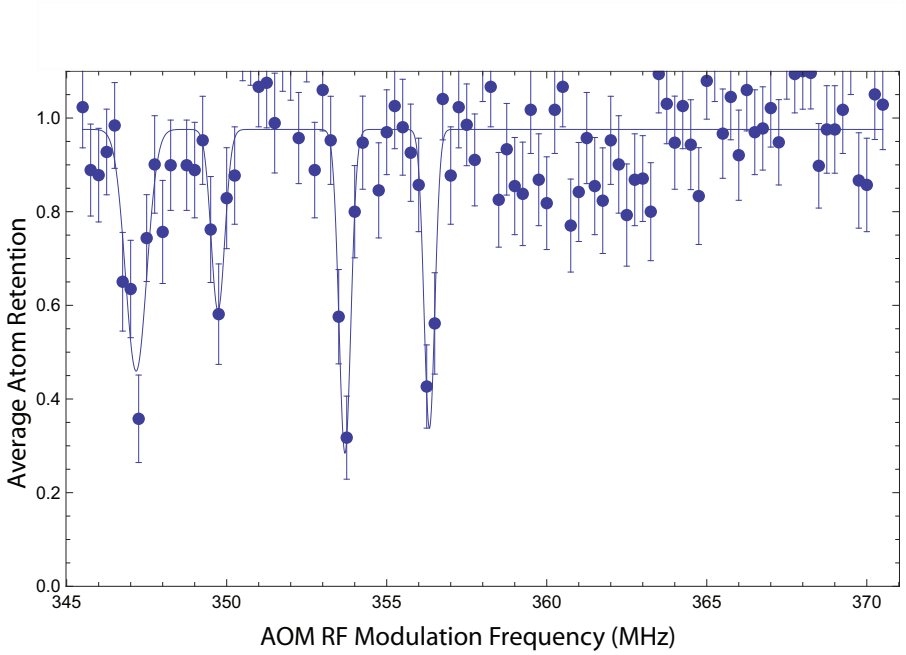

Figure 9.6 Two photon spectroscopy of the $|5s_{1/2}, F = 2, m_F = 0\rangle \leftrightarrow |97d_{5/2}\rangle$ and $|5s_{1/2}, F = 2, m_F = 0\rangle \leftrightarrow |97d_{3/2}\rangle$ transitions used to determine the bias magnetic field strength. The line centers of the four expected transitions are observed at: 347.17, 349.73, 353.69, and 356.33 MHz. The Zeeman splitting corresponds to a bias magnetic field strength of ∼3.6 Gauss.

Table 9.3 Two photon Rydberg excitation parameters for the $|5s_{1/2}, F = 2, m_F = 0\rangle \leftrightarrow |97d_{5/2}\rangle$ and $|5s_{1/2}, F = 2, m_F = 0\rangle \leftrightarrow |97d_{3/2}\rangle$ transitions.

Parameter	Laser 1	Laser 2
λ (nm)	780.25	479.33
Polarization	σ^-	σ^+
Laser frequency: $\omega/2\pi$ (GHz)	384226.2	625435.2
Optical Power (mW)	0.0023	12.2
Intermediate detuning: $\Delta/2\pi$ (GHz)	-1.1	1.1

and $|F = 2, m_F = 0\rangle \leftrightarrow |97d_{3/2}, m_J = \pm 1/2\rangle$ transitions. The spectral data is fit with four

Gaussian distributions to determine the transition line centers. The corresponding frequency separations are used to calculate the bias field strength. Due to fine structure mixing of the $97d_{5/2}$ and the $97d_{3/2}$ states the Zeeman shifts of these levels are not perfectly linear. The observed frequency shifts agree well with a bias magnetic field of 3.6 Gauss. One advantage of performing a bias field measurement through two-photon spectroscopy of the Rydberg levels is that the atomic sample can be initialized into one particular magnetic sublevel. As demonstrated in Section 8.2, measuring the magnetic field strength through two-photon ground state Rabi flopping prohibits the use of optical pumping thus allowing the atomic sample to randomly distribute into the different magnetic sublevels of the F=2 ground state. This randomized initialization drastically limits the amplitude of the observed spectroscopic peaks. The Rydberg magnetic bias field measurement is in good agreement with the two photon ground state spectroscopy data.

9.3 Rabi Flopping Between Ground and Rydberg States

The Rydberg blockade gate requires the ability to reliably transfer a ground state atom into a Rydberg state. Like the ground state Rabi flopping, it is possible to coherently drive a single atom via a two photon Rydberg transition. Upon establishing the parameters necessary to drive the atoms resonantly, it is possible to transfer a single atom to the Rydberg state with very high probabilities. This is demonstrated in Figure 9.7, where the atoms are being driven resonantly between the $|F = 2, m_F = 2\rangle \leftrightarrow |79d_{5/2}, m_J = 1/2\rangle$ states. This experiment uses the same timing protocol shown in Figure 9.1. This experiment, however, measures the atom retention as a function of the Rydberg Rabi pulse duration. Table 9.3 lists the pertinent laser parameters used to generate this two-photon Rydberg Rabi flopping curve. In this experiment the magnetic bias field is oriented orthogonal to the addressing beams, and parallel to the FORT site to site axis. The Rabi flopping curve is fit with an exponentially decaying sinusoidal function to appropriately determine the experimentally observed Rabi flopping frequency.

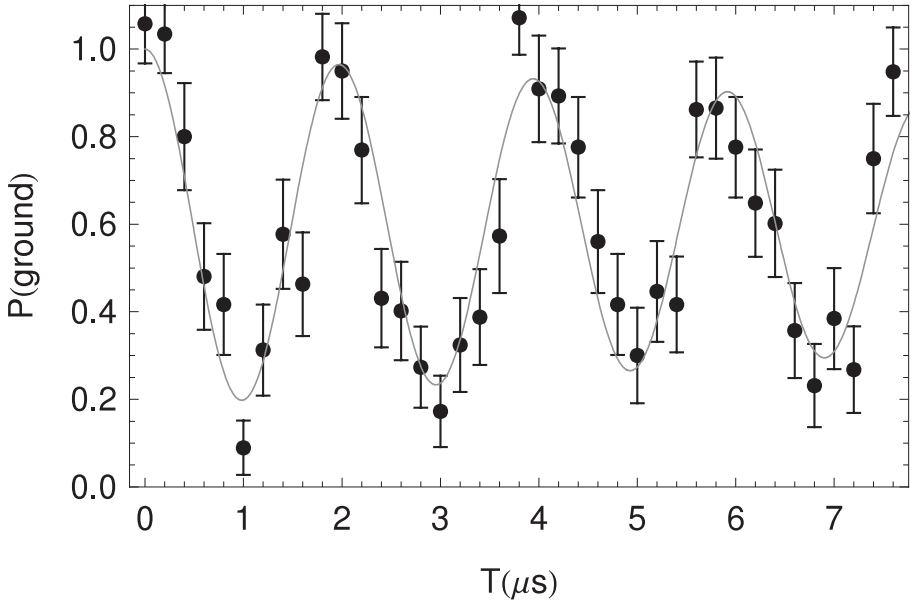

Figure 9.7 Rydberg Rabi Flopping between the $|5s_{1/2}, F = 2, m_F = +2\rangle \leftrightarrow |79d_{5/2}, m_J = +1/2\rangle$ states. Using π polarized laser fields and a magnetic bias field of 11.5 Gauss.

Table 9.4 Two photon Rydberg transition parameters for $|5s_{1/2}, F = 2, m_F = +2\rangle \leftrightarrow |79d_{5/2}, m_J = +1/2\rangle$.

Parameter	Laser 1	Laser 2
λ (nm)	780.25	479.48
Polarization	π	π
Laser frequency: $\omega/2\pi$ (GHz)	384225.7	625250.7
Optical Power (mW)	0.0019	26
Intermediate detuning: $\Delta/2\pi$ (GHz)	-2.4	2.4

The optical potential used to confine the atoms in the previous Rydberg Rabi flopping curve has a maximum depth of approximately 4.0mK. The trap is lowered for approximately 8μs to allow the atoms to be excited to Ryberg levels. The atom temperature is $\sim$0.2mK. This graph is fit with an exponentially decaying sinusoidal function: $P_{Ryd}(t) = 1 - (A -$

$Ae^{-t/\tau_d}\cos(2\pi f't))$. The amplitude, A, is approximately 0.41, while the oscillation frequency, f', is fit to 0.51MHz. The efective two photon Rydberg Rabi frequency, Ω', is thus given by: $\Omega'=2\pi\times 0.51$MHz. The decay constant, τ_d, is $\sim 21\mu$s.

Using the beam waist parameters and optical powers one would expect the efective Rydberg Rabi frequency to be approximately $2\pi\times 0.58$MHz. This matches the measured Rabi flopping frequency to within about 10%. This error can be attributed to small spatial misalignments, and a small fraction of the laser power being present in servo side-bands to lock the lasers to the reference cavity. Due to these small errors, the intensity of the laser beams at the target atoms will be slightly lower than anticipated. Because the peak laser intensity scales like the beam waist squared, a $\sim 20\mu$m axial misalignment of the 780nm addressing laser beam would lower the laser beam intensity by about 20% (see Equation 4.2).

The predicted detection efficiency of about 90% suggests that the amplitude of the Rydberg Rabi flopping should have been closer to 0.45 (see Section 9.1). This varies from the observed amplitude of 0.41 by about 10%. This deviation from ideal can be attributed to imperfect optical pumping ($\sim$5%), and Doppler broadening of the excitation ($\sim$ 5%).

The Rydberg Rabi flopping data can also be utilized to examine crosstalk between the FORT sites. Figure 9.8(a) illustrates the response of an atom to an excitation beam aligned to the adjacent FORT potential. For comparison, Figure 9.8(b) demonstrates the Rydberg Rabi flopping response within the aligned optical potential. The data sets displayed in Figure 9.8 are collected simultaneously. Post processing is used to filter instances when the crosstalk or targeted sites initially contained an atom, thus allowing us to separate the experiment into a Rydberg Rabi flopping measurement and a crosstalk measurement. Filtering the data in this manner eliminates experimental uncertainties due to long term drifts in experimental parameters.

The level of crosstalk observed for Rydberg Rabi flopping is significantly smaller than the ground state Rabi flopping. Like the ground state Rabi flopping, the level of crosstalk is low due to the 10μm spatial separation of the FORT potentials. The AC Stark shift that must be compensated for in the Rydberg transitions are much larger than those from the

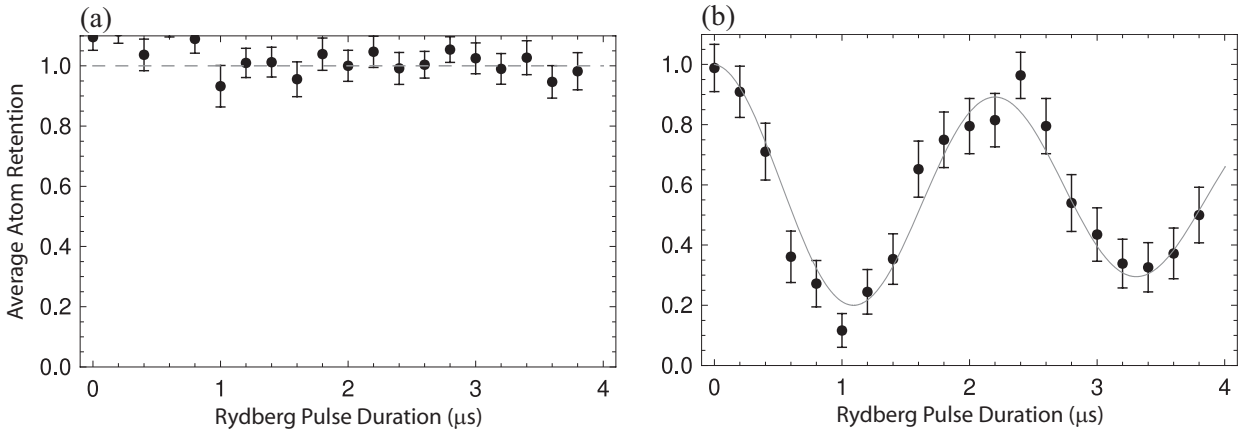

Figure 9.8 Examination of Rydberg Rabi flopping crosstalk while driving the $|5s_{1/2}, F = 2, m_F = +1/2\rangle \leftrightarrow |79d_{5/2}, m_J = +1/2\rangle$ transition. Plot (a) measures the crosstalk, while (b) reports the expected Rydberg Rabi flopping on the targeted site. Both (a) and (b) are extracted from the same trial.

Table 9.5 Two photon Rydberg transition parameters for $|5s_{1/2}, F = 2, m_F = +2\rangle \leftrightarrow |79d_{5/2}, m_J = +1/2\rangle$.

Parameter	Laser 1	Laser 2
λ (nm)	780.25	479.48
Polarization	π	π
Laser frequency: $\omega/2\pi$ (GHz)	384225.7	625250.7
Optical Power (mW)	0.0022	26
Intermediate detuning: $\Delta/2\pi$ (GHz)	-2.4	2.4

ground state Rabi flopping transitions. This difference is primarily due to the intermediate detuning of the Rydberg transitions being much smaller than those used by the ground state transitions.

Using an analysis similar to the one performed in Section 8.3 we can see that the maximum ammount of crosstalk observed is given by:

$$P_{(Cross,Max)} = \frac{C|\Omega_R|^2}{C|\Omega_R|^2 + (\Delta_+ - C\Delta_+)^2} \tag{9.4}$$

Once again the term C represents the reduced laser beam intensities due to spatial misalingment. By merely approximating the values based on the experiment′s conditions, (C$\sim$0.05, $|\Omega_R|\sim 2\pi$ 0.5MHz, $\Delta_+\sim 2\pi$ 3 MHz), we readily see that the maximum population transfer in the neighboring site should be $\sim 1\times 10^{-3}$. To first order this value agrees with our observation. This analysis indicates that the AC Stark shift can be beneficial towards suppressing crosstalk.

Chapter 10

The Rydberg Blockade Effect

10.1 Rydberg Blockade Mechanisms

The atomic radii of Rydberg atoms scale roughly like $\sim n^2$, where n is the principle quantum number of the atom. The outer electron of an atom excited to an energy level of $n > 45$ is typically found more than 100nm from the nucleus. The vastly exaggerated size of these atoms gives rise to a range of interesting properties. The polarizability of a Rydberg atom scales like $\sim n^7$, while the dipole moment scales like $\sim n^2$. The dipole moment of a polarized Rydberg atom can dramatically perturb the energy levels of a neighboring atom, as illustrated in Figure 10.1. These perturbations are large enough to shift an atom out of resonance with the driving field. The electrostatic dipole-dipole interaction between two atoms is given by

$$V_{dd} = \hbar\Delta_{dd} = \frac{1}{4\pi\epsilon_0 R^3}\left[\mu_1 \cdot \mu_2 - 3\left(\frac{(\mu_1 \cdot r_{12})(\mu_2 \cdot r_{12})}{R^2}\right)\right] \tag{10.1}$$

where μ_1 and μ_2 are the dipole moment of atoms 1 and 2, respectively. Also, $\vec{r_{12}} = \mathrm{R}\ \hat{r}_{12}$ is the atomic separation between atoms 1 and 2 [Saffman and Walker, 2005].

In these blockade experiments we attempt to drive multiple atoms into the same Rydberg state simultaneously. The dipole-dipole interaction causes the reaction

$$|n, l, j\rangle + |n, l, j\rangle \rightarrow |n_s, l_s, j_s\rangle + |n_t, l_t, j_t\rangle$$

to ensue. The Rydberg state that we are trying to drive both atoms into are represented by $|n, l, j\rangle$. The states $|n_s, l_s, j_s\rangle$ and $|n_t, l_t, j_t\rangle$ represent Rydberg states whose combined energy

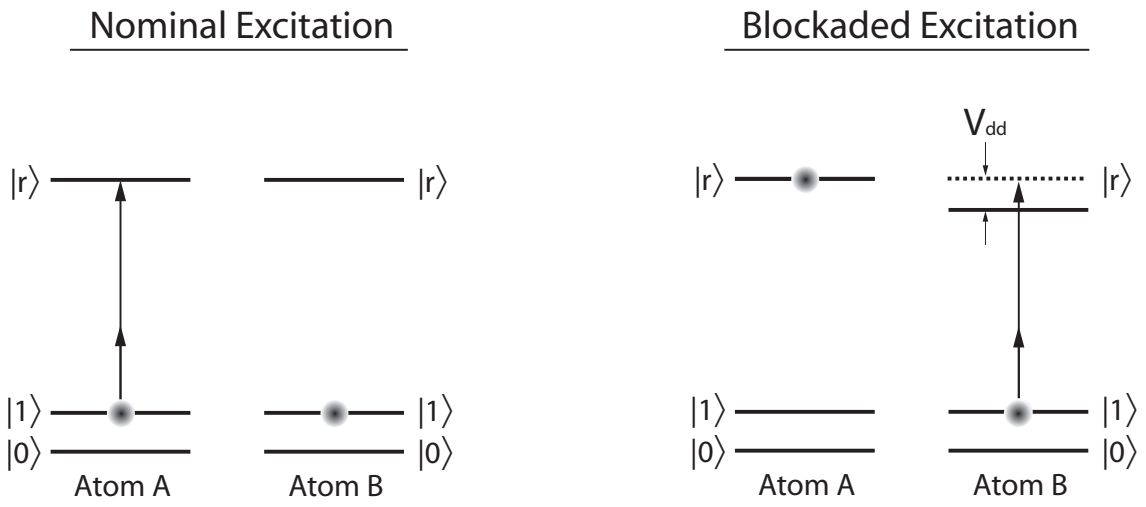

Figure 10.1 Energy level diagram illustrating the Rydberg blockade mechanism. The first atom is driven resonantly to a Rydberg level. The energy level of the second atom is off-resonance and cannot be driven into a Rydberg state by the same driving field.

is nearly degenerate with the two initial Rydberg states. The difference in energy of the reactants and products is called the Förster defect.

$$\delta \;=\; E(|n_t, l_t, j_t\rangle) + E(|n_s, l_s, j_s\rangle) - 2E(|n, l, j\rangle)$$

At large distances the atom-atom interactions will be dominated by van der Waals type interactions that arise from V_{dd} in second order [Walker and Saffman, 2008]. These atom-atom interactions will scale like R^{-6}. For atom-atom separations on the order of $\sim 8\mu$m the van der Waals interaction can become large enough to mix the fine structure levels together. As the dipole-dipole interactions become more comparable to the energy differences between nearby states, these interactions become resonant and follow a R^{-3} scaling [Walker and Saffman, 2008]. The energy shifts of the initial states are determined by the effective second-order perturbation operator of the van der Waals interaction:

$$H_{vdW} = \sum_{s,t} \frac{V_{dd}|s,t\rangle\langle s,t|V_{dd}}{-\delta_{s,t}}$$

The intermediate states $|s,t\rangle$ represent two atom energy levels. The sum is applied over the intermediate states which follow the selection rules of the dipole operator V_{dd}. The odd

parity of the dipole operators μ_1 and μ_2 result in an initial two atom state $|n_1 l_1 j_1 m_1 n_2 l_2 j_2 m_2\rangle$ being mixed with states of $l_1 \pm 1$ and $l_2 \pm 1$ [Walker and Saffman, 2008]. The total projection of the angular momentum along the z-axis is conserved, $M = m_1 + m_2$. However, m_1 and m_2 can change by ± 1 or 0. The principal quantum numbers, n_1 and n_2, and the individual total angular momenta, j_1 and j_2, quantum numbers may also change [Walker and Saffman, 2008]. The Förster defect, $\delta_{s,t}$ is the energy defect of each reaction with respect to the initial two atom Rydberg states.

The effects of these dipole-dipole interactions are measured in localized atomic ensembles and between two well separated single atoms. We begin our study of the Rydberg-Rydberg atom (n=43) interactions upon ensembles of atoms confined to a single optical potential. We then examine n=79 and n=90 Rydberg-Rydberg interactions between atoms confined in separate FORT potentials. The experimental techniques developed in the study of these Förster interactions provide a means of developing a neutral atom CNOT gate.

10.2 Atomic Ensemble Observations of Rydberg Excitation

In this section Rydberg-Rydberg interactions are studied between multiple atoms confined within a single optical potential. Like the Rydberg Rabi flopping experiments (Section 9.3), these interactions are observed by loading multiple atoms into a particular FORT well and driving them with the Rydberg excitation lasers for varying lengths of time. The atomic ensembles used in these experiments are optically pumped into the $|F = 2, m_F = 2\rangle$ state, while a bias field of 11.5 Gauss is applied along the vacuum chamber′s vertical axis. The laser fields are π-polarized relative to this bias field, and set to resonantly drive the atom samples to the $|43d_{5/2}, m_J = +1/2\rangle$ Rydberg level. The 10mK FORT potential is only dropped for 4μs during these trials. Retention of $|F = 2, m_F = 2\rangle$ ground state atoms is recorded as a function of the Rydberg Rabi pulse duration.

When operating with multiple atoms in a FORT potential, the typical method used to measure the number of atoms present before each trial can be problematic. As demonstrated in Section 5.3, multi-atom retention between a first and second camera exposure is typically

lower than 50%. This retention level cannot be used to reasonably renormalize the data. Instead, we measure the average number of atoms in the optical potential during the entire trial by interleaving a calibration cycle with the experiment cycle as shown in Figure 10.2.

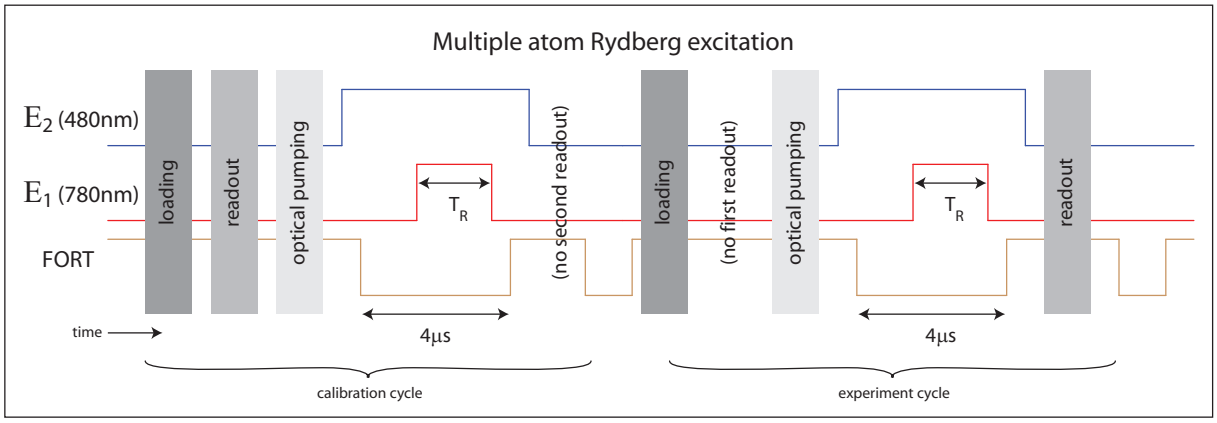

Figure 10.2 Timing protocol implemented while performing Rydberg Rabi flopping upon ensembles of atoms within a single FORT potential. Bias field timings removed for clarity. Note that the FORT is dropped after each half of the cycle to ensure similar FORT loading statistics for the calibration and experiment portions of the experiment.

In each measurement, a calibration readout is used to gather statistics on atom loading. The loading statistics of the experiment and calibration cycles are equivalent. This provides a means of determining the average number of atoms present in each Rydberg Rabi flopping iteration. The probability of retaining an atom for each iteration is calculated by dividing the average experiment cycle signal by the average calibration cycle signal. The average number of atoms loaded during each Rabi flopping curve is calculated by comparing the average calibration signal against the average signal from a single atom.

For consistency a standard single atom Rabi flopping experiment, as outlined in Section 9.3, is performed using two camera readout protocols in a single experiment cycle. The camera readout performed prior to Rydberg excitation is used to ensure a single atom is present for each experiment cycle analyzed. The laser timings shown in Figure 9.1 illustrate the protocol used in this experiment. The single atom response to the Rydberg excitation lasers are shown along side the ensemble Rydberg Rabi flopping curves in Figure 10.2. This

comparison helps to ensures that the ensemble data is being renormalized in a manner consistent with our single atom processing techniques. Both the single and multi-atom plots are once again fit with a decaying sine wave of the form $1 - A + Ae^{-t/\tau_d}\cos(\Omega' t)$.

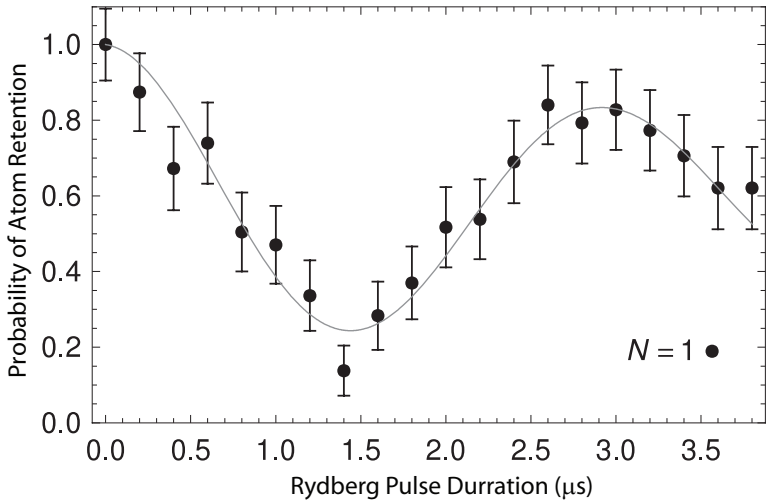

Figure 10.3 Single atom Rydberg Rabi flopping between $|5s_{1/2}, F = 2, m_F = +2\rangle \leftrightarrow |43d_{5/2}, m_J = +1/2\rangle$. The following fit parameters were found: $\Omega'/2\pi = 0.34$MHz, A = 0.4, $\tau_d = 6\mu$s. Table 10.2 reports the laser conditions used to take this data.

Table 10.1 Two photon Rydberg transition parameters for $|5s_{1/2}, F = 2, m_F = +2\rangle \leftrightarrow |43d_{5/2}, m_J = +1/2\rangle$.

Parameter	Laser 1	Laser 2
λ (nm)	780.25	480.51
Polarization	π	π
Laser frequency: $\omega/2\pi$ (GHz)	384224.7	623901.2
Optical Power (mW)	0.0012	9.0
Intermediate detuning: $\Delta/2\pi$ (GHz)	-3.4	3.4

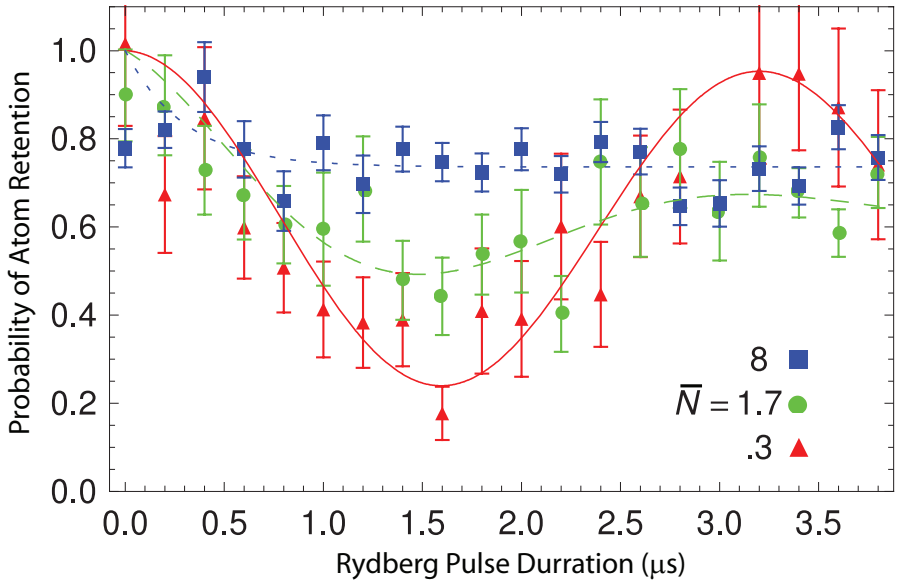

Figure 10.4 Rydberg Rabi flopping curves for ensembles of atoms. $|5s_{1/2}, F = 2, m_F = +2\rangle \leftrightarrow |43d_{5/2}, m_J = +1/2\rangle$ transition. $\bar{N}$ is the average number of atoms loaded into the FORT for each particular data set. The curve fits for $\bar{N}$=0.3 and $\bar{N}$=1.7 give fits for $\Omega'/2\pi$ of 0.31MHz and 0.30MHz respectively. The fits for the amplitudes are 0.39 and 0.37 respectively. Rapid dephasing of the $\bar{N}$=8 prevent oscillations from being observed. Table 10.2 reports the laser conditions used to take this data.

The Rydberg Rabi flopping curve produced by the average atom loading of 0.3 atoms has very similar fit parameters to the Rydberg Rabi flopping curve generated by the single atom signal. In order to attain 0.3 average atoms from the Poissonian loading statistics, described in Section 5.2, we can expect that approximately 74% of the measurements contain 0 atoms, 22% contained 1 atom, while less than 4% of the measurements contained 2 or more atoms. Therefore, the majority of non-zero atom signals observed from the $\bar{N}$=0.3 Rydberg Rabi flopping curve are generated by single atom trials. The zero atom events merely contribute noise to the Rydberg Rabi flopping plot.

From the Rabi flopping curves (Figures 10.3 and 10.4) it is clear that the higher average loading Rydberg Rabi flopping curves result in rapidly dephased signals. The amplitudes and coherence times of the observed signals have clearly degraded. This degradation of the

Rydberg Rabi oscillations can be explained through blockade interactions within the atomic samples. The interaction strength observed in this experiment is the result of an average interaction due to all of the possible spatial orientations of Rydberg atoms within the trap. While indicative of a van der Waals blockade mechanism these experimental parameters do not readily give rise to the implementation of a CNOT gate. Further studies of Rydberg-Rydberg interactions between single atoms are discussed in Section 10.3.

10.3 Rydberg Blockade Between Two Single Atoms

In this experiment we investigate blockade interactions between two distinct atoms localized in separate FORT potentials approximately 10μm from each other. In this configuration the atoms can be individually addressed with little crosstalk between sites, as demonstrated in Section 9.3. In these experiments we are driving the atoms between the $|5s_{1/2}, F = 2, m_F = +2\rangle \leftrightarrow |79d_{5/2}, m_J = +1/2\rangle$ states with π polarized light. This excitation takes place in the presence of an 11.5 gauss field in FORT potentials of approximately 5mK. The single atoms possess $\sim$200μK temperatures. The ability to perform individual atom excitations allows a control atom to be promoted into a Rydberg state with high probability. Through Förster interactions the control atom can be utilized to blockade a neighboring target atom from being promoted into a Rydberg state as well. This blockade effect is illustrated in Figure 10.1.

The experimental protocol used to investigate this effect is outlined in Figure 10.5. The magnetic field and laser beam orientations are outlined in Figure 10.6. This experiment begins by loading both FORT potentials simultaneously, and performing a readout protocol to predetermine how many atoms are present during each trial. We designate the top FORT potential as our control site. To begin the blockade protocol we must first drive the control atom into a Rydberg state using a π-pulse. The addressing lasers are then redirected towards the target atom (bottom FORT-site), and a variable length Rydberg Rabi laser pulse is applied to the atoms. A final laser pulse is used to return the control atom to its original state. The retention of the target atom is then measured as a function of the Rydberg Rabi

excitation pulse. We repeat the entire procedure with the roles of the top and bottom FORT sites reversed to eliminate the possibility of an experimental bias in our procedure. The retention of atoms in the target site after performing this sequence of laser pulses illustrates how often the control atom is blockading the target atom.

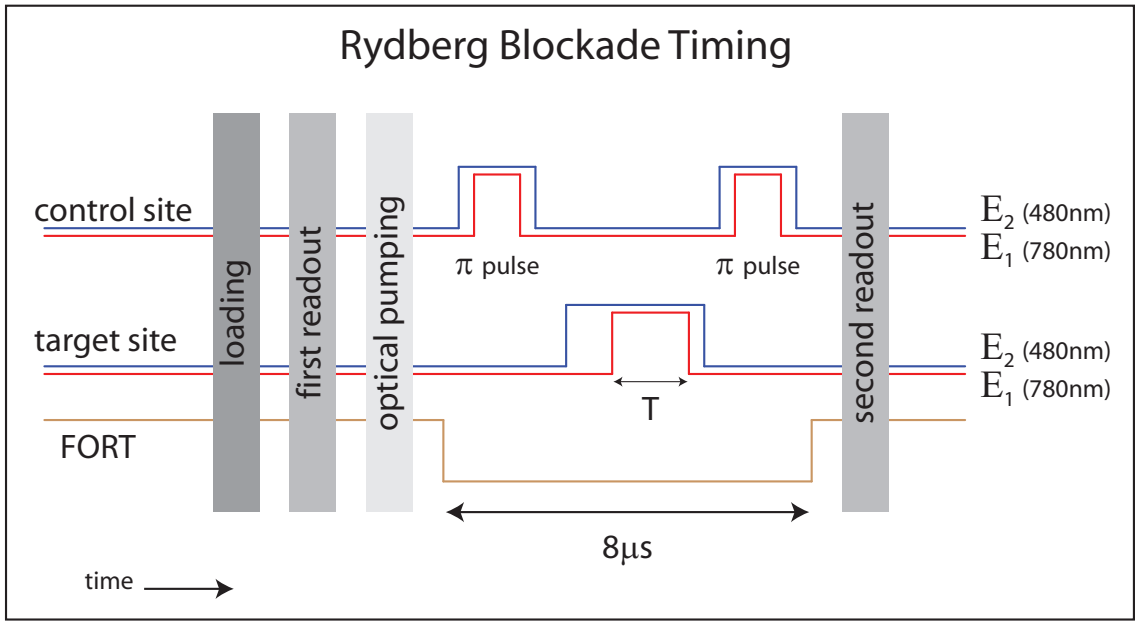

Figure 10.5 Protocol used to detect Rydberg blockade between two atoms.

Because the FORT potentials are being loaded stochastically, it is necessary to post process the data. The first camera readout protocol is used to filter data into two smaller data sets. The first filtering process extracts trials in which the target FORT site contains a single atom, and the control site is vacant. These data points serve as a control experiment where the target atom undergoes Rydberg Rabi flopping (Section 9.3). The second filtering method requires both FORT sites to be simultaneously occupied at the beginning of the experiment. This ensures that a control atom is present during Rydberg excitation, and available to blockade the excitation of the target atom. We further filter this reduced data set to also require the presence of a control atom during the second camera readout protocol. If the control atom is lost prior to when the Rydberg excitation pulse is applied to the target atom, we will not observe blockade. Demanding a control atom to be present before and

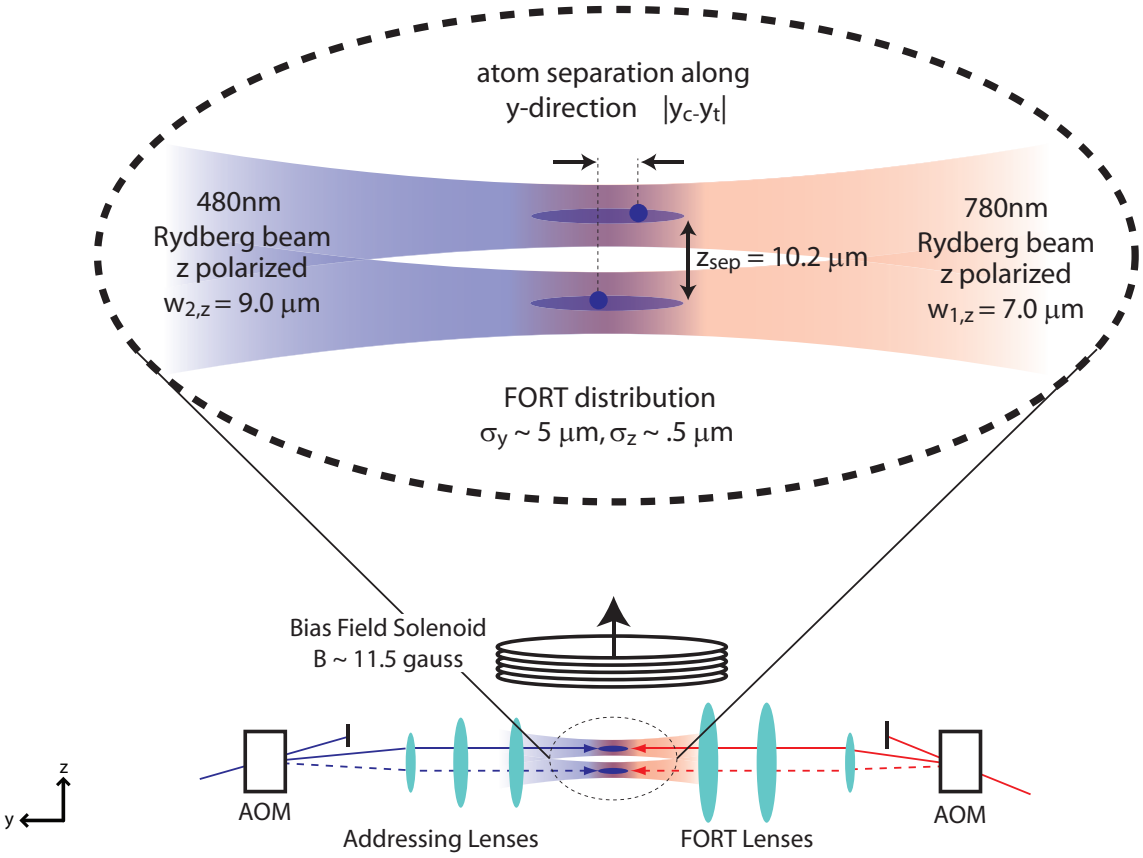

Figure 10.6 This figure outlines the spatial orientation of the FORTs, Rydberg Rabi laser beams, and the bias magnetic field. The FORT and 780nm Rydberg excitation lasers are copropagating. The 480nm laser is aligned to counterpropagate against the 780nm laser. This figure loosely illustrates how specific FORT sites can be individually addressed by the laser beams.

after the experiment protocol eliminates the possibility of the control atom being lost prior to blockading the target atom excitation.

This method of recording all trials and filtering the data set provides a means of simultaneously recording an blockaded Rydberg Rabi flopping experiment (Section 9.3) as well as the blockaded Rydberg Rabi flopping curve. Collecting the control and blockade experiments simultaneously ensure that systematic drifts are not responsible for the observed blockade signal. The roles of the two FORT potentials are then reversed (control site↔ target site)

and the blockade experiment is then repeated. This consistency check eliminates the possibility of a systematic bias. Both sets of the blockaded and non-blockaded Rydberg Rabi flopping curves are shown in Figure 10.7.

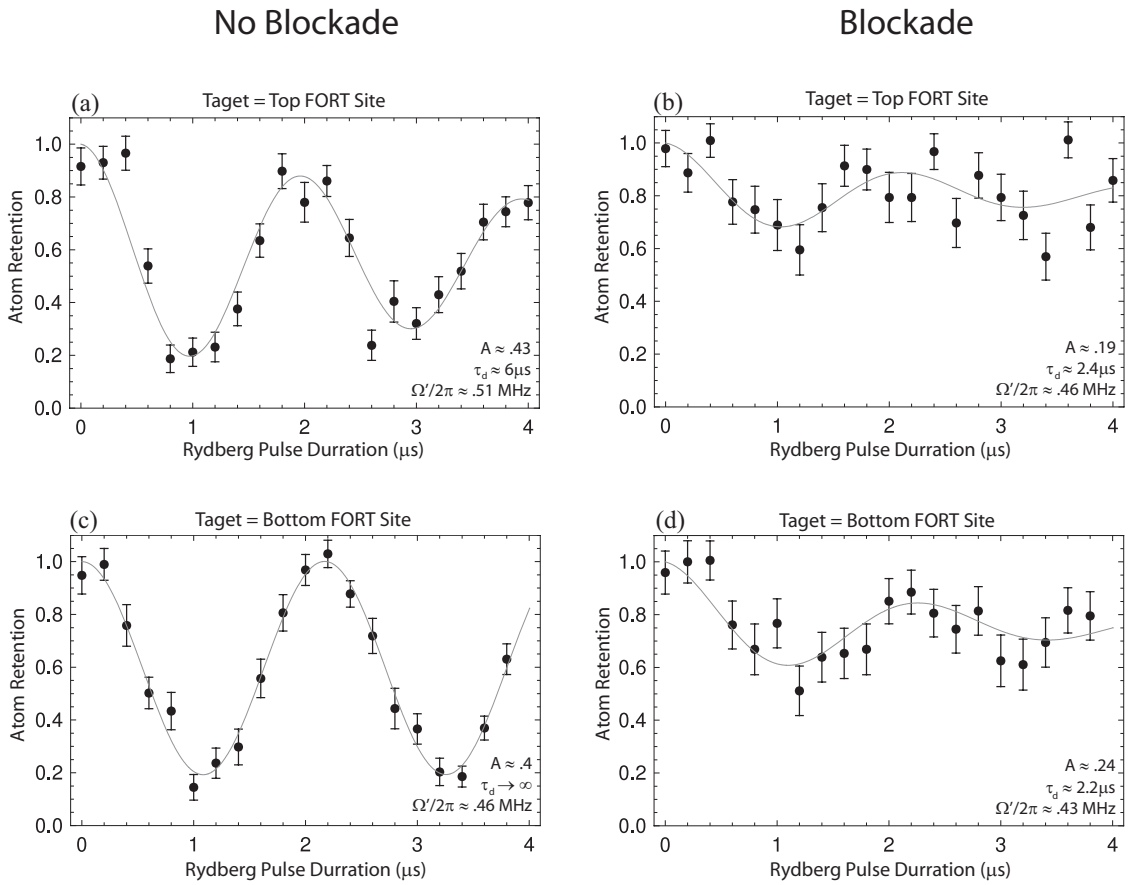

Figure 10.7 Rydberg blockade measurement using the $|5s_{1/2}, F = 2, m_F = +2\rangle \leftrightarrow |79d_{5/2}, m_J = +1/2\rangle$ transition. In plots (a) and (b) the target atom is the top site. In plots (c) and (d) the bottom FORT potential is the target site. Data points from plots (b) and (d) require the presence of an atom in the control site before and after the Rydberg excitation pulses.

Figure 10.7 clearly demonstrates that the presence of an atom in the control site has a definite affect upon the target atom′s response to a Rydberg Rabi excitation pulse. It should be reemphasized that the target and control atoms are separated by $\sim 10\mu$m. The Förster interaction is clearly shifting the atomic energy levels further than the linewidth of the two

Table 10.2 Two photon Rydberg transition parameters for $|5s_{1/2}, F = 2, m_F = +2\rangle \leftrightarrow |79d_{5/2}, m_J = +1/2\rangle$ shown in Figure 10.7.

Parameter	Laser 1	Laser 2
λ (nm)	780.25	479.48
Polarization	π	π
Laser frequency: $\omega/2\pi$ (GHz)	384225.7	625250.7
Optical Power (mW)	0.0022	26
Intermediate detuning: $\Delta/2\pi$ (GHz)	-2.4	2.4

photon Rydberg transition. In Figure 10.7 all four plots are fit with exponentially decaying sinusoidal functions: $1-A+Ae^{-t/\tau_d}\cos(\Omega' t)$. From plots 10.7(a) and 10.7(b) we see that the Rydberg Rabi flopping amplitudes decrease from 0.43 to 0.19 and that the decay constant decrease from about 6μs to 2.4μs. Likewise, between 10.7(c) and 10.7(d), we can observe a decrease in the flopping amplitude from 0.4 to 0.24. The decay time constants once again dramatically decrease.

The strength of the blockade effect must be related to the reduced Rydberg Rabi flopping observed in Figure 10.7. Furthermore, when the shift in the target atom′s energy levels exceeds the linewidth of the laser-atom coupling one can anticipate that the atom will not be driven into a Rydberg state. To properly assess how well the blockade effect is operating within our system, one must try to account for the strength of the Rydberg interactions. In accounting for the long range Rydberg-Rydberg interactions one must consider the coupling between the 79d states with other nearly degenerate two atom states; specifically, 79d+79d $\leftrightarrow$ 80p+78f and 79d+79d $\leftrightarrow$ 81p+77f. The use of a magnetic bias field generates state mixing between the $79d_{5/2}$ and $79d_{3/2}$ manifolds further complicating this calculation. As reported in the supplementary information of [Urban et al., 2009], the interaction strength for our experimental conditions are calculated numerically by considering all 436 two atom fine structure states taken from (79d, 79d), (80p, 78f), and (81p, 77f). The resulting 436x436

Hamiltonian matrix is numerically diagonalized to find the molecular eigenvalues as a function of the two atom separation R. This calculation includes energy offsets calculated from quantum defect data, Zeeman couplings, and the dipole-dipole interaction [Urban et al., 2009].

The probability of observing two simultaneously excited Rydberg atoms, P_2, can be approximated by

$$P_2 \;=\; \sum_{\phi} \frac{\Omega_R^2 |\langle \phi | rr \rangle|^2}{\Omega_R^2 + 2\Delta_\phi^2}$$

where $|\phi\rangle$ is a molecular eigenstate, and $\hbar\Delta_\phi$ is the energy of the molecular state for a particular atom-atom separation and orientation. The term P_2 can be used to parameterize the effective blockade shift, B, as a function of the atom-atom separation via

$$P_2 \;=\; \frac{\Omega_R^2}{\Omega_R^2 + 2B^2}.$$

The individual Rydberg Rabi flopping blockade measurements differ from each other due to the finite atom temperatures. The separation and spatial distribution of the atoms vary for each excitation pulse of the target atom. (see Figure 10.6). As a result the blockade interaction will vary for each trial. The maximum effective blockade interaction occurs when the two atoms are located at the minima of the FORT potentials, separated by 10.2μm in the z dimension and 0μm in the x and y dimensions. The effective blockade shift in the presence of a 11.5 gauss magnetic field with a excitation Rabi frequency of 0.51MHz is calculated to be 3.1MHz, [Urban et al., 2009]. When the control and target atoms are separated in the y-dimension we expect to observe reduced interaction strengths. When the atoms become separated far enough, the shift of the Rydberg energy levels become comparable to the linewidth of the laser driven transition once again enabling the excitation of the target atom. This blockade leakage allows the target atom to oscillate to some extent. The distribution of blockade shifts sampled during each measurement cause the target atoms to oscillate at different rates. This variation of Rabi oscillations results in the rapid decoherence of the blockaded cases (b,d) of Figure 10.7.

Using Monte Carlo simulations based on the random atom distributions within the FORT, and expected Doppler broadening one would expect the average effective blockade shift to be ∼1.1MHz, and predict $P_2 \sim 0.14$, [Urban et al., 2009]. After including additional experimental imperfections, caused by optical pumping, imperfect Rydberg atom detection, and having to renormalize for unavoidable target atom loss, the Monte Carlo simulations predict Rydberg Rabi flopping with an amplitude of 0.19, [Urban et al., 2009]. This agrees well with the experimentally observed values of 0.19 and 0.24 shown in Figure 10.7(b,d). Additional information on these simulations and interaction calculations can be found in [Urban et al., 2009].

It is possible to enhance the degree of the blockade by merely increasing the Rydberg state′s principal quantum number. This blockade measurement is repeated for the $|90d_{5/2}, m_J = 1/2\rangle$ state. A Rydberg Rabi flopping curve, and blockaded Rydberg Rabi flopping curve are shown in Figure 10.8. It is clear that the Rydberg excitations are more thoroughly blockaded for this system. With technical improvements to the experimental apparatus one can expect reductions in the observed blockade leakage.

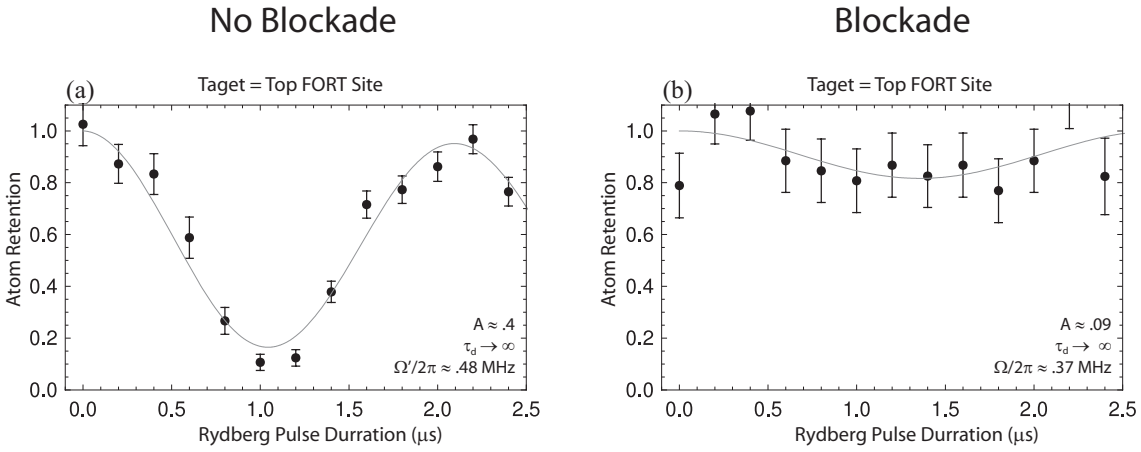

Figure 10.8 Rydberg blockade measurement using the $|5s_{1/2}, F = 2, m_F = +2\rangle \leftrightarrow |90d_{5/2}, m_J = +1/2\rangle$ transition. In plots (a) and (b) the target atom is the top site. Data points from plots (b) require the presence of an atom in the control site before and after the Rydberg excitation pulses.

Table 10.3 Two photon Rydberg transition parameters for $|5s_{1/2}, F = 2, m_F = +2\rangle \leftrightarrow |90d_{5/2}, m_J = +1/2\rangle$ shown in Figure 10.8.

Parameter	Laser 1	Laser 2
λ (nm)	780.25	479.38
Polarization	π	π
Laser frequency: $\omega/2\pi$ (GHz)	384226.72	625376.6
Optical Power (mW)	0.0022	16.5
Intermediate detuning: $\Delta/2\pi$ (GHz)	-1.4	1.4

Chapter 11

The CNOT Gate

The controlled-NOT (CNOT) gate is a logical operation, whose output is dependent upon the state of two input qubits. In quantum computations this operation is unitary. If we consider a control and target qubit, the CNOT operation will flip the state of the target qubit ($|0\rangle \leftrightarrow |1\rangle$) if the control state is in the logical $|1\rangle$ state. A truth table for several input states is shown in Table 11.1.

Table 11.1 Ideal CNOT Gate

Input $\lvert C, T\rangle$	Output $\lvert C, T\rangle$
$\lvert 0, 0\rangle$	$\lvert 0, 0\rangle$
$\lvert 0, 1\rangle$	$\lvert 0, 1\rangle$
$\lvert 1, 0\rangle$	$\lvert 1, 1\rangle$
$\lvert 1, 1\rangle$	$\lvert 1, 0\rangle$

Because the operation is quantum mechanical in nature, linear superposition input states must result in an appropriate superposition of output states. For instance, $\frac{1}{\sqrt{2}}(|0,0\rangle + |1,0\rangle)$ $\rightarrow \frac{1}{\sqrt{2}}(|0,0\rangle + |1,1\rangle)$. This result is significant because a non-entangled superposition input state has been transformed into an entangled Bell state. The input state $\frac{1}{\sqrt{2}}(|0,0\rangle + |1,0\rangle)$ can merely be rewritten as the product of the target state, and a control bit placed in a superposition state, $\frac{1}{\sqrt{2}}(|0\rangle + |1\rangle)|0\rangle$. An entangled state, like the Bell state $\frac{1}{\sqrt{2}}(|0,0\rangle + |1,1\rangle)$,

cannot be rewritten as the product of two individual qubits in superposition states. In this section we demonstrate the ability to create entangled states through the application of an entangling operation.

In Section 10.3 we saw how the excitation of a control atom to a Rydberg state can be utilized to blockade a target atom from making the same transition. This blockade mechanism is the core of our two-qubit entangling operation. Various schemes for entangling qubits through Rydberg mediated dipolar interactions exist. Our entangling protocol relies upon the controlled-phase operation first examined by [Jaksch et al., 2000] in which the dipole interaction is assumed to be much larger than the Rydberg Rabi flopping rate.

In a controlled-phase operation, the control atom can be used to blockade a 2π Rydberg rotation of the target atom. If the target atom shifts out of resonance due to the presence of a Rydberg atom in the control site then nothing happens to the target atom. If the control atom is not in a Rydberg state, then the target atom will be driven through a 2π Rydberg Rabi rotation, and will return to the ground state. During this 2π rotation the atom will accumulate a π phase shift. Therefore, the target atom will accumulate phase depending upon whether or not the control atom is in the appropriate state. This protocol is illustrated in Figure 11.1. Table 11.2 illustrates the phase gate output for different input states.

Table 11.2 Phase gate operation performed upon four different input states. It is assumed that the blockade shift is many times larger than the Rydberg Rabi frequency Ω

Input	Step 1	Step 2	Step 3	Output
$\|C,T\rangle$	π pulse on C	2π pulse on T	π pulse on C	$\|C,T\rangle$
$\|0,0\rangle$	$\|0,0\rangle$	$\|0,0\rangle$	$\|0,0\rangle$	$\|0,0\rangle$
$\|0,1\rangle$	$\|0,0\rangle$	$e^{i\pi}\|0,0\rangle$	$e^{i\pi}\|0,0\rangle$	$-\|0,0\rangle$
$\|1,0\rangle$	$e^{i\pi/2}\|r,0\rangle$	$e^{i\pi/2}\|r,0\rangle$	$e^{i\pi}\|1,0\rangle$	$-\|1,0\rangle$
$\|1,1\rangle$	$e^{i\pi/2}\|r,1\rangle$	$e^{i\pi/2}e^{i\frac{\pi\Omega}{2\Delta}}\|r,1\rangle$	$e^{i\pi}e^{i\frac{\pi\Omega}{2\Delta}}\|1,1\rangle$	$\approx -\|1,1\rangle$

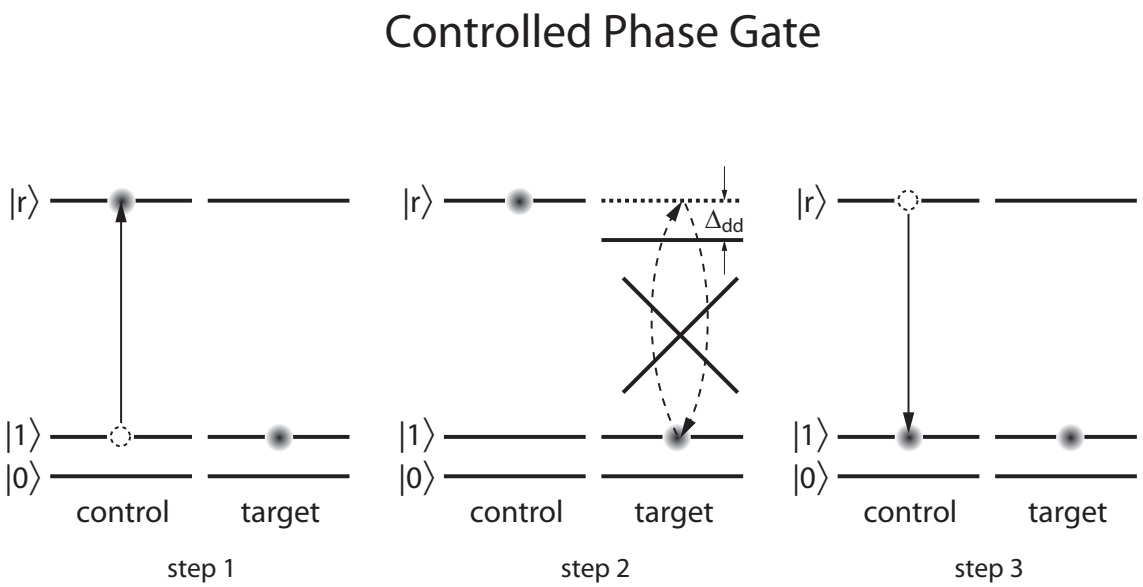

Figure 11.1 Controlled phase gate protocol performed on the $|1,1\rangle$ state. The control atom is excited into the Rydberg state, accumulating a phase shift of $\pi/2$. The control Rydberg atom prevents the target atom from undergoing its 2π rotation via the Rydberg state. The control atom is returned to the $|1\rangle$ state and accumulates another $\pi/2$ phase shift. Therefore, the $|1,1\rangle$ state accumulate a π phase shift.

This controlled phase gate is normally supplemented by additional single qubit operations in order to create the entangling CNOT operator. Our experiment uses a modified version of a CNOT protocol put forth by [Ohlsson et al., 2002]. This modified CNOT protocol still relies upon the controlled-phase operations proposed by [Jaksch et al., 2000]. However, our entangling operation is implemented exclusively with π-pulse operations. A timing diagram in Figure 11.2 illustrates the pulse sequence used in these demonstrations.

The experiment performed to demonstrate this entangling operation begins by loading and initializing two atoms into $|F = 2, m_F = 0\rangle$ ground states through optical pumping. This atomic state will be defined as the logical $|1\rangle$ state. The bias field, 3.6 gauss, was applied by two pairs of shim coils oriented along the FORT laser beam axis. The FORT potential of each optical well is approximately 5.1mK and the atom temperatures are $\sim$200μK. The $|97d_{5/2}, m_J = +5/2\rangle$ Rydberg state is accessed through two photon Rabi flopping using σ^+

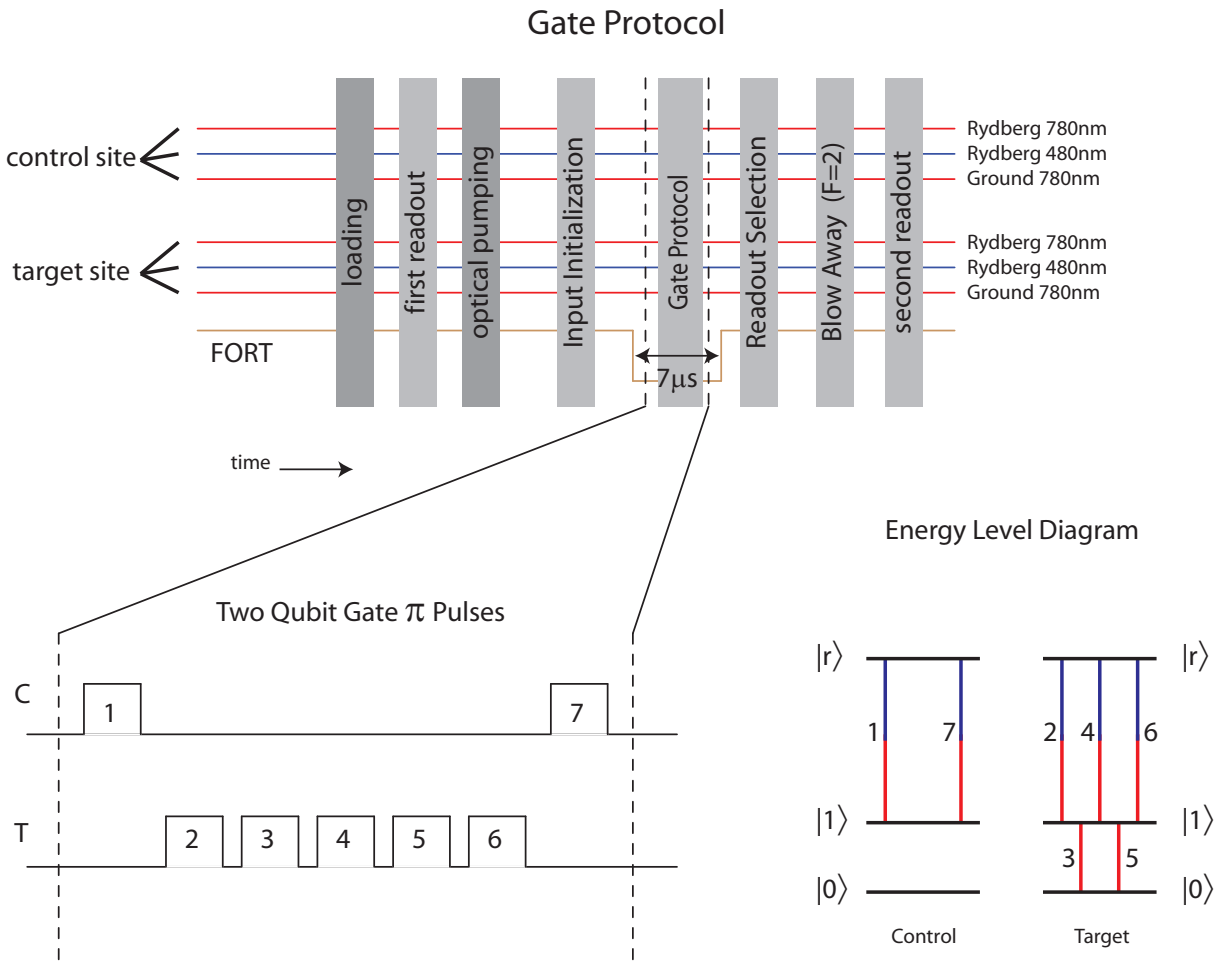

Figure 11.2 Two qubit gate protocol. Typical atom loading, optical pumping, camera readouts, and blowaway sequences are used. Entangling operation performed using both Rydberg and ground state transitions. Pulse durations set to be π pulses. Input initialization and output selection protocols described further in text.

polarized laser beams. The lasers used to drive the ground state transitions are also σ^+ polarized.

From the initialized $|1,1\rangle$ state we prepare one of four input states: $|0,0\rangle$, $|0,1\rangle$, $|1,0\rangle$, or $|1,1\rangle$. This is accomplished by driving the ground state Rabi transitions between the $|1\rangle \leftrightarrow |0\rangle$ transition with π pulses as necessary (Chapter 8). For instance, if one required the state $|1,0\rangle$, then a single π pulse would be applied to the target qubit of the $|1,1\rangle$ state. In this

notation the first qubit is designated the control qubit, while the second qubit is designated the target qubit $|C,T\rangle$.

Upon initializing the qubits into one of four different states the entangling protocol begins. This is accomplished by applying the seven pulse sequence, shown in the bottom of Figure 11.2. These pulses are also indicated in the energy level diagram at the bottom right of Figure 11.2 for clarity. From the pulse sequence it is clear that when the control atom is initialized to the $|0\rangle$ state, the control atom will remain in the same state. The Rydberg π pulses 1 and 7 cannot resonantly excite the atom. If the target atom is in state $|1\rangle$, the atom will be driven into and out of the Ryberg state by pulses 2 and 4 (pulse 3 off resonance). The π pulse number 5 will drive the atom into the $|0\rangle$ state within a phase factor (pulse 6 now off resonance). If the target atom starts in state $|0\rangle$ pulses 2 and 5 have no effect while pulse 3 flips the target atom$'$s logic state, and pulses 4 and 6 drive the atom into the Rydberg state and back to $|1\rangle$ within a phase factor. A truth table stepping through each necessary laser pulse for the four possible input states is shown in Table 11.

Table 11.3 Two qubit gate operation performed upon four different input states. Phase accumulation due to AC Stark shifts have been omitted from the table to emphasize phase accumulation through ground and Rydberg Rabi rotations.

Input $\|C,T\rangle$	Step 1 π_{ryd-C}	Step 2 π_{ryd-T}	Step 3 π_{grnd-T}	Step 4 π_{ryd-T}	Step 5 π_{grnd-T}	Step 6 π_{ryd-T}	Step 7 π_{ryd-C}
$\|0,0\rangle$	$\|0,0\rangle$	$\|0,0\rangle$	$i\|0,1\rangle$	$-\|0,r\rangle$	$-\|0,r\rangle$	$-i\|0,1\rangle$	$-i\|0,1\rangle$
$\|0,1\rangle$	$\|0,1\rangle$	$i\|0,r\rangle$	$i\|0,r\rangle$	$-\|0,1\rangle$	$-i\|0,0\rangle$	$-i\|0,0\rangle$	$-i\|0,0\rangle$
$\|1,0\rangle$	$i\|r,0\rangle$	$i\|r,0\rangle$	$-\|r,1\rangle$	$-\|r,1\rangle$	$-i\|r,0\rangle$	$-i\|r,0\rangle$	$\|1,0\rangle$
$\|1,1\rangle$	$i\|r,1\rangle$	$i\|r,1\rangle$	$-\|r,0\rangle$	$-\|r,0\rangle$	$-i\|r,1\rangle$	$-i\|r,1\rangle$	$\|1,1\rangle$

If the control atom begins in the $|1\rangle$ state we can immediately recognize from pulse 1 that the Rydberg blockade process will be utilized to prevent the target atom from undergoing any Rydberg transitions. Specifically, pulses 2, 4 and 6 will always be off resonant regardless

of the target atom′s initial state. Furthermore, pulses 3 and 5 will flip and then return the target atom to its original logic state. In summary, if the control bit is initialized to the $|1\rangle$ state, the target atom′s logic state will remain the same to within an acquired phase factor.

To measure this operation′s density matrix we measure each of the four possible output states. The state selective readout method, discussed in Section 8.1, ejects atoms in the $|F = 2\rangle$ state. In order to directly measure the probability of qubits in the $|1\rangle$ logic state it is necessary to apply ground state rotations to flip the qubit logic state prior to applying the atom ejection protocol described in 8.1. It is necessary to directly observe all possible output states directly due to the atom loss nominally observed between camera exposures. It is insufficient to merely readout the $|0, 0\rangle$ logic state and assume that absent signal is lost to the three other possible qubit states. Therefore, we arrange ground state Rabi rotations to allow readout of each particular set of qubit states.

For example, we will imagine that the output state for a particular input is given by $|p, q\rangle$. The output state $|p, q\rangle$ is observed first by applying the blowaway and readout protocols, revealing how often state $|p, q\rangle$ corresponds to the logic state $|0, 0\rangle$. The procedure is then repeated with an additional π ground state Rabi rotation applied to the control atom prior to the blowaway procedure. The application of the additional π pulse allows us to observe how often $|p, q\rangle$ corresponds to the state $|1, 0\rangle$. A similar technique is utilized to observe how often the output state corresponds to the $|0, 1\rangle$ and $|1, 1\rangle$ states. All four possible outcomes are directly observed for each of the four possible inputs. The probability outputs are normalized to account for the imperfect atom retention. Single atom retention is of order 85%, Section 5.2. Therefore, the observed two atom probabilities are renormalized by $1/0.85^2$ to compensate for potential atom loss from either site. Recording many trials enables us to reconstruct this two-qubit gate. This is shown in Figure 11.3. The laser beam conditions from these experiments are outlined in 11.

The probabilities of observing particular output states resemble the density matrix of an ideal CNOT gate, but do not show the qubit phases. Whether or not the target state′s output changes is dependent upon the initial state of the control bit. In this probability

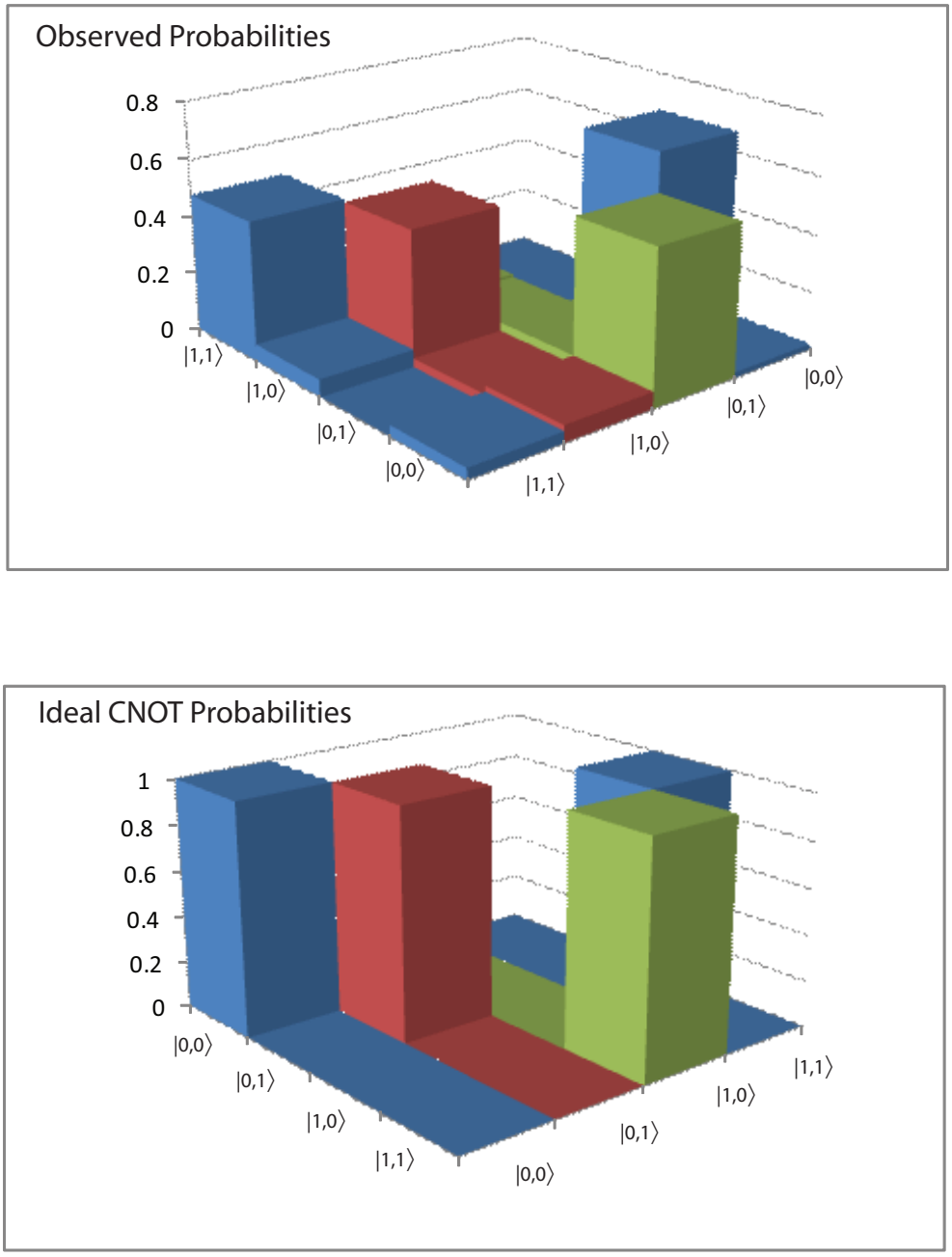

Figure 11.3 Density matrix of the observed output state probabilities. The density matrix of an ideal CNOT gate is shown for comparison. Note that by simply redefining our basis states, the observed entanglement density matrix closely resembles an ideal CNOT gate.

distribution it is clear that the state of the target bit is altered when the control qubit′s initial state is $|0\rangle$.

Table 11.4 Laser beam conditions necessary to enact two qubit gate. Two photon Rydberg transition parameters for the $|5s_{1/2}, F = 2, m_F = 0\rangle \leftrightarrow |97d_{5/2}\rangle$ transition. Ground state Rabi laser drives the $|5s_{1/2}, F = 2, m_F = 0\rangle \leftrightarrow |5s_{1/2}, F = 2, m_F = 0\rangle$ transition.

Parameter	Laser 1	Laser 2	Lasers 3 & 4
Transition	Rydberg	Rydberg	Ground State
λ (nm)	780.25	479.33	780.36
Polarization	σ^+	σ^+	σ^+
Laser frequency: $\omega/2\pi$ (GHz)	384226.2	625435.2	∼384173.5, ∼384167.7
Detuning: $\Delta/2\pi$ (GHz)	-1.1	1.1	∼54.6, ∼60.4
Optical Power (mW)	0.0023	12.2	0.097 (∼0.0485 each)

By merely redefining our logic states, $|F = 1, m_F = 0\rangle \rightarrow |1\rangle$ and $|F = 2, m_F = 0\rangle \rightarrow |0\rangle$, the target qubit′s logic state will now change if the control state is in the $|1\rangle$ state. Therefore, upon redefining the qubit basis states it is possible to compare the measured density matrix with that of an idealized CNOT gate. After redefining the qubit logic states the experiment′s measured probability density is given by:

$$\mathbf{U}_{exp} = \begin{pmatrix} 0.48 & 0.06 & 0 & 0.04 \\ 0.05 & 0.47 & 0.03 & 0.06 \\ 0.04 & 0.03 & 0.06 & 0.53 \\ 0 & 0 & 0.67 & 0.02 \end{pmatrix} \qquad \mathbf{U}_{CNOT} = \begin{pmatrix} 1 & 0 & 0 & 0 \\ 0 & 1 & 0 & 0 \\ 0 & 0 & 0 & 1 \\ 0 & 0 & 1 & 0 \end{pmatrix}$$

The fidelity of the operation, as compared to an ideal CNOT probability matrix, can be defined as $F = \frac{1}{4}Tr(|\mathbf{U}_{CNOT}^T|\mathbf{U}_{exp}) = 0.54$. It should be noted that the ratio of the expected events to the low probability events is of order ∼17 to 1.

Further refinements of the entangling gate are necessary. The gate errors are in part due to imperfect state preparation and readout. The state preparation is examined by looking at an initialization density matrix. This matrix is prepared by measuring the four output

states from each of the four possible input states in the absence of the entangling laser pulses. The bias field and FORT are still modulated. The probability density is shown in Figure 11.4. The deviations observed between the ideal and observed state initializations can be explained by imperfect optical pumping, cross talk between sites, and the use of imperfect π pulses for input initialization and readout selection.

The reduction in gate fidelity, observed in Figure 11.3, might also be attributed to background gas atoms colliding with Rydberg atoms during the gate operation. These elastic collisions can quench the Rydberg atoms thereby inhibiting the gate′s performance. The quenching cross sections are known to scale like the geometrical cross section of the Rydberg atom [Hugon et al., 1983] up to n ∼30. This potential decoherence mechanism is examined by exciting an atom into a Rydberg state waiting several microseconds, and then trying to return the Rydberg atom to its initial state. The atom retention is observed to be dependent upon the delay time between the Rydberg excitation and de-excitation pulses. Through allowing the Rydberg atom a longer amount of time to engage in collisional interactions we enhance the probability of the Rydberg atom being lost. Atom loss is observed to be of order $\sim 10 - 15\%$ with a delay of 5μs.

Despite these difficulties we possess the ability to perform this entangling protocol upon superposition states as well. The timing protocol outline in Figure 11.2 is used once again, however, the ground state initialization pulse on the control qubit is modified such that the atom is placed in a superposition of states by applying a $\pi/2$ pulse. The target atom is merely prepared into the $|0\rangle$ or $|1\rangle$ logic state. In this discussion we are still using the convention $|5s_{1/2}, F = 1, m_F = 0\rangle \leftrightarrow |0\rangle$ and $|5s_{1/2}, F = 2, m_F = 0\rangle \leftrightarrow |1\rangle$.

Once again all four possible output states are measured to determine the probability of observing a particular output. Figure 11.5(a) and 11.5(b) show the results from placing the target atom in the $|0\rangle$ and $|1\rangle$ states respectively. The output states suggest that the entangling operation may have generated a nonseparable superposition state. If we write $\psi_s = |00\rangle + e^{i\phi_s}|11\rangle$ or $\psi_s = |01\rangle + e^{i\phi_s}|10\rangle$, where ϕ_s is a phase angle, the state ψ_s cannot be perfectly rewritten as $\psi = (a_c|0\rangle + b_c|1\rangle)(a_t|0\rangle + b_t|1\rangle)$. A set of amplitudes a_c, b_c, a_t, and

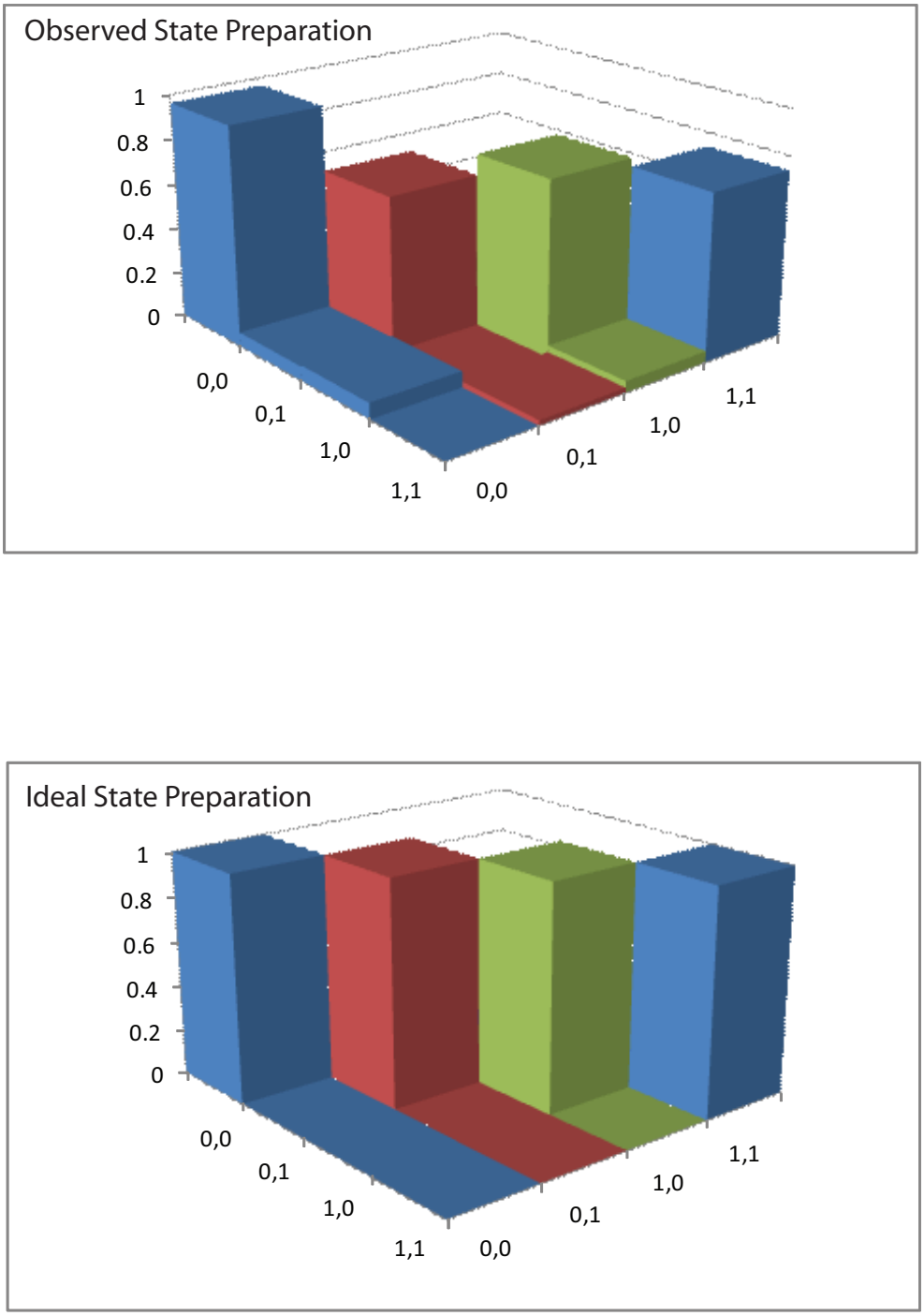

Figure 11.4 Density matrix illustrating the observed input state fidelities. The density matrix of an ideal initialization is shown for comparison.

b_t do not exist to completely describe the observed probability amplitudes from the output states ψ_s. Research to improve upon these results is on going.

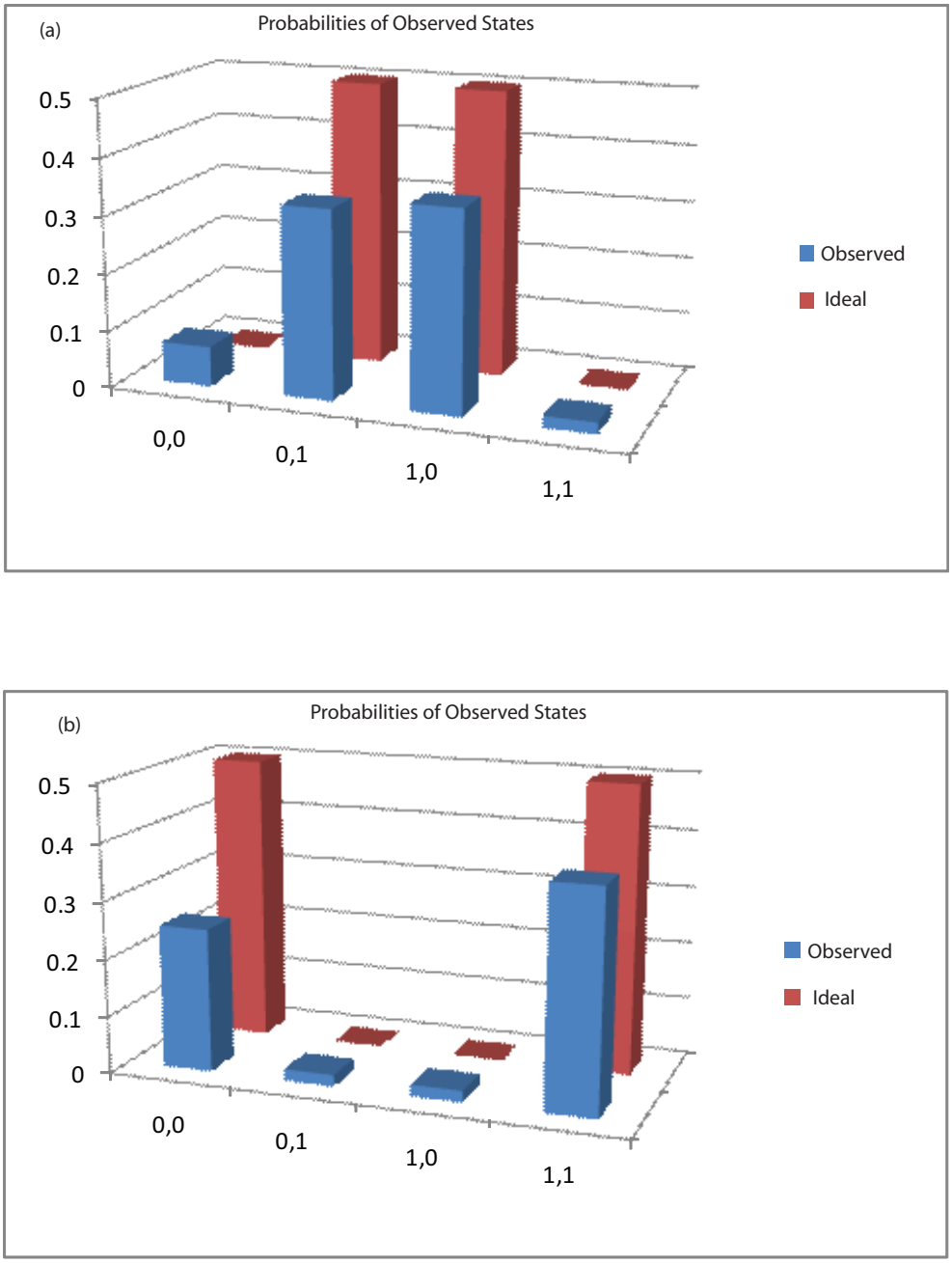

Figure 11.5 CNOT gate performed on input state prepared in a superposition state. To within a global phase factor the input state of (a) is $\frac{1}{\sqrt{2}}(|0,0\rangle + e^{i\phi}|1,0\rangle)$. Likewise, the input state of (b) is $\frac{1}{\sqrt{2}}(|0,1\rangle + e^{i\phi}|1,1\rangle)$. The phase angle, ϕ, is acquired during the state preparation $\pi/2$ pulse upon the control atom. The measurement of the four possible output states for each case reflect that the states are entangled.

Chapter 12

Scalability

The viability of a quantum computing scheme depends upon the system′s scalability. For a real quantum computer to be practical the physical resources necessary must be considered along with the number of operations required to perform the calculation. While the fundamental goal of a quantum computer is to reduce the number of operations or steps necessary to perform a calculation, the resources devoted to making the calculation must also scale proportionally with the complexity of the algorithm. Physical resources incorporate the number of qubits required to perform a calculation as well as the number of fields or elements required to entangle the required qubits. In future work we hope to fully address the issue of scalability associated with loading atoms into the optical potentials. In this chapter preliminary experiments are presented showing progress in utilizing Rydberg blockade to address this issue.

As demonstrated in Section 4.5, a linear scaling exists between the required physical resources necessary to generate the atom trapping sites in our quantum register. Specifically, the amount of laser power required to generate additional optical traps grows linearly with the number of traps necessary. However, we are still limited by stochastic methods of loading atoms into these quantum registers. While it is simple to increase the number of FORT potentials available, it is difficult to simultaneously load a single atom into all of the sites. If we imagine that we possess q FORT potentials, and the probability of loading an atom into a single FORT potential is p, then the probability of simultaneously observing all of the FORT

potentials occupied will scale like p^q. The number of loading cycles required to observe all of the FORT potentials simultaneously occupied scales exponentially with q, unless p = 1.

In order to attain a fully scalable system a deterministic means of loading the FORT must be attained. The generation of a deterministic single atom source is proposed in [Saffman and Walker, 2002]. This proposal outlines a scheme utilizing dipole blockade to excite a single Rydberg atom from an ensemble of atoms confined within a FORT potential. A laser pulse can be used to transfer this Rydberg atom to a different ground state energy level thereby allowing one to eject the remainder of the atomic ensemble. Such a scheme can be used to deterministically load the lattice sites of the FORT potential.

We implement a variation on the procedure outlined by [Saffman and Walker, 2002]. A timing protocol is shown in Figure 12.1. In this experiment, we load multiple atoms into the FORT potentials, and optically pump the ensemble to occupy the $|5s_{1/2}, F = 2, m_F = 0\rangle$ state. The atoms held within the bottom FORT potential are then addressed using a combination of ground state and Rydberg Rabi flopping excitations. The driving fields are set to be resonant and provide π pulses. A Rydberg pulse is used to promote a single atom into the $|90d_{5/2}, m_J = -5/2\rangle$ state. The remaining ground state atoms are then driven, using a two photon Rabi π pulse, into the $|5s_{1/2}, F = 1, m_F = 0\rangle$ state. The Rydberg atom is returned to its original ground state, $|5s_{1/2}, F = 2, m_F = 0\rangle$. The ensemble and single atom are then simultaneously driven using a ground state Rabi π pulse, thereby, flipping their states. The atomic ensemble now occupies the $|F = 2, m_F = 0\rangle$ state while the single atom occupies the $|F = 1, m_F = 0\rangle$ state. Upon applying the blow away protocol, a single atom should remain in the FORT.

Observations from implementing this protocol are shown in Figure 12.2. From the plots in Figure 12.2 it is clear that the combination of Rydberg, ground state, and blow away pulses drastically reduce the probability of observing two atoms within the FORT potential during the second atom readout. The average atom loading observed during the first camera shot is roughly ~ 2.5 atoms. In the bottom FORT site approximately 33% of all trials possess a single atom during the second readout phase. There are virtually no two atom events

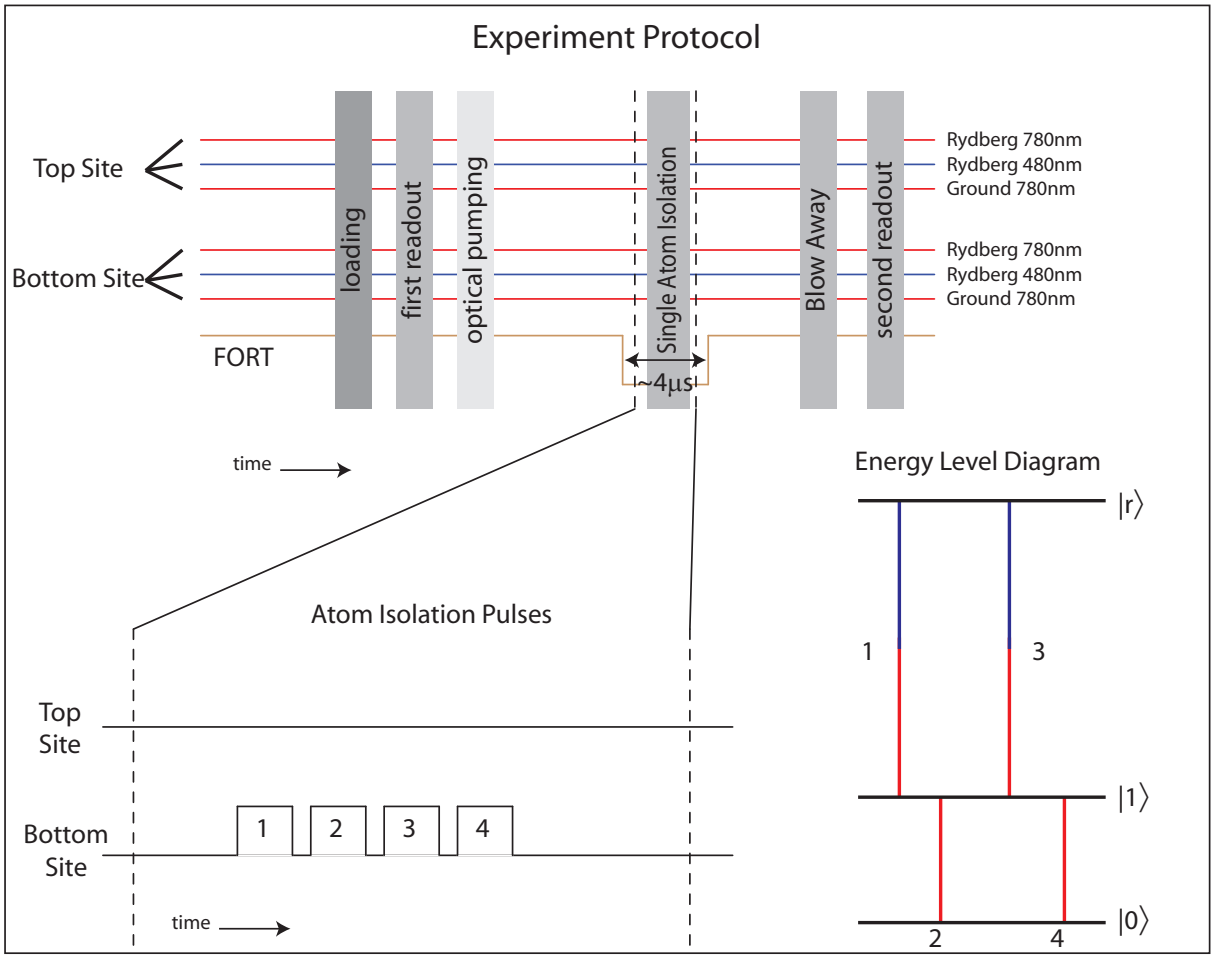

Figure 12.1 Protocol used to try and deterministically load a single atom. Typical atom loading, optical pumping, camera readouts, and blow away sequences are used. Atom isolation protocol relies upon both Rydberg and ground state transitions. Integrated pulse durations set to be π pulses. The initial π pulse is used to drive a single atom into a Rydberg state. The remaining ensemble is then driven with a ground state two photon excitation. The Rydberg atom is returned to the ground state. The ensemble and single atom are both driven with another two-photon ground state Rabi flopping pulse, thus switching their ground states. The blow away pulse removes the F=2 ensemble atoms.

observed during the second readout protocol. In the top FORT site, where the addressing laser beams are absent, only about 3% of the trials contain a single atom signal. It is clear that the pulse sequence provides a means of transferring a single atom into a state that will not be ejected during the blow away pulse.

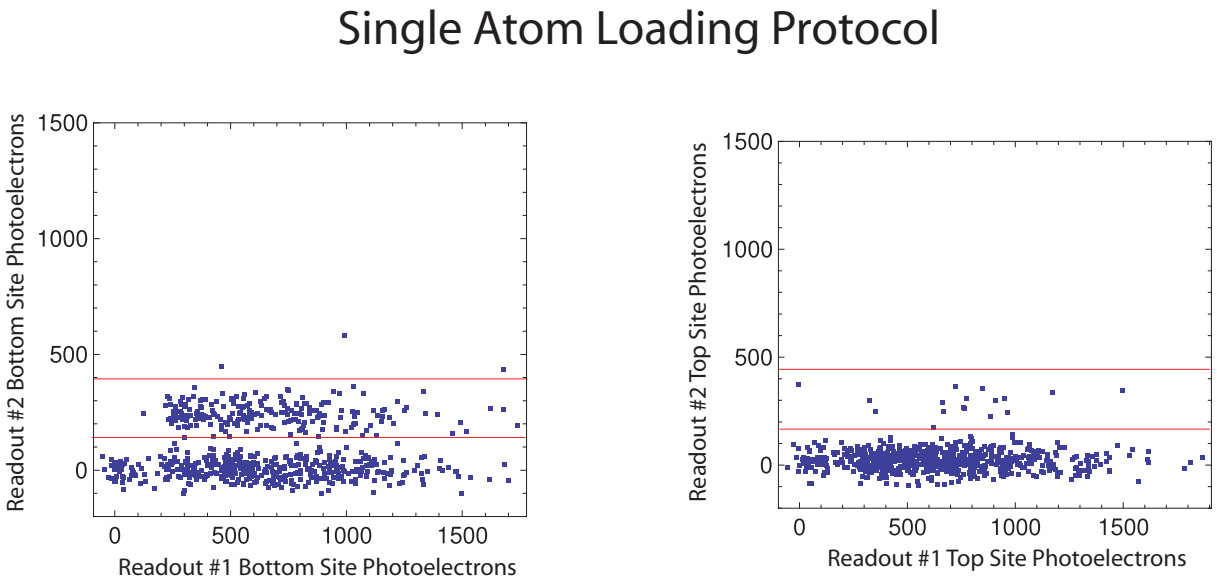

Figure 12.2 These plots show preliminary observations from a single atom loading procedure. The timing protocol illustrated in Figure 12.1 is implemented. The plot on the left represents the observed atom signal of the second readout procedure as a function of the signal observed from the first readout procedure. The graph on the left represents the signal from the bottom FORT site, while the graph on the right illustrates the atom signal from the top FORT site. The lasers are directed at the bottom FORT site during these trials.

Using a simplistic model that presumes ideal blockade between adjacent FORT atoms it is possible to arrive at an order of magnitude estimate of the probability of observing a single atom during the second camera readout. This estimate is obtained by looking at the expected success of each individual π-pulse. The estimates used for the expected success rates of the four π-pulses are based on previous experimental observations. The average atom loading used to obtain the data in Figure 12.2 is $\sim$2.5 atoms. Using Equation 5.3, it is possible to calculate the expected probability of loading a particular number of atoms for each single atom loading trial. The lifetime of the FORT potential limits atom retention between readout protocols to roughly 85%. The optical pumping efficiency used in this experiment is $90-95\%$ efficient (see Sections 3.5 and 8.3). The population transfer observed from a two photon ground state Rabi flopping π-pulse is approximately 95%. As explained

Table 12.1 Laser beam conditions necessary to enact loading protocol. Two photon Rydberg transition parameters for the $|5s_{1/2}, F = 2, m_F = 0\rangle \leftrightarrow |90d_{5/2}, m_J = -5/2\rangle$ transition. Ground state Rabi laser drives the $|5s_{1/2}, F = 2, m_F = 0\rangle \leftrightarrow |5s_{1/2}, F = 2, m_F = 0\rangle$ transition.

Parameter	Laser 1	Laser 2	Lasers 3 & 4
Transition	Rydberg	Rydberg	Ground State
λ (nm)	780.25	479.38	780.35
Polarization	σ^-	σ^-	σ^-
Laser frequency: $\omega/2\pi$ (GHz)	384226.2	625376.2	$\sim$384174., $\sim$384168.2
Detuning: $\Delta/2\pi$ (GHz)	-1.1	1.1	$\sim$54.1, $\sim$59.9
Optical Power (mW)	0.0023	12.2	0.097 ($\sim$0.0485 each)

in Section 8.3 the inefficiency observed in the ground state Rabi flopping is primarily due to imperfections in optical pumping. The population transfer from a two photon Rydberg state Rabi flopping π-pulse is about 80% efficient (see Section 9.3). It should also be noted that the Rydberg atom detection efficiency is expected to only be 90% successful, and also suffers from inefficiencies in optical pumping.

For simplicity this order of magnitude estimate will assumes the blockade efficiency is ideal and that only a single atom is ever excited by the two photon Rydberg excitation π-pulses. In the strong blockade regime and the presence of multiple atoms one expects to see an effective Rabi frequency enhanced by the square root of the number of atoms in the blockade sample [Heidemann et al., 2007]. The duration of a π-pulse is therefore dependent upon the number of atoms in the sample. In this experiment we have set the Rydberg excitation pulse durations equal to a π-pulse for a single atom system. Therefore a single atom in a trial containing k atoms will undergo a $\sqrt{k}\pi$-pulse during steps 1 and 3 of this experiment protocol (see Figure 12.1).

The success rate of navigating a single atom through each step is crudely estimated by multiplying the probabilities of each step being successful. As discussed in Section 9.3 the

population transfer from a Rydberg Rabi pulse is sinusoidal in nature. In the high blockade limit the effective Rydberg Rabi frequency will be proportional to the number of atoms being driven in the FORT. Therefore, the success rate of a π-pulse driving a single atom into the Rydberg state, P_{step1}(k) will be dependent upon k, the number of atoms initially in the FORT. P_{step3} is independent of k, due to the fact that the ground state Rabi flopping π-pulse (step 2) will have transferred virtually all of the ground state atoms into the $|0\rangle$ logic state. The likelihood of initially loading k atoms is given by $\frac{\mathrm{N}^k e^{-\mathrm{N}}}{k!}$. The parameter N is the initial average atom loading of the FORT potential. Each trial can also fail to isolate a single atom due to poor optical pumping and atom losses from the FORT. Concatenating all of these probabilities we arrive at:

$$P(k_{final}=1) \approx (P_{Opt-Pump})(P_{retention})\sum_{k=0}^{\infty}\frac{\mathrm{N}^k e^{-\mathrm{N}}}{k!}(P_{step1}(k))(P_{step2})(P_{step3})(P_{step4})$$

For the particular experimental conditions applied in obtaining the data from figure 12.2, we see that the expected single atom population is given by:

$$\approx (0.95)(0.85)\sum_{k=0}^{\infty}\frac{2.5^k e^{-2.5}}{k!}(0.47-0.47\cos(\sqrt{k}\pi))(\frac{0.95}{0.95})(0.47-0.47\cos(\pi))(\frac{0.95}{0.95})$$

$$\approx 0.31$$

Note that the probability of success of the ground state Rabi flopping π-pulses have been renormalized to factor out errors contributed by optical pumping ($\approx \frac{0.95}{0.95}$). Likewise the Rydberg excitation π-pulse amplitudes, 0.47, have been renormalized to account for inefficiencies in optical pumping and Rydberg atom detection ($\approx \frac{0.8}{0.9\times0.95\times2}$). Based on this simple model and our previous Rabi flopping observations the expected probability of finding a single atom in the trap is approximately 31%. This matches well with the observed 33% single atom loading.

This loading protocol would clearly benefit from shortening the initial Rydberg excitation pulse thereby optimizing the single atom population transfer for atom samples with $k \sim N$. By shortening the initial Rydberg excitation pulse from $\pi \rangle \ \pi/1.7$ one would expect to see roughly 55% of the trials to result in a single atom being loaded in the FORT. The single

atom loading probability can be further enhanced by increasing the initial average atom loading, N, and reoptimizing the initial Rydberg excitation pulse length. Setting N=6 and excitation pulse 1 to $\pi/3.21$ the single atom loading probability increases to about 66%.

It is clear that this loading procedure still requires a great deal of work before completely deterministic atom loading can be achieved. The number of single atom observations made at the end of this specialized loading protocol ($\sim$33%) is comparable to a nominal loading protocol. This loading technique, however, does virtually eliminate multi-atom observations during the second readout protocol. Optimization of this loading protocol, or variants of this protocol have the potential to develop single atom loading.

Chapter 13

Conclusion

The focus of these experiments is to observe and characterize the coherent state manipulation of single atom qubits for the purpose of developing a quantum computer. As part of working towards this goal we have developed the ability to cool and trap $\sim$200μK ^{87}Rb atoms into two $\sim$3.0μm sized FORT potentials separated by 10.2μm. Proof of principle experiments demonstrate the number of FORT potentials can be scaled up in a practical manner. Once trapped in a FORT potential, an atom can be state initialized using optical pumping techniques to either the $|F = 2, m_F = 0\rangle$ or $|F = 2, m_F = +2\rangle$ hyperfine ground states with efficiencies of $\sim$90-95%. The $\sim$3.7μs trap lifetimes allow adequate time to carry out coherent two photon Rabi excitations between single atom detection protocols.

We have performed coherent single atom two photon Rabi flopping experiments between the $|F = 2, m_F = 0\rangle \leftrightarrow |F = 1, m_F = 0\rangle$ states. By defining the qubit logic states $|0\rangle$ and $|1\rangle$ as $|F = 1, m_F = 0\rangle$ and $|F = 2, m_F = 0\rangle$ we can use the Rabi oscillations to manipulate our qubit logic states with fidelities $\sim$95% at megahertz flopping rates. The differential AC Stark shift generated by the $\sim$10μm addressing laser beams is 188kHz. The qubit crosstalk incurred by the $\sim$10μm addressing beams is of order 0.20. Implementing smaller beam waists ($\sim$4.1μm) reduces crosstalk to less than 1.4×10^{-3}. While using these smaller beam waists the exponential decay rate of the two photon Rabi flopping coherence is observed to be 870μs.

Coherent single two photon Rydberg Rabi flopping experiments are performed between ground and Rydberg excited states with principle quantum numbers ranging from 43$\leq$n$\leq$97.

These experiments are the first to observe Rydberg blockade on the single atom level. The blockade effect between two atoms separated by more than 10μm is shown to have reduce Rydberg Rabi oscillations to the $90d_{5/2}$ by $\sim$75%. Preliminary tests on implementing the blockade effect in a two qubit entangling gate are demonstrated. Work towards using the blockade effect to achieve single atom loading is also presented.

These experiments can benefit from more efficient atom loading and state preparation. Generating colder atom samples and improving optical pumping efficiencies will improve the fidelity of both two photon Rabi flopping processes. In the foreseeable future Rabi flopping between the hyperfine ground states will require higher fidelity, faster flopping rates and less crosstalk. As pointed out in the thesis many of these goals are attainable by simply decreasing the addressing beam waists. A viable quantum computer will eventually require error correcting laser pulse sequences to mitigate qubit decoherence. Research in utilizing ground state Rabi flopping pulses for this purpose will become necessary. Rydberg Rabi flopping must also attain higher fidelity population transfers as well as longer decoherence times. Both of these elements can benefit from lower vacuum chamber pressures. Incorporating a more efficient means of Rydberg atom detection can improve characterization of the Rydberg Rabi flopping. These elements can be used to attain higher fidelity entangling gates.

This work demonstrates vast progress towards attaining the five DiVincenzo criteria of a neutral atom quantum computer. The future of this experiment is set on utilizing the coherent state manipulation of neutral atoms for quantum information processing. The need to perform more complicated entangling gates, such as the Toffoli gate is in the foreseeable future. Research on performing rudimentary quantum algorithms, such as the quantum Fourier transform, will also become necessary. In rather general terms, both of these goals require the implementation of more qubits, and the refinement of many of the processes characterized within this thesis. Ultimately, there do not appear to be any fundamental problems preventing the actualization of a neutral atom quantum computer.

Bibliography

Acousto-Optic Product Catalog. Neos Technologies Inc. Product Catalog, (dated 2002).

Andor. Andor-measured specifications accompanying andor camera, (dated may 20, 2004). 2004.

S. Bize, Y. Sortais, M. S. Santos, C. Mandache, A. Clairon, and C. Salomon. High-accuracy measurement of the ^{87}Rb ground-state hyperfine splitting in an atomic fountain. *Europhysics Letters*, 45(5):558–564, 1999.

Gary C. Bjorklund. Frequency-modulation spectroscopy: a new method for measuring weak absorptions and dispersions. *Opt. Lett.*, 5(1):15–17, 1980.

R. A. Boyd, J. L. Bliss, and K. G. Libbrecht. Teaching physics with 670-nm diode lasers-experiments with fabry-perot cavities. *Am. J. Phys.*, 64(9):1109–1115, 1996.

E. Brion, L. H. Pedersen, and K. Mølmer. Adiabatic elimination in a lambda system. *J. Phys. A: Math. Theor.*, 40:1033–1043, 2007.

Steven Chu, J. E. Bjorkholm, A. Ashkin, and A. Cable. Experimental observation of optically trapped atoms. *Phys. Rev. Lett.*, 57(3):314–317, 1986.

David P. DiVincenzo. The physical implementation of quantum computation. *Fortschr. Phys.*, 48(9-11):771–783, 2000.

D. Frese, B. Ueberholz, S. Kuhr, W. Alt, D. Schrader, V. Gomer, and D. Meschede. Single atoms in an optical dipole trap: towards a deterministic source of cold atoms. *Phys. Rev. Lett.*, 85(18):3777–80, 2000.

Thomas F. Gallagher. *Rydberg Atoms*. Cambridge University Press, digitally printed paperback 2005 edition, 1994.

J. L. Hall, L. Hollberg, T. Baer, and H. G. Robinson. Optical heterodyne saturation spectroscopy. *Appl. Phys. Lett.*, 39(9):680–682, 1981.

R. Heidemann, U. Raitzsch, V. Bendkowsky, B. Butscher, R. Löw, L. Santos, and T. Pfau. Evidence for coherent collective rydberg excitation in the strong blockade regime. *Phys. Rev. Lett.*, 99(16):163601, 2007.

M. Hugon, F. Gounand, P.R. Fournier, and J. Berlande. Inelastic collisions between high rydberg (n≈40) and ground-state rubidium atoms at thermal energies. *J. Phys. B: At. Mol. Opt.*, 16(14):2531–2538, 1983.

D. Jaksch, J. I. Cirac, P. Zoller, S. L. Rolston, R. Côté, and M. D. Lukin. Fast quantum gates for neutral atoms. *Phys. Rev. Lett.*, 85(10):2208–2211, Sep 2000.

T. A. Johnson, E. Urban, T. Henage, L. Isenhower, D. D. Yavuz, T. G. Walker, and M. Saffman. Rabi oscillations between ground and rydberg states with dipole-dipole atomic interactions. *Phys. Rev. Lett.*, 100(11):113003, 2008.

Todd A. Johnson. Rabi Oscillations and Excitation Blockade Between Ground and Rydberg States of Single Optically Trapped Rubidium Atoms, "Doctoral Thesis, University of Wisconsin-Madison", 2008.

Changsoon Kim, Caleb Knoernschild, Bin Liu, and Jungsang Kim. Design and characterization of mems micromirrors for ion-trap quantum computation. *IEEE Journal of Selected Topics in Quantum Electronics*, 13(2):322–329, 2007.

Sangtaek Kim, R.R. Mcleod, M. Saffman, and K.H. Wagner. Doppler-free, multiwavelength acousto-optic deflector for two-photon addressing arrays of rb atoms in a quantum information processor. *Applied Optics*, 47(11):1816–1831, 2008.

Caleb Knoernschild, Changsoon Kim, Bin Liu, and Jungsang Kim. Mems-based optical beam steering system for quantum information processing in two-dimensional atomic systems. *Opt. Lett.*, 33(3):273–275, 2008.

S.J.M. Kuppens, K.L. Corwin, K.W. Miller, T.E. Chupp, and C.E. Wieman. Loading an optical dipole trap. *Phys. Rev. A*, 62(1):013406/1–13, 2000.

Wenhui Li, I. Mourachko, M. W. Noel, and T. F. Gallagher. Millimeter-wave spectroscopy of cold rb rydberg atoms in a magneto-optical trap: Quantum defects of the ns, np, and nd series. *Phys. Rev. A*, 67(5):052502, May 2003.

D. A. Lidar, I. L. Chuang, and K. B. Whaley. Decoherence-free subspaces for quantum computation. *Phys. Rev. Lett.*, 81(12):2594–2597, 1998.

Michael G. Littman and Harold J. Metcalf. Spectrally narrow pulsed dye laser without beam expander. *Phys. Rev. Lett.*, 17(14):2224–2227, 1978.

M. D. Lukin, M. Fleischhauer, R. Cote, L. M. Duan, D. Jaksch, J. I. Cirac, and P. Zoller. Dipole blockade and quantum information processing in mesoscopic atomic ensembles. *Phys. Rev. Lett.*, 87(3):037901, Jun 2001.

Kurt W. Miller, Stephan Drr, and Carl E. Wieman. rf-induced sisyphus cooling in an optical dipole trap. *Phys. Rev. A*, 66(2):023406–8, 2002.

Michael A. Nielsen and Isaac L. Chuang. *Quantum Computation and Quantum Information*. Cambridge University Press, 2000.

N. Ohlsson, R.K. Mohan, and S. Kroll. Quantum computer hardware based on rare-earth-ion-doped inorganic crystals. *Opt. Commun.*, 201:71–77, 2002.

Line Hjortshøj Pedersen. Neutral Atom Quantum Computing with Rydberg Blockade, Department of Physics and Astronomy, University of Aarhus, 2006.

Daryl W. Preston. Doppler-free saturated absorption: Laser spectroscopy. *Am. J. Phys.*, 64 (11):1432–1436, 1996.

E. L. Raab, M. Prentiss, Alex Cable, Steven Chu, and D. E. Pritchard. Trapping of neutral sodium atoms with radiation pressure. *Phys. Rev. Lett.*, 59(23):2631–2634, 1987.

Worawarong Rakreungdet, Jae Hoon Lee, Kim Fook Lee, Brian E. Mischuck, Enrique Montano, and Poul S. Jessen. Accurate microwave control and real-time diagnostics of neutral atom qubits, 2008. arXiv:0811.3634v1[quant-ph].

Georges Reymond, Nicolas Schlosser, Igor Protsenko, and Philippe Grangier. Single-atom manipulations in a microscopic dipole trap. *Phil. Trans. R. Soc. Lond. A*, 361(1808): 1527–1536, 2003.

M. Saffman and T. G. Walker. Creating single-atom and single-photon sources from entangled atomic ensembles. *Phys. Rev. A*, 66(6):065403, Dec 2002.

M. Saffman and T. G. Walker. Analysis of a quantum logic device based on dipole-dipole interactions of optically trapped rydberg atoms. *Phys. Rev. A*, 72(2):022347, 2005.

Peter W. Shor. Polynomial-time algorithms for prime factorization and discrete logarithms on a quantum computer, 1996. arXiv:quant-ph/9508027v2.

Daniel A. Steck. Rubidium 87 D Line Data. Available online at http://steck.us/alkalidata (revision 2.1.1, 30 April 2009).

E. Urban, T. A. Johnson, T. Henage, L. Isenhower, D. D. Yavuz, T. G. Walker, and M. Saffman. Observation of rydberg blockade between two atoms. *Nat. Phys.*, 5(1): 110–114, 2009.

Thad G. Walker and Mark Saffman. Consequences of zeeman degeneracy for the van der waals blockade between rydberg atoms. *Phys. Rev. A*, 77(3):032723, 2008.

Carl Wieman, Gwenn Flowers, and Sarah Gilbert. Inexpensive laser cooling and trapping experiment for undergraduate laboratories. *Am. J. Phys.*, 63(4):317–330, 1995.

Amnon Yariv and Pochi Yeh. *Optical Waves in Crystals*. John Wiley and Sons, Inc., 1984.

D. D. Yavuz, P. B. Kulatunga, E. Urban, T. A. Johnson, N. Proite, T. Henage, T. G. Walker, and M. Saffman. Fast ground state manipulation of neutral atoms in microscopic optical traps. *Phys. Rev. Lett.*, 96(6):063001, 2006.

I.T. Young, R. Zagers, L.J. van Vliet, J. Mullikin, F. Boddeke, and H. Netten. Depth-of-focus in microscopy, 1993. SCIA'93, Proc. of the 8th Scandinavian Conference on Image Analysis (Tromso, Norway, May 25-28), NOBIM, Norwegian Society for Image Processing and Pattern Recognition, Tromso, Norway.

DISCARD THIS PAGE

Appendix A: Photon Counting Optics

A.1 EMCCD Spatial Calibration

The camera system is calibrated using a negative USAF test pattern (NT38-256) from Edmund Optics. The test pattern consists of sets of horizontal and vertically aligned bars of varying sizes. These sets of bars are broken into groups, and each group consists of six elements. One element possesses a set of 3 vertically aligned bars and 3 horizontally aligned bars. The period, T, in line pairs per millimeter for a particular element is ideally given by the equation: $T = 2 * 2^{-(Group+(Element-1)/6)}$.

A large collimated 780nm laser beam is used to back illuminate the USAF test pattern. The test pattern is aligned to the camera system using a LineTool Co. model NRH three axis translator. This translator has higher precession than the translation stages of the camera system. As indicated in Figure $A.1$, 2 periods of element G3E3 spanned ≈93 pixels. G3E3 has a spatial frequency of 10.1 cycles/mm. A quick first order estimate of the effective EMCCD pixel size is 2.13μm. The factory specified pixel sizes of the Andor Ixon DU-860 EMCCD is 24x24μm. The ratio of the camera pixel size to the effective pixel size indicates the magnification of the system is approximately 11.3.

One method to account for the blurring of our camera system is to characterize the optical system′s inherent point spread function (PSF). If one were to image an infinitesimal point source of light with an ideal lens, the collected light would refocus into a blurred distribution. The lack of barrel or pincushion aberration in Figure A.1 allows us to assume the PSF is shift invariant. Therefore, the resulting camera image is simply a magnified convolution of the PSF with the object plane of our imaging system. Mathematically, we may represent the object plane as a superposition of impulses, or delta functions.

$$O(x_o, y_o) = \int\int O(p, q)\delta(x_o - p, y_o - q)dudv$$

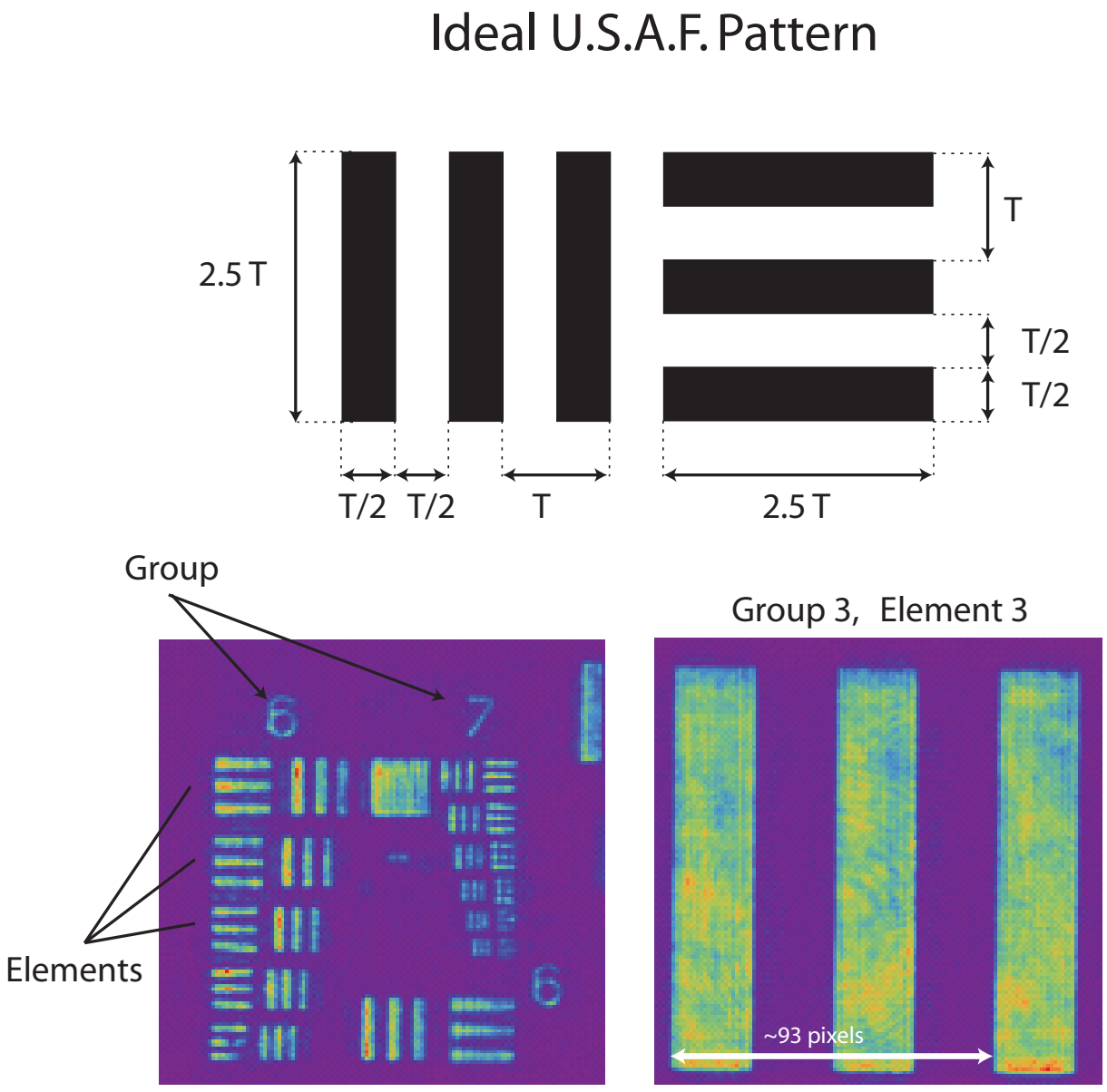

Figure A.1 Ideal USAF chart pattern. The repetitive pattern is laid out in Groups and Elements. Actual images taken using the EMCCD are shown below. The line spacings from Group 3 Element 3 (G3E3) are used to calibrate the device. The white line superimposed over the image indicates roughly 93 EMCCD pixels.

where x_o and y_o are the coordinates in the object plane. The corresponding magnified image is expressed mathematically as:

$$I(x_i, y_i) = \int\int O(p, q)PSF(x_i - Mp, y_i - Mq)dudv.$$

PSF(x_i-Mp,y_i-Mq) is the image resulting from a single impulse, or delta function, located at coordinates (p,q). This blurring effect was first investigated by imaging the output of a single mode optical fiber. The full width at half maximum (FWHM) of the convolved intensity distribution was approximately 2 pixels, or roughly 4.3μm. The variance of this distribution would be about FWHM/$2\sqrt{2ln(2)}$= 1.8μm. This merely gives an approximation of the PSF due to the fact that the fiber tip is not a perfect point source relative to the effective size of the EMCCD pixels.

The PSF is further characterized by deconvolving line profiles from the USAF chart image. A step function is used to model a single dimension of an ideal USAF element, with period T, while the PSF is approximated by a Gaussian intensity profile of functional form:

$$PSF(x) = \frac{1}{\sqrt{2\pi}\sigma_{optics}} e^{-x^2/2w_{optics}^2}.$$

The ideal convolution function uses error functions (Erf) to model the line profiles:

$$I(x) = \frac{A}{2}\Bigg(-Erf[\tfrac{4s-5T-4x}{4\sqrt{2}\sigma_{optics}}] + Erf[\tfrac{4s-3T-4x}{4\sqrt{2}\sigma_{optics}}] - Erf[\tfrac{4s-T-4x}{4\sqrt{2}\sigma_{optics}}] - Erf[\tfrac{4s+3T-4x}{4\sqrt{2}\sigma_{optics}}] + Erf[\tfrac{4s+5T-4x}{4\sqrt{2}\sigma_{optics}}] + Erf[\tfrac{4s+T-4x}{4\sqrt{2}\sigma_{optics}}])\Bigg) + B.$$

In this equation T is the period of the ideal USAF element, s accounts for translational shifts of the USAF target within the image plane, σ_{optics} is the variance of the PSF, A is the intensity of the ideal modulated signal, and B accounts for a non-zero background intensity. The idealized and convolved functions are illustrated in Figure A.2.

The image of the U.S.A.F. chart G3E3 that is used to calibrate the magnification of the camera system is also used to determine the PSF of the optics. The line profile displayed is acquired by averaging the signal from 75 pixel rows near the center of the USAF image (see Figure A.3). Mathematica is used to determine the best fit of I(x) for the line profile. The free parameters (T, σ_{optics}, A, s, B) indicate an effective pixel size of 2.15μm and a PSF variance of approximately 1.5$\pm$0.1μm. This is in good agreement with the variance used to approximate the atom temperatures in [Urban et al., 2009] and roughly agrees with the fiber tip observations.

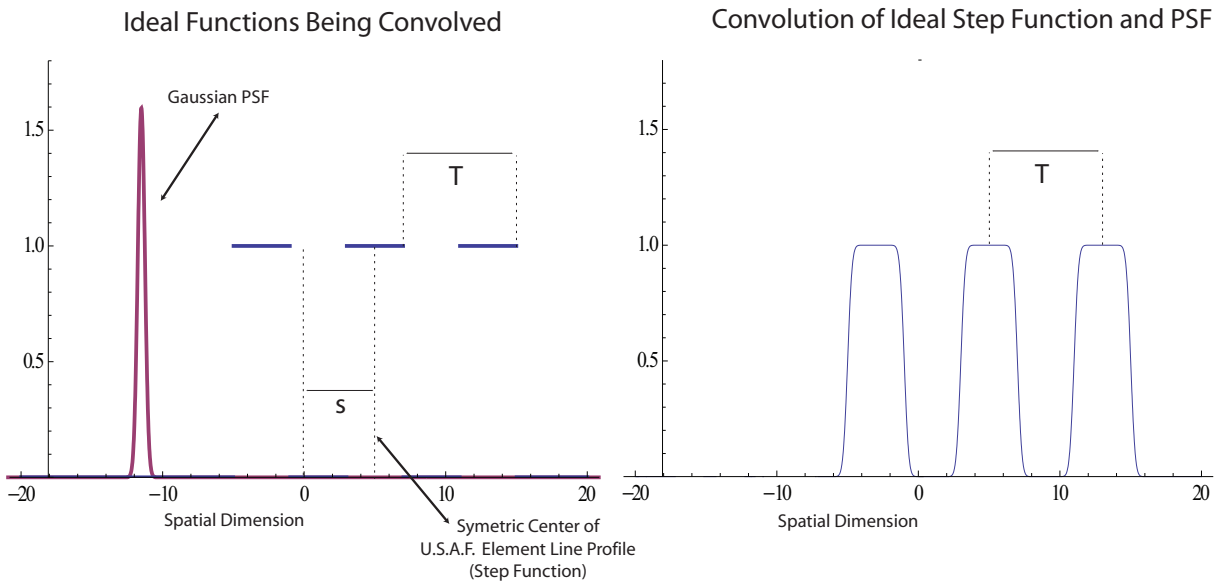

Figure A.2 Idealized line profiles of U.S.A.F. element, PSF and the resulting convolution of the two functions. The period of the U.S.A.F. element is labeled T. The standard deviation of the PSF is defined as σ_{optics}. The relative magnitude of the PSF is normalized such that an integral over the PSF is equal to unity. The relative amplitude of the convolved function is slightly less than 1.0.

A.2 EMCCD Alignment Hardware

The EMCCD camera system is assembled as a single unit, thus enabling us to characterize the camera′s performance prior to aligning the unit to the chamber. The custom triplet lenses are mounted into a custom aluminum cage system. This cage is then mounted to a 1″ thick aluminum base plate. The relay lenses, iris, and optical filters are mounted directly to the EMCCD camera. The EMCCD camera is then mounted to a sliding base plate (camera carriage) which is connected to the same aluminum base plate used to mount the custom optical elements. This large base plate rests upon a second 1″ base plate. The two plates meet at three points of contact. The contact points are large high load bearing micrometers (1 × Newport BM30.10, 2 × Newport BM25.40). The separation, pitch, and roll of the plates can be controlled much like a mirror mount. The lower base plate is mounted to two sets of orthogonally mounted large Newport UMR 12.40 precision linear translation stages.

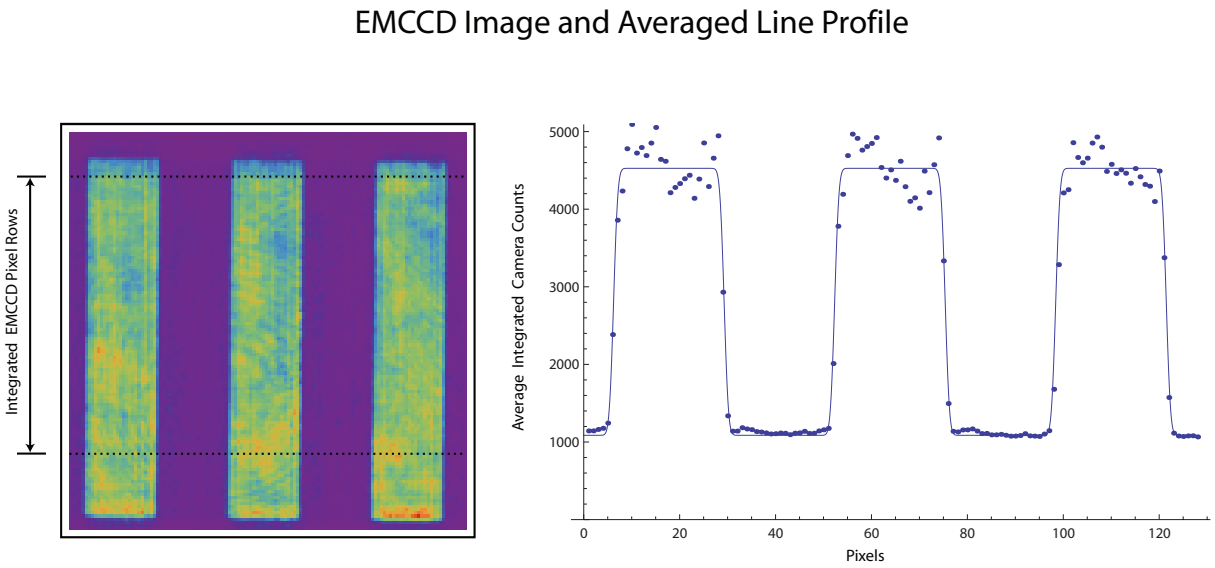

Figure A.3 Image and line profile used to characterize the PSF of the EMCCD imaging system. The fit function (discussed in text) characterizes the effective pixel size as 2.15μm and the PSF variance as 1.5$\pm$0.1μm.

The translators are controlled by another set of BM25.40 actuators. The focus of the imaging system is translated parallel to the optical table using these actuators. These actuators have $\sim$1μm sensitivity, and the actuator increments are labeled in 10μm intervals. The precision of the actuators is on the order of the imaging system′s depth of focus. Several pictures of the assembled and aligned system are shown below.

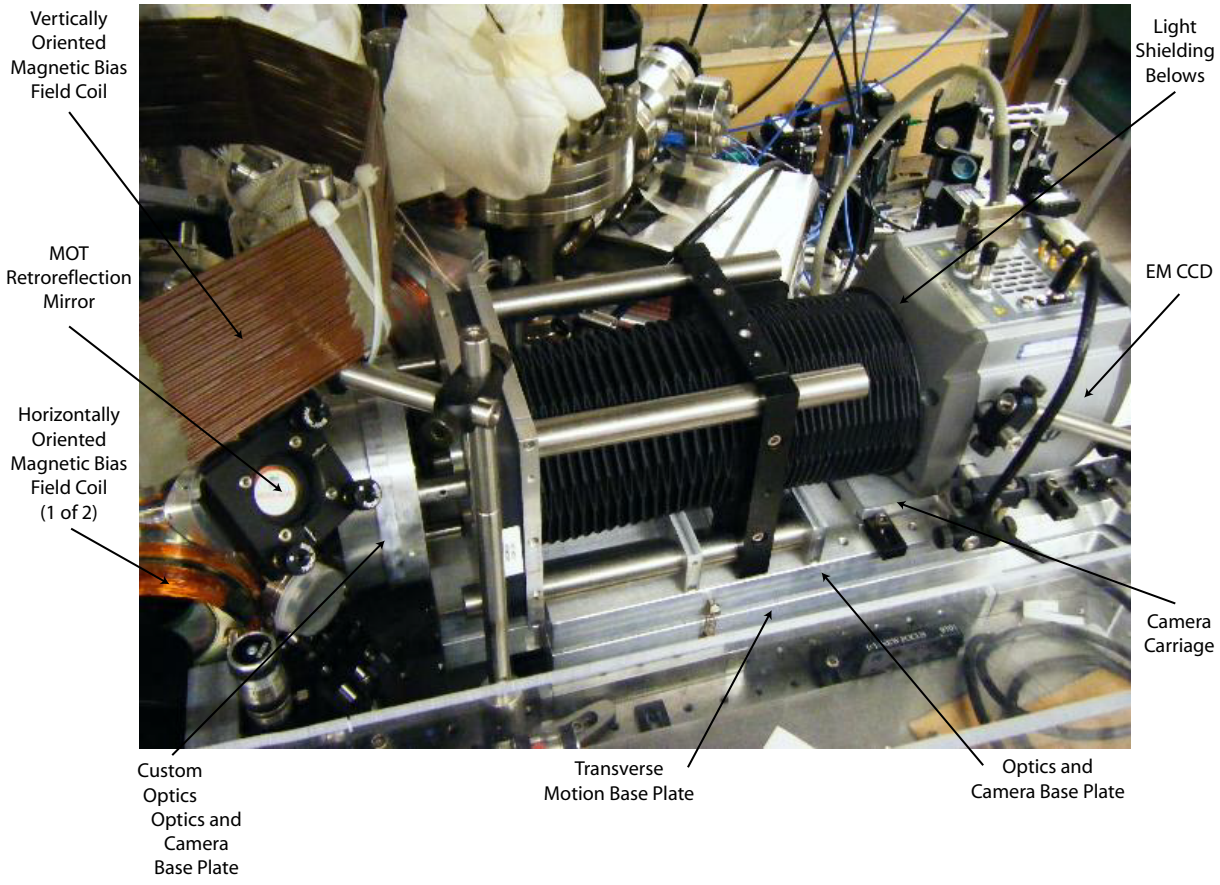

Figure A.4 Sideview of optical system.

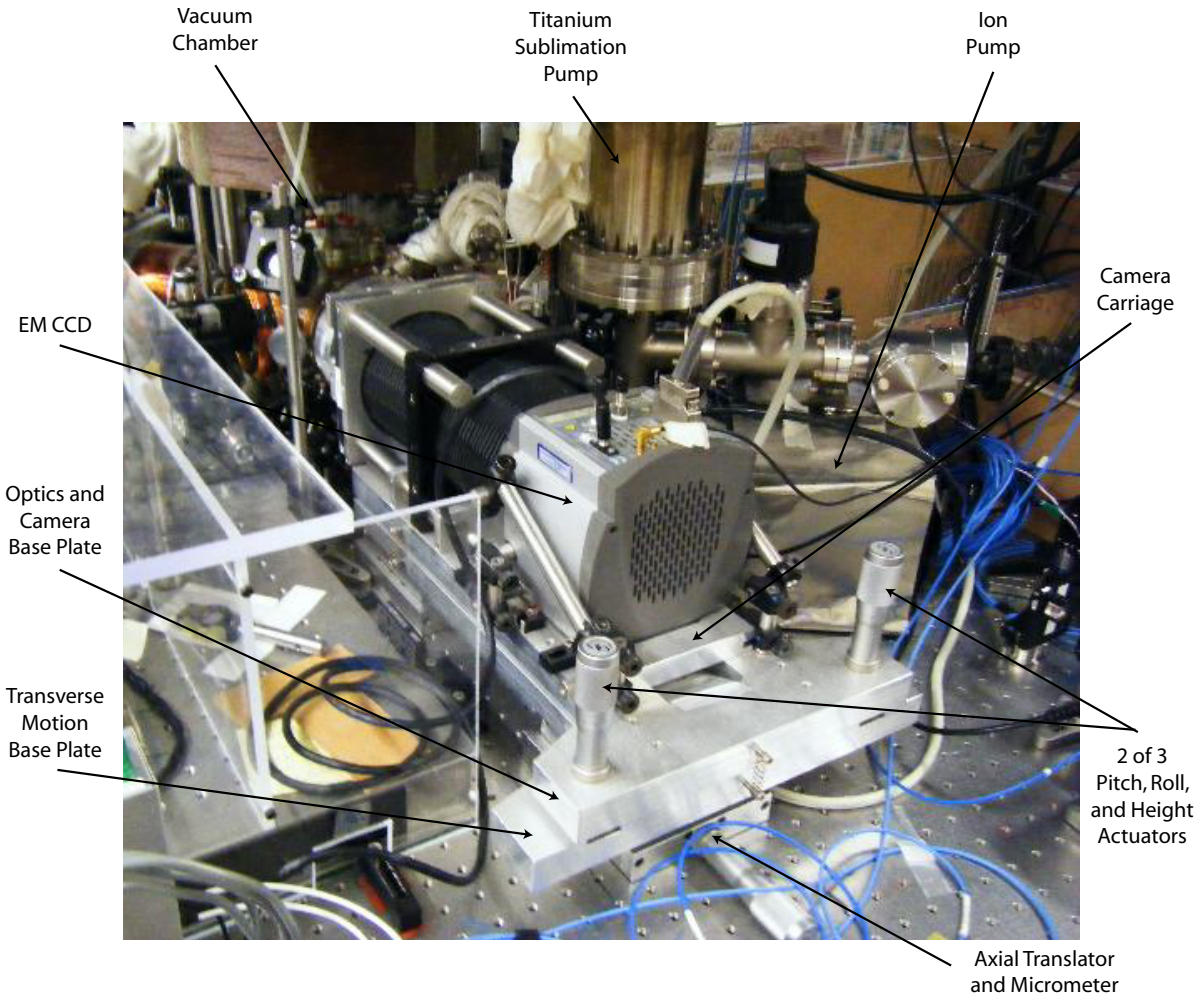

Figure A.5 3/4 view of system from EM CCD side.

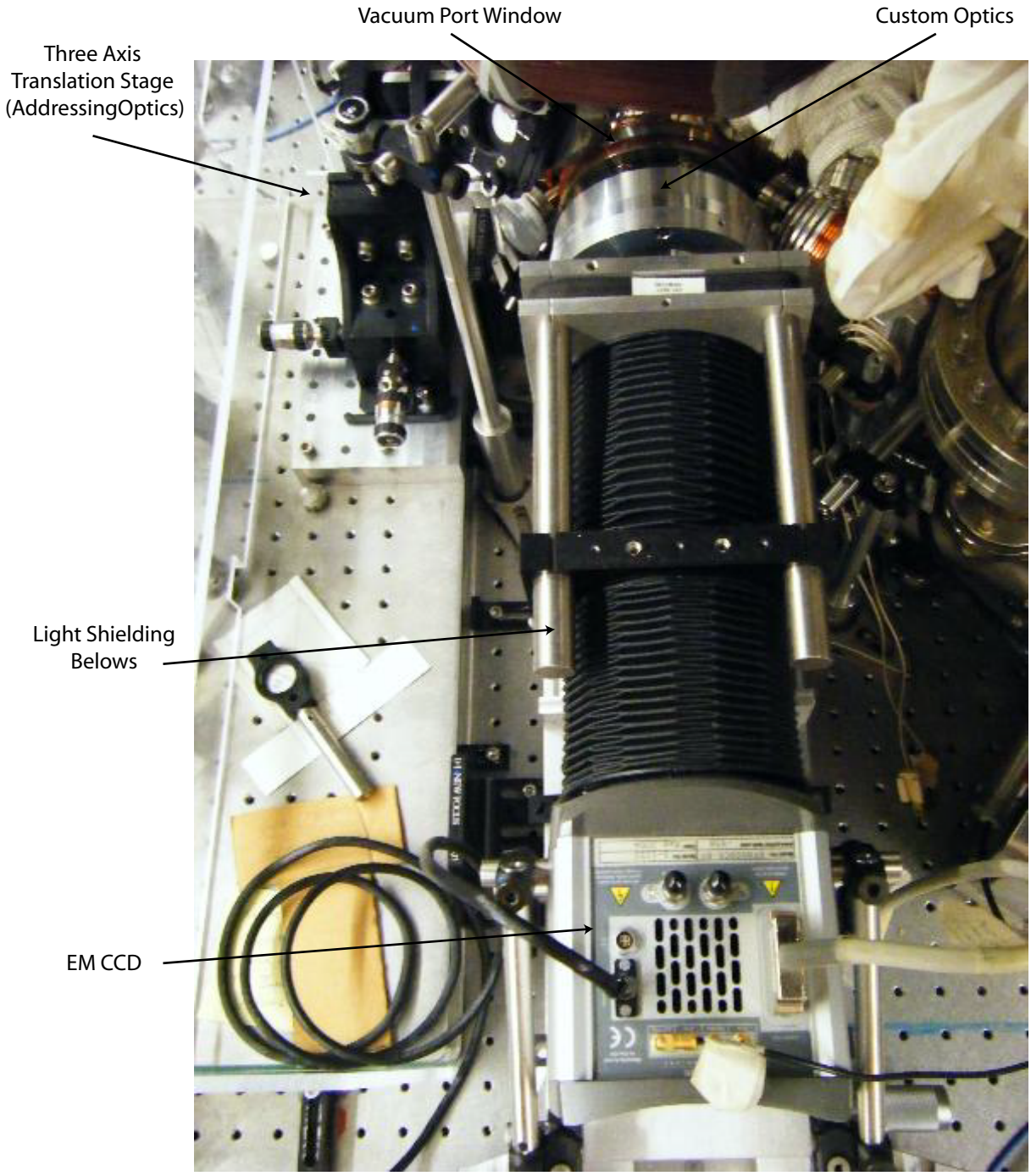

Figure A.6 Overhead view of optical system.

Appendix B: FORT Alignment

This section discusses the alignment of the FORT optics used to generate two optical potentials. This discussion presumes that the system has been pulled away from the vacuum chamber for access to the laser beam output. The first step is to collimate and level the fiber output within the first level of the cage system. The collimation is set by projecting the laser beam to a wall more than ∼5 meters away and visually minimizing the spot size. The system uses an angle polished fiber and a flat polished FC connector thus making it not possible to completely center the laser beam within the first layer of the cage system. The collimating lens is mounted within an XY cage translator to ensure that the laser beam can travel level through the cage system. It is important for the laser to be normal to the calcite beam displacer. The first turning mirror can be removed and an extension can be attached to the top rail of the cage system to provide a longer path over which the laser beam can be inspected and leveled. A two foot extension is more than adequate. The wave plate and calcite beam displacer should be aligned such that the two beams are vertically separated. The turning mirrors are used to align both laser beams through the second cage layer.

The second cage layer was installed to integrate the diffractive element used to generate the 6 optical potentials. When optimizing the system for two optical potentials it is assumed that the 1:1 telescope and diffractive elements are removed. The laser beams should be aligned such that they straddle the center of the beam path. When using the diffractive element the calcite crystal should be rotated such that the laser beams are horizontally displaced from each other but still centered through the second cage path. The 1:1 telescope should be collimated by minimizing the laser beam waists in the far field. This can be accomplished by removing a turning mirror from the second cage layer of the FORT optics, or by temporarily inserting a pick-off mirror. The separation of the laser beams should also maintain a constant separation. The diffractive optical element is then installed at the focus between the optical elements. The collimation of the telescope is readjusted to ensure that the laser beams split by the calcite crystal are still propagating parallel with one another.

The placement of the optical element is optimized by ensuring that the diffracted beams are traveling parallel to one another. It is not necessary to install the diffractive element and telescope. When conducting experiments with single, or double optical potentials it is advisable to remove these elements if they are not necessary.

The laser beams are now transmitted through the third cage level. This layer contains a reducing telescope. The optical elements of this level should be unscrewed from their cage mounts before alignment. The turning mirror at the end of this level should be removed and an extension should be added to the optical cage. Once the laser beams are aligned the turning mirror should be restored and an alignment jig (target) should be placed in front of the dichroic beam splitter and the f≈1000mm focal length lens of the fourth and final cage section. Without the telescope optics in place the laser beams should be centered through the fourth cage level. Once the laser beams are centered in the forth level the input to the telescope can be installed in the third level. Because the laser beams are not hitting the lenses on axis it is difficult to use retro-reflections to align these lenses. The spatial alignment (XY) of the input to the telescope should be centered using the target placed in front of the f≈1000mm focal length lens in the fourth level and the XY translator. The telescope′s output lens is inserted into the optical train and is initially spaced by the sum of the focal lengths of the telescope. This can be initially approximated using a ruler. The lens transverse positioning is optimized by aligning the beams to the reference target in the fourth cage level using the XY cage translator.

The lens separation is optimized by ensuring that the laser beams are propagating parallel to each other. This step is rather difficult and requires some approximation due to the fact that the collimated beam outputs of the telescope have small waists and large divergence angles. Upon reaching the target of the fourth cage level the $1/e^2$-beam waists are of order $\sim$2cm. The separation of the laser beams after the telescope are expected to be $\sim 70\mu$m. Therefore, the laser beams are approximately parallel when they are nearly overlapping at the target. Since the target is located nearly 1 meter from where the laser beams are collimated, perfectly overlapping lasers at the target will give a propagation error of less

than 70μrad. A CCD camera imaging the target can be used to assist in nearly overlapping the laser beams. To ascertain if the beams are overlapping it is beneficial to rotate the wave plate before the calcite crystal thereby modulating the laser beam intensities out of phase with one another.

After removing the target the f≈1000mm lens′ axial position can be optimized. The lens position is translated until the beam waists are collimated. The collimation is verified by monitoring the lens output using a shearing interferometer. In order to observe the interferogram properly it is necessary to observe each laser beam separately. Once again, the laser power can be controlled using the wave plate located before the calcite crystal. The custom triplet can now be aligned to the system.

The optomechanical lens mount designed for the triplet is joined to a three axis translation stage which allows the laser beam focus to be accurately positioned within the vacuum chamber. The optomechanical mount is adjoined to the translation stage with three 1/4-20 screws which compress small o-rings. Compressing the o-rings provides pitch and yaw control of the optomechanics. The triplet optomechanics is comprised of two pieces. The first piece houses a large plano convex lens and is adjoined to the large 3-axis translation stage. The second piece houses the large biconvex and the aspherical lenses. These lenses are separated by a Delron ring. The two lens holders are adjoined with a spring and actuator style mount. The separation between the first and second optical elements can be adjusted using the three fine pitch AJS127-0.5H actuators. On axis, the nominal spacing between the backside of the first lens and the front edge of the second lens should be 2.3mm.

In making this final set of lens alignments it is necessary to use a the CCD camera system described in Appendix E. The lens is typically set on axis with the rest of the optical assembly using the 3-axis translation stage. A port window is placed in the optical beam path after the triplet lens. The lensing of the port window is important to the final beam waists of the system. The pitch, yaw and separation of the optomechanics should be coarse aligned before trying to image the final beam waists on the CCD camera. Once the camera and FORT system are aligned, the depth of the camera should be scanned to inspect the

system for coma aberration. Very dramatic coma aberrations can be induced by improperly aligning the pitch or yaw of the triplet. These errors can be compensated by compressing the o-rings adjoining the triplet′s optomechanics to the three axis stage. The 1/4-20 bolts used to compress the o-rings must be adjusted in pairs to modify pitch and yaw separately due to the bolt layout. Adjusting the pitch and yaw of the triplet requires the camera position to be shifted to compensate for beam steering. Upon properly aligning the triplet the beam waist will appear cylindrically symmetric while scanning the depth of the CCD camera.

It is important to scan the depth of the CCD camera to ensure that the laser beams are not intersecting. While optimizing the spacing between the lenses of the third cage level it was necessary to make an approximation. It is important to ensure that this approximation was not performed sloppily. The final FORT beam waists must propagate parallel to one another. While scanning the camera focus the separation of the FORT beams should remain constant. It is also important to confirm that the triplet lens can be translated using the 3-axis linear stages without compromising the FORT spot sizes. In order to scan the triplet′s position several millimeters the imaging CCD camera will need to be translated as well. After making these final consistency checks the FORT optical assembly is ready to be aligned to the vacuum chamber.

Aligning the FORT to the vacuum chamber can be time consuming and very frustrating. Typically, buttresses are locked down to the optical table to assist in this process. If the buttress positions are being used the FORT position can generally be restored to within $\pm 50\mu$m of its original positioning. If it is not possible to reuse the buttresses, then as a good starting point, the FORT cage rails should be used to crudely center and align the laser orthogonal to the vacuum chamber window. Once the FORT assembly has been roughly aligned and locked down to the optical table, the triplet can be translated to align the FORT beams to the MOT. If the optical addressing assembly (Section 6.4.2, Figure 6.10) that is integrated into the FORT optics has been aligned with the FORT, this laser beam can be used to establish an initial alignment between the FORT and MOT beams. This is accomplished by sending an on resonant (F=2↔F=3) laser beam into the 780nm addressing

beam optical fiber to destroy the MOT. When the MOT is decimated with very little optical power the FORT will be aligned with the MOT.

If the FORT is being aligned from scratch a 780nm laser beam can be temporarily sent through the FORT optical fiber to perturb the MOT. If the optical system opposing the FORT assembly is aligned to the MOT it is possible to use this as a reference for the FORT beam path. By walking the FORT 3-axis stage, the opposing 780nm addressing laser beam can aligned to the rest of the FORT optics. Upon optimizing FORT position it should be possible to observe atoms loaded in the FORT wells. If atoms are not observed, it is common for the FORT wells to initially be located out of the focal plane of the photon counting optics. The FORT actuator should be scanned along this axis first. If atoms are still not being observed ALL experiment cycle timing parameters, ALL laser beam powers, MOT beam detunings, MOT beam alignments, magnetic fields (gradient and shim), optical shutters, and camera parameters should be double and triple checked by multiple people in the lab. Over-kill when double checking these systems can save you A LOT of time and frustration. If these parameters look reasonable, increase the background Rubidium vapor pressure and increase the FORT beam power. Keep in mind that the linear translation stages used to translate the custom triplet lenses become magnetized over time. Their residual field can greatly perturb the MOT and readout protocol efficiency. It will require time for their fields to polarize. Exercising patience can prevent needless random searches through MOT parameters and beam alignments.

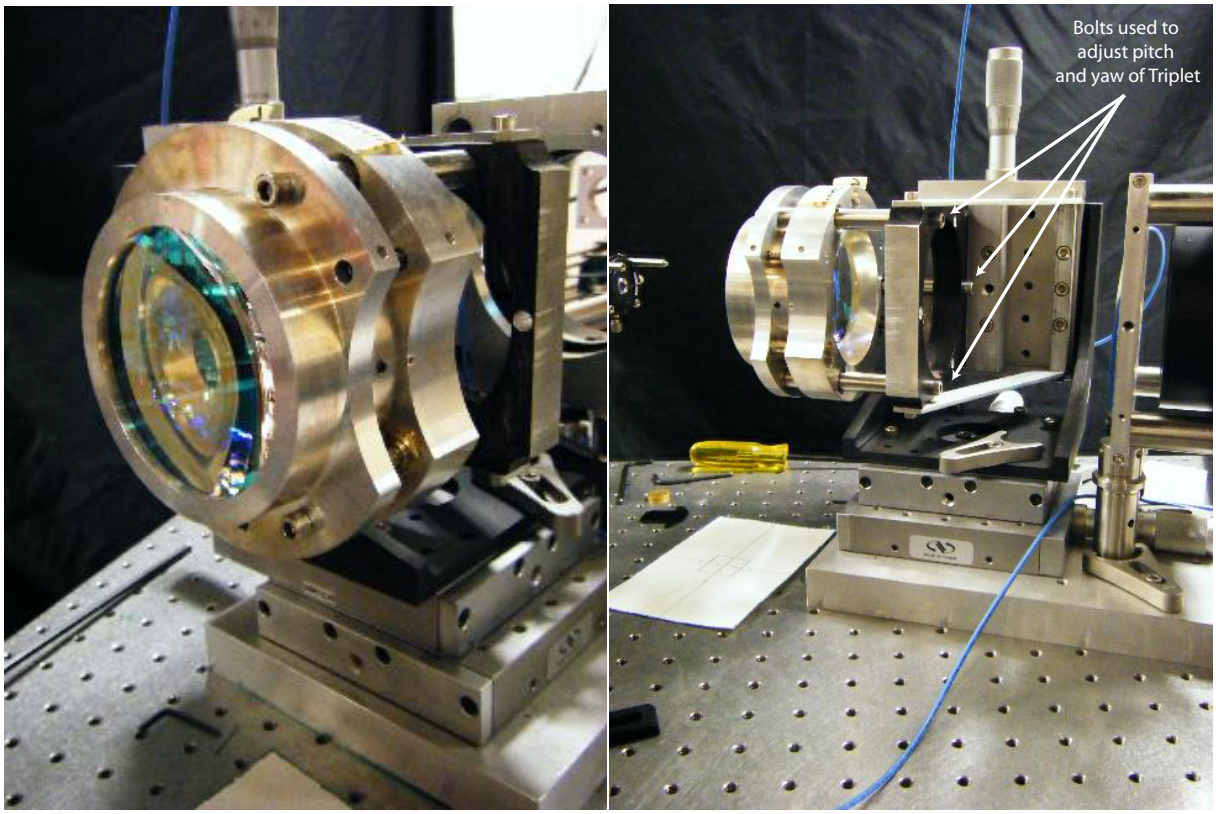

Figure B.1 Pictures of the FORT custom triplet.

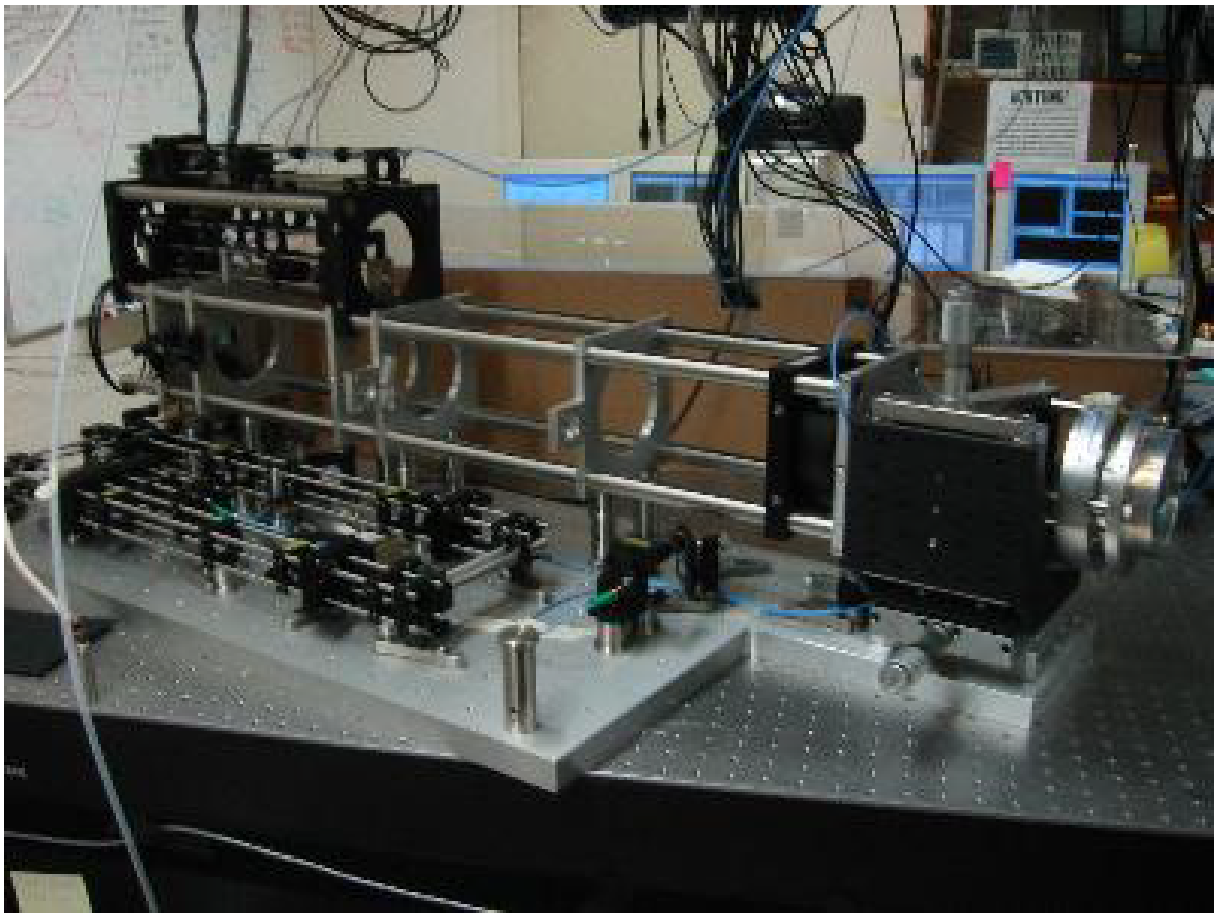

Figure B.2 Picture of the FORT optics.

Appendix C: Addressing Beam Alignment

The addressing optics have a lengthy alignment protocol as well. Two assemblies are used to allow the various laser beams to be directed at the qubits. One assembly integrates a 780nm laser beam into the FORT optics with the use of a dichroic beam splitter. The other assembly combines a 780nm laser beam with a 480nm laser beam. This section merely illustrates how to align the system. For specific details on the custom designed triplets refer to Section G.

To align the 780nm and 480nm laser assembly, begin by aligning the 480nm laser. The 480nm and 780nm lasers are joined with a dichroic beam splitter and the 480nm laser uses this beam splitter as a turning mirror. Since, adjustments to the dichroic beam splitter will shift the alignment of the 780nm laser beam, it is necessary to finalize the positioning of the 480nm laser beam first. This alignment procedure begins by collimating the 480nm optical fiber output. All of the optical elements should be coarse aligned within the cage setup. This involves separating adjacent lenses by the sum of their focal lengths with the exception of the final two lenses. The AOM, which is mounted to a three axis translator, should be initially translated out of the beam path. The 480nm laser beam should be aligned to the center of all of the beam paths. The spacing between the lenses can be more rigorously optimized by collimating the laser beam in the far-field. With the exception of the final two lenses, the laser beams can be collimated by minimizing the beam waists in far-field limit. The Rayleigh ranges of the intermediate waists through out the system are less than $\sim$3 meters. Setting the beam collimation after the second to last lens requires the use of a shear plate. After setting the spacing of the optics the laser beams should be recentered through the entire cage system.

The AOM should be translated into the system and the diffraction efficiency should be optimized. The AOM must be placed a focal length away from the subsequent lens in the optical beam path. The position of the AOM is set by translating the unit axially along the beam path. The diffracted laser beams of the AOM should propagate parallel to one

another after traversing the lens. The last two sets of turning mirrors are used to center the desired diffracted beam order through the remainder of the cage system. An iris eliminates the undesired AOM beam orders. The position of the collimating lens after the dichroic beam splitter should be set using a shear plate. A port window is placed a few centimeters away from the final lens to simulate the effects of the vacuum chamber windows. The final beam waist can be imaged on a CCD camera. The size and position of the iris is optimized while viewing the beam with a CCD camera.

This procedure is nearly identical for setting the adjoining 780nm laser beam. It is advisable that the coarse alignment of this optical beam path be set prior to aligning any optical elements. The position of the achromatic collimating lens, having been established using the shear plate and the 480nm laser beam must not be moved. Therefore, the coarse positions of this optical beam path should be established by working backwards from the collimating lens. The spacing between adjacent lenses is set to the sum of the lens pair′s focal lengths. This helps ensure that both the 480nm and 780nm laser beams can be simultaneously collimated prior to reaching the final triplet lens.

The alignment procedure for the 780nm laser beam then follows the same steps as the previously aligned 480nm laser beam up to the achromatic triplet. Instead of translating the triplet, it is necessary to translate the short focal length lens ahead of the dichroic beam splitter. If this lens needs to translate more than a few millimeters, the 780nm beam path should be rough aligned again.

The polarizations of the laser beams need to be set using a combination of wave plates prior to characterizing the laser beam waists and translating the AOMs. This procedure is provided in Appendix D. The characterization of the beam waists are performed using the calibrated CCD camera setups described in Section E. It is crucial that the foci of the 780nm and 480nm laser beams coincide with one another. Due to the fact that the magnification of the imaging system varies for different wavelengths it is necessary to view the foci on a bare CCD camera. The CCD camera should be positioned at the focus of the 480nm laser beam. The 780nm lens just ahead of the dichroic beam splitter should be translated until

the two foci are in the same plane. The final turning mirror of the 780nm beam line can be used to align the 780nm laser to the 480nm focus. After making this final adjustment the laser beams are ready to be characterized and the optical system can be aligned to the vacuum chamber. If the opposing optical system (the FORT and counter-propagating 780nm Rydberg laser) are aligned it is possible to use these beam lines as a reference for alignment. The 780nm laser beam can be roughly aligned to the FORT beam path by translating the final triplet of the addressing optics.

An optical assembly capable of addressing individual qubits with a 780nm laser beam is also integrated into the FORT optical array. The alignment of this optical system is carried out in a very similar fashion to the 480 and 780nm addressing system. The FORT laser beams are aligned first. The 780nm optical elements are coarse aligned by spacing adjacent lenses by the sum of their focal lengths working backwards from the f≈1000mm lens. The positioning of the FORT-780nm optical elements are carried out as outlined for the 480-780nm laser system. Upon finalizing the alignment procedure the laser beams should be characterized and aligned to the vacuum chamber.

C.1 Lens Selection

The AOMs of the addressing laser beams are designed to operate using the same RF driving frequencies. Our ability to perfectly align multiple laser beams to a single qubit is limited by the optical arrays used to convert the angular deflection of the AOM into a linear translation of the beams. To discuss these limitations further it is useful to first point out several underlying principles used in designing the apparatus. As illustrated in Figure C.1(top), a ray of light passing through the focus of an ideal lens will merely be transformed into a ray traveling parallel to the optical axis. This very simple concept can be used to explain the nature of a Galilean telescope. Separating two lenses by a distance equal to the sum of the focal lengths creates an optical system capable of amplifying a ray′s input angle (Figure C.1(bottom)). The AOM diffraction angle is proportional to the diffraction order, the wavelength of the laser beam and the inverse of the AOM acoustic wavelength.

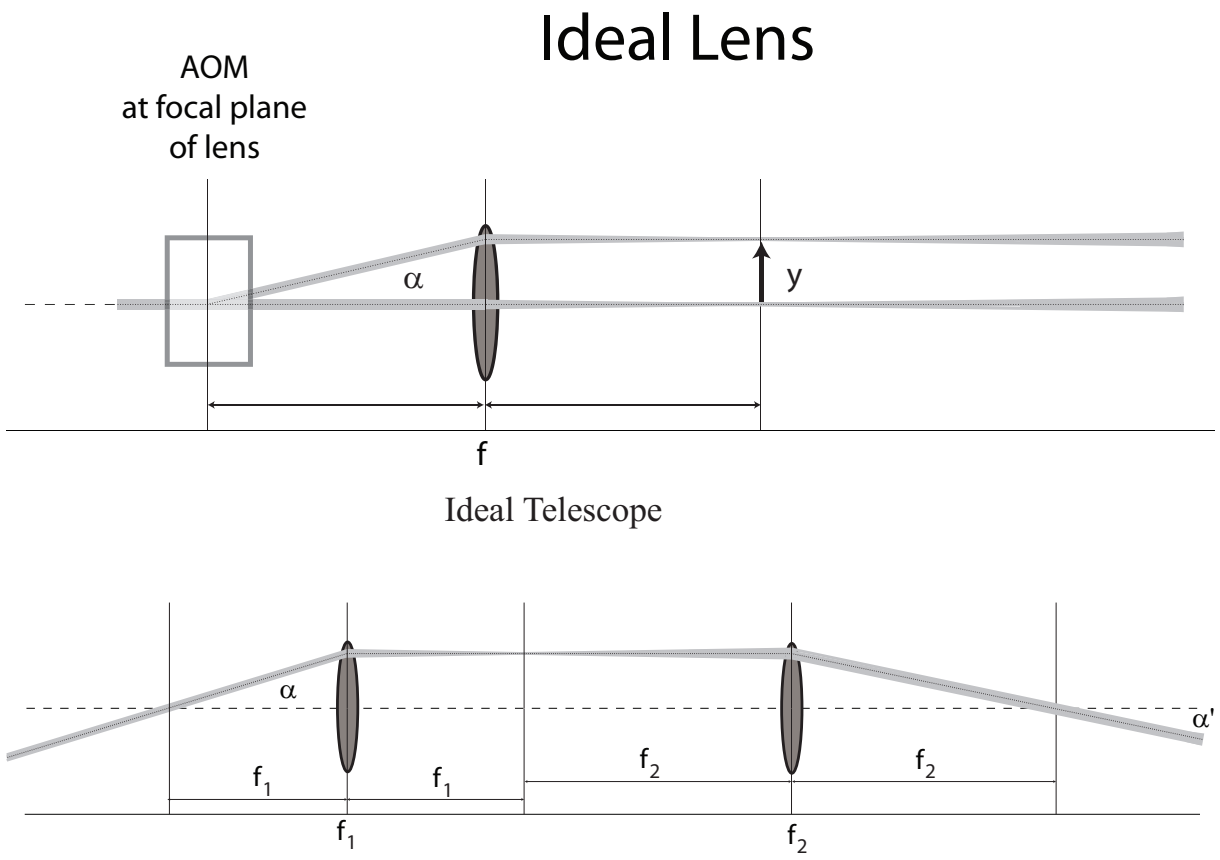

Figure C.1 Top: Illustration of how an ideal lens can be used to convert an angular input into a linear translation. Bottom: Illustration of two lenses being used as a telescope. The input angle is magnified by the ratio of the input focal length divided by the output focal length. $M = \frac{\alpha'}{\alpha} = -\frac{f_2}{f_1}$

The lenses immediately following the AOMs in each arm of the addressing system can be thought of as telescopes. The subsequent three lenses of each arm are identical (f=50mm, 175mm or 400mm, and ∼110mm). Using these very basic ideas and a little algebra it becomes trivial to arrive at the necessary telescopic ratios of the telescopes following the AOMs to match the linear translations of each beam in the vacuum chamber.

$$\frac{\lambda_{780}}{\lambda_{480}} = \frac{M_{480nm}}{M_{780nm}} = \frac{f_{1\ 480nm}/f_{2\ 480nm}}{f_{1\ 780nm}/f_{2\ 780nm}} \approx \frac{13}{8}$$

Our ability to achieve this desired ratio is limited by our selection of lenses. The angular magnification in the 780nm beam line is roughly 0.3, while the angular magnification in

480nm optical path is 0.5. Therefore, the ratio of the magnifications used are 0.5 / 0.3 which differ from the desired ratio by about $\sim$2%.

This error is much greater in the design and layout of the counter-propagating 780nm laser beam system. The design is slightly more complicated by the fact that this laser must pass through the custom FORT optics. The lens selections used to convert the angular AOM shift into a linear translation generate a 14% error. The linear translations of the three laser beams versus change in AOM-RF frequency are shown in Table 6.4.2. A description of how these measurements are performed is contained in Appendix E.

Appendix D: Setting Beam Polarizations

As mentioned in Appendix C, the polarization of the three addressing laser beams need to be oriented in a particular manner in order to drive the desired optical transitions. The polarization of these laser beams are set using a combination of $\lambda/2$ and $\lambda/4$ wave plates. We require the use of both wave plates to compensate for the polarization dependent reflections of the dichroic beam splitters. The polarizations of the laser beams are analyzed by passing the lasers through a rotating $\lambda/2$ wave plate and a fixed polarizing beam splitter. The optical power transmitted through the polarizing beam splitter is monitored on an oscilloscope with the use of a power meter. To generate a circularly polarized laser beam the $\lambda/2$ and $\lambda/4$ wave plates of the optical trains are oriented to minimize the oscillatory signal of the power meter. The light is linearly polarized when the oscillatory response of the power meter is maximized. The orientation of the polarization must also be confirmed after optimizing the $\lambda/2$ and $\lambda/4$ wave plates. The orientation (vertical / horizontal) of linear polarizations are confirmed with a polarizing beam splitter. The helicity of circularly polarized beams are checked using a Fresnel-Rhomb prism and a polarizing beam splitter. The Fresnel-Rhomb prism acts like a $\lambda/4$ wave plate, and will convert a circularly polarized beam into a horizontally or vertically polarized beam depending upon the laser beam′s helicity. The polarizing beam splitter is used to deduce the orientation of the linearly polarized beam. A wave plate can be used for the same purpose, however, particular optics manufacturers have been found to not properly label the optical axes of their wave plates. This can result in faulty determinations of beam helicity. The fast and slow axes of a Fresnel-Rhomb cannot easily be confused. The Fresnel-Rhomb can also be used to inspect both the 780nm and 480nm laser beams. The equipment used to orient the laser beam polarizations are shown in Figures D.1, D.2 and D.3.

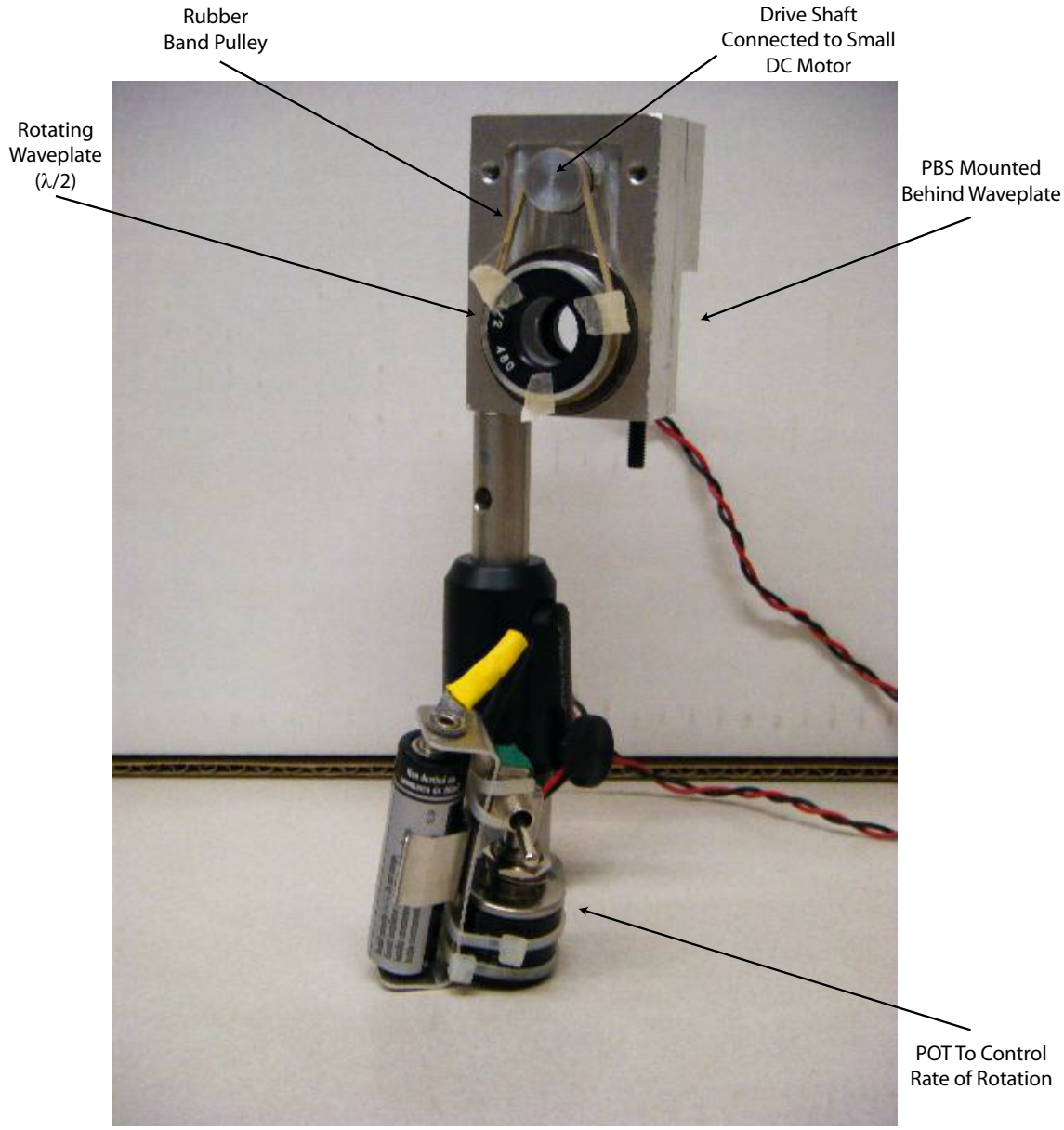

Figure D.1 Input side of the spinning $\lambda/2$ wave plate used to optimize the laser beam polarizations. Polarizing beam splitter mounted on rear side of unit. A POT and small DC motor are used to automatically spin the wave plate.

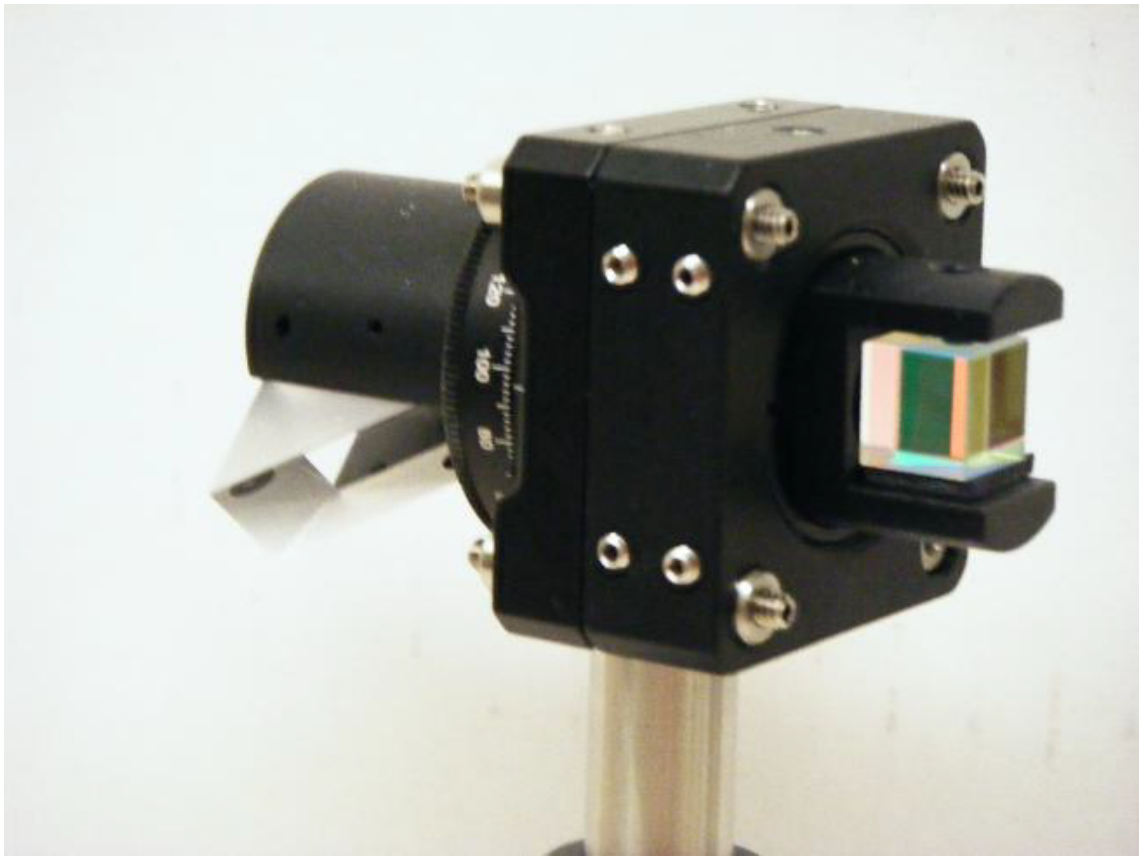

Figure D.2 Output side of Fresnel-Rhomb and polarizing beam splitter setup.

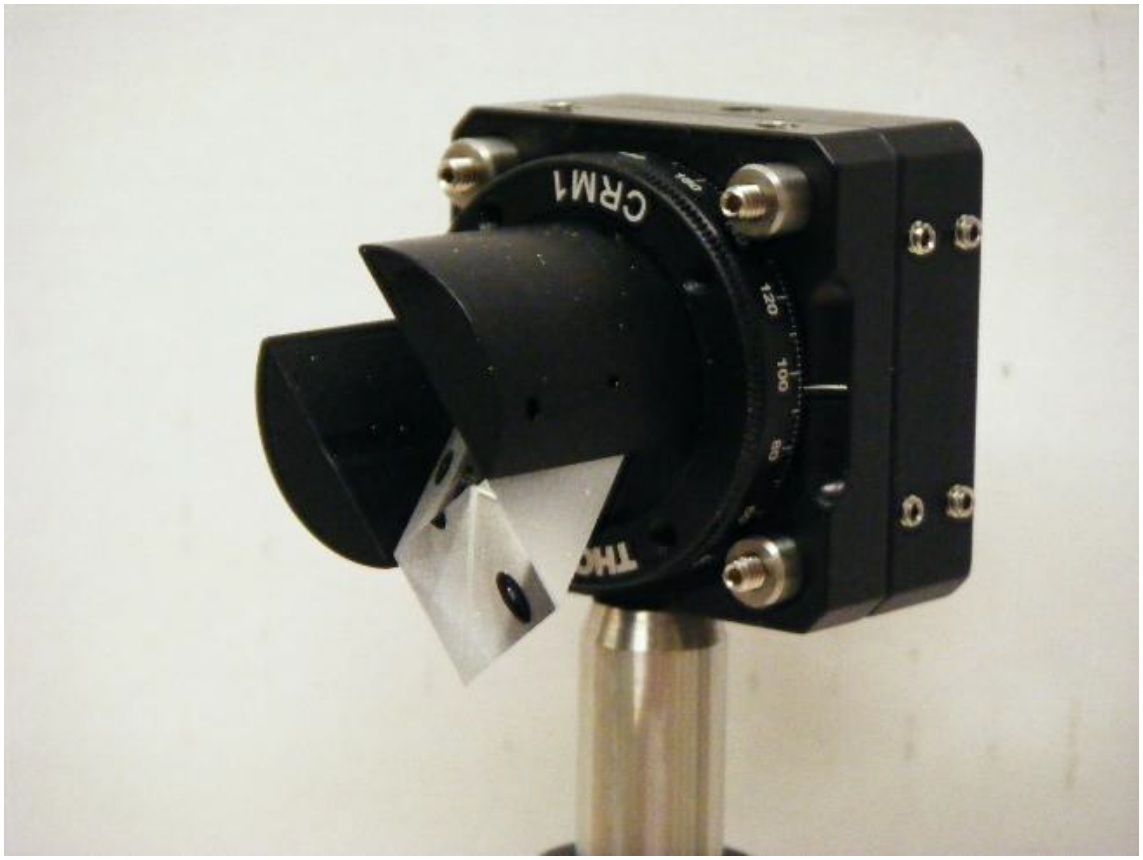

Figure D.3 Input side of Fresnel-Rhomb and polarizing beam splitter setup.

Appendix E: Laser Beam Characterization

The characterization of the laser beams, and our ability to control the linear translations of the addressing beams are evaluated using a calibrated imaging system. The imaging system consists of a Thorlabs C230TM-B asphere, rigidly mounted to a Watec CCD camera. The pixel size of the Watec camera is 6.35μm by 7.4μm. The camera images are retrieved using frame grabbing software from Epix. The imaging system is shown in Figures E.1 E.2.

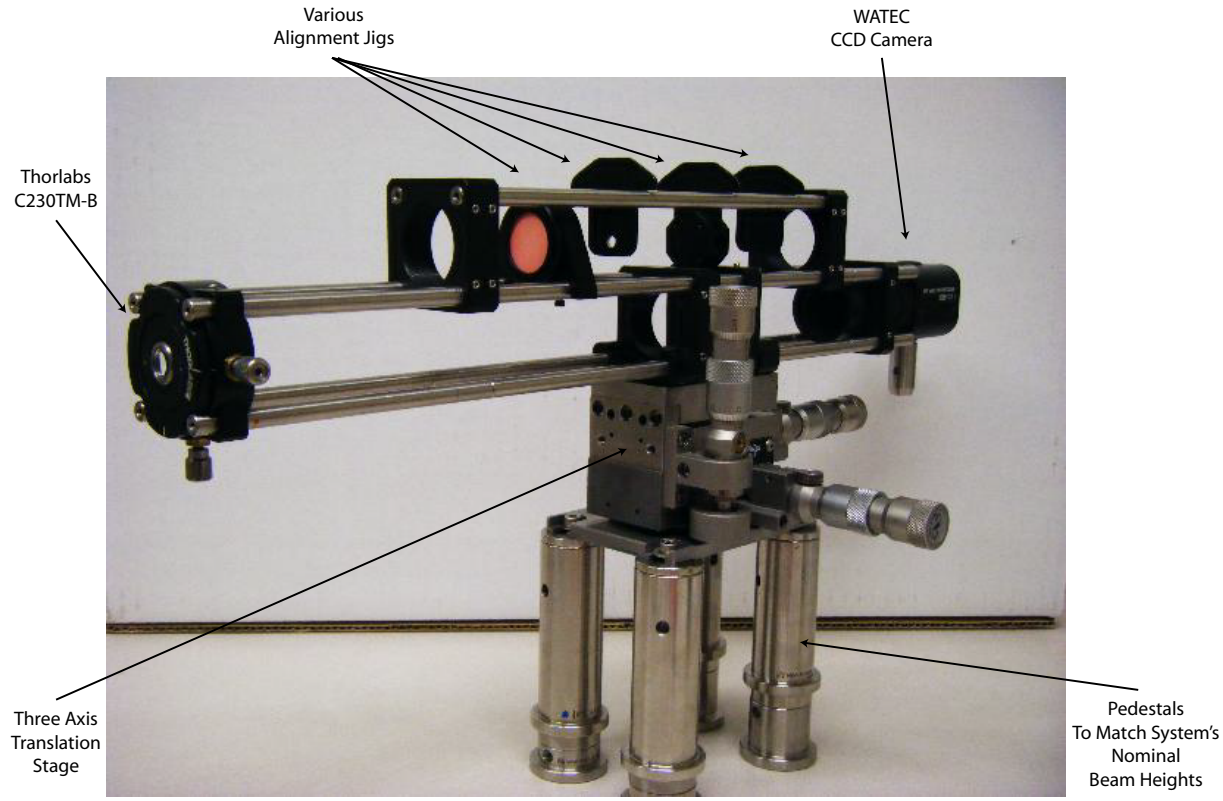

Figure E.1 CCD imaging system used to measure laser beam waists.

The imaging optics calibrations are performed by back illuminating an Edmund Optics USAF Resolution Target 2″ SQ Negative target (Part Number: NT38-256) with a large collimated monochromatic source. The calibrations are very similar to those outlined in Section A. It is important to calibrate the imaging system for each required wavelength. To ensure accurate beam waist measurements one must confirm that the intensity response

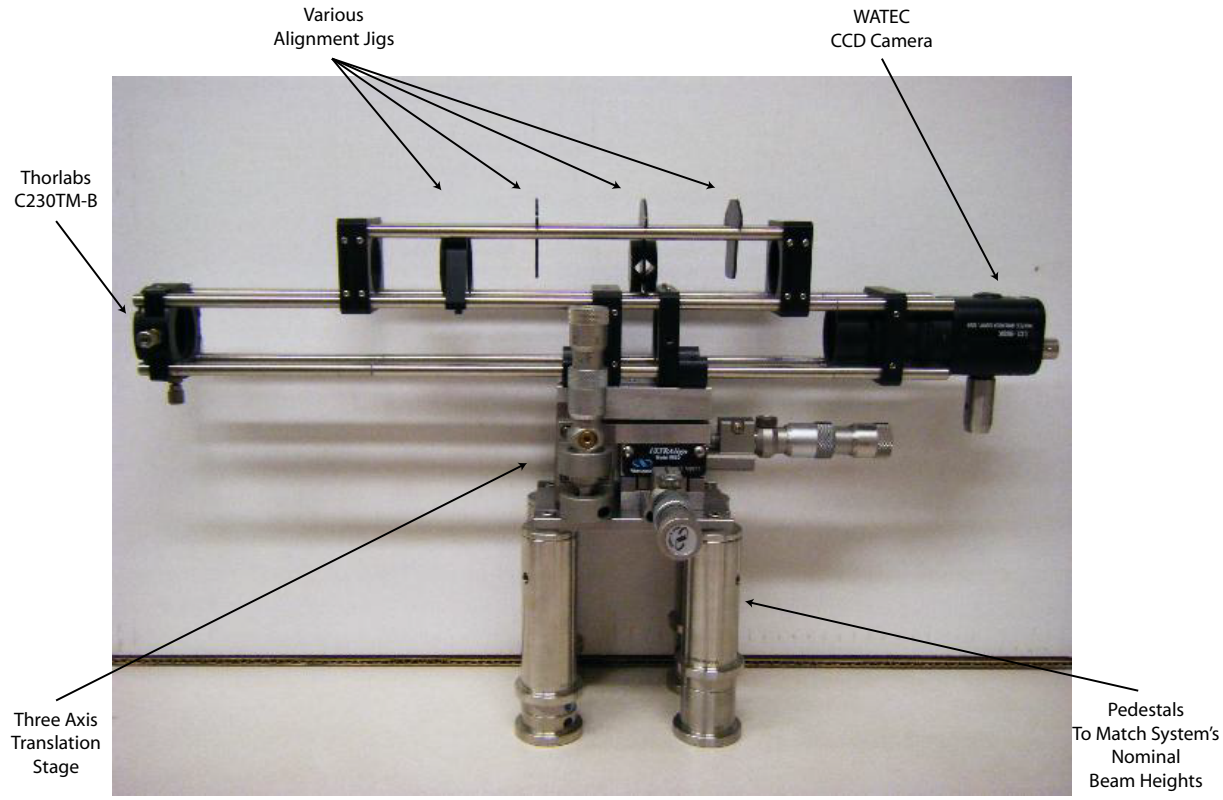

Figure E.2 CCD imaging system used to measure laser beam waists.

of the imaging system is linear. The gamma factor of the Watec CCD camera is set equal to 1, and the linearity of the system is confirmed by observing the camera's background subtracted signal as a function of the optical power being imaged. All measurements are performed with a non-zero background signal. Table E provides a list of the magnifications for several commonly used wavelengths. Table E provides a list of the laser beam parameters measured using the calibrated CCD imaging system. Several figures of various CCD images are provided to illustrate how these measurements are made, and why the addressing beams are asymmetric in nature. The asymmetric aspect ratios of the addressing laser beams are caused by the AOMs. This is demonstrated with Figures E.3 and E.4. Figure E.5 shows a 780nm addressing laser beam misaligned from the FORT potentials. Laser beam attenuation is performed prior to fiber optic links thereby preventing the cameras from saturating and removing the need for neutral density filters.

Table E.1 Addressing Laser Beam Parameters

Wavelength	Imaging System Magnification
1010nm	43.3
480nm	44.4
780nm	43.5

Table E.2 Addressing Laser Beam Parameters

$1/e^2$ Laser Beam Waists	Horizontal w_x (μm)	Vertical w_y (μm)
480nm Laser Beam	9.1	10.5
780nm (FORT-side) Laser Beam	7.0	11.9
780nm (480nm-side) Laser Beam	6.8	12.9
1030nm Laser Beam	2.9	2.9
1030nm FORT Separation	0	10.1
AOM Translation	(μm/MHz)	
480nm Laser Beam	1.52	
780nm (FORT-side) Laser Beam	1.82	
780nm (480nm-side) Laser Beam	1.57	

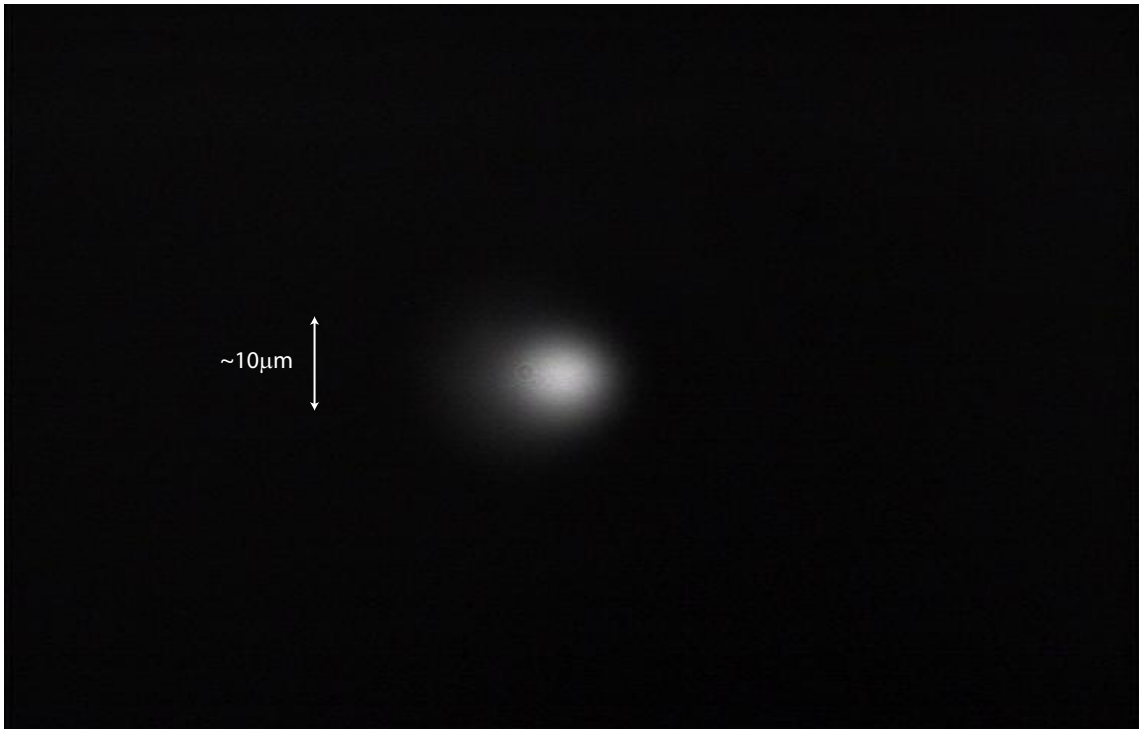

Figure E.3 Image showing the FORT side 780nm addressing laser beam prior to installing the AOM.

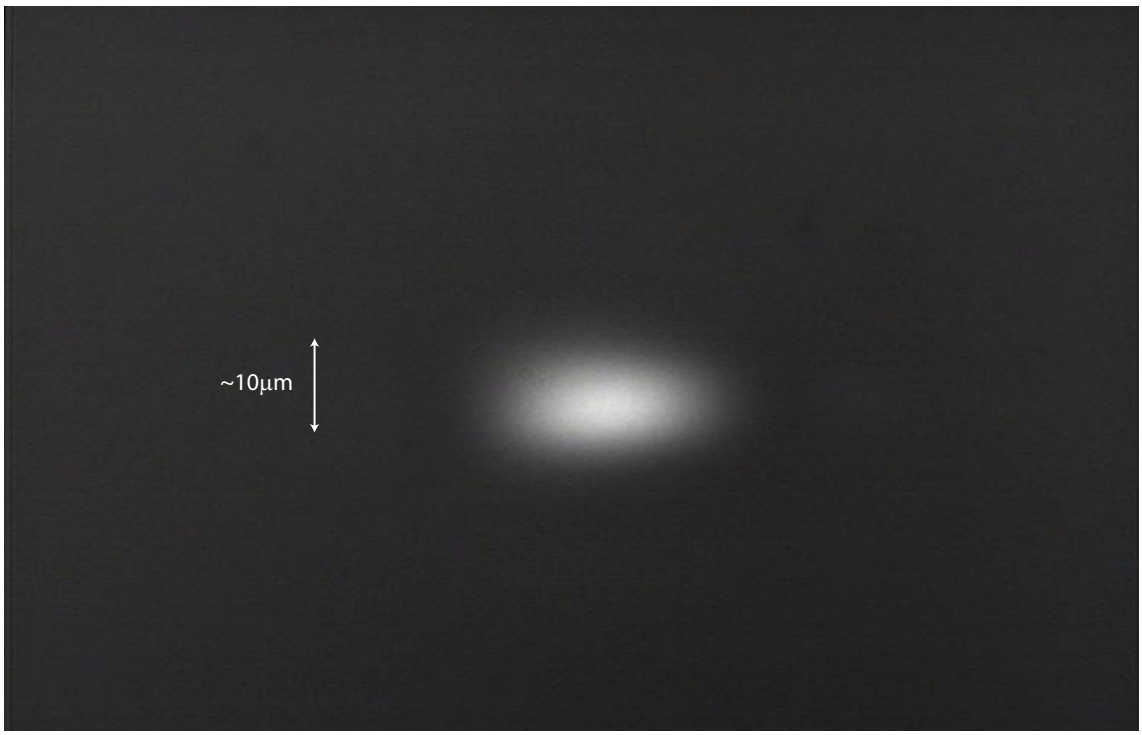

Figure E.4 Image showing the FORT side 780nm addressing laser beam after installing the AOM. Note that the laser beam has become asymmetric.

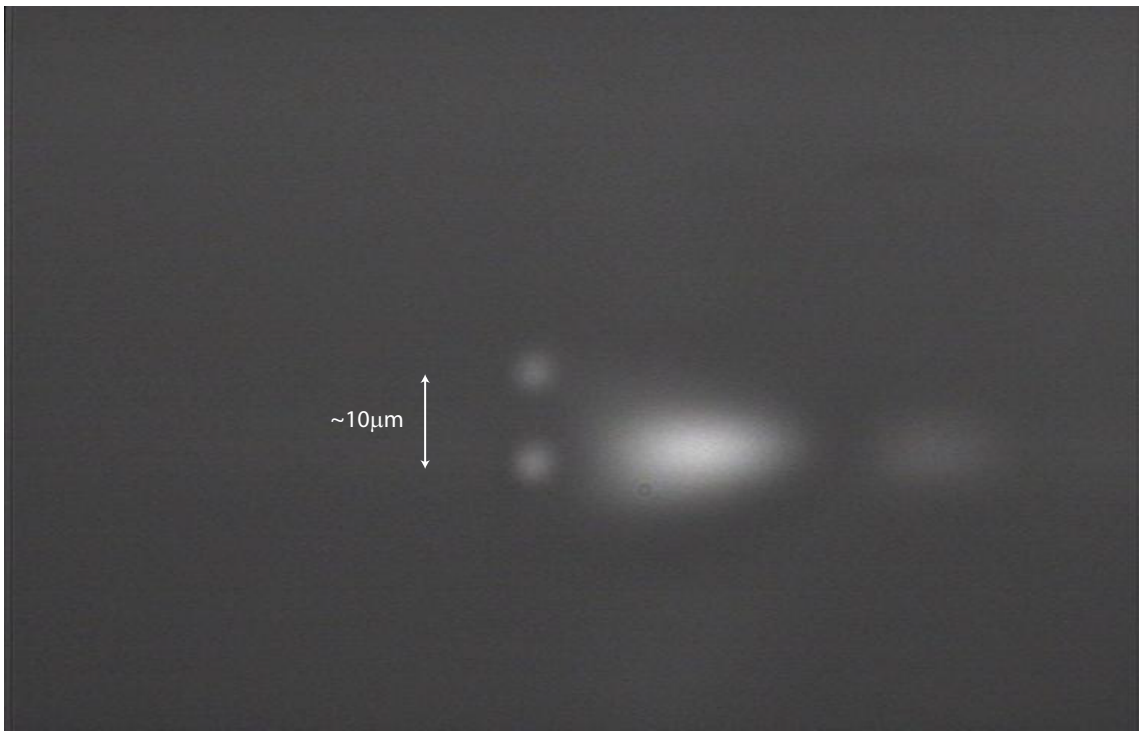

Figure E.5 Magnified image of two FORT potentials and a purposely misaligned 780nm addressing laser beam. The image is focused to the FORT beams.

Appendix F: Alignment Tools and Calibrations

Aligning laser beams to 3μm FORT potentials is by no means a simple task. A great deal of time has gone into developing tools to quickly and reliably establish alignment between the FORT wells and the three addressing laser beams. This section briefly covers the alignment procedures and tools used to target the qubit lattice points. The beam alignment requires an iterative alignment protocol, and as always there is more than one way to successfully align a laser beam to a target. This description is just one suggestion. This discussion presumes that coarse alignment to the FORT potentials has been established.

If none of the addressing laser beams are well aligned to the FORT sites, then begin with the ground state Rabi flopping laser beam sent into the chamber through the FORT optics. This initial alignment can be done relatively sloppily, because it will need to be realigned again using a two photon Rydberg transition. These experiments resemble two photon spectroscopy experiments. However, both the laser beam pulse duration and the two photon resonance frequency are fixed. The laser beam is scanned spatially through the chamber by walking the mirror mount ahead of the f=60mm lens shown in Figure 6.10. By scanning the two orthogonal axes of the mirror mount and recording the transition probabilities as a function spatial alignment we can determine optimal beam alignment. Using a two photon Rydberg transition, the 480nm laser beam can be aligned by spatially scanning the custom triplet mounted to the three axis translation stage. Upon completing this alignment it is advisable to return to the FORT side 780nm laser beam alignment. Now that the triplet has been aligned to the FORT sites, the 780nm laser beam (from the 480nm laser setup) can be aligned to the vacuum chamber. This is performed by once again spatially scanning the laser beam via a mirror mount.

Walking the 480nm laser beam is a straightforward task. The translation stage used Newport DS-4F actuators. The actuators are graduated at $\sim 1\mu$ increments. The full coarse travel is about 8mm while the fine controls have 0.3mm full travel. The backlash from the

actuators is negligible; however there is a small amount of backlash from the translation stages (¡ 1μm).

Reliably translating a laser beam using a mechanical mirror is difficult, but necessary in this experiment. Two methods have been established to measure the relative position of the laser beam. The 780nm addressing beam (opposing FORT beams) is aligned using a protractor and an Allen key. Figures F.1, F.2, and F.3 illustrate how the Allen key is modified and used to advance the mirror mount actuator. The protractor can be used to establish relative angular positions of the actuator. Backlash must be monitored in order to position the laser beam properly.

The 780nm addressing beam (copropagating with FORT beams) is aligned using a POT based alignment system (see Figure F.4). An Allen key is mounted to a mirror mount actuator and a POT. The resistance value of the POT is used to obtain a relative position of the laser beam within the vacuum chamber. Steering the laser beam in this method provides a reliable way of repeatedly rotating the mirror mount actuators.

The axial positioning of the laser beams is the most difficult problem associated with aligning the addressing beams to the qubits. Optimization of these axes is pursued by scanning the laser beam foci along the axial dimension and observing the transition probability as a function of beam position. The 480nm laser beam focus is scanned by translating the custom triplet lens. The 780nm addressing laser beam foci are positioned by axially translating short focal length lenses within the optical cages. Axial alignment of the FORT-780nm laser beam requires the movement of the f=60mm focal length lens. Axial alignment of the other 780nm laser beam requires the translation of the final f=50mm focal length lens. Translating the foci far enough to see an appreciable change in the probability of atom excitations is difficult due to the fact that the Rayleigh ranges of the addressing laser beams are relatively long ($\sim$0.25mm). Translating the lenses on the order of 1mm requires the laser beams$'$ transverse alignments to be reacquired. The size of the axial range that the foci must be translated and the difficulty of having to realign the transverse dimensions of the laser beams make this alignment technique very time consuming. While it is relatively easy to

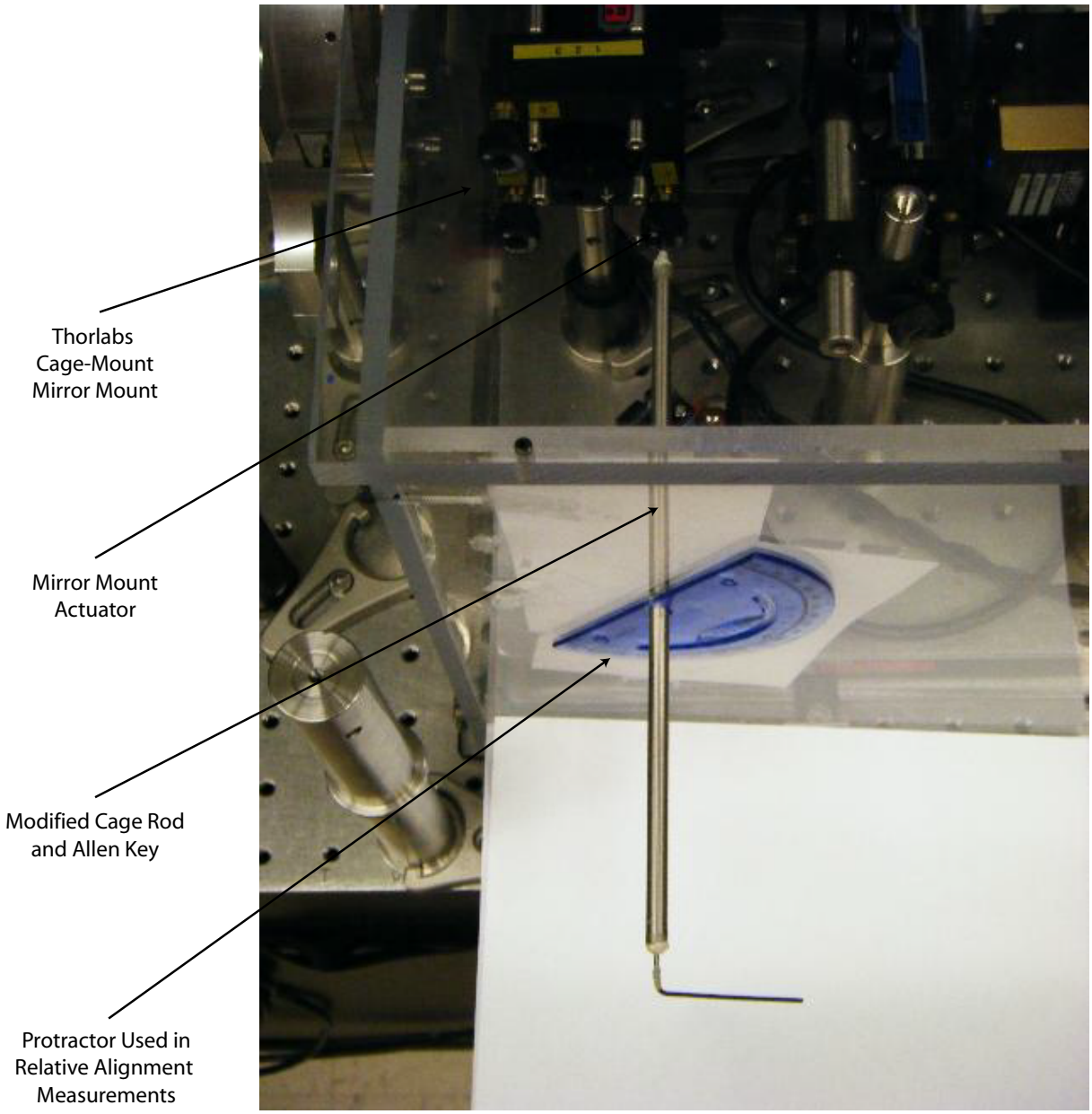

Figure F.1 Overhead view of optical addressing system with Allen key alignment jig

align the laser beams within $\pm 1 \mu m$ transversely, a considerable effort must be expended to axially align the laser beams within $\pm 1/2$ a Rayleigh range. The effects of alignment errors are examined in chapter 8 and 9.

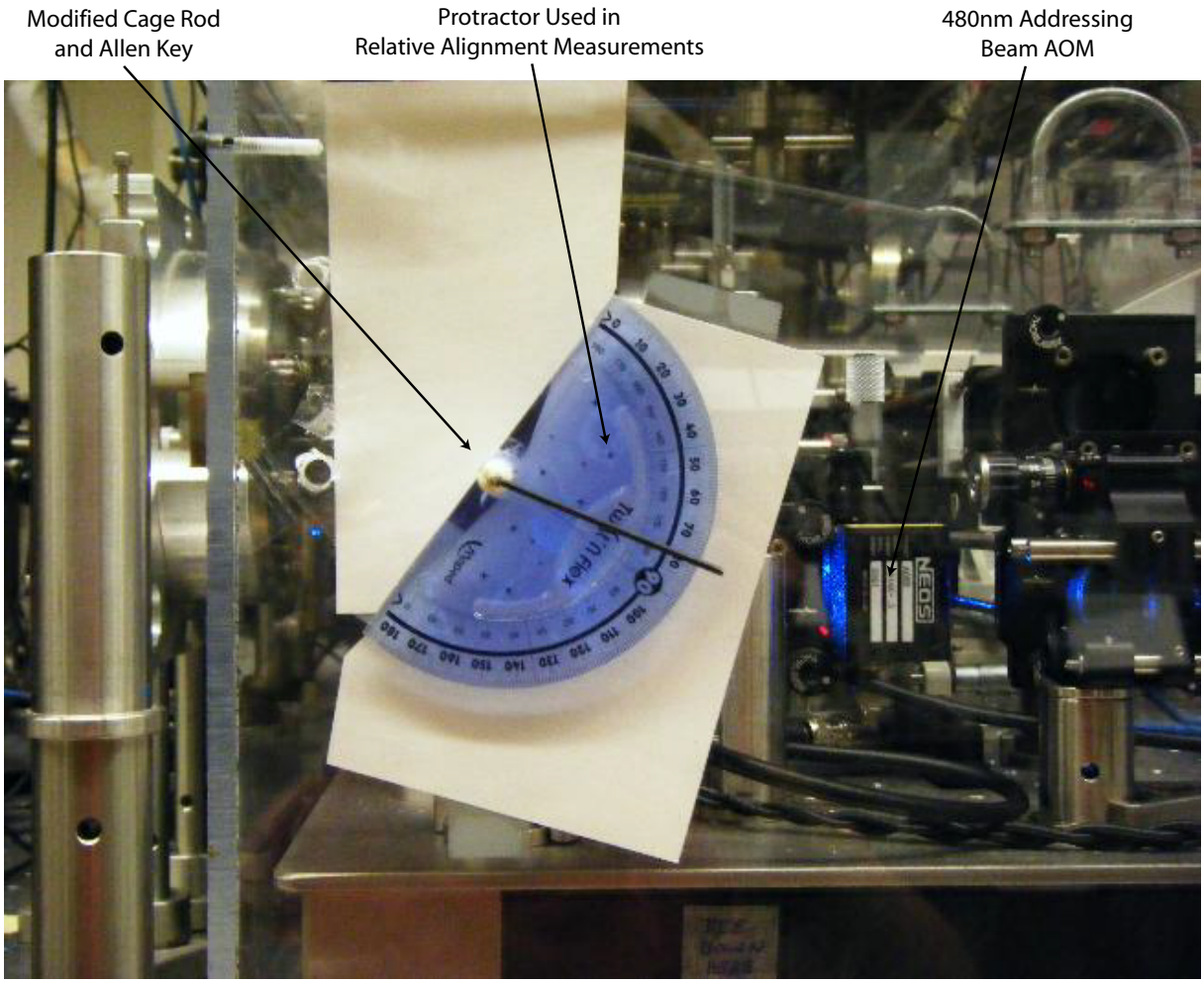

Figure F.2 End on view of the alignment Allen key jig and protractor used to acquire relative laser beam positions.

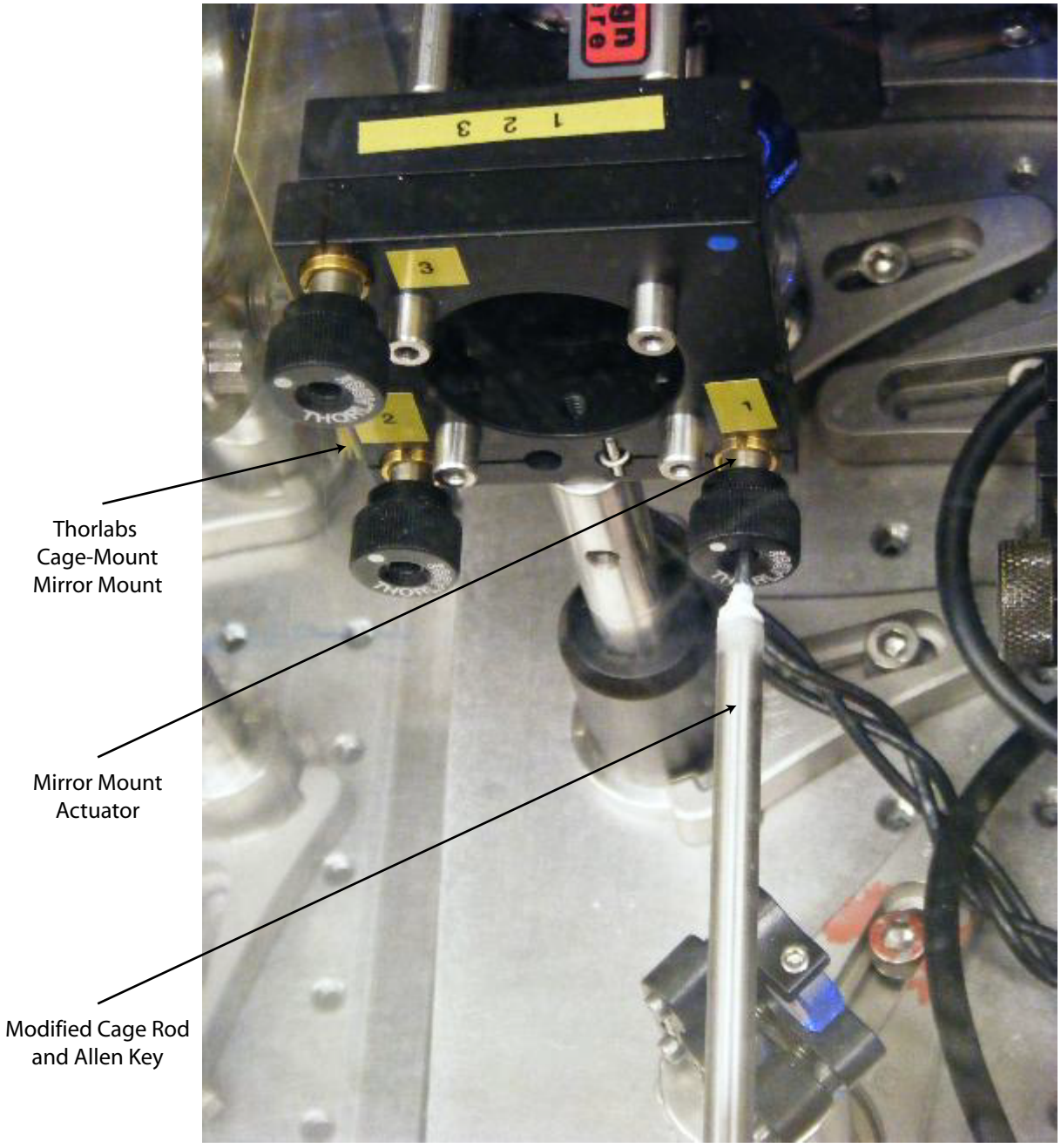

Figure F.3 Close up view of cage mount and Allen key.

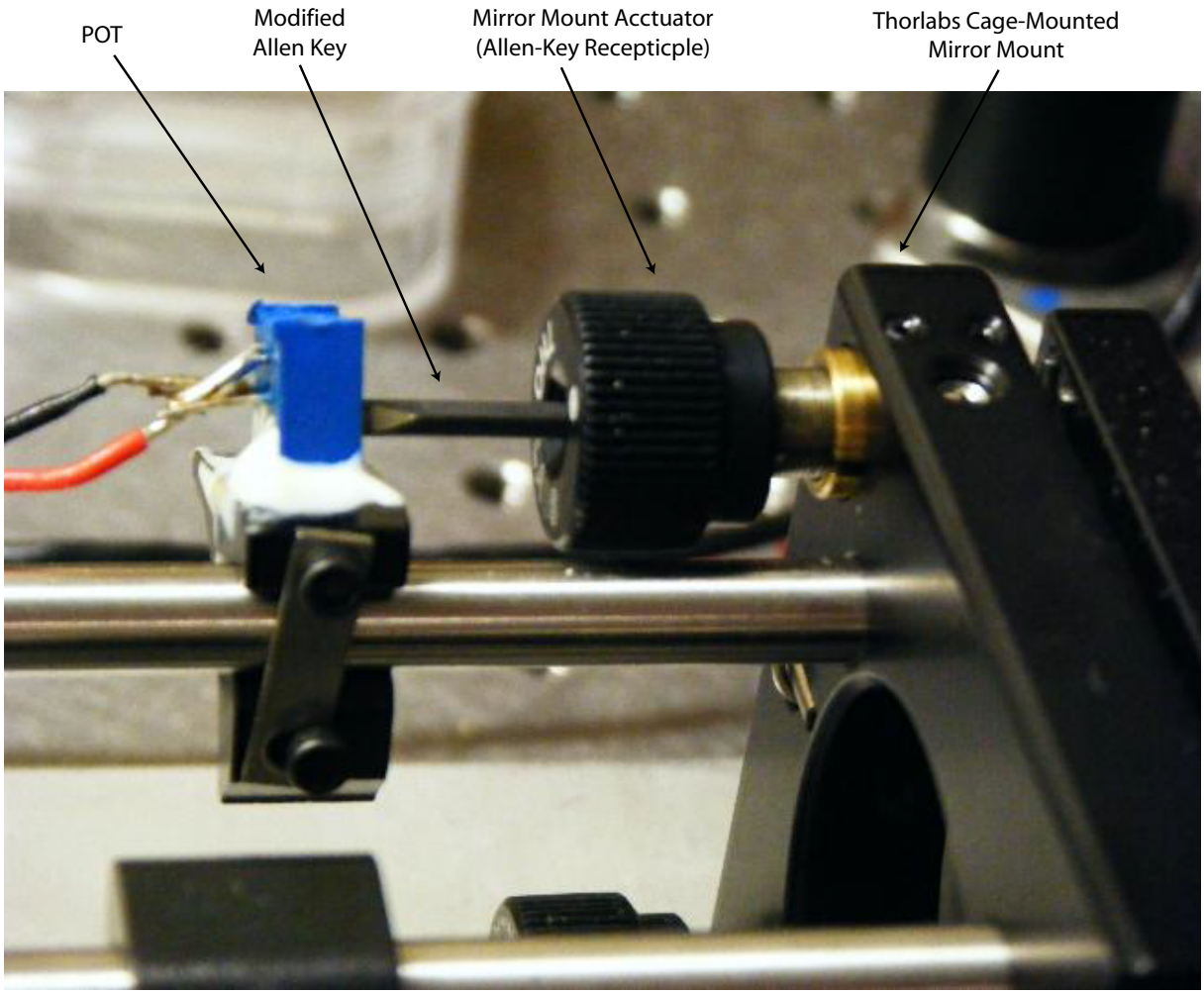

Figure F.4 Close up view of POT-mirror mount alignment jig. The POT and mirror mount are coupled through a modified Allen key thus providing relative actuator position via resistance measurements.

Appendix G: Custom Lens Characteristics

This section contains a listing of the custom lens curvatures, spacings, and associated ray traces. The ray trace figures are all drawn to scale. Many of the curvatures listed in these tables contain tolerances with more than 6 significant digits. The lens information is presented in the following order: FORT lenses, fluorescence imaging lenses, and finally addressing optics. The surface of the lenses follow the general formula:

$$f(r) \;=\; \frac{(Curv)\; r^2}{1+\sqrt{1-s\;(Curv)^2\;r^2}} + a_2 r^2 + a_4 r^4 + ... + a_n r^n,$$

where the optical axis is defined as $\hat{z}$. The deviation of the surface of the lens, f(r), is plotted as a function of r, the transverse distance from the optical axis. The lens surfaces are therefore characterized by the constants: Curv, s, a_2, a_4, ..., a_n. In the case of the addressing optics, s = 1. The table of fluorescence optics characteristics lists the parameter s as Shape. The relative positions of the on axis lens surfaces are listed in columns Zvx. All lengths are given in units of millimeters.

13 surfaces			Achromat lens, JML biconvex, optimax test plates, LINOS achromat										
Index	Zvx	Xvx	Curv	Mir/Lens	Diameter	s	a2	a4	a6	a8			
---	-----.------	------	----------	----------	---------	----------	-----E-----	------E----	-----E----	------E---	----------		
1.000000000	994.323435000		0.000480077	Lens	100.000000000	1.000000000							
SF12	1003.323435000		0.002190916	Lens	100.000000000	1.000000000							LINOS achromat 332313
BK7	1015.823435000		-0.001892076	Lens	100.000000000	1.000000000							
1.000000000	1040.823435000			Iris	100.000000000	1.000000000							
1.000000000	1140.275072000		0.014830194	Lens	95.000000000	1.000000000							JML lens CPX10298
BK7	1162.575072000 e		0.000000000	Lens	95.000000000	1.000000000							
1.000000000	1164.875011000		-0.000500000	Lens	95.000000000	1.000000000							
S-TIH11	1172.435011000 g		0.014830194	Lens	95.000000000	1.000000000							
1.000000000	1179.666262000		0.055914285	Lens	90.000000000	-0.032000000	-0.018056000	9.033300000E-07	-4.071000000E-11				
S-BSL7	1203.616262000		-0.002253267	Lens	90.000000000	1.000000000							
1.000000000	1230.523789000			Lens	70.000000000	1.000000000							
silica	1237.003789000 o			Lens	70.000000000	1.000000000							
1.000000000	1310.027964000 ?			Film	120.000000000	1.000000000							

Figure G.1 FORT achromatic triplet lens designs

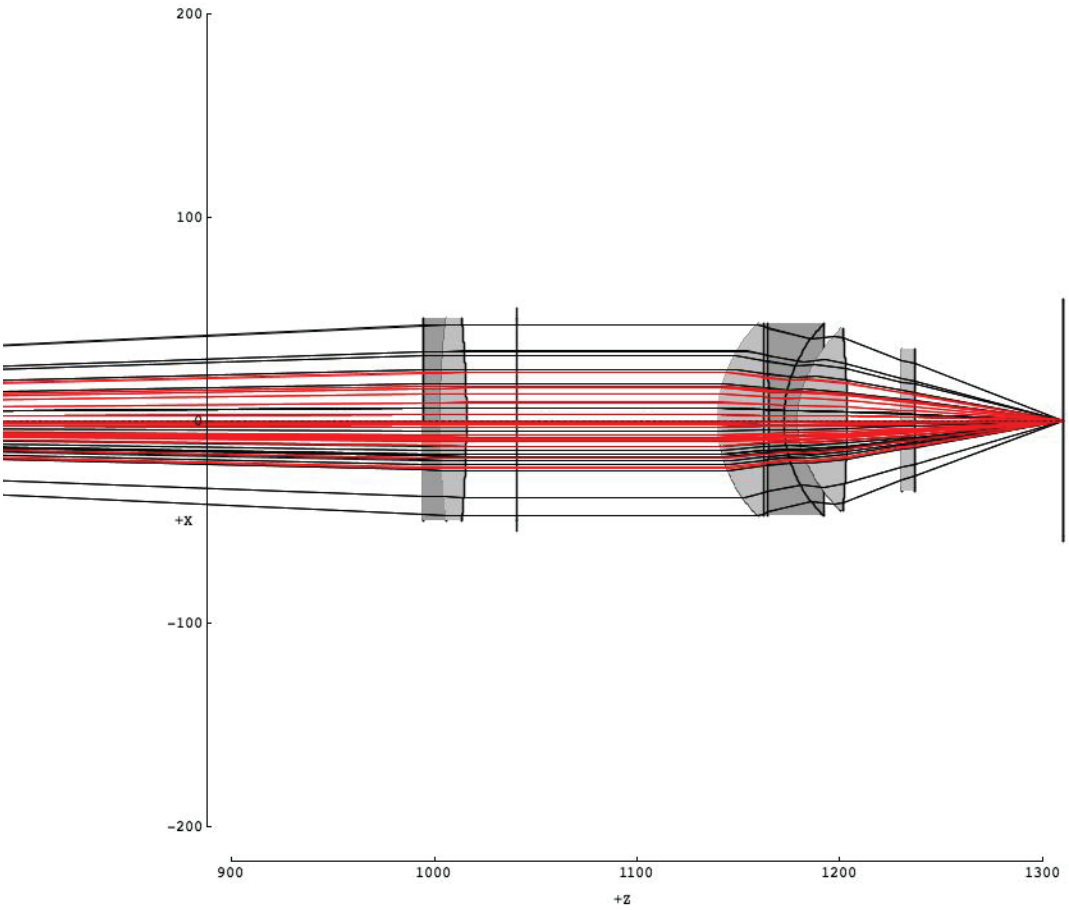

Figure G.2 FORT achromatic triplet ray trace

10 surfaces																					
Index		Zvx		Curv		Mir/Lens		Diameter		Pitch		Shape		A4		A6		notes			
---	:	-----.------	:	----------	:	---------	:	---------	:	---------	:	---------	:	----------E--	:	-------E---	:	----------	:		
1.000000000	:	73.020000000	:		:	Lens	:	70.000000000	:		:	1.000000000	:		:		:		:		
silica	:	79.500000000	:		:	Lens	:	70.000000000	:		:	1.000000000	:		:		:		:		
1.000000000	:	95.501307000	:	0.000000000	:	Lens	:	100.000000000	:		:	1.000000000	:		:		:		:		
S-TIH6	:	115.501307000	c	-0.013370000	:	Lens	:	100.000000000	:		:	-0.451200000	:	-2.143000E-07	:	6.306000E-12	:		:		
1.000000000	:	117.501307000	c		:	Iris	:	100.000000000	:		:	1.000000000	:		:		:		:		
1.000000000	:	120.501307000	c	0.003883000	:	Lens	:	100.000000000	:	0.100000000	:							JML CPX10495	:		
BK7	:	129.501307000	c	0.000000000	:	Lens	:	100.000000000	:	0.100000000	:								:		
1.000000000	:	186.548974000	?	0.003213000	:	Lens	:	95.000000000	:	-0.100000000	:							JML CPX1052	:		
BK7	:	193.148974000	h	0.000000000	:	Lens	:	95.000000000	:	-0.100000000	:								:		
1.000000000	:	378.653802000	?		:	Film	:	83.000000000	:		:	1.000000000	:								

Figure G.3 Custom lenses used in the fluorescence imaging system

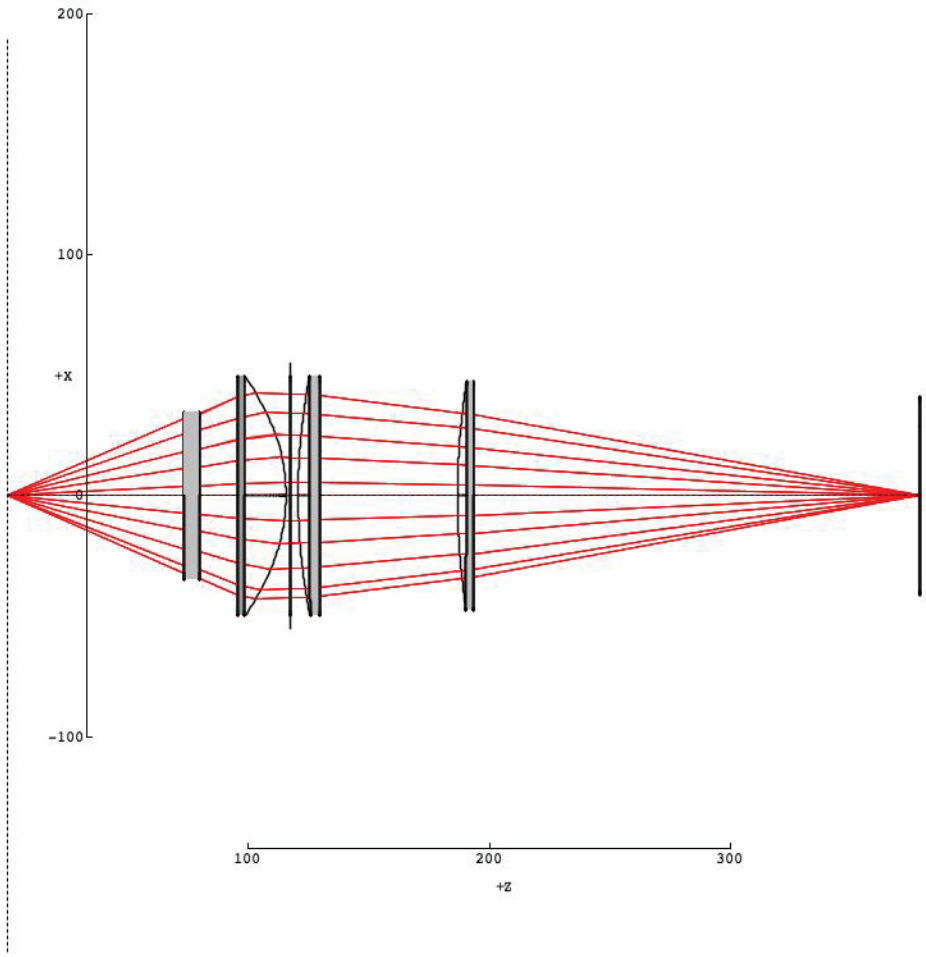

Figure G.4 Ray trace of lenses used in fluorescence imaging system

15 surfaces				Achromat lens													
Index		Zvx		Xvx		Curv		Mir/Lens		Diameter		Pitch		Tilt			
---	:	-----.------	:	------	:	----------	:	---------	:	---------	:	-------	:	-------	:	----------	
1.000000000	:	-300.000000000	:		:	0.000000000	:	Lens	:	25.400000000	:			0.000000000	:		:
BK7	:	-274.600000000	:		:	0.000000000	:	Lens	:	25.400000000	:			0.000000000	:		:
1.000000000	:	0.000000000	:	0.000000000	:	0.001467460	:	Lens	:	50.800000000	:				:	JML DBL14215	
F4	:	3.000000000	:	0.000000000	:	0.006122570	:	Lens	:	50.800000000	:				:		:
BK7	:	12.000000000	:	0.000000000	:	-0.004281560	:	Lens	:	50.800000000	:				:		:
1.000000000	:	100.000000000	:		:		:	Iris	:	50.000000000	:				:		:
1.000000000	:	104.402520000	:		:	0.011057054	:	Lens	:	50.800000000	:	0.000000000			:	KPX196	:
BK7	:	111.042520000	:		:	0.000000000	:	Lens	:	50.800000000	:	0.000000000			:		:
1.000000000	:	114.761680000	:		:	0.013449890	:	Lens	:	50.800000000	:	0.000000000			:		:
SF11	:	119.419400000	:		:	0.023850410	:	Lens	:	50.800000000	:	0.000000000			:		:
1.000000000	:	132.275050000	:		:	0.021913966	:	Lens	:	50.800000000	:	0.000000000			:	KPX184	:
BK7	:	142.997050000	:		:	0.000000000	:	Lens	:	50.800000000	:	0.000000000			:		:
1.000000000	:	159.000000000	:		:	0.000000000	:	Lens	:	65.000000000	:	0.000000000			:		:
silica	:	165.480000000	:		:	0.000000000	:	Lens	:	65.000000000	:	0.000000000			:		:
1.000000000	:	239.000704000	?		:		:	Film	:	25.000000000	:	0.000000000			:		:

Figure G.5 Lens specifications of the addressing beam optics. The triplet lens mounted into a 2” long Thorlabs Lens tube have a weight of 6.3oz. The mass of the lens is critical when mounting the lens upon the particular translation stages

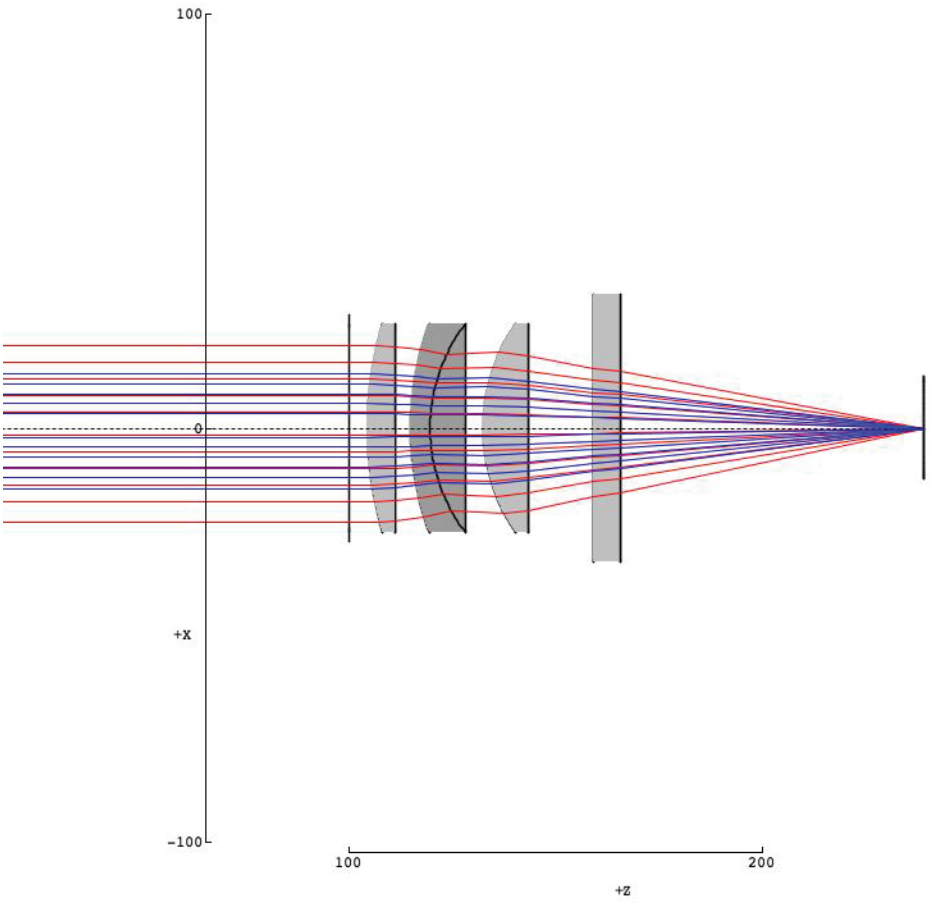

Figure G.6 Ray trace of achromatic lens designs used in addressing optics system. Triplet lens used to combine and refocus the 780nm and 480nm addressing beams.

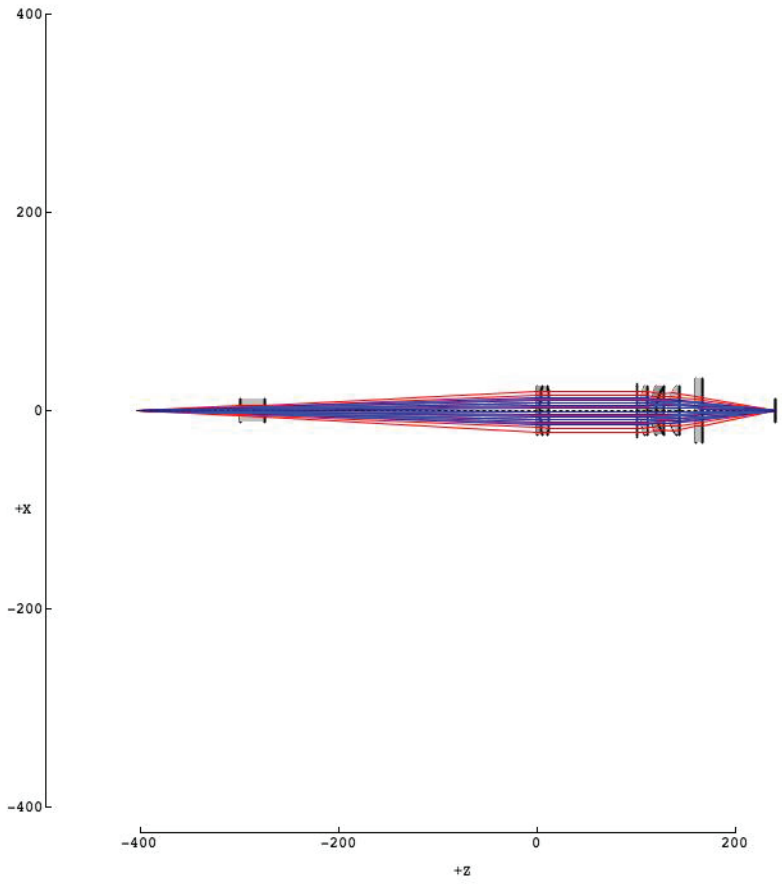

Figure G.7 Ray trace of achromatic lens designs used in addressing optics system. This ray trace includes the dichroic beam splitter used to combine the 780nm and 480nm addressing beams.